Isolated Graphene Edge Nanoelectrodes:
Fabrication, Selective Functionalization, and Electrochemical Sensing

Dissertation
zur Erlangung des akademischen Grades
doctor rerum naturalium
(Dr. rer. nat.)
im Fach: Chemie
Spezialisierung: Angewandte Analytik und Umweltchemie

eingereicht an der
Mathematisch-Naturwissenschaftlichen Fakultät
der Humboldt-Universität zu Berlin

von

M. Sc. Anur Yadav

Präsidentin der Humboldt-Universität zu Berlin
Prof. Dr.-Ing. Dr. Sabine Kunst
Dekan der Mathematisch-Naturwissenschaftlichen Fakultät
Prof. Dr. Elmar Kulke

Gutachter/innen:
1. Prof. Dr. Kannan Balasubramanian
2. Prof. Dr. Michael W. Linscheid
3. Prof. Dr. Norbert Esser

Tag der mündlichen Prüfung: 07-07-2021

Die vorliegende Arbeit wurde im Arbeitskreis von Prof. Dr. Kannan Balasubramanian am Institut für Chemie der Humboldt-Universität zu Berlin in der Zeit von November 2016 bis Oktober 2020 angefertigt.

Abstract

Graphene promises a variety of applications in energy, sensing, and catalysis, because of its unique one-atom-thick two-dimensional structure and electronic properties. The two regions of the graphene sheet at the molecular level - the basal plane and the edge, have distinct structural as well as electronic properties. The superior chemical and electrocatalytic properties of the edge along with an additional advantage of their nano-size make it an ideal electrode material in the field of analytical chemistry. However, it is important to isolate and distinguish the edge exclusively from the basal plane for its realization, which remains a challenging prospect.

First, this thesis presents a simple photolithography-based method to realize the isolated monolayer graphene edge (or GrEdge) nanoelectrode on an insulating substrate. The millimeter-long and a nanometer-wide GrEdge is found to behave like a nanowire with a high aspect ratio of 10^6-to-1. Further, the use of electrochemical modification (ECM) is demonstrated to selectively functionalize the graphene edges with metal nanoparticles (Au, Pd, Pt) and organic moieties (polymeric aromatic amino groups and diazonium salts) in a non-covalent/ covalent manner to tune the chemistry of the edge. The attachment of metal nanoparticles was used to exploit surface-enhanced Raman scattering (SERS) to characterize the chemistry of both the pristine and the functionalized GrEdge.

Subsequently, the voltammetric response at GrEdge nanoelectrodes (in both pristine and modified forms) is investigated using two redox probes: outer-sphere, ferrocenemethanol (FcMeOH) and inner-sphere, ferricyanide ($Fe(CN)_6^{3-}$). The GrEdge exhibits very high mass transport rates, characteristic of nanoelectrodes. Accordingly, the voltammetric response is found to be dictated by the kinetics of heterogeneous electron transfer (HET), attributed to the nanoscale geometry and a unique diffusional profile at the GrEdge nanoelectrodes. At the GrEdge electrode, high HET rates are observed: at least 14 cm/s for FcMeOH with a quasi-Nernstian behavior; and 0.06 cm/s or higher for $Fe(CN)_6^{3-}$ with a kinetically controlled response. Upon selective modification of the edge with gold nanoparticles, the HET is found to be reversible, with the voltammetric curves showing a mass-transport-limited Nernstian response for both kinds of probes. Furthermore, the fast HET kinetics enables the sensing of the reduced form of nicotinamide adenine dinucleotide (NADH) and flavin adenine dinucleotide (FAD) with low onset potentials and down to low micromolar concentrations. Upon modification of the GrEdge with nanoparticles, the sensing of FAD

is further improved, and for NADH, it remains the same. Hence, this thesis improves the understanding of the edges of graphene and their chemistry. It also realizes isolated GrEdge as a new class of nanoelectrode which forms an important basis within the fields of fundamental electrochemistry and analytical sciences.

Keywords: graphene, graphene edge, chemical functionalization, electrochemistry, electrochemical modification (ECM), nanoelectrodes, ultramicroelectrodes (UME), heterogeneous electron transfer (HET), HET kinetics, electrochemical sensing.

Zusammenfassung

Graphen verspricht eine Vielzahl von Anwendungen in den Gebieten Energie, Sensorik und Katalyse aufgrund seiner einzigartigen, nur ein Atom dicken zweidimensionalen, Struktur und seinen elektronischen Eigenschaften. Die beiden Bereiche der Graphenschicht auf molekularer Ebene - die Basalebene und die Kante - haben unterschiedliche strukturelle und elektronische Charakteristika. Die herausragenden chemischen und elektrokatalytischen Eigenschaften der Kante zusammen mit ihrer vorteilhaften Größe auf der Nanoskala machen sie zu einem idealen Elektrodenmaterial im Bereich der analytischen Chemie. Für ihre Darstellung ist es jedoch wichtig, die Kante von der Basalebene zu isolieren und zu differenzieren, was eine Herausforderung darstellt.

In dieser Arbeit wird zunächst eine einfache, auf Photolithographie basierende Methode zur Darstellung einer isolierten Graphenkante (kurz: GrEdge) einer Monolage als Nanoelektrode auf einem isolierenden Substrat vorgestellt. Trotz ihrer Millimeter-Länge verhält sich die nur einen Nanometer breite GrEdge-Elektrode wie ein Nanodraht mit einem hohen Seitenverhältnis von 10^6 zu 1. Des Weiteren wird der Einsatz von elektrochemischer Modifikation (ECM) demonstriert, um die GrEdge selektiv mit Metall-Nanopartikeln (Au, Pd, Pt) und organischen Schichten (polymerisierte aromatische Aminogruppen und Diazoniumsalze) nicht-kovalente oder kovalente zu funktionalisieren, wodurch die Chemie der Kante verändert werden kann. Durch die Anbringung von Metall-Nanopartikeln kann zusätzlich oberflächenverstärkte Raman-Spektroskopie (SERS) genutzt werden, um die chemische Beschaffenheit sowohl der unberührten als auch der funktionalisierten GrEdge zu charakterisieren.

Anschließend werden GrEdge-Nanoelektroden hinsichtlich ihrer elektrokatalytischen Eigenschaften in voltammetrischen Messungen getestet. Hierzu werden zwei Redox-Sonden verwendet: Ferrocenmethanol (FcMeOH) mit intermolekularem sowie Ferricyanide ($Fe(CN)_6^{3-}$) mit intramolekularem Elektronentransfer-Mechanismus. Die GrEdge weist sehr hohe Massentransportraten auf, was charakteristisch für Nanoelektroden ist. Dementsprechend wird die voltammetrische Antwort von der Kinetik des heterogenen Elektrontransfers (HET) diktiert, was auf die nanoskalige Geometrie und ein einzigartiges Diffusionsprofil an den GrEdge-Nanoelektroden zurückzuführen ist. An der GrEdge-Elektrode werden hohe HET-Raten beobachtet: mindestens 14 cm/s für FcMeOH mit einem quasi-Nernst'schen Verhalten und 0,06 cm/s oder höher für $Fe(CN)_6^{3-}$ mit einer kinetisch kontrollierten Reaktion. Nach der selektiven Modifikation der Kante mit Goldnanopartikeln erweist sich der

HET als reversibel, wobei die voltammetrischen Messkurven für beide Redoxmoleküle ein massentransportbegrenztes Nernst'sches Verhalten aufweisen. Darüber hinaus ermöglicht die schnelle HET-Kinetik die Detektion der reduzierten Form von Nicotinamid-Adenin-Dinukleotid (NADH) und Flavin-Adenin-Dinukleotid (FAD) mit niedrigen Ansatzpotentialen und hinunter bis zu niedrigen mikromolaren Konzentrationen. Durch die Modifikation der GrEdge mit Nanopartikeln wird die Detektion von FAD verstärkt, während sie für NADH gleichbleibt. Entsprechend verbessert die vorliegende Arbeit das Verständnis der Kante von Graphen und deren Chemie. Zusätzlich wird die isolierte GrEdge als eine neue Klasse von Nanoelektrode eingeführt, welche einen wichtigen Baustein in der Entwicklung der grundlegenden Elektrochemie und der analytischen Wissenschaften bildet.

Stichwörter: Graphen, Graphenkante, chemische Funktionalisierung, Elektrochemie, elektrochemischer Modifikation (ECM), Nanoelektroden, Ultramikroelektroden (UME), heterogener Elektronentransfer (HET), HET-Kinetik, elektrochemischer Sensorik.

Acknowledgements

First and foremost, I would like to express my appreciation and gratitude to my PhD supervisor, Prof. Dr. Kannan Balasubramanian, for welcoming me into his group from the beginning, his guidance and professional support and the honest scientific discussions, which led me to write this thesis. I thank my co-supervisor Prof. Dr. Michael W. Linscheid for his guidance. I am likewise grateful to SALSA and Humboldt-Universität zu Berlin for the PhD fellowship.

I am grateful to all the past and present members of the Balasubramanian Group for their support, the great discussions, and the friendly atmosphere in the lab. My special thanks to Dr. Laura Zuccaro, who has helped me in the lab at the start of my PhD, and Michael Winterfeld for helping with the chemical orders and all the other technical things in the lab. I am thankful to Rodrigo, Michel, Tilmann, Nur Selin and everyone with whom I had the chance to collaborate during my PhD project. I am grateful to Dr. Thomas Schmidt for his help with Raman spectroscopy and scanning electron microscopy. I thank all the people who made time and gave their wonderful insight on my PhD thesis.

I thank the SALSA administration, especially to Stefanie Sellon, Dr. Virginia Merck, Katharina Schultens, and Pablo Lores Lareo for their guidance in organization and administrative managements. My gratitude goes to my new friends in Berlin and all my dearest friends from IISER days. I must express my warmest appreciation to Josua, who provided amazing support in times when they were most needed.

Lastly, my appreciation goes to my family. I owe a debt of gratitude for the support and sacrifice of my parents, Prem Sheela and Lalit Mohan, to guide me and provide for me in life and in my education. I dedicate this work to my family.

Berlin, 26-04-2021
Anur Yadav

Contents

1

Introduction and State-of-the-Art

1.1 Introduction

Carbon is one of the most abundant elements on earth. The diverse nature of chemical bonding and the ease of synthesis makes carbon the important and fundamental element in biological as well as material sciences. Specifically, carbon-based materials have long been used as electrodes in both physical and analytical electrochemistry since the historical application of graphite electrodes in isolation of alkali metals from their compounds, demonstrated by Sir Humphrey Davy. Carbon electrodes have the ability to carry a large amount of electrical current, low cost, wide potential window, relatively inert electrochemistry, and electrocatalytic activity for a wide range of redox species. They have superior electrochemical properties than those of metals due to their lower charge carrier density around the Fermi level and rich surface properties.[1] Carbon as an electrode material has many different forms, having large stable frameworks of interconnecting bonds with different hybridizations and dimensions, owing to its catenation ability: zero-dimensional (0D) fullerenes, one-dimensional (1D) carbon nanotubes (CNTs), and three-dimensional (3D) graphite. The common classical carbon electrodes are graphite, glassy carbon, and carbon black. The new class of carbon electrodes (fullerenes, vapor-deposited carbon films, and microfabricated carbon structures) have distinct properties compared with the classical ones and enable novel applications in sensing, electrocatalysis, and electronics.

The realization of the 2D carbon crystal happened in 2004 when Geim and Novoselov successfully isolated, identified and investigated the electronic properties of graphene,[2–4] based on which they received the Nobel Prize in Physics "for groundbreaking experiments regarding the 2D material graphene." Graphene is an atomic layer of sp^2 hybridized network of carbon atoms packed into a 2D honeycomb lattice,[3,4] and can be considered as the elementary building block for the sp^2 hybridized carbon allotropes of other dimensionalities.

On a molecular level, a single layer of graphene sheet has two distinct regions, based on the structural as well as electronic properties - the basal plane which consists of the 2D conjugated sp^2 carbon atoms and the edge whose creation breaks the aromaticity of the honeycomb lattice. The edge may consist of the defective 1D line (one-atom-thick) of carbon atoms with dangling bonds, and is expected to alter the properties of graphene locally and exhibit specialized properties different from that of the basal plane. They have superior chemical reactivity[5–7] and electron transfer (ET) properties than the relatively inert basal plane.[8–12] The role played by the edges becomes dominant when narrowing down graphene sheets to edge-rich structures such as graphenenanoribbons (GNRs), e.g., by lithographic patterning.[13–18] Electronic properties, in particular, depend strongly on the influence of the edges, for example, GNRs with widths below 20 nm can generate a bandgap that is dependent on the ribbon width and crystallographic orientation of the edges.[19–21] Therefore, stronger nanosize effects are expected on the properties of edge-rich graphene, which are governed mainly by electronic correlations, their morphology, and consequent boundary conditions.[22–26] Hence, the graphene edge is of extraordinary interest, which has important implications on the physical and electrical properties of graphene.[12,19,27]

The further narrowing down of graphene is needed to reduce the basal plane to the smallest possible width, in order to address the edge of graphene selectively (or in an isolated form). However, the realization of isolated graphene edge is challenging since it cannot be realized in a free-standing form of carbon edge. Such a graphene form (isolated graphene edge) will have the maximum influence of the edge on the characteristic properties separated by the basal plane. In theory, the isolated graphene edge represents a 1D line defect in the 2D graphene, and it may be considered as an ideal 1D system with the thinnest wire electrode[28,29] that one could realize due to its nanoscale geometry. Hence, it may be expected that the electrochemistry at such electrodes is unique with a (quasi) steady-state behavior, which is a typical characteristic in case of nanoelectrodes. This kind of electrode behavior provides a possible application to study fast heterogeneous electron transfer (HET) kinetics, as has been demonstrated with other nanoelectrodes such as single carbon nanotubes (CNTs) and nanoparticle.[30–32] However, in the reports until now, the isolated graphene edge with complete isolation of the effect of the basal plane has not been demonstrated. The observed cyclic voltammetric (CV) profiles have shown diffusion-limited response without indication of a (quasi) steady-state behavior.[12,33] Moreover, there is still no report about values of ET rates at an isolated graphene edge. By comparison, at 1D individual CNTs the electrochemistry was found to be kinetically limited,[34,35] with a high mass transport rate and has allowed the probing of fast electrode kinetics (ET rate > 1 cm/s for a ferrocene redox probe).[30] Therefore, a new fabrication method is required in order to isolate the edge and its properties from the basal plane. This thesis aims to reveal important aspects of the so-far unknown properties of the isolated edge, in particular its electrochemical properties and their implications for electrochemical sensing. In addition,

the thesis also provides a concept to selectively modify the edge, and its subsequent effect on the ensuing properties.

In this thesis, the isolated monolayer graphene edge was realized using photolithography. The chemistry at the edge was modified with nanoparticles and organic groups for its potential use in catalysis and sensing devices. Further, its electrochemical properties (in both unmodified and modified forms) were investigated to probe the nanoelectrode behavior and to study the fast ET kinetics at such electrodes. The sensing performance of the isolated graphene edge electrodes was evaluated for the reduced form of nicotinamide adenine dinucleotide (NADH) and flavin adenine dinucleotide (FAD).

State-of-the-Art

Section 1.2 discusses the fundamental understanding of graphene edges. The creation of the edges leads to breaking of the bonds between sp^2 hybridized carbon atoms, forming the unstable dangling bonds. The presence of dangling bonds makes edges more reactive chemically and active electrochemically, in comparison to the relatively inert basal plane. Majority of the published work to realize graphene edges focuses on the edge-rich forms of graphene and bulk graphene: GNRs, nanopatterned graphenes, etc.;[7,19,36] and edge-plane pyrolytic graphite (EPPG), solution-processed graphene oxide, multilayer graphene edges.[9,37–39] Lithographic patterning using plasma etching is the most common method to fabricate edge-rich graphene, which may also be used to realize the isolated edges. The realization of a 1D isolated graphene edge is important to reduce the effect of the basal plane completely from the 2D graphene device. However, there are not many reports highlighting the importance of exclusive or isolated edges. There are very few demonstrations of devices realized based on isolated monolayer graphene edges.[12,40]

Section 1.3 summarizes the chemical functionalization of graphene edges, which has primarily been investigated in liquid-based exfoliation procedures.[10,41–43] Other methods include plasma etching[16,19,44–46] as well as organic synthesis.[47,48] However, complete selectivity of the edges for functionalization has hardly been achieved. Electrochemical modification has been used frequently to functionalize graphene-related materials.[49–51] ECM along with its simplicity provides selectivity by utilizing the ET chemistry, thus, the modification can be localized to the conductive area of substrates. A review of ECM-based methods (metal nanoparticle electrodeposition, electropolymerization, and aryl diazonium chemistry) is presented here for modification of graphene and isolated edges.

Section 1.4 reviews the characterization methods which can be used to study graphene edges. It has been possible to investigate the graphene edge at an atomic scale using high-resolution electron microscopy methods, without any specialized fabrication.[52–55] For isolated edges prepared using lithographic patterning, the presence of an insulating polymer layer, however, acts as an obstacle for such analytical tools. Raman spectroscopy is highly sensitive to edges, defects, and doping in graphene.[56–63] Further, the deposition of metal

nanoparticles on graphene and functionalized graphene is demonstrated, which has been used to achieve surface-enhanced Raman scattering (SERS) effect, and consequently, to identify the chemical groups attached to graphene after functionalization.[50,51,64,65] A similar SERS strategy can be employed to gather spectroscopic information about the chemistry of the functional groups present or formed at the graphene edges.

Section 1.5 reviews the electrochemical studies which have been performed using a variety of redox probes at the graphene edge and basal plane electrodes. In most studies, the presence of edge and defect sites enhances the ET properties of graphene electrodes produced from different methods (e.g. exfoliated, vapor-deposited, etc.), and in both monolayer and multilayer forms - edge plane sites in EPPG, individual CNT ends, stacked graphene nanofibers with open edges, edge-like graphitic islands in CVD-graphene.[1,8–11,38,66–70] On the other hand, the isolated graphene edge of a single-layer CVD-grown graphene sheet is different from the surface edge-planes of HOPG or the ends of individual CNTs. Given its size of $\sim$ 1 nm (ideal case), it has an additional advantage of nanoelectrode behavior,[12] which is important to study fast ET processes that are often too fast to investigate with conventional electrodes.[30–32,71,72] This section also involves a brief discussion on the differences between the nanoelectrode and conventional macroelectrode electrochemical behavior. Further, the electrochemical sensing abilities of edge-rich (and isolated) graphene electrodes towards biomolecules such as double-stranded DNA and all four bases,[37,73] β- reduced form of nicotinamide adenine dinucleotide (NADH),[38] ascorbic acid (AA),[12,73] uric acid (UA),[12,73,74] etc. are summarized.[26,74] The excellent properties of graphene and nanoelectrode behavior make isolated graphene edge a desirable electrode material for electrochemical sensing of chemical and biological molecules in the field of analytical chemistry.

1.2 Graphene Edge

At the edges of a graphene sheet, the σ bonds between adjacent carbon atoms of the sp^2 hybridized network break and disrupt the honeycomb lattice of graphene. There are two main configurations of the edges, depending on the crystallographic orientation of the lattice: zigzag and armchair edges (figure 1.1). However, the edges often consist of complex geometries (a mixture of both), since they typically do not develop along a unique crystallographic direction. The disruption of the π conjugation network also increases the energy of the electrons at the edge sites, leading to a significant change in chemical reactivity and electronic properties in comparison to the relatively inert basal plane.

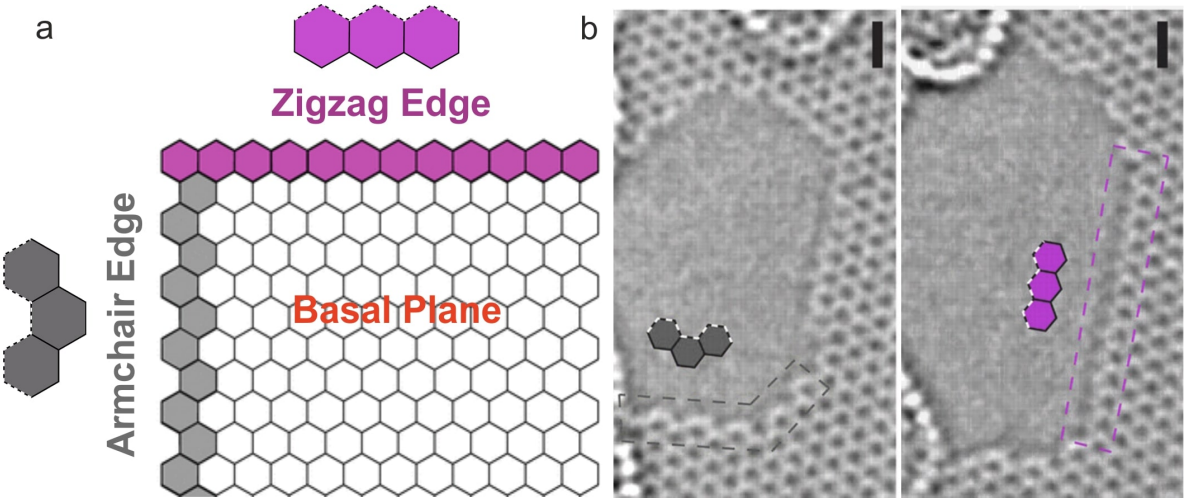

Figure 1.1: (a) Schematic of a graphene sheet showing basal plane and edge regions, along with the two main configurations of the edges: armchair and zigzag edges. (b) TEM image of the configurations of the carbon atoms at the edge of graphene: armchair configuration (on left panel) shown in inset box consisting of roughly 12 hexagons with a turn; and zigzag configuration (on right panel) shown in inset box with long continuous segment 12 hexagons. Reproduced from references [75] with permission of the American Association for the Advancement of Science.

1.2.1 Properties: Basal Plane Vs Edge

In an ideal environment without any reactants, the edge consists of the unstable σ and π dangling bonds,[62,76,77] with the formation of unsaturated sp^2 and p_z orbitals,[78] where the carbon atoms comprise of the di-radical groups. The dangling bonds upon exposure to air or solution are prone to termination by various capping moieties (oxygen-containing groups) or adsorption of other reactive species.[79] In contrast, a perfect basal plane is inert to chemical reactions under ambient conditions since it has no edge sites or defects (in theory), leading to the carbon atoms with satisfied valances, thereby, no presence of unstable dangling bonds. Experimentally, it has been shown through the chemical functionalization of graphene that the reactivity of edges is higher than that of the basal plane.[5–7] For example, Sharma *et al.*

reported the higher number density of functional groups at the edges than the bulk graphene after functionalization with diazonium salts, and with at least two times higher reactivity at the edges (figure 1.2A).[6] Several electrochemical studies have reported the stronger electrocatalytic activity of graphene edges in comparison to the basal plane.[12,38,67,74,80] In short, for the carbon atoms localized on basal plane and different types of edges, the chemical reactivity and electronic properties depend on their conjugation system, thereby yielding discrepancies in electrical, magnetic, and chemical properties.

The properties of high edge density-based graphene nanostructures are deeply rooted in the atomic configuration of the edges. Figure 1.2Ba shows the formation of armchair (red) and zigzag (blue) edges by cutting the graphene along two crystallographic directions. In GNRs, zigzag edges are energetically less stable than armchair edges, even though they have a lower number of dangling bonds per unit edge length. This can be explained by the formation of different bonds and Clar's representation for both edges. Firstly, the formation of triple bonds between the outer carbon atoms reduces the energy of the electrons at armchair edges,[78] while for zigzag edges, the p_z electrons are instead confined on each outer carbon atom maintaining a radical singlet configuration responsible for the so-called 'edge state' making them very energetic (figure 1.2Ba).[21,81] Secondly, from a chemical perspective, graphene can be represented as a polycyclic aromatic hydrocarbon (PAH), and Clar's theory is used to explain the reactivity of PAH.[82–84] PAH is a common name given to aromatic hydrocarbons with more than two unsubstituted benzene rings fused together. The six delocalized π electrons in a benzene ring are depicted by a circle called a Clar sextet and can be assigned to a carbon hexagon if it allows two complementary Kekulé resonant configurations.[27] According to Clar's rule, the representation with the maximum number of Clar sextets is the most stable structure for the π electron network of small PAH molecules.[85,86] Graphene has maximum Clar sextets with all electrons belonging to it and no isolated C=C bonds. Such structure is referred to as fully benzenoid and is indicative of higher thermodynamic stability and lower chemical reactivity.[83] In other words, the most stable structure of a PAH molecule is the one maximizing the number of aromatic rings among its unit cells. This explains the low chemical reactivity of graphene.

For graphene edges, the disruption in the π conjugated network breaks the perfect Clar formula. This introduces localized C=C bonds with distinct edge geometry and aromaticity depending on the type of edge. Zigzag-edged graphene molecules cannot be represented by a fully benzenoid structure (independent of the width), since they exhibit a limited number of Clar sextets with a large number of reactive localized double bonds at the edge.[26,84] The zigzag geometry promotes infinite isomeric Clar structures (as depicted by the green arrows in figure 1.2Bb), primarily because aromatic rings can slide along the length of the GNRs, highlighting the intrinsic reactivity of the molecule.[87] In contrast, armchair edges may allow a lower number of localized C=C bonds with a limited number of Clar's structures and even a fully benzenoid structure, independent of the width of the structure, indicating a lower

chemical reactivity. In figure 1.2Bc, i (fully benzenoid structure) has a unique isomeric structure, whereas iii has a unique isomeric structure with double bonds localized at the edges; ii has localized or reactive double bonds on the edges with two resonant structures

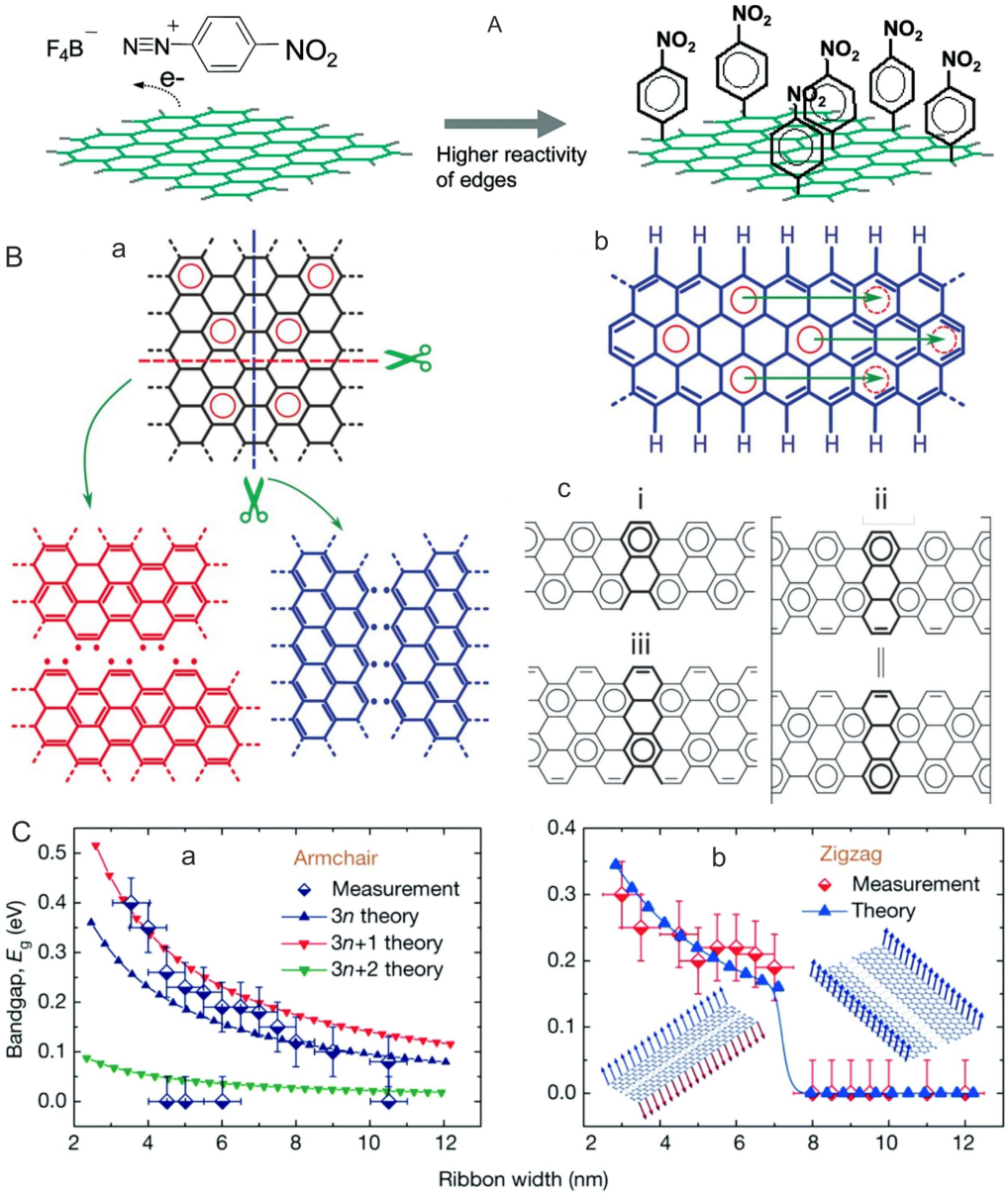

Figure 1.2: (A) The high reactivity of the edges leads to higher number density of functional groups at the graphene edges than its basal plane after the functionalization. Adapted from reference [6]. (B) Different edges of graphene: (a) Formation of edges by cutting the graphene along two crystallographic directions: zigzag edges and the singlet radical bond (blue) and armchair edges and rearrangement of radicals into triple bonds (red). (b) Zigzag edged GNR, the green arrows depict the isomeric structures obtained by sliding the position of the aromatic rings across the GNR. (c) Armchair-edged GNR, the number of isomeric structures, and the presence of localized double bonds depend on the width of the GNR. (C) Bandgap measured as a function of ribbon width in (a) armchair and (b) zigzag nanoribbons. Reproduced from references [6], [26], [84], [88] and [20] with permissions of American Chemical Society, Wiley, Elsevier and Nature Publishing Group.

with its reactivity between a benzenoid system and localized double bonds. The bandgap is a measure of electronic properties in graphene-based materials. A perfect graphene lattice has a bandgap of zero. For Graphene edges, the breaking of pristine symmetry of graphene leads to changes in its electronic structure, thereby the bandgap. The bandgap can be tuned for GNR by changing the width of the ribbon: armchair-edged GNR (in figure 1.2Ca) displays an inverse proportionality to the ribbon width, while for zigzag edges (figure 1.2Cb), a bandgap of 0.2 - 0.3 eV is observed when their widths are less than 7 nm and it vanishes (semiconductor-to-metal transition) for width more than 8 nm.[20,21]

In most PAH representations, molecules are terminated by mono-hydrogenated carbons (C−H) at the edge. The specific functionalization and aromaticity of the edge are thermodynamic criteria and are still poorly understood for graphene.[89] It depends on the chemical activity of the functional group (or chemical environment such as oxygen, carbon dioxide, water, and ammonia) and the specific chemistry of the carbon atoms in its proximity.[90]

1.2.2 Edge-Rich Forms of Graphene (Nanographenes)

Edges are formed during all the graphene production methods from exfoliation-based to chemical growth methods.[2,8,91] However, it is essential to minimize the basal plane region as much as possible in order to see the significant contributions from the edge on the characteristic properties (e.g. bandgap) of graphene.[19,26,27,92] In literature, the edge-rich graphene nanostructures are referred to as nanographene.[93] Such structures can be divided on the basis of the size of the structure and chemical nomenclature of 35 fused PAHs recognized by the 1957 IUPAC rules.[82] Molecular graphene is defined as PAHs having sizes of 1 to 5 nm,[93] nanographene can be a graphene fragment ranging from 1 to 100 nm in size, and once the size exceeds 100 nm, they can be directly regarded as graphene (figure 1.3a). An ideal graphene lattice can be represented as a PAH that consists of an infinite number of benzene rings. The edge-rich graphene nanostructures are realized in the following forms:

- GNRs are very finite 1D stripes of graphene with a width of few nanometers (10-100 nm) (figure 1.3a) synthesized using methods such as CVD growth,[94] metal-based catalytic cutting[95] and unzipping of CNTs.[96] The combination of photolithography and reactive ion etching (RIE) or plasma etching is another common method to etch and narrow down the graphene from the edges as well as to pattern different structures (figure 1.4a).[13,97] They have been explored widely to examine the edge and nanoscale size effects on bandgap and chemical reactivity in graphene.

- A densely patterned graphene sheet with a lot of regularly arranged holes with extreme density of edges is another example. For example, Jessen *et al.* fabricated graphene superlattice (figure 1.3b) where the graphene sheet is enclosed in van der Waals heterostructures, and it consists of triangularly arranged holes with a period of 35 nm and minimum feature sizes of 12-15 nm.[98] Graphene nanomesh (GNM) and

nanopatterned graphene are other such kind of edge-rich structures.[36,99] However, these nanostructures are fabricated using very elaborate lithography.

- Graphene nanopores are nanosized pores fabricated in graphene monolayer for potential applications of translocation of atomic or molecular species (such as single-molecule DNA). The pores are obtained by placing a graphene sheet over a microsize hole in an appropriate membrane and drilling a nanosize hole (2-40 nm) in it using an electron beam,[100,101] or etching (in O_2 or O_3,[102,103] liquid-phase oxidative etching,[104,105] nanoparticle-catalyzed etching[106]).

- Graphene quantum dots (GQDs) are irregularly shaped 0D nanostructures of graphene with sizes ranging from several to 100 nm (figure 1.3a). They demonstrate quantum confinement and edge effects leading to their photoluminescence properties. The energy bandgap of GQDs can be controlled by their size and surface chemistry (different density of sp^2 sites) properties.

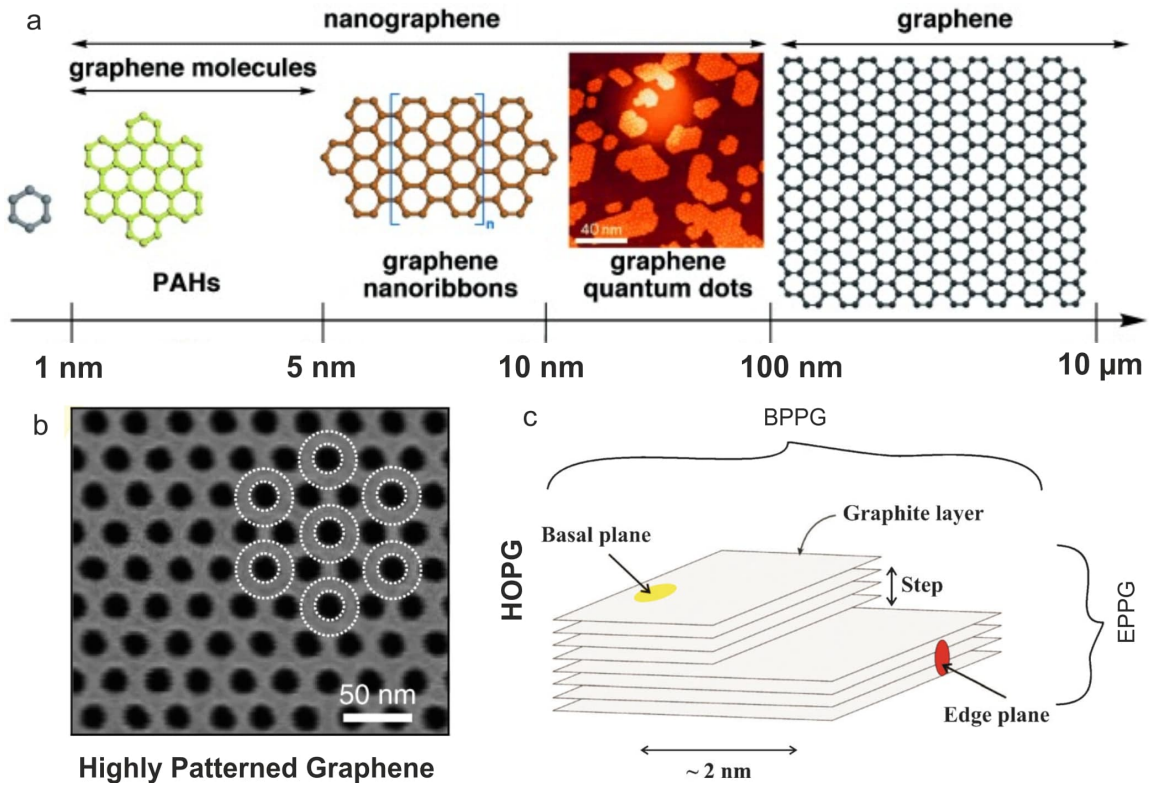

Figure 1.3: (a) Schematic illustration of graphene terminology according to their size scale: Graphene molecules (1-5 nm); ideal GNRs have width <10 nm; GQDs have sizes ranging from several to 100 nm. Nanographene units are graphene fragments with diameters of <100 nm, while graphene should exceed 100 nm in both directions. (b) Scanning electron microscopy image of the grapene superlattice encapsulated in van der Waals heterostructure. (c) Schematic representation of a HOPG surface showing discrete basal and edge planes like-sites/defects which exhibit contrasting behaviours in terms of electrochemical activity. Reproduced from references [107], [98] and [38] with permissions of Wiley, Nature Publishing Group and Royal Society of Chemistry.

- The highly ordered HOPG consists of parallel layers of graphite where surface defects occur in the form of steps exposing the edges of the graphite layers as shown in figure 1.3c. The two planes of HOPG are called Edge-plane pyrolytic graphite (EPPG) and basal-plane pyrolytic graphite (BPPG). EPPG electrodes are fabricated from HOPG by cutting the desired electrode geometry such that the layers of graphite lie perpendicular to the basal plane surface of HOPG.[68] Due to their different nature of the chemical bonding and atomic structure, the two planes exhibit different electrochemical properties.[38,68,69]

1.2.3 Graphene Patterning (Narrowing) using Plasma Etching

Of all the fabrication methods, lithographic patterning provides highly edge-rich graphene with significantly reduced basal plane region. This is typically achieved either by decreasing or narrowing down the graphene width to few nanometers or etching holes in the graphene sheet to form a superlattice or nanomesh to increase the proportion of edges.[18,36,99] Lithographic patterning has also drawn great attention because of its easy approach to top-down fabrication and large-scale device integration.[4,97] It is commonly used along with RIE or plasma etching to pattern nanostructures in the microfabrication industry. RIE is a plasma-based etching process where the highly reactive species interact with the substrate or thin films in a mechanical and/or chemical manner. Typically, the patterning process involves: the coating of a substrate or a thin film (e.g. graphene) with a resist or polymer mask (an insulating layer) in the required regions (or in a required pattern), etching the exposed areas of the substrate, and stripping of the remaining resist (figure 1.4). For graphene, the charged ions and radicals in the plasma react with the carbon atoms of the uncovered region of graphene resulting in etching of that region. Lithographic patterning offers better control in varying the widths of GNRs (figure 1.4A,B,C),[13,15,18] or the spacing between each hole in an edge-rich highly patterned graphene consisting of an array of holes (figure 1.4D).[98,99] For example, Chen and group synthesized 20-500 nm wide GNRs using electron-beam lithography followed with oxygen plasma etching.[108] In other reports, GNRs of widths 6-31 nm were fabricated using nanowires as the etching masks followed by oxygen plasma etching;[15] GNRs of width less than 5 nm were fabricated using hydrogen plasma to selectively etch the graphene from the edges,[16] and dry anisotropic etching method.[17]

However, graphene nanostructures of sub-10 nm width needed elaborate and expensive nanofabrication techniques such as block copolymer lithography, electron-beam lithography, nanosphere lithography, nano-imprint lithography, and scanning tunneling microscope lithography.[18,36,98,99,109] Although the top-down lithography and etching technique is very successful in the fabrication of edge-rich graphene, patterning methods have only produced nanostructures of widths down to $\sim$ 10 nm because of the limits of lithography resolution. In all these cases, although the edge effects dominate the characteristic properties, the contribution due to the basal plane is not excluded completely.

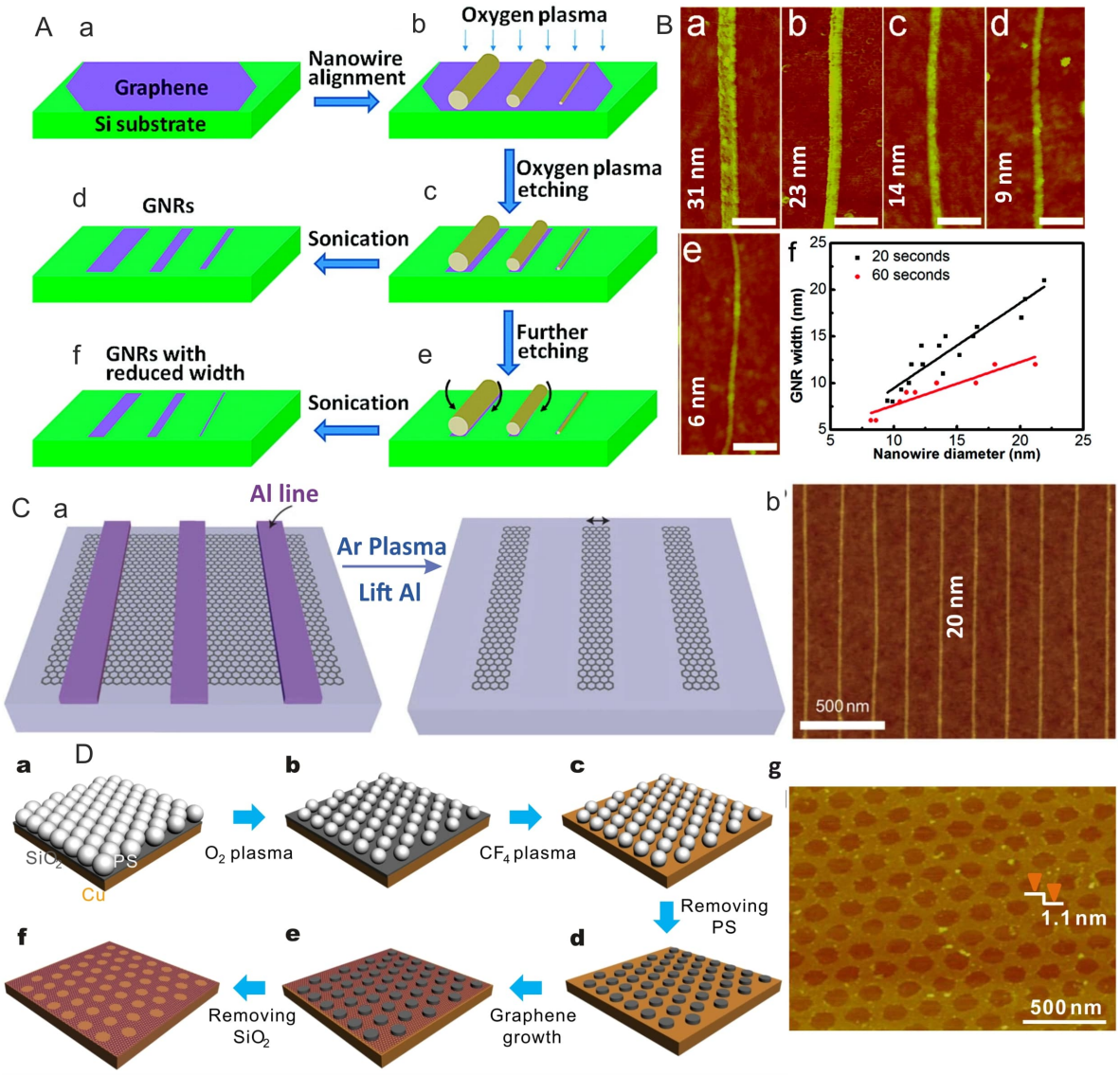

Figure 1.4: (A) Schematic for the fabrication process to obtain GNRs by oxygen plasma etching and a nanowire etch mask; (B) AFM images of selected GNRs with widths of about (a) 31 nm, (b) 23 nm, (c) 14 nm, (d) 9 nm, and (e) 6 nm. Scale bars: 100 nm. (f) Scaling of the GNR width with mask nanowire diameter for two different oxygen plasma etching times of 20 s (black) and 60 s (red). (C) Schematic for the GNR fabrication process using Al line and Ar plasma etching. (b) AFM image of a 20 nm width GNR array at $\sim$ 200 nm pitch. Reproduced from references [15], [13] and [99] with permissions of American Chemical Society and Nature Publishing Group.

1.2.4 Isolated Graphene Edge

The ability to selectively address only the atomic edge of monolayer graphene representing a 1D line of defects is not straightforward and has not been explored, since it cannot be realized in a free-standing form of carbon edge. The edge boundary is completely isolated from the basal plane region in this case and it is referred to as isolated graphene edge. One way to realize it is using the basal plane region of graphene as mere support to edge by appropriately covering or embedding the basal plane with a polymer layer and then

exposing the edge boundary (by means of mechanical cutting or etching). In this way, the contribution from the inert basal plane on the characteristic properties of the graphene edge is the bare minimum. There are only three reports in the literature on the realization of such edges.[12,33,40] The isolated graphene edge was fabricated for the first time by Yuan and co-workers. They embedded the monolayer graphene sheet selectively with an insulating thin film of epoxy resin (ER) as shown in figure 1.5A: for only the basal plane (without edges), ER was coated around the graphene sheet such that a square window was left in the middle; and for the isolated edge, entire graphene sheet was embedded in ER and then vertically cut to expose its cross-section.[12] However, the complete isolation of the basal plane effect has not been demonstrated as indicated by the diffusion-limited voltammetric response in these reports.

Other method includes fabricating isolated edge in a nanopore like structure (shown in figure 1.5B) called graphene edge embedded nanopore (GEEN) where the fabrication requires elaborate and complicated processes like the deposition of the insulating layers and forming holes with focused ion-beam milling (FIB) and deep reactive-ion etching (DRIE).[40] In both examples, the main aim was to separate the electrochemical activity of isolated graphene edge from basal plane contribution.

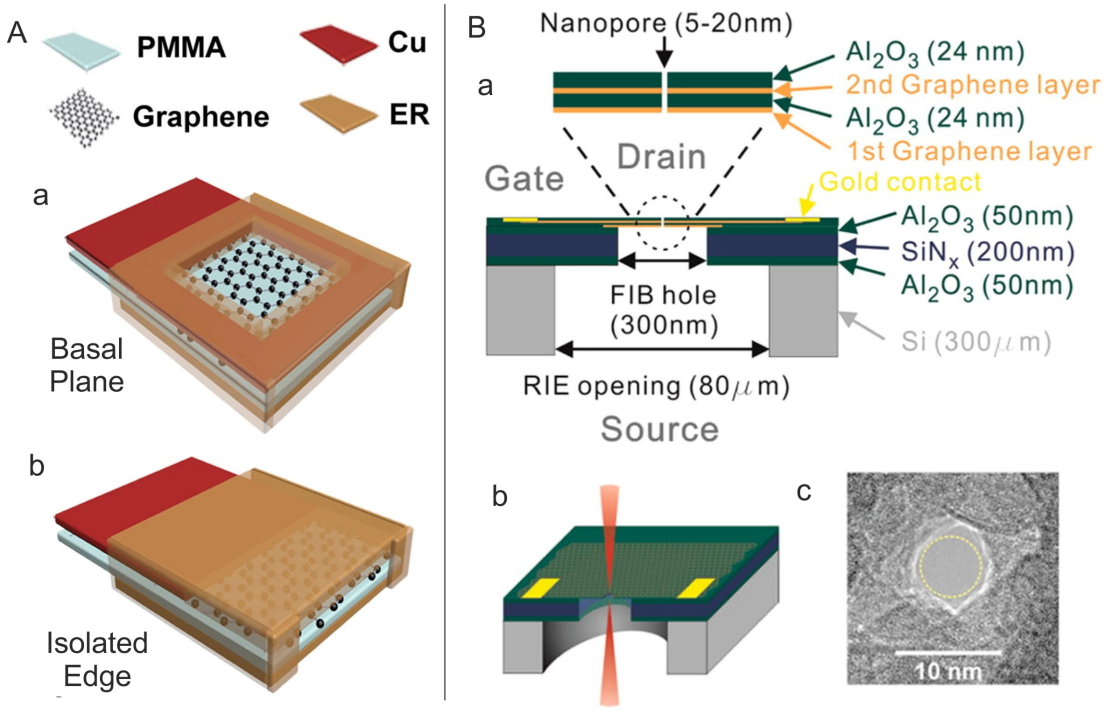

Figure 1.5: (A) The configurations of isolated (a) basal plane and (b) edge electrodes, of CVD graphene sheet embedded in epoxy resin (ER). (B) A graphene edge embedded nanopore (GEEN) structure: (a) Schematic of graphene-embedded stacked membrane structure and fabrication showing the thickness of each layer as well as diameters of RIE, FIB, and nanopore holes. (b) Focused electron beam (CBED mode) in TEM is used to fabricate a single nanopore of 5-20 nm diameter. (c) TEM image of a 5 nm nanopore. Reproduced from references [12] and [40] with permissions of Nature Publishing Group and American Chemical Society, respectively.

1.3 Chemical Functionalization

Chemical functionalization of graphene-based nanostructures is required to obtain new properties, improve processability, and expand the range of potential applications.[110,111] Graphene-based materials are poorly soluble in most of the solvents, have zero bandgaps, and have inertness to a chemical reaction, and all these properties are essential for their realization in any form of application.[112,113] The attachment of functional groups can improve and tune these properties. For example, by chemically modifying CNTs, graphene, and GNRs, electronic devices including transistors and sensors have been demonstrated.[112,114–117]

The different types of functionalization can be classified under metal decoration, covalent and non-covalent attachment depending on the interaction between the graphene and functional groups. The covalent functionalization leads to the formation of bonds on the basal plane of the carbon lattice which changes the hybridization of graphene carbon atoms from sp^2 to sp^3, introduces defects, and disrupts the intrinsic properties of graphene. Non-covalent functionalization involves molecule-to-graphene intermolecular forces (e.g. π-π, cation-π) and is particularly attractive since it preserves the conjugated π-system of graphene. The addition of phenyl radicals, diazonium compounds, carbenes, or Diels-Alder cycloaddition reactions to graphene is a common covalent method, while metal nanoparticle decoration, surfactants, polymers, small aromatic, and organic groups are explored under non-covalent methods.

1.3.1 Functionalization of Graphene Edges (Examples)

The density of the functional groups after any functionalization is usually high at the edges because of their relatively high reactive nature.[5,6] However, complete selectivity of the edges for functionalization have hardly been achieved. In literature, chemical functionalization of edge-rich graphene has primarily been investigated in liquid-based exfoliation procedures. Other methods include plasma etching in different environments as well as organic synthesis. Several techniques such as the use of oxidizing agents, diazonium chemistry, plasma etching in different environments, bottom-up synthesis, and electrochemical modification have been used frequently.

- Liquid-based functionalization is the most common method for edge modification and can be divided into two broad approaches. The first approach involves functionalization of the graphite (using organic reactions, e.g. diazonium electrografting)[118] followed by the exfoliation (using methods like sonication, ball milling, etc.)[119,120] of the edge functionalized graphene. For example, in situ reaction of graphite with 4-bromophenyl radical, followed by its sonication.[120] The main disadvantage of this method is that the edge selectivity for the functional groups is only in the case of a bulky molecule (e.g. 4-bromophenyl) that does not intercalate between graphitic lay-

ers. In the second approach, functionalization is carried on the edge of the graphene flakes which are already exfoliated in solution. For example, exfoliated graphene flakes are functionalized with a PAMAM dendron by two different schemes (figure 1.6): (I) cycloaddition reaction of paraformaldehyde (conjugated with α-amino acid) with graphene, followed by condensation reaction with dendron and (II) graphene with the carboxylic acid group on the edges is directly subjected to an amide condensation reaction with the dendron. It is apparent from the TEM images (captured after the addition of gold particles to the dispersions for the identification of the reaction sites) that Au particles are present both on the basal plane and the edges for scheme I, while in contrast, the particles are mostly present at the edges for scheme II. The major drawback here is that both the schemes lack edge selectivity as evident by the functionalization occurring at the basal plane surface even in the case of scheme II, although at a lower density.

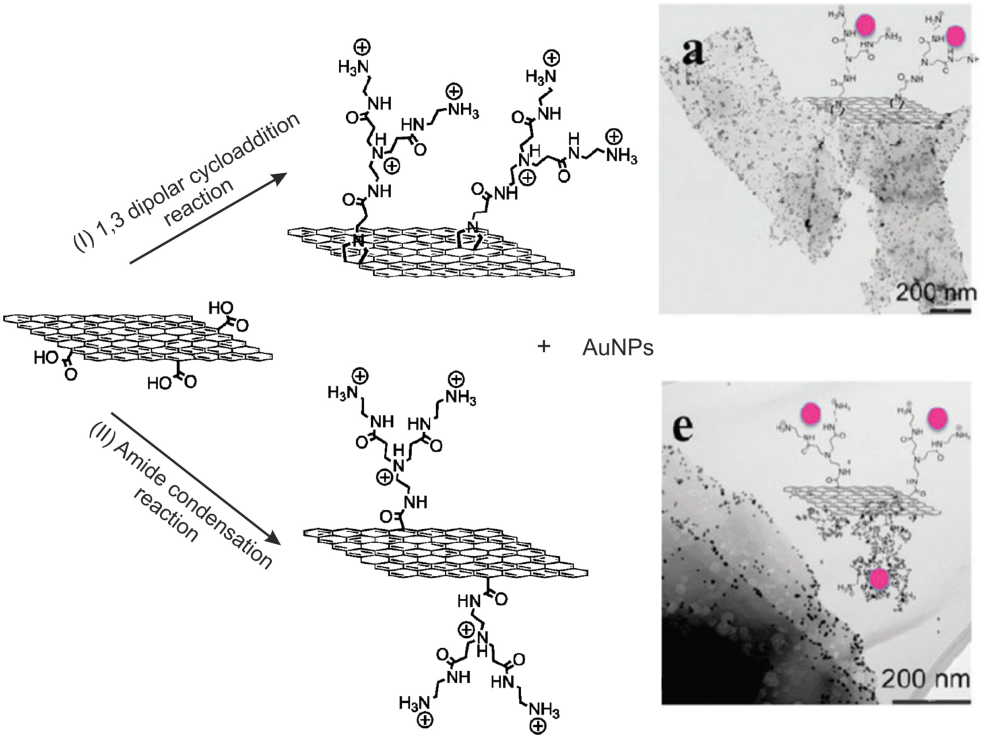

Figure 1.6: Selective functionalization of graphene bulk or graphene edges: Scheme I involves cycloaddition of PAMAM dendron to graphene, Scheme II involves amide condensation reaction of PAMAM dendron with oxidized groups on graphene edges followed by addition of Au particles in both products. The final product obtained from Scheme I has nanoparticles everywhere on the graphene surface, while from scheme II the density of nanoparticles is higher at the edges. Reproduced from reference [121] with permission of Royal Society of Chemistry.

- There are two examples of chemical modification of the graphene edge carried out in the gas phase in ultrahigh vacuum at low temperatures. Using surface assisted coupling, tetrapyrroles were fused covalently to a graphene edge,[122] while in another

report individual tetrafluoro-tetracyanoquinodimethane molecules were fixed on the graphene edge by using an electronically inert molecular anchor.[123] For both cases, the graphene edge was partially modified by using an elaborate and indirect methodology.

- Reactive plasma etching is typically used to pattern edge-like structures via photolithography in graphene.[97] It involves a reaction between graphene carbon atoms and reactive plasma species. The functionalization depends on the type of plasma gas (H_2, O_2, NH_3) and starts preferentially from the reactive sites on graphene surface such as edges and defects.[13,16] In hydrogen gas plasma, etching leads to the formation of the mono-hydrogenated and di-hydrogenated edge (depending upon the chemical activity, i.e., the partial pressure of H_2 and temperature)[19,44] while the basal plane remains preserved.[45] Similarly, in oxygen plasma, edge undergoes oxidation to form groups like ketone and ether (theoretical prediction)[124] depending on the chemical activity of O_2 as well as and the structural configuration of the edges. In NH_3 plasma, selectivity of the edge or basal plane depends on the plasma treatment with respect to mild (25 W) or harsh (45 W) conditions. It has been shown experimentally that the mild conditions promote the doping at the edges with nitrogen atoms, while in harsh conditions, the dopant atoms target the middle of the graphene plane.[46] In another example, GNRs were covalently functionalized through the formation of the carbon-nitrogen bond at the edge by nitrogen species using high-power electrical Joule heating in NH_3 gas, leading to n-type electronic doping.[125]

- Organic Synthesis is a bottom-up approach for synthesizing the edge functionalized GNRs or nanographene. It involves the surface-assisted polymerization of molecular building blocks of aromatic molecules, which is a multi-step process. After the polymerization, the polymer undergoes the process of dehydrogenation (for the planarization of the molecule) to obtain the final sp^2-bonded nanographene.[47,48] One of the drawbacks is that the surface-assisted synthesis requires an ultrahigh vacuum (UHV) to avoid any contamination, which in turn can also degrade the edges.

Drawbacks of Above Methods The main disadvantage of all the above methods is that they are not selective enough towards the edge. In liquid exfoliation-based methods, graphene flakes are not in their pristine form as they may get modified already during the exfoliation process. Also when dispersed in solution, single object control and observation is not possible.[41,42] In the chemical synthesis method, another important issue is that the achievable size of graphene does not reach the size of graphene produced from the mechanical exfoliation or chemical vapor deposition (CVD) method. The large area, single layer, and high-quality of CVD graphene makes it a suitable candidate for applications in electronic transistors, electrode material, and electrochemical sensing devices.[74] In other methods, the graphene edge was modified partially.[122,123] Therefore, the selective homogeneous modifica-

tion of the edge of a single graphene sheet under ambient conditions has not been explored yet and remains a challenge.

One way in which the functionalization can be selectively directed towards the isolated graphene edges is through electrochemistry. This can be done by utilizing the conductive nature of graphene. In the case of an isolated graphene edge sample, the only conductive component of the sample is the exposed 1D line of edge atoms, since the basal plane region which is protected by the insulating polymer acts as a mere contact between the electrode lines and the edge. Therefore, only the exposed edge comes in contact with the electrolyte during the measurement, making it selective for functionalization and probing using electrochemistry.

1.3.2 Electrochemical Modification (ECM)

ECM is an electrochemistry-based functionalization method that involves techniques such as electrodeposition, electrospinning, electrochemical doping, and electrochemical polymerization. The basic principle is the creation of electroactive species from a precursor in the vicinity of a working electrode (WE) through charge transfer with the WE (graphene or graphene edge in this thesis). The charge transfer can be achieved by the application of an applied current (galvanostatic) or a voltage (potentiostatic) (as shown in figure 1.7A,B for gold deposition on CNT). One of the advantages of these methods is that the voltammogram or the chronoamperometric profile measured or the parameters of ECM can provide information such as the underlying coupling mechanism and the size or thickness of the grafted functional groups.[126,127] In addition, ECM can be carried out in ambient conditions. ECM also provides some degree of selectivity because the modification can be localized to the conductive substrates that are electronically in contact with the potentiostat, leaving adjacent insulating materials with no modification. For example, in the case of graphene (in contact with the potentiostat) on Si/SiO_2 substrate, the modification will happen only on the conductive graphene sheet and not on the insulating Si/SiO_2 substrate. The electroactive species either precipitate or deposit or form a coating on the graphene surface through the redox process. These species also often have a tendency to self-react or polymerize leading to electropolymerization or forming a layer on WE. The polymerization can occur either through non-covalent or covalent interaction with the carbon atoms of the graphene. The interaction type depends on the precursor and electrochemical conditions.

1.3.2.1 Metal Nanoparticle Decoration

Nanoparticles (NPs) have been shown to contribute towards electrocatalytic, sensing, and plasmonic properties of CNTs and graphene-based hybrid materials.[30,115,128–133] For example, graphene decorated with metal NPs has been used for sensing of gases such as H_2,[134] and NO_2.[135] Many techniques have been demonstrated for the formation of such NP hybrids

including direct deposition through metal evaporation,[136–138] from nanoparticle colloidal solutions,[139,140] spontaneous reduction of metal ions to NPs,[141,142] and electrochemical deposition (or electrodeposition).[49,50,126,143,144] The electrodeposition method has several advantages over other methods. It directly positions the nanoparticles on the material of interest or WE and allows a high degree of control in terms of nucleation and growth of nanoparticles providing defined and uniform size through variation of different deposition parameters: metal salt solution, potential applied, time. It also requires no prior treatment of the graphitic materials, allowing the study of pristine as well as functionalized graphene-based materials. Therefore, electrodeposition has proved as an attractive route for the deposition of metal NPs from its salt solution through reduction using an appropriate potential.

Penner and co-workers have demonstrated the NP deposition at selective sites, i.e., along step edges (in the form of nanowires) or on the basal plane of HOPG by using different deposition parameters (figure 1.7C).[143,145] This is because nucleation occurs preferentially at step edges or defects on the graphite surface, and can be explained in terms of an energetic preference of nuclei for sites of high coordination on the surface.[146] For the electrodeposition of metal NPs at HOPG surfaces, step edge selectivity is also promoted by their ability to catalyze ET to metal ions in solution.[147] The presence of metal particles on CNTs and graphene provides a twofold purpose of functionalization as well can be utilized as efficient surface-enhanced Raman scattering (SERS).[49,50,126,148] Until now, there is only one demonstration of the modified isolated graphene edge electrode with nanoparticles used for realizing glucose sensors.[149]

1.3.2.2 Electropolymerization (Covalent or Non-Covalent)

Electropolymerization is a well-known tool for the preparation of organic films on various substrates because of its experimental simplicity. The polymerization is often performed by electrochemical oxidation of the appropriate monomers. This method in comparison to normal oxidative polymerization does not require the use of an oxidizing agent, instead, a positive potential is applied between the WE and RE via cyclic voltammetry, and is often performed at room temperature. The active species or cation radical sites are generated in monomer (polymer) molecule, through the charge transfer with the WE, thus, initiating the polymer growth. The active species or cation radicals tend to react further with the precursor or self-polymerize subsequently leading to the propagation step and formation of a coating on WE. The film/layer thickness can be controlled by controlling the potential at which the deposition is performed as well as the time of deposition. Electropolymerization also provides selectivity since the polymer growth can be localized to the conductive substrates that are electronically in contact with the potentiostat, leaving adjacent non-conductive materials uncovered by the polymer. This method modifies the surface homogeneously and with high coverage. The thickness of electropolymerized insulating films is often self-limiting because

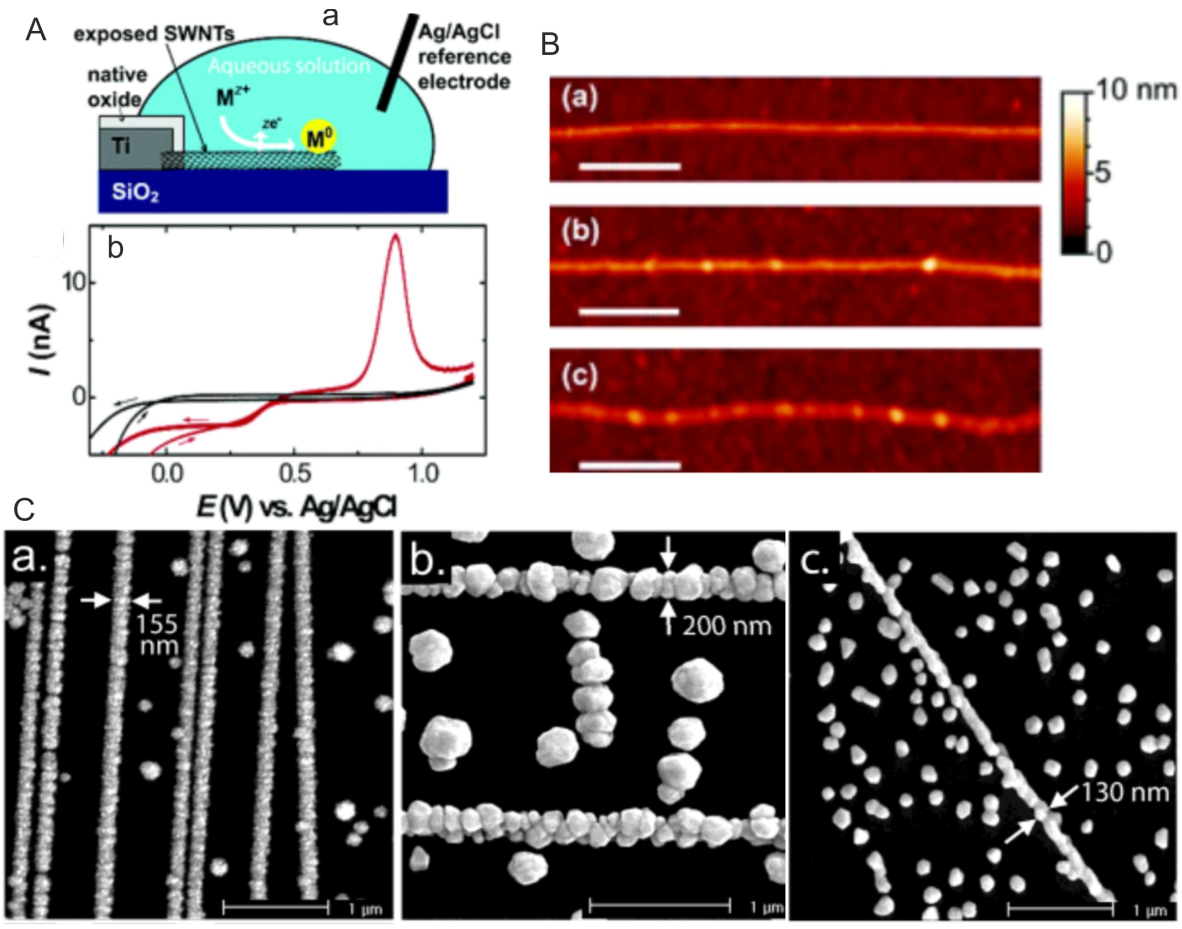

Figure 1.7: (A) Gold NPs deposition on CNT electrode: (a) Schematic illustration of the experimental set up. (b) Cyclic voltammetric response of the SWNT electrode (red line) in the presence of 0.2 mM $HAuCl_4$ and 100 mM KCl showing a reduction wave and stripping peak in the negative and positive scan directions, respectively. (B) AFM images obtained in air pre (a) and post-Au deposition at varying nucleation potentials: (b) 0.2, and (c) -0.2 V vs Ag/AgCl at separate nominally identical CNT electrode devices. The deposition time was 20 s. Scale bar is 300 nm. (C) Selective deposition of NPs on edge planes of HOPG shown by scanning electron micrographs of (a) nickel, (b) silver, and (c) gold nanowires on the HOPG terraces, while the basal plane region shows lower density of NPs. and basal Reproduced from references [126] and [145] with permission of American Chemical Society.

the rate constant for polymerization rapidly decreases as the film thickness increases. This method has been used for the synthesis of a wide variety of polymeric products from different classes of monomers (aromatic amines, phenols, thiophenols, aromatic hydrocarbons, and heterocycles).[150] One of the major use is in the field of conducting polymers, with common polymers like polyaniline[151,152] and polypyrrole.[153,154] On graphene-based materials, it has already been used to coat the individual CNTs and graphene sheets non-covalently with the polymer layer.[49,51] In edge-rich graphenes, polyaniline functionalized GNRs have been used as a platform for high-performance microbial fuel cells.[155]

1.3.2.3 Diazonium Chemistry (Covalent)

This is the most common functionalization method for graphene which occurs through a reaction between aryl diazonium salt and graphene. On graphene, diazotization happens thermally or using electrochemistry (ECM), however, in the case of other materials (e.g on gold), it can also occur spontaneously. The ECM of graphene with diazonium precursors is typically carried out by an applied voltage, which reduces the aryl diazonium salt to aryl radical species through an ET reaction with the graphene electrode. Consequently, the aryl radical forms a covalent bond with the graphene carbon atoms.[80,127] On graphene, functionalization with amine-,[156] carboxylic acid-,[70] nitro-,[6] aryl diazonium salts has been reported. The passivation of GNRs and edges of exfoliated graphene through diazonium chemistry has also been reported previously.[110,116,119,120] There is only one report, where diazonium functionalization has been carried out at isolated graphene edges.[33] However, a non-steady-state and large hysteresis observed in the voltammetric behavior of the fabricated edge indicates to the contribution from basal plane region in the electrochemistry of edge.

1.4 Characterization of Graphene Edges

A variety of techniques like Raman spectroscopy,[60,61,157] atomic force microscopy (AFM),[50,51] X-ray photoelectron spectroscopy (XPS),[158], electrochemistry,[74,80,158] have been used to characterize the structure, topography, chemical functionalities, electrochemical and electronic properties of both the basal plane and edges (or defects) in graphene. At atomic resolution, it has been possible to distinguish the chemical and the atomic structure of the edges with respect to the basal plane using high-resolution scanning probe microscopy,[52,54] and electron microscopy.[53,55,75] They include scanning tunneling electron microscopy (STEM), transmission electron microscopy (TEM), electron energy-loss spectroscopy (EELS).[26] However, these techniques have been used locally at the graphene boundaries without any polymer layer. In the case of isolated graphene edges, the polymer layer present on top of the graphene sheet makes it hard to spatially resolve the graphene edge using the conventional characterization tools because of the organic and insulating nature of the polymer.[12]

This section discusses the two main tools, which are used in the thesis for the characterization of isolated graphene edge electrodes: Raman spectroscopy (and SERS) and electrochemistry. Raman spectroscopy is sensitive to edges or defects in graphene, and it can also provide important information about the chemical composition of the functional groups after functionalization of edges via SERS. Electrochemistry can be used to probe the isolated graphene edges by utilizing the conductive nature of graphene. Since it is the only conductive component of the edge samples, thus, as long as the 1D line of carbon atoms constituting the edge is exposed below the surface of the polymer, it can come in contact with the solvents and probed using electrochemistry.

1.4.1 Raman spectroscopy

Raman spectroscopy is considered an ideal characterization tool for carbon-based materials because of its non-invasive and non-destructive nature, offers high resolution, and provides structural and electronic information about the material. Since the first Raman spectrum of graphite was recorded $\sim$ 50 years ago,[159] it has become one of the most widely used techniques for the characterization of disordered and amorphous carbons like fullerenes, nanotubes, diamonds, carbon chains, etc.[160] Due to the zero bandgap of graphene, all wavelengths of incident radiation are resonant, making Raman spectroscopy in particular even more useful for its characterization providing information about both the structural and the electronic properties.[57] In addition, Raman spectra of all carbon-based materials have an advantage in data analysis since it shows only a few prominent features, with a considerable amount of information provided by the shape, intensity, and position of the Raman peaks.[160] For example, it can distinguish between different forms of carbon (e.g. graphite and graphene) by the differences in their peak features.[57] It also gives information related to unwanted products, structural damages, functional groups, and chemical modifications introduced during the preparation of graphene samples, and can be used for quality control. Any variation of electronic properties due to defects, edges, or doping has effects on the position, width, and intensity of the Raman peaks.

The typical Raman spectrum of graphene (figure 1.8) shows characteristic peaks: *D* ($\sim$ 1330 cm^{-1}), *G* ($\sim$ 1585 cm^{-1}), *D'* ($\sim$ 1620 cm^{-1}), and *2D* ($\sim$ 2640 cm^{-1}) at an excitation wavelength of 633 nm, each corresponding to an inelastic scattering event of the incident light by the lattice of graphene.[60] Collectively, they represent the signature of graphene in a Raman spectrum. The presence of only *G*-and *2D*-peaks in the Raman spectrum is an indication of defect-free graphene. The defect or an edge site breaks the symmetry of

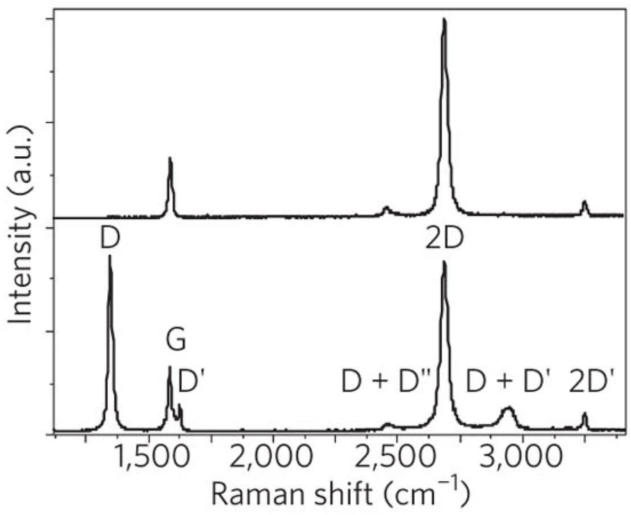

Figure 1.8: Raman spectra of pristine (top) and defected (bottom) graphene, with the labelled main peaks. Reproduced from reference [60] with permission of Nature Publishing Group.

the honeycomb lattice by disrupting the π conjugated network and consequently influences the vibrational modes of the graphene, leading to an increase in the disorder-related *D* and *D'*.[56,58,161,162] Similarly, when the covalent functionalization changes the hybridization of the carbon atoms from sp^2 to sp^3, for example, through diazonium chemistry, there is a strong *D*-peak and increase in intensity ratio I_D/I_G. Another important information which can be obtained from the Raman spectrum of graphene is charge transfer doping (e.g. through oxidation) since the Raman peaks are sensitive to change in electronic properties of graphene. A blue- and red-shift of the *G* and *2D* peaks occur upon *p*- and *n*-type doping, respectively. Doping also reduces the intensity of the *2D* peak, thereby decreasing the I_{2D}/I_G ratio.[59] The doping effect due to the oxidation of graphene edge has been studied on patterned graphene constriction produced by electron beam lithography and oxygen plasma etching. It was found that there is a decrease in the I_{2D}/I_G ratio of the graphene nanoconstriction when moving from its center to the edges.[163] In another example, the treatment of graphene in mild NH_3 plasma resulted in animation at its edges, as well the chemical doping confirmed by the redshift (n-type doping) of the *G* peak.[46]

Hence, based on the Raman spectrum of pristine (or modified) graphene, one can probe the functionalization of graphene in terms of covalent or non-covalent attachment as well as the charge transfer doping. However, it is not capable of directly identifying the composition of the functional groups attached to the graphene sheet or its edge.

1.4.2 Surface-Enhanced Raman spectroscopy (SERS)

The attachment of noble metal NPs to a material gives an added advantage of their strong localized surface plasmon resonance (LSPR) absorption in the visible range of the electromagnetic spectrum.[128,164] LSPR refers to the collective oscillation of electrons (called surface plasmons) on the metal NPs excited by the incident photons at the resonant frequency. The LSPR effect enables the enhanced and tunable electromagnetic fields called hot spots as well as the light absorption and scattering processes. This leads to 'electromagnetic' enhancement in the Raman signal of material by orders of magnitude through the exhibition of surface-enhanced Raman spectroscopy (SERS), when the nanoparticles are present in the vicinity of the material.[165,166] In addition to the LSPR effect, the charge-transfer effect through an electronic interaction between the material and NPs further increases the Raman signal by 'chemical' SERS enhancement.[136,166] The LSPR wavelength of these nanoparticles typically falls in the visible/near-infrared region, depending on the material, dimensions, and morphology of the nanostructures.[128,164] The electromagnetic field depends on both the LSPR and laser excitation wavelengths as well as the polarization of the light.[165]

2D nanomaterial like graphene is an ideal material to investigate SERS because of its large area, well-known Raman spectrum, sample reproducibility, and controllable height down to the atomic scale.[64,65] SERS has been used for investigating the interfacial reactions between graphene and nanoparticles,[50] the SERS effect itself with CNTs and graphene as test

molecules,[50,64,65,148] and characterization of the functional group of chemically functionalized CNTs and graphene.[51] In contrast to other techniques, the use of electrodeposition to obtain AuNPs directly on the chemical functionalities ensures an intimate coupling between the two, thereby promising a very high Raman enhancement.[50,148] Heeg *et al.* demonstrated Raman enhancement up to 10^3 from graphene suspended in a nanoscale gap between two closely spaced gold nanodisks (figure 1.9A).[65] Balasubramanian and group studied the evolution of Raman enhancement ($\sim$ 2 orders of magnitude) by systematically increasing the size and density of gold particles deposited on graphene (figure 1.9B).[50]

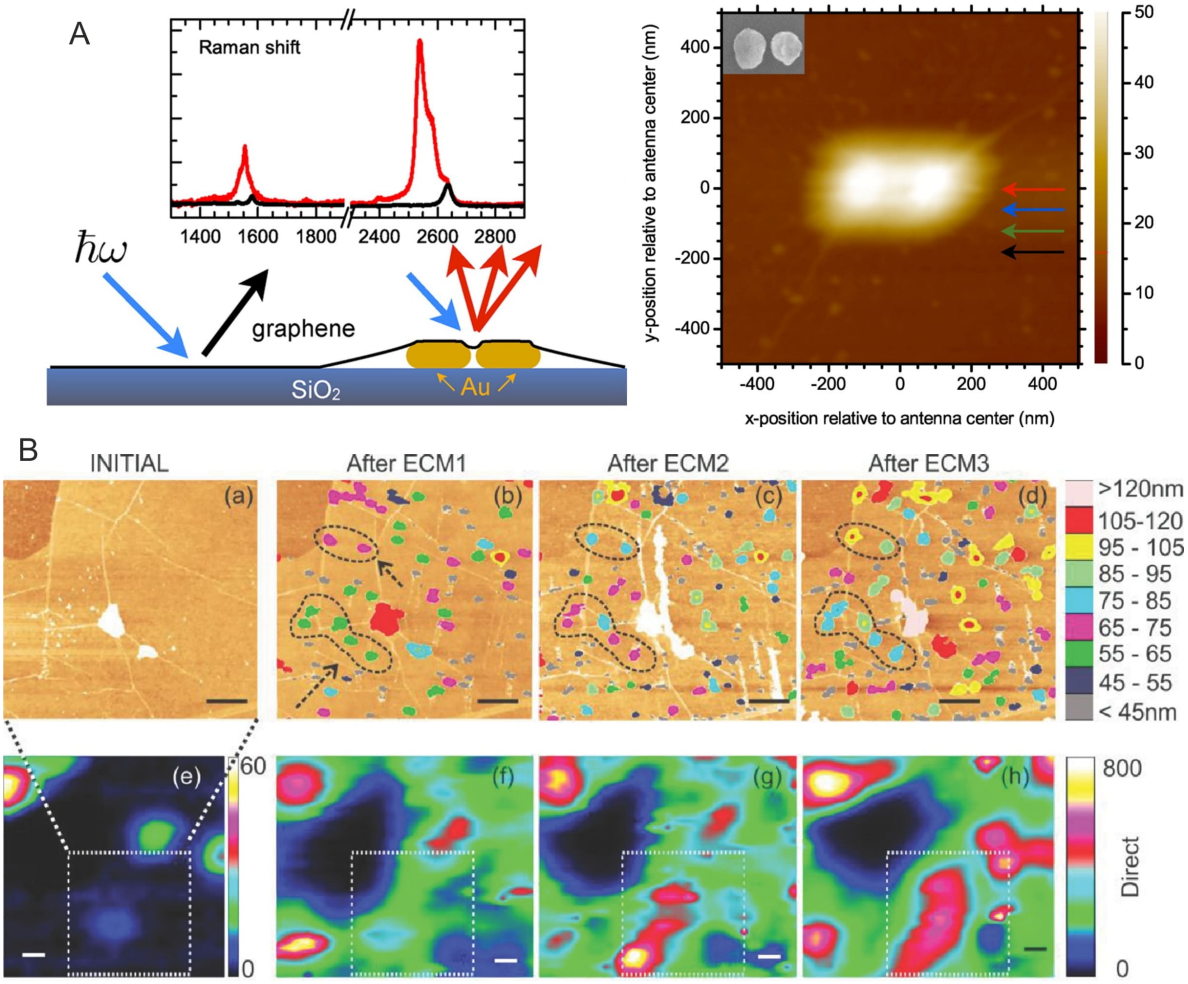

Figure 1.9: (A) Raman spectra (normalized to the 2D peak) of graphene placed on the double structure for excitation wavelength 638 nm. Sketch of the sample configuration. AFM image of graphene placed on top of the double structure. (B) Raman enhancement with increasing particle size. (a-d) The first row shows AFM images of the same area (a) before and (b-d) after 3 consecutive ECM steps. It is apparent that in the marked areas, the heights of the particles increase with every ECM step without the introduction of new particles. (e-h) Raman maps of the *G*-peak intensity (integrated from 1560-1610 cm^{-1}). The area in the Raman maps where the AFM images were taken is identified with a square. It is clear that the Raman intensities in the second row increase from (e) to (h). Scale bar is 1 µm. excitation wavelength is 633 nm. Reproduced from references [65] and [50] with permission of American Chemical Society and Wiley, respectively.

Identification of the Chemical groups attached to Graphene Another advantage of SERS is in the identification of the chemical groups attached to the surface of graphene electrodes after functionalization, as demonstrated by the controlled deposition of gold nanoparticles (AuNPs) on to the non-covalently functionalized the surface of graphene.[51] The deposited AuNPs (either individually or gaps in between them) at the nanoscale level act as local hotspots leading to the enhancement in Raman signal of the characteristic vibrational modes of the molecules attached to graphene. Graphene was non-covalently modified with poly(pyrrole) (PPy) which is a common polymer broadly used for the fabrication of sensing devices. Figure 1.10a-c shows the AFM images of pristine graphene (Gr), after its functionalization with PPy (Gr-PPy) and subsequent attachment of the AuNPs (Gr-PPy-AuNPs). The schematic is shown in figure 1.10d. In figure 1.10e Raman spectrum for Gr-PPy graphene (in red) shows the characteristic *G*- and *2D* peaks with no additional peaks of the PPy layer while for Gr-PPy-AuNPs (in blue), it shows the various vibrational modes associated with PPy.

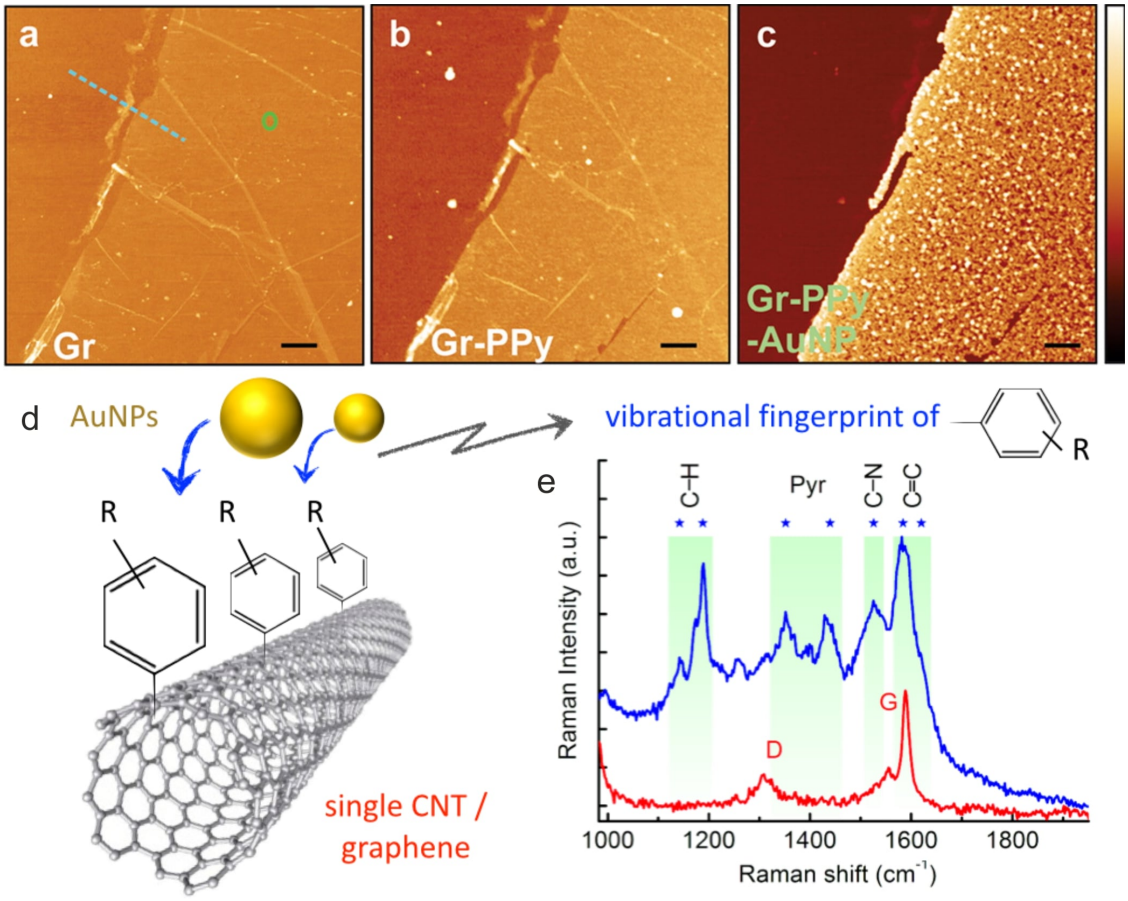

Figure 1.10: Vibrational fingerprinting of functionalized graphene. AFM images before, (a) after electropolymerization with PPy (b), and after subsequent attachment of AuNPs (c) Scale bar is 1 m. (d) Schematic of the sample configuration and method. (e) Raman spectra compared at different stages of functionalization, measured at the spot shown in (a). The peaks marked by (*) are attributed to the PPy layer on graphene. Reproduced from reference [51] with permission of the American Chemical Society.

1.5 Electrochemistry

Electrochemistry is a discipline that has a wide range of applications, ranging from detection of analytes to energy storage. An electrochemical reaction happens via the flow of electrons at the interface of the material (electrode). Carbon-based materials in the forms of graphite, carbon fibers, glassy carbon, CNTs, graphene, etc. have long been used as electrodes in both physical and analytical electrochemistry. From a fundamental perspective, electrochemistry allows us to better understand the role of edge and basal plane sites of graphene on the heterogeneous electron transfer (HET) rates. Studies of electrochemical reactions of pristine and functionalized CVD graphene can be roughly divided into two categories: fundamental HET electrochemistry with well-known redox probe reactions such as ferrocyanide and ruthenium hexamine to better understand the role of edge and basal plane sites of graphene on the HET rates; sensor applications such as the detection of uric acid, dopamine, glucose, and hydrogen peroxide.[80]

Electrode Reaction and Rate The electrochemical reaction at the electrode is investigated by studying the HET with classical redox couples such as ferrocenemethanol, FcMeOH $(0/+)$; hexaammineruthenium, $Ru(NH_3)_6^{2+/3+}$; hexacyanoferrate, $Fe(CN)_6^{3-/4-}$ and hexachloroiridate, $IrCl_6^{2-/3-}$. For a general electrode, under the application of a constant or linear potential over time, the redox probes (electroactive species or analytes) undergo oxidation/reduction in the electrolytic solution. A heterogeneous charge transfer will occur at the electrode-solution interface, i.e., the flow of electrons between the electrode and the electroactive species. On considering an overall electrode reaction: $O + ne^- \longrightarrow R$, where O is reduced to R, the electrode reaction rate depends on the rates of the following processes:

- Mass transfer of electroactive species: reactants O from the bulk solution to the electrode interface, and vice-versa for products R.
- ET between the electrode surface and the electroactive species.
- Chemical reactions before or after the ET.
- Other surface reactions (adsorption, desorption or electrodeposition)

Mass transport or transfer arises either from differences in electrical/ chemical potential at the two locations or from the movement of a volume element of solution. There are three modes of mass transport: diffusion (movement of species under the influence of concentration gradient), migration (movement of charged species under the influence of electric field), and convection (results due to action of a force on the solution like a pump, a flow of gas or even gravity). However, the electrochemical systems are designed such that only the diffusion effect contribution to mass transport is relevant. Generally, the other

contributions are reduced to negligible levels, by the addition of an inert electrolyte at a concentration much higher than that of the electroactive species (migration effect); and by preventing stirring and vibrations in the electrochemical cell (convection effects). In the thesis, mass transport is always discussed in terms of contributions only from diffusion effects. The simplest reactions (e.g, in the case of the redox couples) involve mass transport and HET (only nonadsorbed species). Therefore, a typical electrochemical reaction comprises three consecutive steps: diffusion of the reactants (O) to the electrode surface, HET, diffusion of products (R) to the bulk solution. The slowest step of the three rates determines the overall kinetics of such a multi-step process and is the basis to classify a process into reversible, quasi-reversible, or irreversible. The reaction rates can be measured experimentally, and depend upon the potential. They can provide significant information about the surface chemistry and morphology of the electrodes.

1.5.1 ET Properties of Graphene Edges and Basal Plane

An important parameter of electrode material is the density of electronic states (DOS) which varies greatly on the different forms of carbon. A higher DOS increases the possibility that an electron of the correct energy is available for the electrode to transfer to an electroactive species. Thus, the HET rate is dependent on the DOS of the electrode material. A perfect basal plane surface of graphene has no edge sites or defects, thereby, carbon atoms have satisfied valances without any dangling bonds. In the case of graphene edges (or defects), the dangling bonds are formed at the edges increasing the local DOS.[7] Thus, the electrochemical activity of a graphene edge is expected to be higher than the basal plane.

The electrochemistry of graphene electrodes has been investigated in detail previously with several types of graphene resulting in observation of different behavior at the basal plane and edge sites.[38,40,67,70,74,167] For example, the HET rate at the basal plane is found to be several orders of magnitude lower than at the edge sites of HOPG, although the conclusions about the exact magnitude are still under discussion.[38,69,74,168] Brownson *et al.* showed that ET properties of CVD graphene are owed to the presence of edge-like sites 'graphitic islands' across the graphene surfaces.[67] Similarly, in other laminar and assembled sheets of graphene electrodes, the presence of edges and defects were found to increase ET rates.[169,170] Such ET behavior can be explained by the lower charge carrier density at the basal plane than the edges.[169] In contrast, several studies also claimed that the basal plane of HOPG was not totally inert and ET occurred not only at the step edges of HOPG but also at the pristine graphitic basal planes.[171] Ambrosi *et al.* compared the behavior of $Fe(CN)_6^{4-/3-}$ at different type of graphene electrodes (Figure 1.11).[172] It was found that the HET rate of the folded edges (f-SGNF) is significantly lower than the open edges (o-SGNF), as evident from the larger peak-to-peak separation (ΔE_{pp}) observed for f-SGNF (335 mV) in comparison to o-SGNF (91 mV). The calculated HET rate constants (k^0) for o-SGNF and f-SGNF were 6.9×10^{-3} and 0.2×10^{-3} cm/s, respectively. The folded edges are structurally

more similar to basal plane sites. EPPG also has a large number of edge plane sites, leading to second-lowest ΔE_{pp} after o-SGNF, and is followed by ΔE_{pp} of GC (glassy carbon). Out of all the electrodes, ET is slowest in BPPG (rich with the basal plane), as indicated by the largest ΔE_{pp}. Hence, the order for the HET rate constant is BPPG $<$ f-SGNF $<$ GC $<$ EPPG $<$ o-SGNF, with the increase in edge sites in the same order.

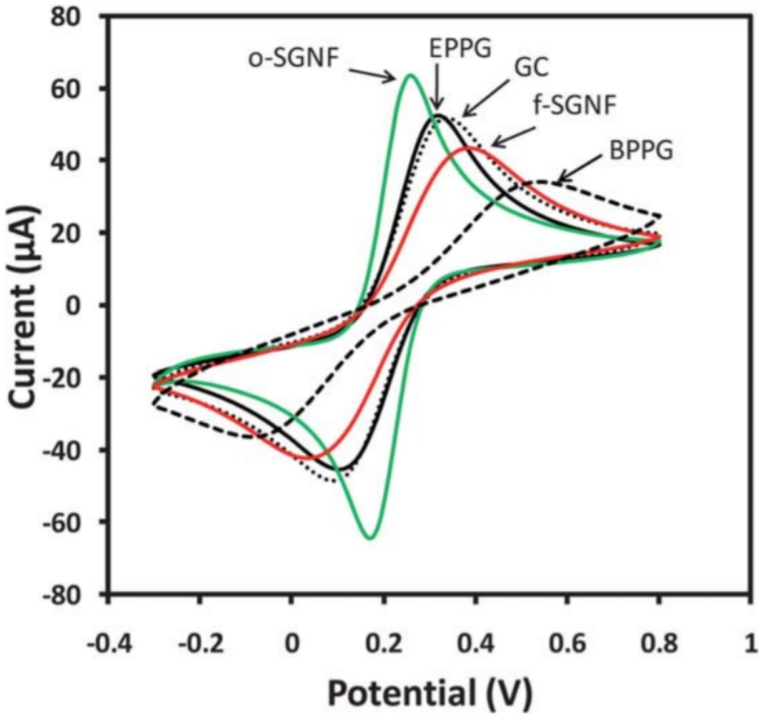

Figure 1.11: CVs of 5 mM $Fe(CN)_6^{4-/3-}$ (in 0.1 M KCl) on stacked graphene nanofibers with open edges, o-SGNF (green); stacked graphene nanofibers with closed edges f-SGNF (red); edge plane pyrotic graphite, EPPG (black); GC (black-dotted); and basal plane pyrotic graphite, BPPG (black-dashed) electrodes. Scan rate: 100 mVs^{-1}. Reproduced from reference [172] with permission of Royal Society of Chemistry.

The electrochemical properties at a single object level have been investigated on individual CNTs and graphene sheets. The open ends of individual CNTs had an accelerated ET rate and an enhanced electrocatalytic activity than their sidewalls, while the side walls were found to have similar electrochemical properties to those of the basal plane of HOPG.[68,173] Li *et al.* reported that for both mechanically exfoliated and CVD-grown monolayer graphene electrodes, the ET rates of FcMeOH were found to be faster ($>$ 10 fold) than at the basal plane of bulk graphite.[174] According to Valota *et al.*, the reduction of $Fe(CN)_6^{4-/3-}$ shows a sigmoidal voltammetric behavior and high ET rates on small exfoliated graphene monolayers (figure 1.12a). Generally, for CVD-grown monolayer graphene sheets of mm^2-scale, the sample with both the basal plane with edges and isolated basal plane without edges (figure 1.12c) have shown low ET rates (k^0<0.1 cm/s), with differing reversibility (depending on the type of measurement - scanning electrochemical cell microscopy or bulk electrolysis) for the classical redox couples mentioned earlier.[11,12]

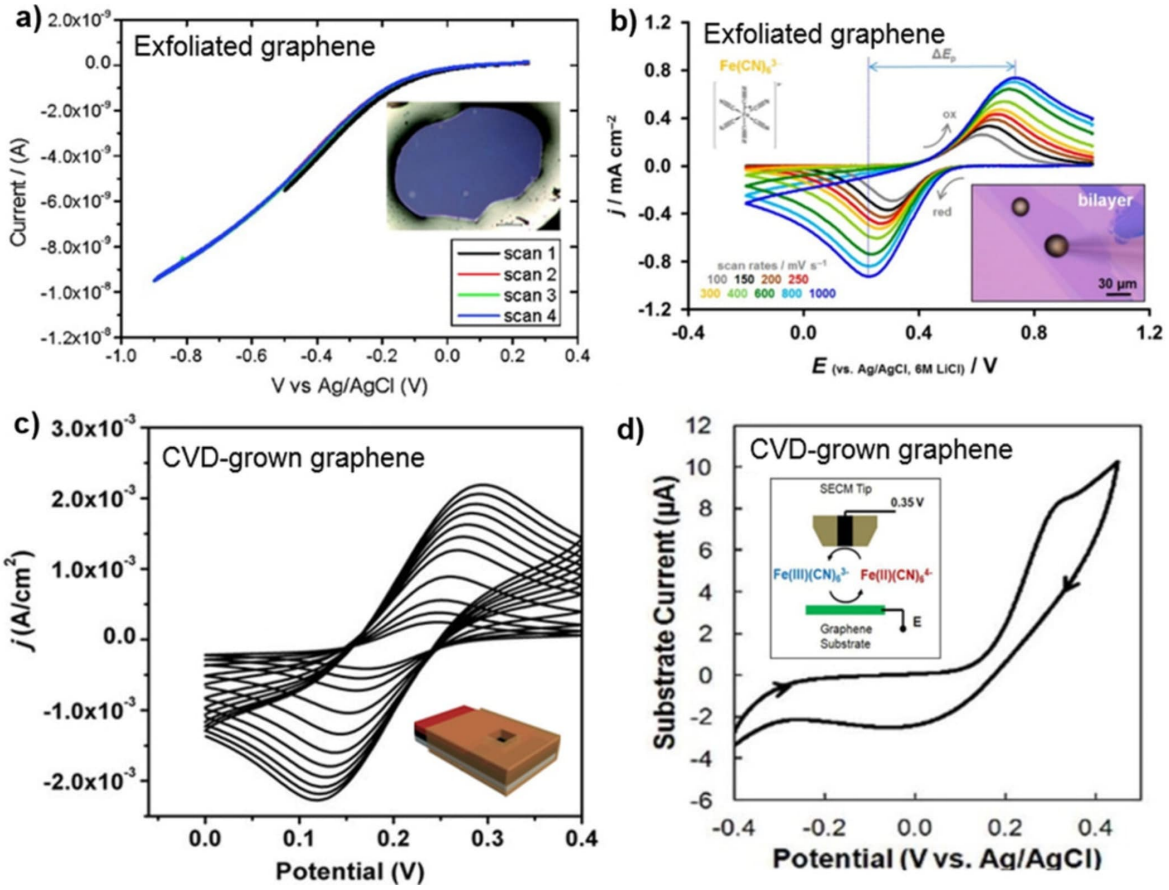

Figure 1.12: CVs of $Fe(CN)_6^{4-/3-}$ with concentration of (a) 1 mM on exfoliated graphene (in 0.1 M KCl) at 5 mVs^{-1} (b) bilayer graphene at different scan rates. The potential was referenced against Ag/AgCl wire in 6 M LiCl and held at the upper vertex potential for 10 s prior to the voltammetry. (c) CVD-graphene isolated basal plane-electrode at 5 mVs^{-1} (in 0.1 M PBS + KCl 0.1 M). (d) 1 mM on graphene electrodes at 20 mVs^{-1} (in 0.1 M PBS + KCl 0.1 M). Reproduced from references [175], [176], [12] and [11] with permission of American Chemical Society and Nature Publishing Group.

Overall, it has been observed that the ET kinetics at graphene electrodes[11,158,167,176] were similar to or worse than that of HOPG.[9,38,80] However, in most studies, the presence of edge sites was found to enhance the ET properties and their absence vice-versa.[1,9–12,66,69] Although, the edge of a single-layer CVD-grown graphene sheet consists of an atom-thick structure of carbon atoms in a 1D line and is different from its own basal plane, as well from the surface edge-plane of HOPG (consisting of many layers) and the ends of individual CNTs. The investigation of electrochemistry at an isolated graphene edge may help provide further clarification on the comparative HET behavior between the edge and the basal plane. The isolated graphene edges given its width of only $\sim$ 1 nm, shows a unique nanoelectrode/ ultramicroelectrode (UME) behaviour.[12]

1.5.2 Macroelectrode Vs Nanoelectrode (or Ultramicroelectrode)

Nanoelectrodes refer to electrodes with at least one dimension (critical dimension) in the nanometre range (typically 1-100 nm). The critical dimension is the dimension that controls the electrochemical response. Nanoelectrodes can be considered a special type of ultramicroelectrode (UME) with smaller critical dimensions. The UMEs were developed initially for use in biological and medical research, however, due to their unconventional properties, these electrodes went unnoticed by the electrochemists at that time.[177] Later, only through the independent works of Wightman[178] and Fleischmann[179] in the early 1980s, UMEs were introduced to electroanalytical chemistry. Since then, there have been numerous studies to study the properties of UMEs in detail transforming the scope of electrochemical studies in various areas of neurophysiology, lithography, and chemical analysis. The experimental behavior of any electrode depends on its size and the thickness of the diffusion layer. The diffusion layer is the electrochemical double layer (EDL), which is formed when an electrode comes into contact with an electrolytic solution under a given potentiostatic control. The double-layer behaves like an electrolytic capacitor consisting of two charged parallel layers, each coming from both the electrode and solution side in the very near vicinity of the electrode. It is formed when the charged layer present on the electrode gets compensated for by a layer of oppositely charged ions in the solution.[180]

In the case of a macroelectrode, the critical dimension of the electrode is greater than the diffusion layer, therefore, a semi-infinite planar or linear diffusion in the direction perpendicular to the electrode surface takes place as shown in figure 1.13a. The resulting current response is typically described as diffusion-limited, giving rise to wave-shaped peaks (figure 1.13b). While in case of a nanoelectrode or UME, the critical dimension is smaller than the thickness of the diffusion layer, thus, convergent diffusion takes place from all directions (the diffusion spatial field depends on the shape of the nanoelectrode, e.g. disk, sphere, ring, cylinder, and band) as shown in figure 1.13c. This subsequently leads to very fast mass transport of electroactive species near the electrode surface, and the process becomes diffusion controlled resulting in the loss of peak shaped to sigmoidal voltammogram (figure 1.13d). Since the concentration of electroactive species reaches a limiting value independent of potential and time, thus the hence the current response reaches a steady state.

Nanoelectrodes offer many advantages over the conventional sized electrodes:

- High mass-transport rate, which allows steady-state voltammetric responses to be readily achieved.
- They have smaller RC constants, which allows measuring even in solutions of high resistance because of the lower influence of solution resistance.
- The ability to respond rapidly to changes in the applied potential allows to accurately monitor electrochemical processes on a low microsecond or even a nanosec-

ond timescale, compared with the tens or even hundreds of milliseconds timescale of conventional macroelectrodes. The property of fast mass-transport rate makes such electrodes particularly useful in studies of very fast HET processes and in determining the kinetic parameters of electrochemical reactions.[181–189]

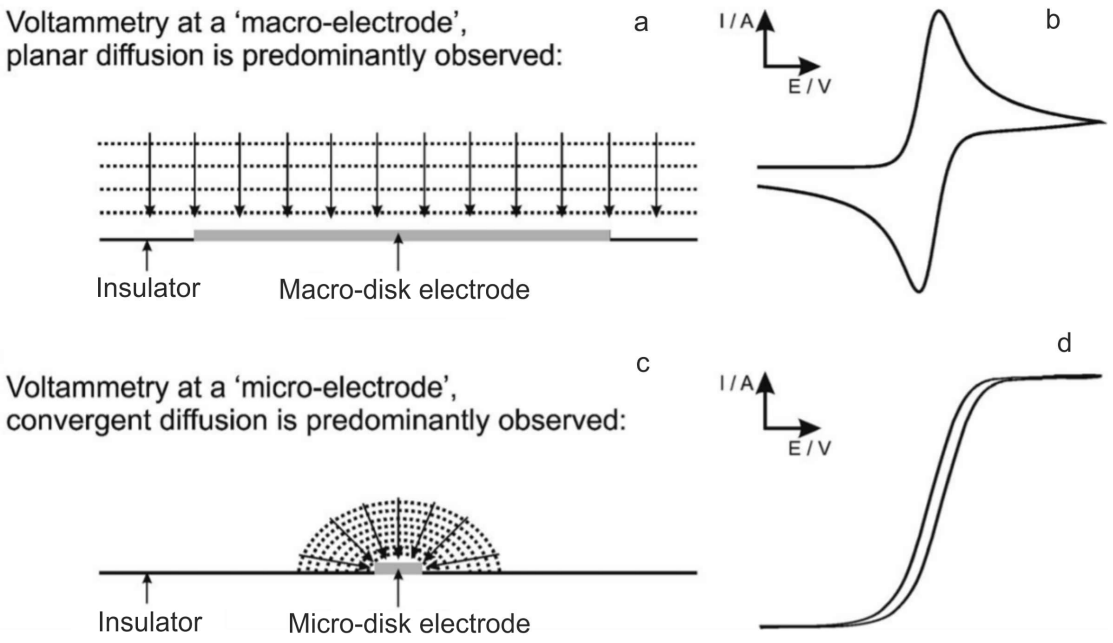

Figure 1.13: The unique differences between the cyclic voltammetric signatures observed at (a,b) a macroelectrode and (c,d) a microelectrode. Reproduced from reference [38] with permission of the Royal Society of Chemistry.

1.5.3 Isolated Graphene Edge

The isolated graphene edge as mentioned earlier has been realized only thrice,[12,33,40] in two forms: an exposed linear edge (width $\sim$ 1 nm and length in few millimeters) sandwiched in an insulating polymer layer (figure 1.14a),[12] and a nanopore edge structure (5 nm pore diameter with a length of the rim around 30 nm) embedded in between two insulating Al_2O_3 layers (figure 1.14d).[40] Since the isolated graphene edge is formed from a single layer of graphene, it has a size of only $\sim$ 1 nm (in an ideal case, when the basal plane is fully protected by resist or polymer layer), which acts as a critical dimension. For an isolated edge electrode prepared using mechanical cutting by Yuan *et al.*, the CV shows a near quasi-steady-state with a sigmoidal voltammogram at a low scan rate of 5 mVs^{-1} (inset in figure 1.14b). This is a typical characteristic of a nanoelectrode or UME, even though the quasi-steady-state is not perfect with a significant amount of hysteresis in forward and backward CV cycles. This slight deviation might be due to a small contribution of linear diffusion, probably because of polymer lift off near the edge exposing a small region of basal plane leading to leakage of the current. At higher scan rates, CV gradually became peak-shaped, similar to the conventional electrode.[12] The current density measured in the presence of 5

mM $K_3Fe(CN)_6$ as an electrochemical probe is around 0.11 A cm^{-2}, which is 4 orders of magnitude higher than the basal plane electrode.

Figure 1.14c presents the capacitive current density which is also found to be up to four orders of magnitude higher for the linear graphene edge electrode than the basal plane (without edges) electrode. The square shape of the voltammetric curves highlights the capacitive behavior at both electrodes.[12] The stronger electrochemical activity of graphene edges has also been reported in a nanopore device. For isolated edge in a nanopore form, the electrochemical current density of more than 12,000 Acm^{-2} (in 1 M KCl) is observed, which is four orders higher than that observed at the linear graphene edge. This is because of the combination of two factors in the nanopore case: higher concentration of electrolyte in the solution, and a smaller edge electrode surface which more promotes a more prominent convergent diffusion regime. The current-voltage characteristic (figure 1.14e) of 5 nm nanopore shows an increase in ionic current with voltage, while the identical currents through

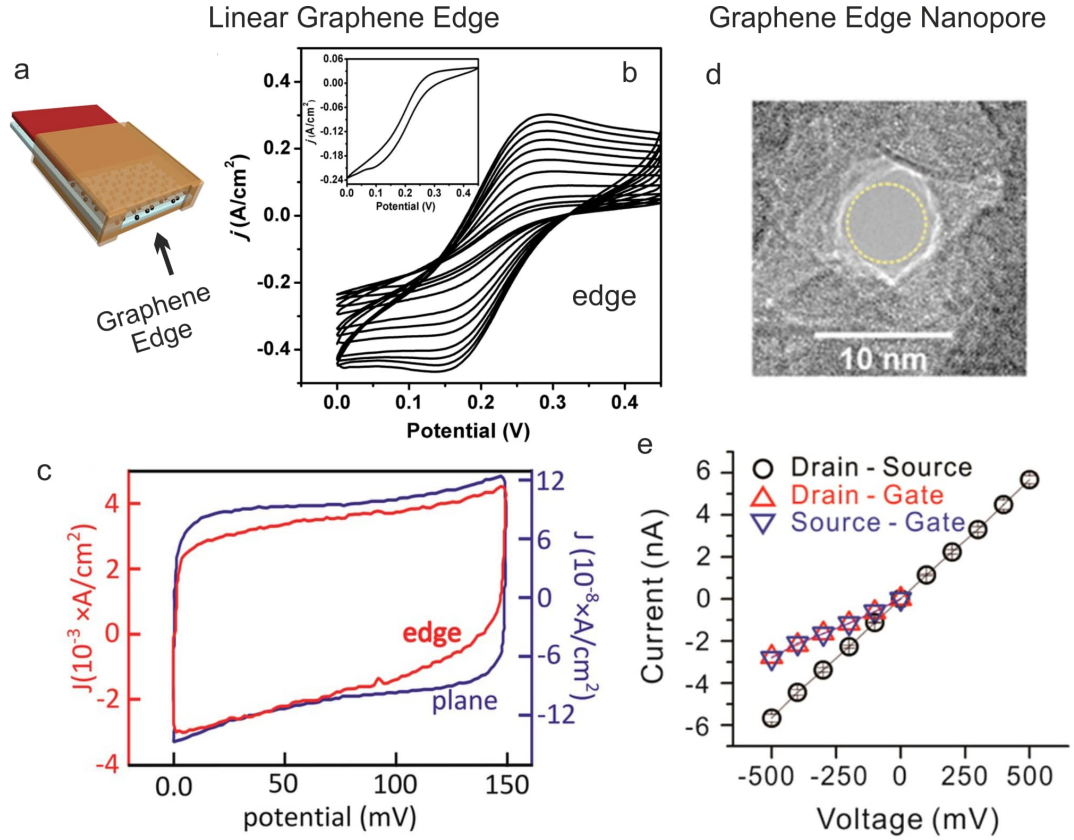

Figure 1.14: (a-c) Isolated graphene edge: (a) The schematic of the isolated edge electrode, (b) CVs showing electrochemical behaviour for 5 mM $K_3Fe(CN)_6$ (in 0.1 M KCl) at the edge electrode, at different scan rates (inset recorded at 5 mVs^{-1}) (c) CVs of the basal plane (blue) and a graphene edge (red) capacitive current density in an aqueous solution of phosphate-buffered saline. Scan rate = 50 mVs^{-1}. (d-e) Graphene embedded edge nanopore (GEEN): (d) TEM image of 5 nm nanopore (e) Current-voltage curve of nanopore ionic current and electrochemical behavior of graphene edge through 5 nm nanopore. Reproduced from references [12] and [40] with permissions of Nature Publishing Group and American Chemical Society.

the drain-gate and source-gate pathways are an indication of the electrochemical exchange at the exposed graphene edge.[40]

However, in the two reports on the isolated graphene edge until now, even though there is an indication of quasi-steady-state behavior at slow scan rates, the response is diffusion-limited, the limit of detection for redox probes is very high ($\sim$ 5 mM) and there is still no detailed study of HET rates, with no reported values of HET rate constant values.[12,33] The possible application to study fast ET kinetics has already been demonstrated with other nanoelectrodes such as single CNTs and individual nanoparticles.[30–32] The development of a new kind of nanoelectrodes made with the isolated graphene edge may accelerate the study of fast ET processes that are often too fast to investigate with conventional electrodes.[71,72] The graphene edge may be considered as an ideal one-dimensional system and is the thinnest wire electrode[28,29] that one could realize. Hence, it may be expected that the electrochemistry at such electrodes is unique. Another motivation to study isolated graphene edge electrodes comes from its selective functionalization using metal NPs, aryl diazonium chemistry salts, and polymerization, which can tune the chemistry as well as the electrochemical properties of the edge. The voltammetric behavior at the modified isolated edge electrode can provide a better understanding of the unique HET behavior at unmodified isolated edge electrodes.

1.5.4 Electrochemical Sensor Applications

Graphene-based materials show promise for many applications in portable chemical and biological sensing devices, as well as in energy storage devices due to their high surface area and conductivity. The electrochemical sensors with different types of graphene are generally tested for the detection of biomarkers such as glucose, β-nicotinamide adenine dinucleotide and its reduced form (NAD+/NADH), hydrogen peroxide (H_2O_2), dopamine (DA), ascorbic acid (AA), and uric acid (UA).[74] The electrochemical sensing depends on ET between the sensing platform (graphene and its derivatives) and the electroactive species (or target molecule for the detection). It is clear from section discussion that there is a need to have exposed edges of graphene to achieve the optimal or higher electrochemical activity, which leads to enhanced HET rate, and thus a greater output signal intensity is expected at the edges. This facilitates the detection of target molecules or biomarkers at a lower applied potential (overpotential).[172]

The higher electrochemical activity of graphene edges and defects with respect to the basal plane led to the development of a new class of redox electrodes that have rich edge chemistry. For example, Lim *et al.* developed a defect rich graphene electrode by increasing the density of defects in epitaxial graphene (Pristine EG) via electrochemical anodization treatment.[73] The resultant defect-rich graphene (Anodized EG) electrode was able to simultaneously detect all DNA bases with sufficient resolution, and with best signals in comparison to Pristine EG, GC, and boron-doped diamond (BDD) electrodes (figure 1.15a, b). It was also able to simultaneously resolve signals from AA, DA, and UA (not shown here). NADH

is another biomarker, whose detection has been studied extensively at different graphene surfaces, due to its importance in amperometric biosensing systems. It is an essential electroactive cofactor in all dehydrogenase reactions for the conversion of important substrates such as alcohol, lactate, and glucose. The redox behavior of NADH has been studied at different graphene surfaces as well. Pumera and co-workers tested NADH with multilayer CVD-graphene transferred onto flexible PET (ML-G-PET) electrodes in comparison to EPPG and BPPG electrodes (figure 1.15c).[190] Similarly, Brownson *et al.* investigated NADH redox properties on CVD-graphene, GC, EPPG, and BPPG electrodes.[38] In both the studies, EPPG electrodes showed better electrocatalytic properties, attributed to the

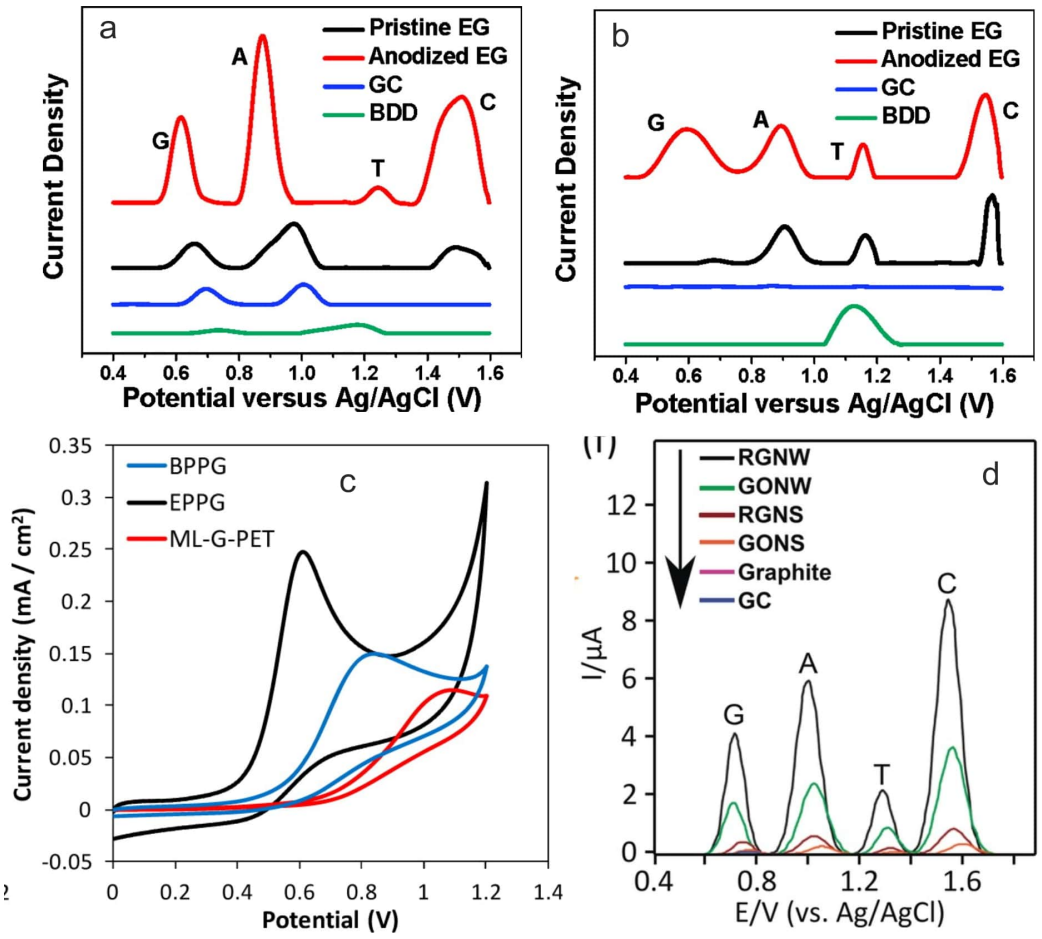

Figure 1.15: (a-b) DPV profiles for pristine epitaxial graphene (pristine EG), anodized EG, GC, and BDD (boron-doped diamond) electrodes in (a) a 30 µM equimolar mixture of G, A, T, and C; (b) 30 µg mL^{-1} dsDNA; Supporting electrolyte: 10 mM KCl/10 mM PBS solution at pH 7. (c) CVs in the presence of 1 mM NADH at BPPG (blue), EPPG (black), and multilayer CVD-graphene transferred to PET (ML-G-PET) (red) electrodes. Supporting electrolyte 50 mM PBS, pH 7.2; scan rate 0.1 V s^{-1} (d) Comparison between the sensitivity of electrodes made from reduced graphene oxide nano-walls (RGNWs), graphene oxide nano-walls (GONWs), reduced graphene nanosheets (RGNSs), graphene oxide nanosheets (GONSs), graphite, and GC in the detection of the oxidation potentials of the four DNA nucleotides guanine, adenine, thymine, and cytosine (0.1 µM in 0.1 M of PBS, pH 7). Reproduced from references [73], [190] and [37] with permission of American Chemical Society.

presence of the higher amount of edge sites. The edges and the surface defects of reduced graphene oxide nano-wall electrodes (RGNWs), which is another edge-rich graphene material, allowed the detection of both single-stranded and double-stranded DNA molecules with improved sensitivity compared to graphite and GC electrodes (figure 1.15d).[37]

The enhanced electrocatalytic activity combined with nanoscale dimensions makes isolated graphene edge electrode an ideal material in analytical chemistry to construct microsensors for detecting chemical and biological molecules. The isolated graphene edge electrodes have been shown to have superior ET properties than the isolated basal plane towards redox of biomolecules: NADH, oxygen reduction reaction (ORR), and AA.[12] At the edge electrode, the oxidation of 5 mM AA shows an oxidation peak centered at 0.30 V (figure 1.16a), while at the basal plane electrode, the corresponding peak is positively shifted to 0.41 V (figure 1.16b). The negative shift in the onset potential clearly indicates a better electrocatalytic activity at the isolated edge electrode. A similar shift in onset potential was also observed for NADH and ORR.

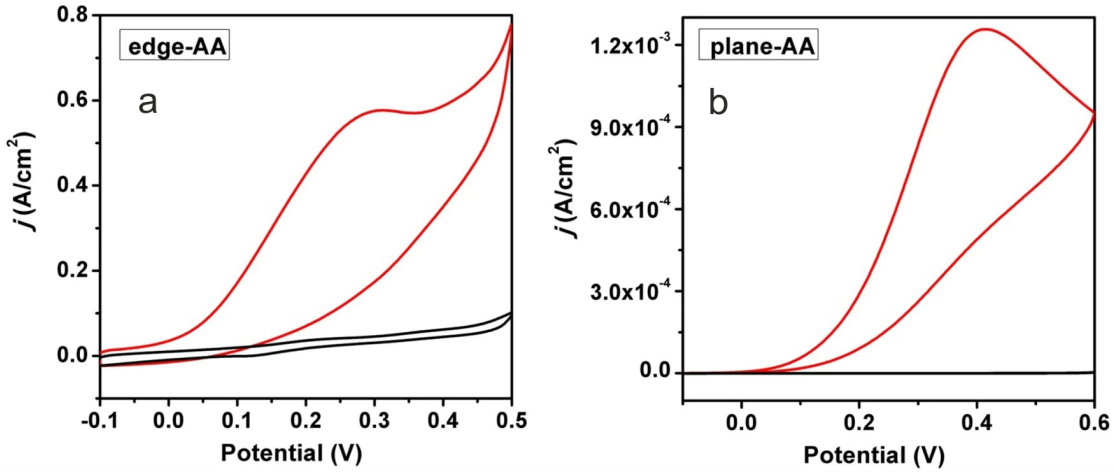

Figure 1.16: CVs of 5 mM AA (in 0.1 M PBS + 0.1 M KCl) at the (a) isolated graphene edge, and (b) isolated basal plane electrodes. Scan rate: 50 mVs^{-1} Reproduced from reference [12] with permission of Nature Publishing Group.

Li *et al.* compared the electrochemical behavior of UA at a graphene nanoelectrode (GNE) (isolated edges prepared using multilayer graphene) with carbon fiber disk microelectrode (CFME) to demonstrate the advantages of the former in charge transfer, and found that the GNE electrode had better ET properties than CFME. For the sensing application of modified isolated graphene edge electrodes (with nanoparticles), there is only one report showing a lower onset potential for the reduction of oxygen, which could be used for realizing glucose sensors.[149] However, the limit of detection (LOD) in all the electrochemical sensing reports at isolated edges is not so low in the range of a few millimolar. There exists very few studies of sensing at isolated graphene edge electrodes (modified and unmodified),[12,149] and it remains to be explored with targets of low LOD and different biomolecules.

2

Objective and Outline

The goals of this thesis are to design a method to isolate graphene edge from the basal plane of the monolayer graphene sheet, to prove if the fabricated edge is really available exclusively, and study its electron transfer properties. The isolated edge will be realized using photolithography, and subsequently characterized using Raman spectroscopy and electrochemistry. It is important to selectively functionalize graphene edge (using electrochemical modification) by nanoparticles and organic groups for tuning the chemistry at the edge and its application in catalysis and sensing devices. The deposition of gold nanoparticles at the edge (or functionalized edge) was used for modification as well as surface-enhanced Raman spectroscopic (SERS) investigation of chemical functionalities at the edge. The isolated graphene edge (width $\sim$ 1 nm) may be considered as an ideal one-dimensional nanowire with unique electrochemical properties owing to its nanoscale dimensions. Therefore, the development of new kind of nanoelectrodes based on graphene edge may find a possible application to study the fast heterogeneous electron transfer (HET) kinetics. The HET kinetics of the isolated graphene edge electrodes (unmodified and modified) is evaluated and analysed using the classical redox probes and a analytical model based on Butler-Volmer kinetics. From an application perspective, graphene edge nanoelectrodes are probed for detecting electroactive species and the realization of electrochemical nanosensors for small biomolecules such as NADH and FAD. The thesis is divided into the following chapters:

Chapter 4: Raman Spectroscopy and SERS on Functionalized Graphene
In order to understand, characterize and modify the edge properties, it is important to study the basal plane of graphene in detail. This chapter talks about Raman spectroscopy as a tool to characterize graphene samples with or without modification, along with a brief demonstration of various functionalization methods based on electrochemical modification (ECM) to modify graphene in a non-covalent and covalent manners. In addition, it also presents surface-enhanced Raman scattering (SERS) as a method to gather chemical infor-

mation about the functional groups covalently attached to graphene surface by vibrational fingerprinting. The methods used in this chapter for basal plane are employed for functionalization and characterization of the isolated graphene edges in the next chapters.

Chapter 5: Fabrication of Isolated Graphene Edge

This chapter demonstrates a simple photolithography-based method to fabricate the exclusive or isolated graphene (monolayer) edge electrodes. The key idea here is to separate the edge from the basal plane effect completely, which is important to study the exclusive edge properties. A simple approach via the insulation of basal plane followed by plasma etching is used to expose the edge of the CVD grown monolayer graphene sheet on an insulating substrate. Further, the exclusive availability of the the fabricated edge is proved using electrochemistry.

Chapter 6: Selective Functionalization of Graphene Edge

This chapter presents a versatile method using electrochemistry for the exclusive or selective functionalization of the edge of a graphene monolayer with different chemical moieties: metal nanoparticles (via electrodeposition) or organic groups (via non-covalent electropolymerization and covalent diazonium chemistry). In this way, different types of functionalization were demonstrated at the isolated edge using electrochemical modification. The deposition of gold nanoparticles at the edge was used for the modification as well as to provide an additional advantage of the surface-enhanced Raman scattering (SERS) effect to detect the chemical moieties formed or present at the pristine and modified graphene edges.

Chapter 7: Electrochemistry at the Graphene Edge Nanoelectrodes

This chapter provides the electrochemical characterization of the edge electrodes using various common redox probes. Graphene edge made of nanometer-thick single-layer graphene displays a nanoelectrode behavior. The characteristic properties of pristine and the nanoparticle modified edge are compared to each other, and further to the basal plane. The edge electrodes show steady-state current response with low capacitance values, negligible ohmic effects, and fast mass transport, unlike the basal plane electrodes. These properties allow for probing faster electron transfer (ET) kinetics, which was investigated by the development of a analytical model based on Butler-Volmer kinetics. The model was used to extract the kinetic parameters such as ET rate (k^0), and further explain the voltammetric behavior of the edge electrodes.

Chapter 8: Analytical Performance of the Graphene Edge Nanoelectrodes

This chapter illustrates the analytical capability of the edge nanoelectrodes in sensing applications. The nanoelectrodes were tested for electrocatalytic properties as well as detection limit towards redox probes, and small molecules like NADH and FAD.

3

Materials and Methods

3.1 Preparation of Graphene electrodes

The two most important methods to produce graphene are the mechanical cleavage of highly-oriented pyrolytic graphite (HOPG),[2] and chemical vapor deposition (CVD).[91] Mechanical cleavage is the first proposed method to isolate millimeter-sized graphene monolayers, and is reported to have a lower density of defects. On the other hand, CVD is used to grow graphene with a large area on different metallic substrates and is now established as a very common method for obtaining monolayer graphene. However, in order to realize devices based on CVD-grown graphene for potential applications, it is necessary to transfer individual graphene sheets onto a suitable substrate and remove residues of the metal substrate (Cu). The selection of an appropriate underlying substrate is important such that it does not affect the properties of an atom-thick layer of graphene. An insulating surface such as Si/SiO_2, glass, or quartz are the suitable substrates. The transfer of CVD graphene onto a substrate is usually achieved using polymer-support and metal etching/transfer. The most common method involves the etching of metal substrate in a solution after coating the graphene sheet by an inert polymer layer (such as PMMA, PDMS, or PS) for mechanical support.[191,192] When the metal substrate is completely etched, the graphene sheet is transferred to the desired substrate followed by the removal of the supporting polymer coating. The final transfer step is delicate and can generate mechanical stress causing minimal structural damages, cracks, folds, and alterations in the graphene sheet. In this work, polystyrene (PS) is used as polymer support as it provides graphene surfaces with minimal organic contamination in comparison to other polymers.[193] One major issue with the wet transfer method is the contamination by the remains of the metallic impurities, which can alter the electronic and electrochemical properties of the transferred graphene.[8,194,195]

3.1.1 Graphene Transfer Method

The Si/SiO_2 chips/substrates consist of photolithographically pre-patterned Ti (50 nm)/Pt (10 nm) electrode lines. The new chips were cleaned in N ethylpyrrolidone (NEP, $\geq$ 98 %, Roth) twice at 55 °C, followed by washing in acetone (VLSI, Selectipur®, BASF) and iso-propanol ($\geq$ 99.9 %, VLSI, Roth), with sonication for 30 minutes in all three steps. For the reuse of old Si/SiO_2 chips with graphene, the chips were treated with oxygen plasma etching (0.6 mbar, 100 mW, 3 min) to remove graphene, followed by cleaning in piranha solution to remove other organic impurities.

CVD-grown graphene (commercially available, from Graphenea Inc., figure 3.1a) was transferred to Si/SiO_2 substrates using a metal-ion-free wet transfer method described above.[195] First, polystyrene (PS, av. Mw 35000, Sigma-Aldrich) was drop-casted onto a big piece of CVD-graphene from its solution in toluene ($\geq$ 99.8% Rotisolv®, Roth) (50 mg/ml), and dried at 75 °C for 10 min. PS layer acts as a polymer support for graphene. Figure 3.1b shows an image of PS-coated graphene foil, which was cut into mall rectangular pieces of approx. 3 mm $\times$ 3 mm (figure 3.1c). The underlying copper was etched in a mixture of water (18.2 Mω, Barnstead Easypure II), hydrochloric acid (37 w%, p.a. Emsure®, Merck) and hydrogen peroxide (30 % p.a., AnalaR NORMAPUR®, VWR) (16:3:1) for 10 min (figure 3.1d). After Cu etching, the color of the graphene-PS changes from reddish brown to transparent (figure 3.1e). The graphene-PS pieces were then washed over subsequent water baths and transferred to the Si/SiO_2 chips as illustrated in figure 3.1h. This was followed by careful drying with compressed gas. Applying too much pressure while drying can lead to cracks and breaking of the graphene sheet. The graphene-PS was transferred such that it was also in contact with the electrode lines (figure 3.1h). This is essential to do any kind of electrochemical reaction or study at the graphene surface. The graphene-PS was then baked/dried in an oven at 95 °C for 10 minutes. Later, PS was removed in toluene (5 minutes with mechanical stirring), followed by drying. Finally, graphene-Si/SiO_2 chips were annealed at 600 °C under nitrogen atmosphere for 1 min to improve the adhesion of graphene onto the silicon chips and remove possible residual organic contamination from the surface of the electrode. The removal of copper trace impurities was carried out by electrochemical etching (e-etching).[195]

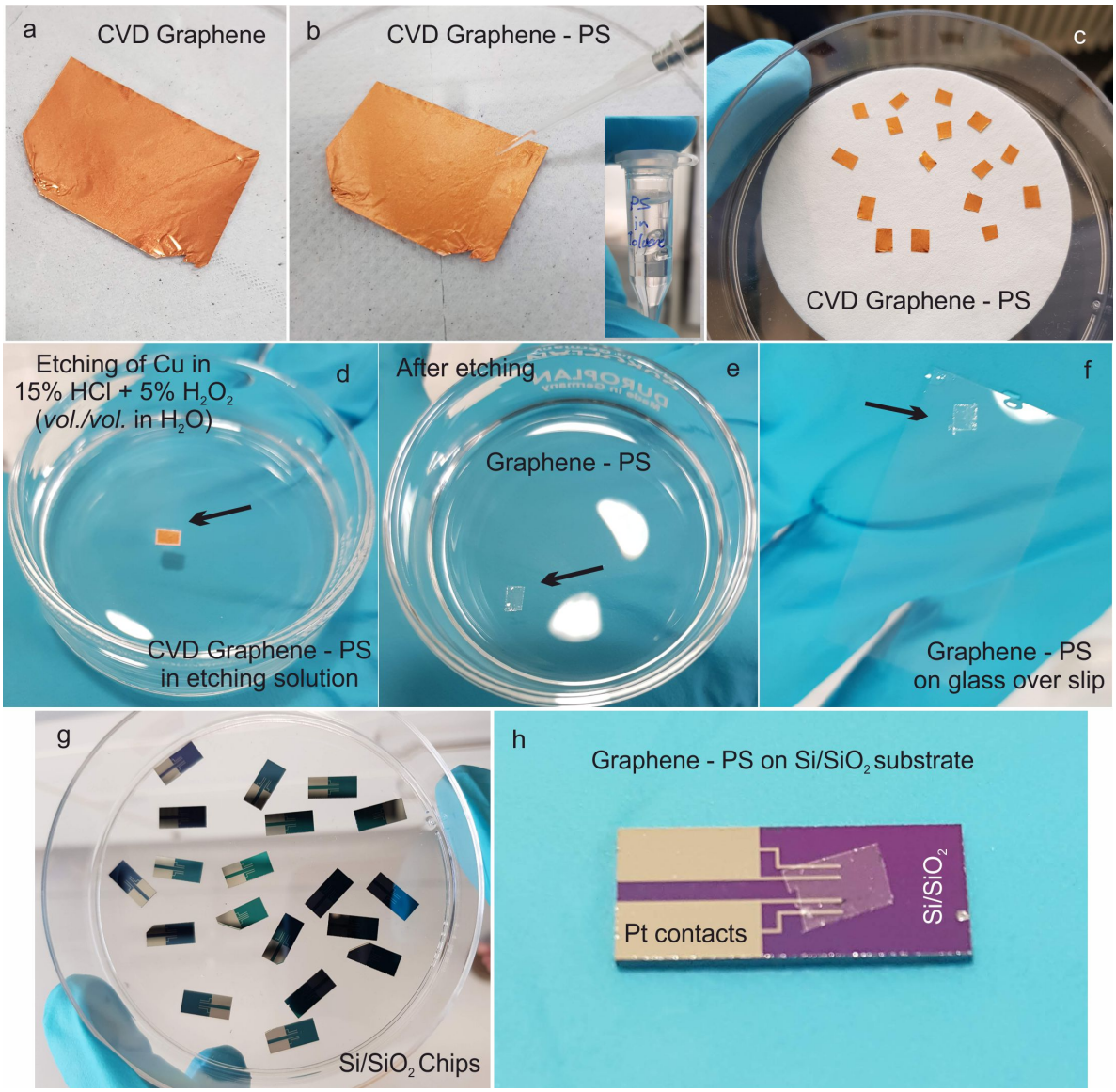

Figure 3.1: Graphene transfer process. Photographic images of (a) CVD graphene as purchased from Graphenea. (CVD graphene after coating with polymer polystyrene (PS). (c) small pieces of graphene-PS. (d) wet etching of Cu in HCl and H_2O_2 solution. (e) graphene-PS in the solution after etching (f) graphene-PS on a glass slip, to fish it out to fresh H_2O. (g) Si/SiO_2 chips. (h) graphene-PS on a Si/SiO_2 chip.

3.2 Electrochemistry

Electrochemistry is an important method to probe reactions involving electron transfer at the electrode (interfaces). Electrochemistry relates the flow of electrons to chemical reactions, often in form of the oxidation or reduction of a metal ion (complex) in inorganic chemistry. It uses tools like cyclic voltammetry, chronoamperometry to investigate these redox processes happening at the electrode. The setup used for an electrochemistry experiment is called an electrochemical cell. The original setup of an electrochemical cell is presented in figure 3.2, with each of the components.

3.2.1 Electrochemical Set up

All electrochemical measurements in the thesis were carried out using a three-electrode system comprising of graphene / graphene edge (GrEdge) / graphene edge modified with gold nanoparticles (GrEdge-AuNPs) as the working electrode (WE), platinum wire ($\phi = 0.5$ mm) as the counter electrode (CE), and a commercial Ag/AgCl (3 M KCl) capillary electrode (WPI Dri-Ref-450) as the reference electrode (RE). The experiments were performed in an electrochemical cell with 15 ml of solution using an Ivium Compactstat potentiostat. The set up is shown in figure 3.2. E-etching, electrochemical modifications, and the measurements with all the redox probes and biomolecules at different graphene-based electrodes were performed in this setup.

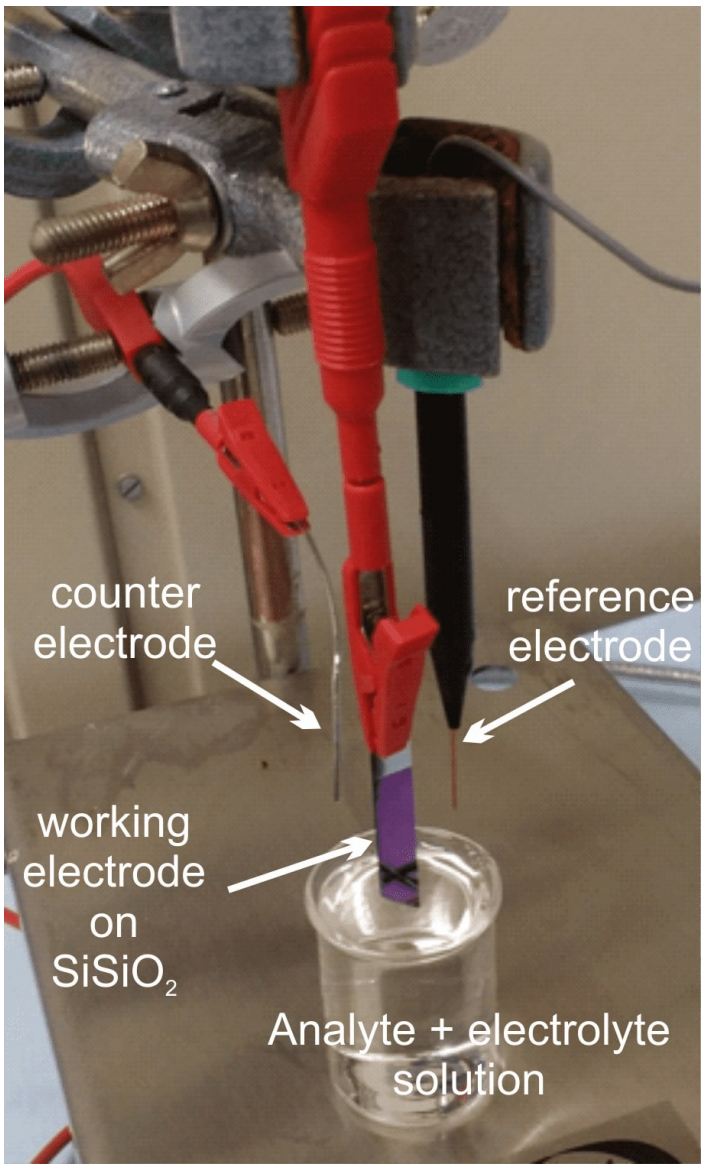

Figure 3.2: Photographic image of the electrochemistry set up, showing the graphene on Si/SiO_2 chip (working electrode), Pt (counter electrode), Ag/AgCl (reference electrode), and the analyte + supporting electrolyte solution in the beaker. All the electrode wires are connected to the potentiostat.

3.2.2 Redox Probes

An analyte or the electroactive specie is the material which undergoes reduction or oxidation at the electrode by means of electron transfer (ET) between them. Redox probes are a class of standard analytes, which are often used to investigate the electrochemical properties of different electrodes. The electrochemical properties of these redox probes are well characterized and can be divided into two classes: inner-sphere and outer-sphere, based on the electron transfer (ET) process at the electrode. It is wise to distinguish between an outer-sphere and an inner-sphere electron transfer process, which differ most significantly according to the sensitivity of their ET kinetics to the surface chemistry of the electrode. The ET rate constant varies on the condition of the electrode surface, with regards to the defects, impurities or adsorption sites and the absence/presence of specific oxygen-containing functionalities on the surface. Outer-sphere redox probes are termed as surface insensitive in which the rate constant is not influenced by the surface state, while the inner-sphere probes are surface sensitive in which the rate constant is influenced by the state of the surface.

For the outer-sphere redox probes (figure 3.3a,b,d,f) - ferrocenemethanol (97 %, Sigma-Aldrich), hexaammineruthenium (III) chloride (98 %, Sigma-Aldrich), and potassium hexachloroiridate (IV) (Sigma-Aldrich), potassium hexachloroiridate (III) (Sigma-Aldrich) are used in this thesis. For the inner-sphere redox probes (figure 3.3c,e) - potassium hexa-

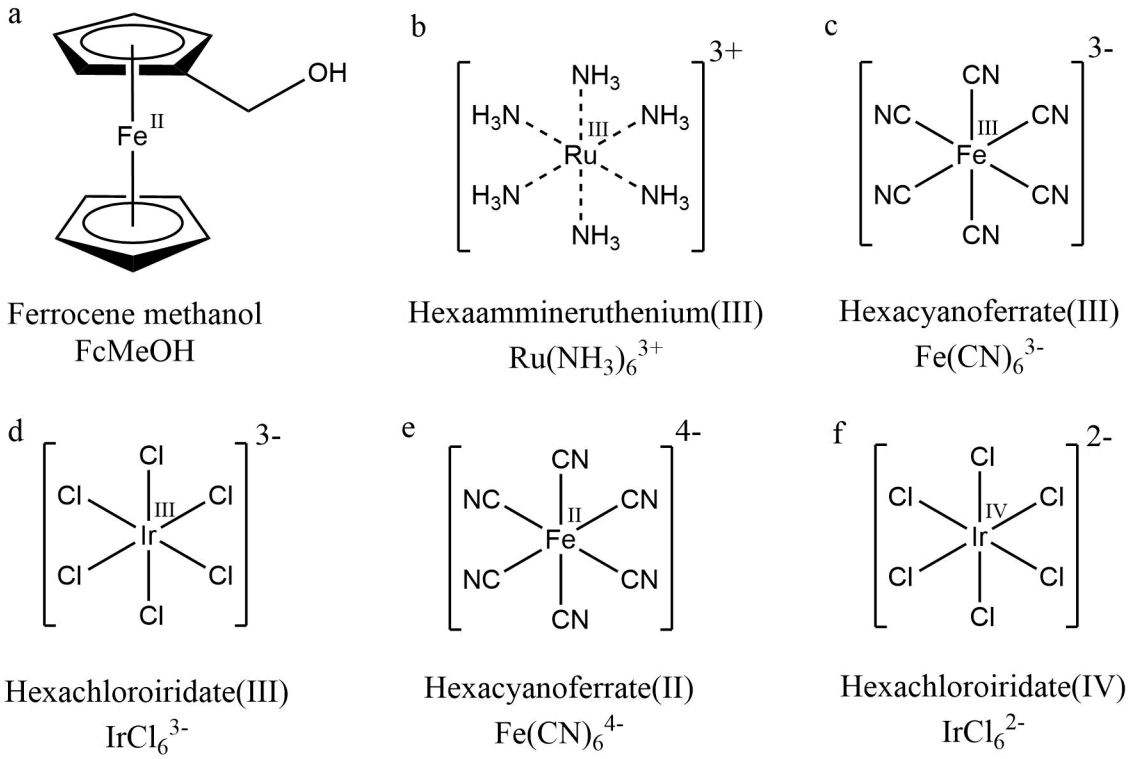

Figure 3.3: Chemical structure of the common redox probes used in this thesis: (a) ferrocenemethonol, FcMeOH (b) hexaammineruthenium, $Ru(NH_3)_6^{3+}$ (c) hexacyanoferrate(III), $Fe(CN)_6^{3-}$ (d) hexachloroiridate(III), $IrCl_6^{3-}$ (e) hexacyanoferrate(II), $Fe(CN)_6^{4-}$ (f) hexachloroiridate(IV) $IrCl_6^{2-}$

cyanoferrate (III) (99 %, Sigma-Aldrich), potassium hexacyanoferrate (II) (Sigma-Aldrich) are used in this thesis. All measurements with the above redox probes were done using potassium chloride ($\geq$ 99.0 %, Emprove® Essential, Merck) as background electrolyte.

3.2.3 Cyclic Voltammetry

Cyclic voltammetry (CV) is a powerful electroanalytical technique to acquire qualitative and quantitative information about any electroactive species and investigate their reduction and oxidation processes. A linear potential sweep is applied to a working electrode at a steady scan rate, first from a negative potential to a positive potential and subsequently in the reverse direction or vice-versa. The resulting current is measured over time, but plotted as a function of the applied potential. It is extensively used in the fields of electrochemistry, inorganic chemistry, organic chemistry, and biochemistry.

Figure 3.4a first shows the linear increase in applied potential with time from -0.3 V to 0.5 V and then the linear decrease with time from 0.5 V to -0.3 V. A typical CV profile obtained for the oxidation of FcMeOH redox probe at graphene electrode is illustrated in figure 3.4b, with the oxidation and reduction peaks. As the applied potential increases from -0.3 V toward the electrochemical oxidative potential of the FcMeOH ($E > 0.1$ V), the current increases from the capacitive (resting) current, resulting in a peak, called the peak anodic (oxidative) potential ($E_{pa} = 0.26$ V). The current then decreases as the applied potential surpasses this point. In the reverse cycle, the applied potential sweeps into the negative direction and the measured current becomes increasingly negative until it reaches the electrochemical reductive potential of the FcMeOH. Once the applied potential surpasses this point, a peak is formed through which, the peak cathodic (reductive) potential ($E_{pc} =$ 0.16 V) can be determined. The differences between the cathodic and anodic current from the resting current are denoted as i_{pc} and i_{pa}, respectively.

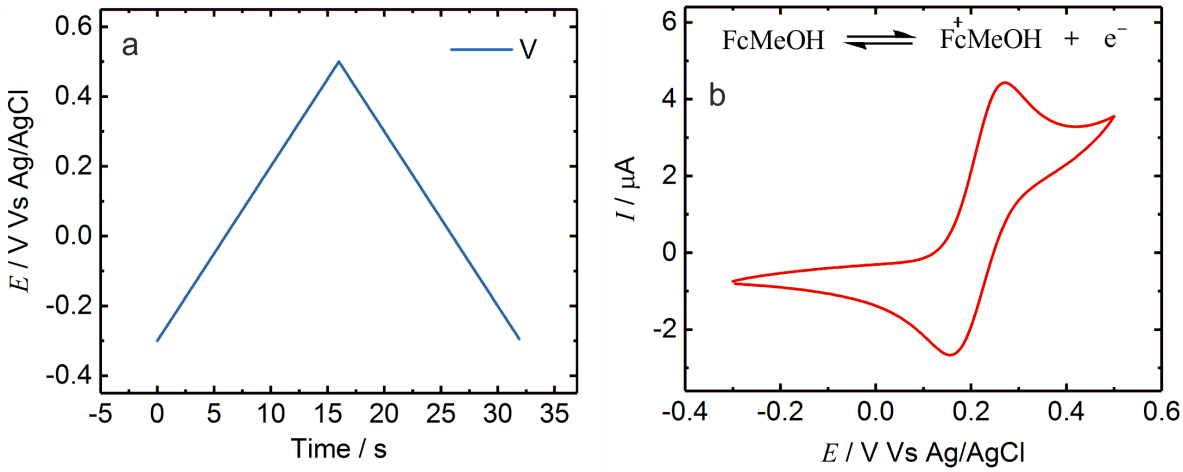

Figure 3.4: (a) Cyclic linear potential sweep between two set points (-0.3 V to 0.5 V) (b) The resulting CV for the oxidation of FcMeOH redox probe at the graphene electrode (WE) Vs Ag/AgCl (RE). Supporting electrolyte: 0.5 M KCl

3.2.4 Chronoamperometry

Chronoamperometry is a time-dependent electroanalytical technique, where a constant potential is applied in steps (for the duration of each step) at the working electrode and the resulting current from Faradaic processes occurring at the electrode (caused by the potential step) is monitored as a function of time. The observed current (at normal-sized electrode) in chronoamperometry is given by the Cottrell equation, which describes the current at any time following a large forward potential step in a reversible redox reaction as a function of $t^{-1/2}$ (t is time), due to the effect of depletion of electroactive species near the electrode surface.[180] Figure 3.4a shows the double potential step of +0.4 V, 15 s and -0.4 V, 5 s applied twice at the graphene electrode. The electroactive specie used here is $KAucl_4$ in 0.1 M $LiClO_4$ supporting electrolyte solution, in order to functionalize or modify graphene with gold nanoparticles. The resulting chronoamperometric profile (figure 3.4a) shows that at the positive potential (+0.4 V) step, current remains constant with no Faradaic processes happening at the electrode. However, at the negative potential step (-0.4 V), there is an increase in reduction current due to the reduction of Au^{3+} species to Au^{0} species. The current of the electrode, measured as a function of time, fluctuates according to the diffusion of the Au^{3+} analyte from the bulk solution toward the graphene surface.

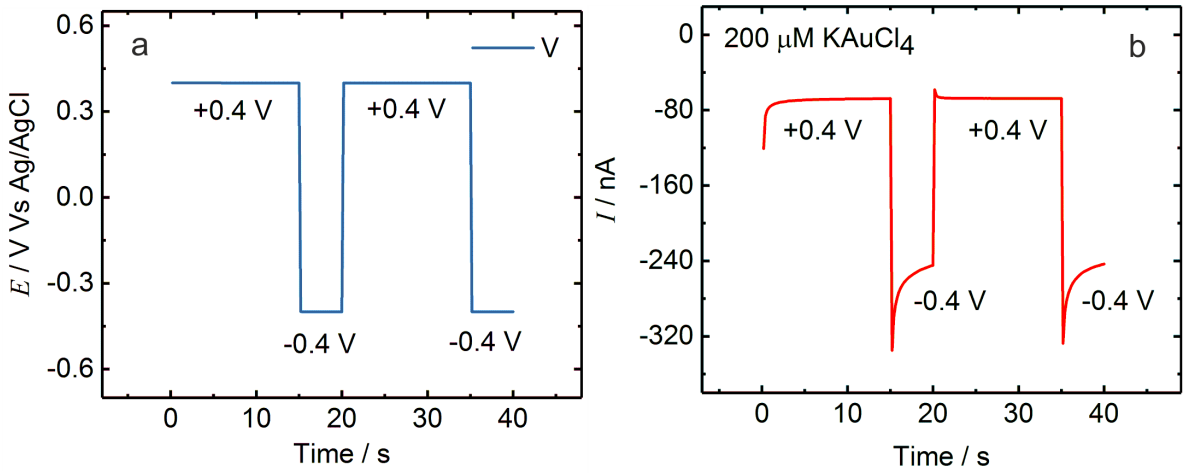

Figure 3.5: (a) The potential-time plot showing double potential step of +0.4 V, 15 s and -0.4 V, 5 s applied twice at the graphene electrode with $KAucl_4$ (analyte) in the solution. (b) The resulting chronoamperometric profile for the deposition of Au particles on the graphene electrode (WE) Vs Ag/AgCl (RE). Supporting electrolyte: 0.5 M KCl.

3.2.5 Electrochemical Modification

The electrochemical modification of graphene with different chemical groups was carried out in the same electrochemical setup described above potentiostatically by application of an appropriate potentials relative to Ag/AgCl using chronoamperometry and CV methods. The precursor salts, background electrolyte and experimental conditions were chosen appropriately, according to the chemical moieties (used for modification) and the electrode.

- **Metal nanoparticles**: The nanoparticles (Au, Pt, Pd) were electrodeposited potentiostatically where the metal salts are reduced using chronoamperometry (e.g. deposition of Au nanoparticles as shown in figure 3.5). Three different precursor salts were needed, namely, potassium gold (III) chloride (Sigma-Alrich), sodium hexachloroplatinate (IV) (Sigma-Aldrich), and sodium tetrachloropalladate (II) (Alfa Aesar). The background electrolyte for all the nanoparticle depositions was 0.1 M Lithium perchlorate, $LiClO_4$ (Sigma-Aldrich). The salt solutions were always prepared right before the electrochemical deposition experiments.

- **Electropolymerization**: For the electropolymerization of graphene, a potential was applied in the aqueous solution of 4-aminobenzylamine, (4-ABA) (98 %, Sigma-Aldrich) in 0.1 M $LiClO_4$ (electrolyte) using CV. A similar method was used for electropolymerization of graphene edge.

- **Diazonium chemistry**: Graphene and graphene edge electrodes were covalently functionalized using diazonium chemistry through CV. For the modification of graphene with benzoic acid, initially, diazonium ions of 4-carboxyphenyl (benzoic acid) were generated *in-situ* by the reaction of 1 mM aminobenzoic acid (Sigma-Aldrich) with 10 mM sulphuric acid (95-97 % AnalaR NORMAPUR®, VWR) and 5 mM sodium nitrite ($\geq$ 98 %, Alfa Aesar) at 4 °C. The color of the solution changes to yellow on the formation of benzoic acid diazonium ions. The formed benzoic acid diazonium ions were then reduced electrochemically by CV to benzoic acid radicals, and subsequently modifying the graphene.

  Graphene sheet was also modified with other aryl group, however, the diazonium salt was bought commercially, 4-nitrobenzenediazonium tetrafluoroborate (97 %, Sigma-Aldrich). Both the salts were directly reduced by CV in their aqueous solution to generate respective aryl radical.A similar method was used to functionalize graphene edge with commercially bought 4-nitrobenzenediazonium tetrafluoroborate.

3.2.6 Electrochemical Sensing

All the electrodes fabricated in this thesis, graphene edge (modified and unmodified) and basal plane were tested with two biomolecules: β-Nicotinamide adenine dinucleotide reduced disodium salt hydrate ($\geq$ 97 %, Sigma-Aldrich), NADH; Flavin adenine dinucleotide oxidized disodium salt hydrate ($\geq$ 95 %, Sigma-Aldrich), FAD. The electrochemical measurements of both NADH and FAD were carried out using CV in 10 mM phosphate buffer (7.2 ± 0.1) with added 0.1 M KCl as supporting electrolyte. Potassium phosphate monobasic ($\geq$ 99.0 %, Sigma), potassium phosphate dibasic ($\geq$ 98.0 %, Sigma-Aldrich) and potassium chloride was used to prepare the phosphate buffer.

3.2.7 Passivation of Graphene Contacts

It is necessary to passivate the part of the graphene sample at the contact region of graphene and Pt electrode lines. This is done to prevent the solution from coming in contact with Pt electrode lines on Si/SiO_2, as it can destroy the graphene in that region, and thus, the graphene may not be in contact with the electrode. When Pt electrode lines come in contact with the solution, it leads to the H_2 evolution reaction, thereby damaging graphene. Therefore, passivation of the interface of graphene-Pt lines is an integral part of the sample preparation process. The thick PS as shown in figure 3.6 prevents the direct contact of Pt electrode lines with the solution during electrochemistry. However, in the case of organic media, PS dissolves, and a different passivation material (e.g. photoresists) need to be used.

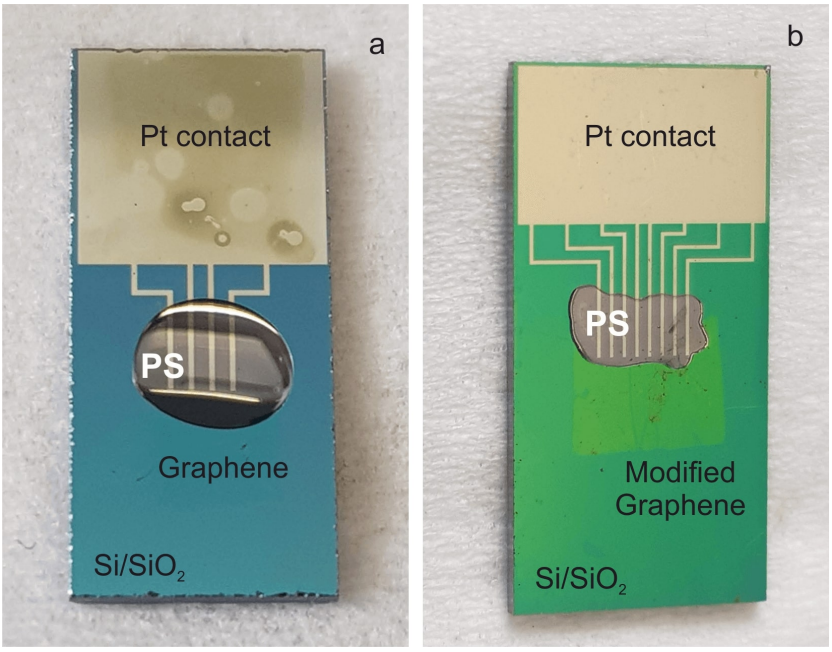

Figure 3.6: Photographic images of graphene on Si/SiO_2, with polystyrene at the interface between graphene and the electrode lines. Polystyrene prevents the direct contact of Pt electrode lines with the solution during electrochemistry.

Photoresists are an important class of passivation materials in microfabrication industry, which are patterned by photolithography under the cleanroom conditions using a maskless aligner MLA100, Heidelberg Instruments (HIMT). In this thesis, two photoresists are used in fabricating the graphene edge electrodes. They are S1805 (Microposit), developer mf-319 (Microposit); and SU-8(10) (Microchem), developer mrDev-600 (Micro Resist Technology). Photoresists are discussed in more detail in the chapter 5 (fabrication of graphene edge electrodes).

3.2.8 Removal of Impurities from Graphene

Following the transfer, it is necessary to ensure that the graphene surface is free of any kind of organic residues or metal impurities. The organic residues are usually removed during the annealing process (at 600 °C). The removal of trace metal impurities in graphene from the etching of underlying copper is more important because they have a stronger impact on the electronic and electrochemical properties of transferred graphene. The effect of trace metal impurities on the electrocatalytic activities of carbon nanotubes (CNTs) and graphene has been reported in the literature.[8,194,195]

One simple way to remove the remaining trace metal/metal oxide particles is using electrochemical etching (e-etching) by using CV in aqueous acidic media. The CV step was performed for 15 cycles in 0.1 M HCl and can be followed in situ by monitoring the oxidation current. Figure 3.7 shows the comparison of 1st and 15th scan cycle. The peak in the red curve (cycle 1) corresponds to the oxidation of copper. In the 15th scan, the copper oxidation peak has disappeared indicating the removal of trace copper impurities.

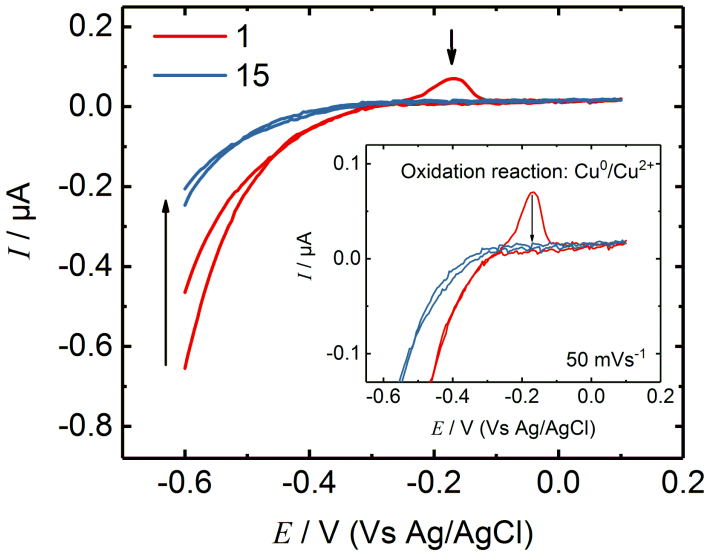

Figure 3.7: Graphene e-etching: CVs of as-transferred graphene for the 1st (red) and 15th (blue) scan cycle. The inset shows the oxidation of Cu^0 to Cu^{2+}, where the disappearance of oxidation peak confirms the removal of trace copper. The black arrow at -0.6 V indicates the decrease in the oxygen reduction current, which occurs due to the removal of the copper traces.

3.3 Characterization and Instrumentation

Following instruments / characterization tools were used in this thesis in order to characterize the graphene and graphene edge electrodes:

- Optical Microscopy: (1) Leica DM4000 M and (2) Zeiss AxioScope.A1 MAT.
- UV-Vis-NIR spectroscopy: (1) Perkin Elmer Lambda 950 S; (2) NanoPhotometer™ UV/Vis Spectrophotometer From Implen GmBH.
- Raman Microscopy: (1) JASCO NRS-4100, equipped with laser wavelengths of 532 nm (max. power 5.6 mW), 632.8 nm (13.6 mW) and 785 nm (39.5 mW), a 1650 $\times$ 256 CCD detector (Andor; air/Peltier-cooled, operating temperature: -60 °C), a 400 1/mm grating and a 100x (NA 0.90) objective) for acquisition of spectra. (2) LabRam HR 800 equipped with a 1024 $\times$ 256 CCD detector (symphony; liquid N_2 cooled), a 300 L mm^{-1} grating, a HeNe laser with an excitation wavelength of 632.8 nm (max. power 9mW), a 100x (NA 0.90) objective, and a detection pinhole of 100 µm.
- Scanning Electron Microscopy (SEM): Jeol JCM-6000 Neoscope, with high-vacuum (approx. 10^{-4} mbar) and low-vacuum modes (around 1 mbar). It also provides elemental analysis data through (energy-disperdive X-ray analysis) EDX in low vacuum mode.
- Atomic Force Microscopy (AFM): A commercial Dimension IV from Bruker working in tapping mode under ambient conditions.
- Electrochemistry: Ivium Compactstat potentiostat.
- Reactive Ion Etching: Diener electronic Femto Plasma.

Optical Microscopy Optical Microscopy is one of the first and easiest characterization techniques to identify graphene on Si/SiO_2 substrate first hand after the transfer process. Figure 3.8a-c shows the optical images of the same graphene sample at different magnifications. An image of the whole Si/SiO_2 substrate/ chip is shown in figure 3.8a, where the outlines of transferred graphene sheet (with slightly different color contrast) are clearly visible, along with graphene's overlap with the electrode lines (this contact is needed to build a connection between graphene and potentiostat in order to perform electrochemical experiments) of the substrate. Optical microscopy also provide information about the quality of transferred graphene in terms of folds, holes and cracks, and if there is some dirt present on the surface. At higher magnifications (Figure 3.8b-c), the intactness of graphene is apparent, however, a tiny dirt particle is also visible (light green circle). On another sample, the small dark dirt like structures are amorphous carbon residues (figure 3.8d-e).

Optical microscopy is also helpful in the quick visualization of the functionalized graphene (e.g. in the case of functionalization with nanoparticles).

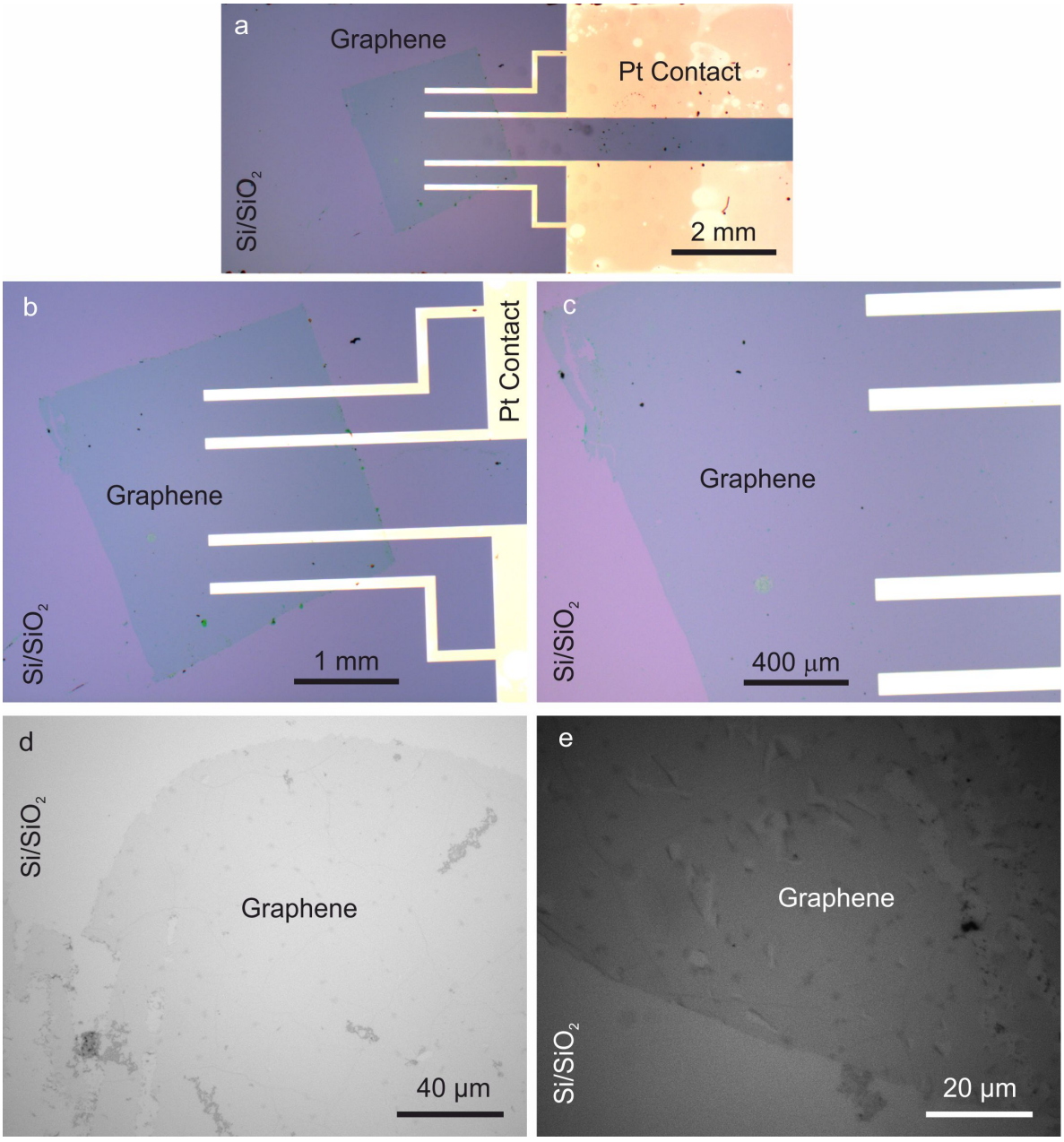

Figure 3.8: Optical images of a typical transferred graphene sheet on Si/SiO_2 substrate after polystyrene removal and annealing process.

Atomic Force Microscopy (AFM) AFM is performed to check the height of the transferred graphene and its intactness. Figure 3.9 presents the comparison of AFM images acquired at the same place before and after the e-etching process of graphene. After the wet transfer of graphene to Si/SiO_2, the trace impurities of Cu are apparent in figure 3.9a. However, after the e-etching process, the difference between both the images is clearly visible as the second AFM image (figure 3.9b) shows the cleaner graphene surface as opposed to the one before e-etching. The height profiles in figure 3.9c verify that only one layer of

graphene (relative height $\sim$ 1 nm) is present, and a slight decrease in height after e-etching further strengthens the removal of trace copper impurities from the graphene surface.

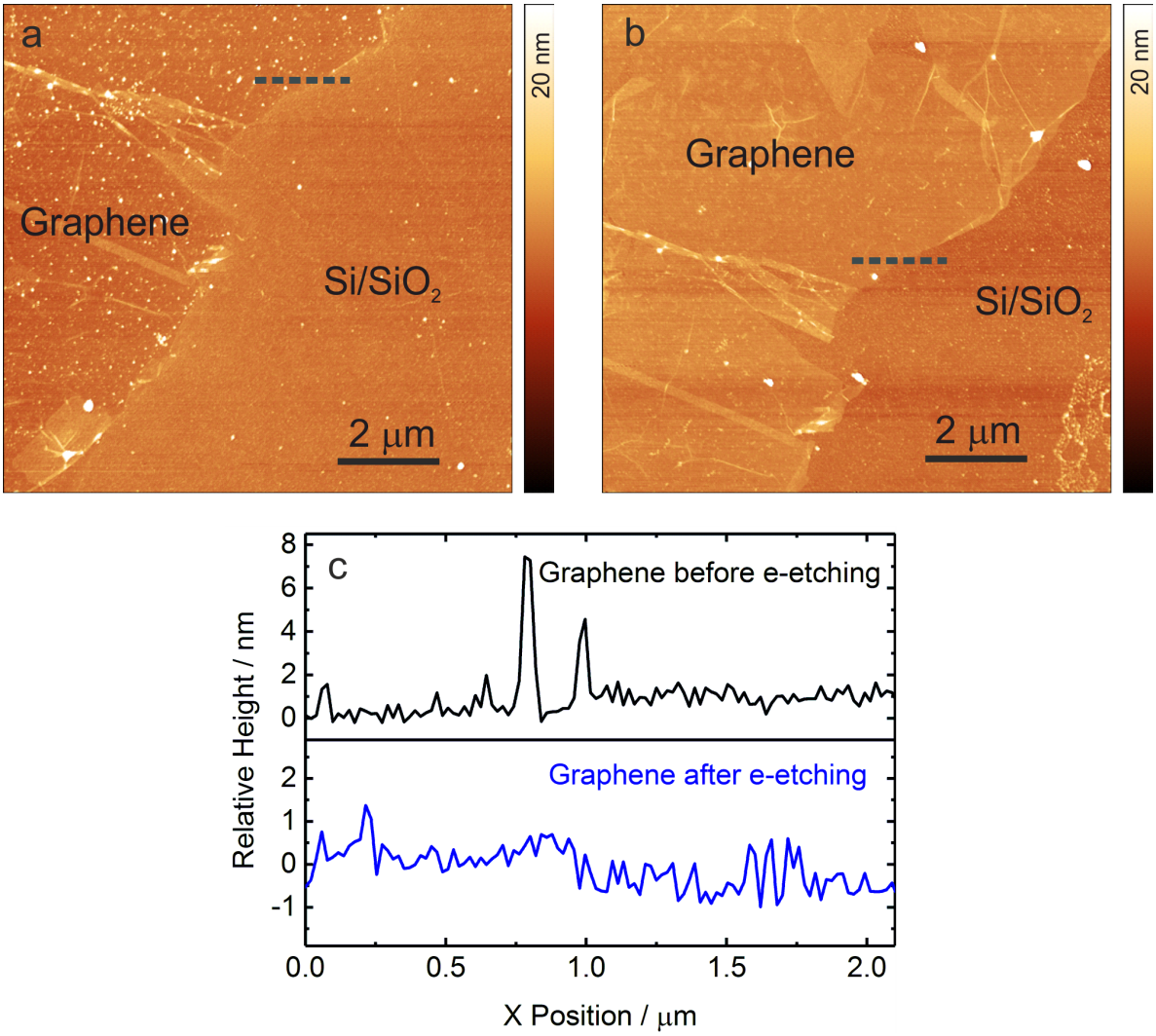

Figure 3.9: (a) and (b) shows AFM of transferred CVD-graphene before e-etching and after e-etching respectively; (c) Relative height profile of graphene before (in black) and after e-etching (in blue).

Raman Spectroscopy The quality control of the transferred graphene is done using Raman spectroscopy. This is important in order to check for structural defects, folds and unwanted products introduced during the transfer process. Figure 3.10 presents the background-subtracted and normalized (with respect to *2D* peak) Raman spectrum of the CVD-grown monolayer graphene transferred on Si/SiO_2. The spectrum (figure 3.10a) shows as expected, only *G* (1580 - 1587 cm^{-1}) and *2D* (2630 - 2640 cm^{-1}) peaks, with negligible intensity *D*-peak (expected at 1320 - 1330 cm^{-1}), indicative of graphene of high quality with minimal defects. The two bands at 520 and 976 cm^{-1} are marked as 'Si' are assigned to multiphonon scattering coming from the substrate Si/SiO_2.[196] Figure 3.10b shows the Raman spectra acquired at five different positions, defect-free region (red) which shows only

2D and *2D* peaks, and the defective region (blue), which shows a weak *D* peak indicative of some kind of disorder and defect. The intensity ratio, $I_{2D}/I_G \sim 3$ for *2D* to *G* peaks in all spectra is suggestive of single layer of graphene.

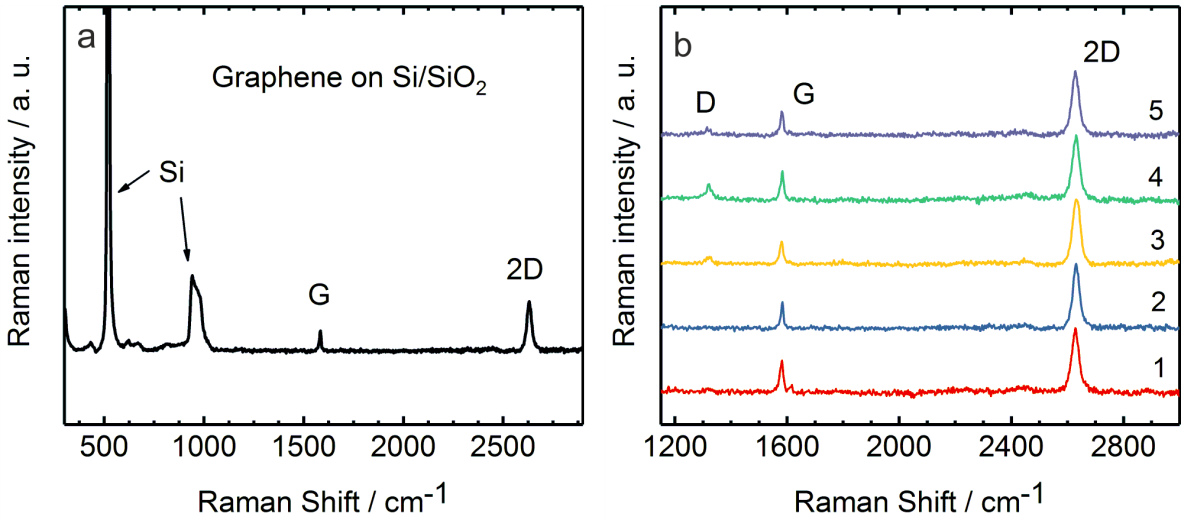

Figure 3.10: Raman spectrum of bare graphene after transfer on Si/SiO_2 showing the clear evidence of primary graphene peaks, *G* and *2D*, with the Si/SiO_2 substrate bands. (b) Raman spectra at five different positions on the graphene sheet. Note: Peaks are normalized to the *2D* peak intensity, Laser excitation wavelength, $\lambda_{ex} = 633$ nm.

4

Raman Spectroscopy and SERS on Functionalized Graphene

The results of the experiments presented here were published in the following manuscripts:

- L J A Macedo, F C D A Lima, R G Amorim, R O Freitas, A Yadav, R M Iost, K Balasubramanian and F N Crespilho, Interplay of non-uniform charge distribution on the electrochemical modification of graphene. *Nanoscale, 2018, 10, 15048-15057*.
- M Wehrhold, T J Neubert, A Yadav, M Vondracek, R M Iost, J Honolka and K Balasubramanian, pH Sensitivity of Interfacial Electron Transfer at a Supported Graphene Monolayer. *Nanoscale, 2019, 11, 14742-14756*.

In order to realize and understand the properties of graphene edge, it is important to know the experimental methods and characterization tools, which have been employed for graphene basal plane samples. The functionalization of graphene in a versatile and simple way is important to tune its electronic, chemical, and structural properties.[110,197] However, a single atomic layer of graphene is strongly influenced by the underlying substrate (through the charge transfer doping), which can affect the functionalization process.[198] This chapter demonstrates Raman spectroscopy as an important tool to study pristine graphene and the doping on graphene. Further, graphene is functionalized with metal nanoparticles (NPs) and organic groups (in a covalent as well as non-covalent manner) by the use of electrochemical modification (ECM) methods. The ensuing interactions between the graphene monolayer and the chemical groups after the functionalization are investigated using Raman spectroscopy. In addition, this chapter also presents surface-enhanced Raman scattering (SERS) approach to identify the functional groups attached to graphene surfaces by vibrational fingerprinting.

4.1 Effect of Substrate on Graphene

Graphene is strongly influenced by the underlying substrate because of the one-atom thickness of single layer graphene. The underlying substrate influences the chemical and electrochemical properties of the transferred single-layer graphene sheet.[199,200] For example, in the case of covalent modification (by diazonium salts) of graphene on different substrates, the reactions proceed rapidly for graphene supported on SiO_2 and Al_2O_3 (sapphire), but negligibly on alkyl-terminated and hexagonal boron nitride (hBN) surfaces.[198]

Figure 4.1 shows Raman spectra of graphene on Si/SiO_2 and a range of other substrate materials, normalized to the *2D* peak intensity on the corresponding substrate. From bottom to top, the substrates are Si/SiO_2, Si_3N_4, Al_2O_3 (c-plane sapphire) and gold (Au) surface. There is clear evidence of primary graphene peaks, *G* (1580-1587 cm^{-1}) and *2D* (2630-2640 cm^{-1}) on all substrates. Additionally, the substrate peaks are also shown. The Si-related band at 976 cm^{-1} on both Si/SiO_2 and Si/Si_3N_4 substrates are assigned to multiphonon scattering.[196] The peaks 1374 and 1404 cm^{-1} on Al_2O_3 are also arising from the substrate itself.[198] In all cases, the *D*-peak (expected at 1320-1330 cm^{-1}) intensity is almost negligible.

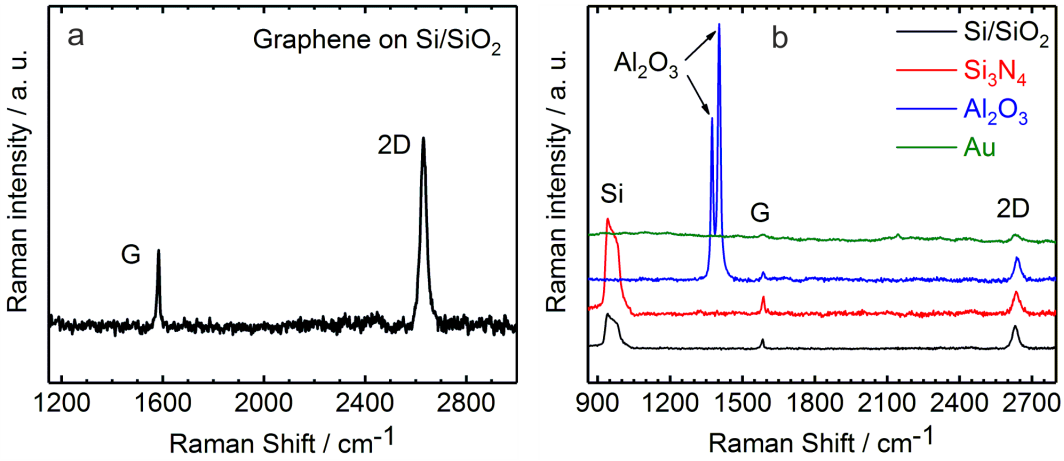

Figure 4.1: Raman spectra of a CVD-grown graphene monolyer on: (a) Si/SiO_2 substrate showing the Raman active modes of graphene. (b) a range of substrate materials - Si/SiO_2, Si_3N_4, Al_2O_3 (c-plane sapphire) and gold (Au) surface (from bottom to top). (All the peaks are normalized to the *2D* peak intensity on the corresponding substrate and laser excitation wavelength, λ_{ex}= 633 nm for acquisition on all substrates).

For detailed analysis, scatter plots of the peak parameters were obtained from the Raman spectra of graphene on all the substrates as shown in figure 4.2. This was compared to the data from the literature reports of monolayer graphene doped by electrostatic gating.[58,59] In figure 4.2a, the full-width at half-maximum (FWHM) of the *G* peak (Γ_G) is plotted against the position of the *G* peak (ω_G). The Γ_G decreases and ω_G increases for increasing *n*- and *p*-doping.[59] Therefore, bare graphene on Si/SiO_2 and Au lies closer to the undoped region while on Al_2O_3 and Si_3N_4, it lies closer to the more doped region. However, the doping type cannot be distinguished from this plot. The *G* and *2D* peak positions (ω_G and ω_{2D}) are

plotted against each other in figure 4.2b to distinguish between the *n*- or *p*-type of doping. Both ω_G and ω_{2D} increase with *p*-type doping, while ω_G increases and ω_{2D} decreases for *n* type doping. The graphene on Si/SiO_2 lies in the undoped region, and graphene on Si_3N_4 is in the *p*-doping region, with the other surfaces lying in between the two.

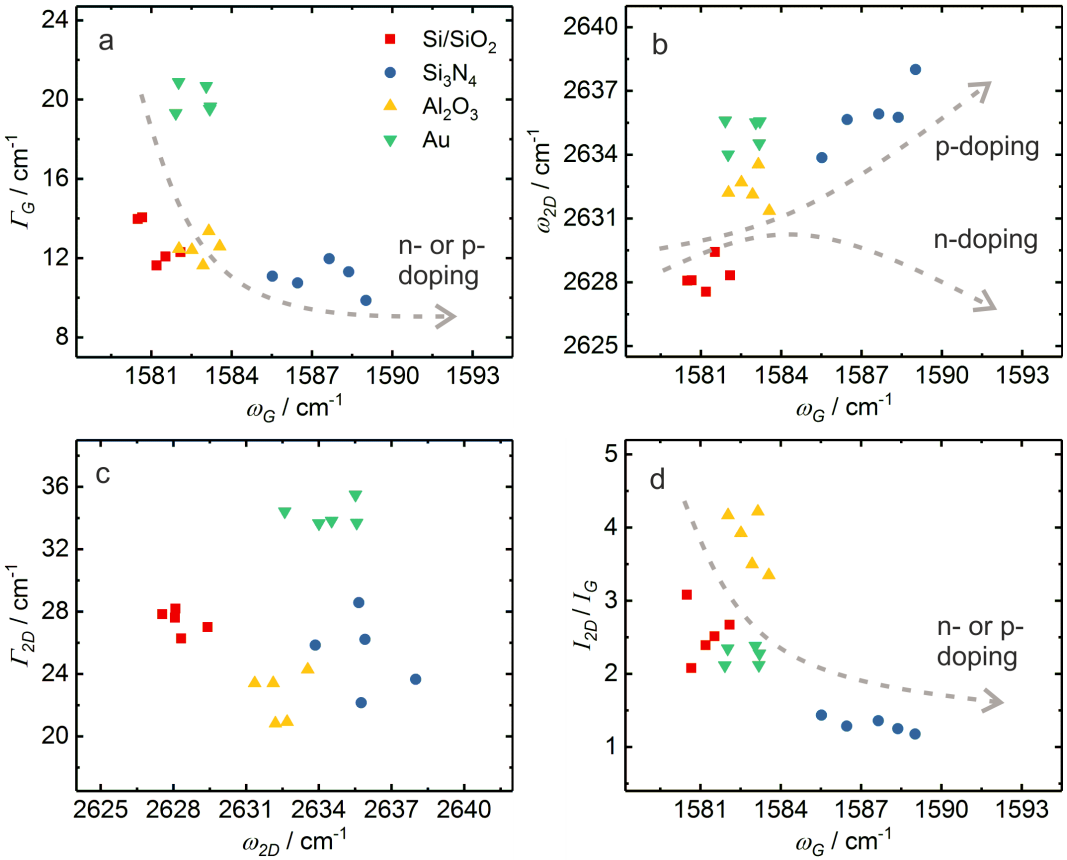

Figure 4.2: Scatter plots of Raman peak parameters of pristine graphene on Si/SiO_2, Si_3N_4, Al_2O_3 (c-plane sapphire) and gold (Au) surface. (a) *G* peak full-width at half-maximum (FWHM, Γ_G) versus *G* peak position (ω_G). (b) *2D* peak position (ω_{2D}) versus *G* peak position (ω_G). (c) *2D* peak FWHM (Γ_{2D}) versus 2D peak position (ω_{2D}). (d) I_{2D}/I_G intensity ratio versus G peak position (ω_G). The direction of arrows (dashed-grey) in a,b,d indicate the increase in doping and its type. (All the data points are obtained after normalizing the Raman spectra w.r.t the *2D* peak intensity on the corresponding substrate and λ_{ex}= 633 nm for aquisition on all substrates)

The FWHM of the *2D* peak (Γ_{2D}) is plotted against its position ω_{2D} in figure 4.2c. Since, ω_{2D} shifts in opposite directions for electron or hole doping (4.2b), the increase in FWHM of *2D* peak is attributed to the presence of electron-hole puddles which leads to higher charge impurity scattering. Graphene on Au exhibits the highest Γ_{2D} values, and graphene on Al_2O_3 has the lowest. On Si_3N_4, the Γ_{2D} is slightly higher than on Al_2O_3 and notably lower than on Si/SiO_2. The electron–hole charge fluctuations (or 'puddles') are usually due to rough surfaces and charged impurities.[154] This points to the fact that gold has the highest electron–hole puddles followed by Si/SiO_2 in the mentioned surfaces. The intensity ratio I_{2D}/I_G is plotted against ω_G in figure 4.2d. The I_{2D}/I_G ratio decreases and

ω_G increases for increasing *n*- and *p*-doping. Graphene on Si/SiO_2, is closest to the undoped region of the plot, followed by Au, Al_2O_3, and finally Si_3N_4 at the most highly doped region.

In summary, graphene on various substrates exhibits different extents of doping and electron-hole charge fluctuations. Graphene is found to be least doped on Si/SiO_2 and gold, with not so low degree of charge fluctuations on both of them. Au surface has the highest broadening of the Γ_{2D} from electron-hole puddles. In contrast, graphene on Al_2O_3 and Si_3N_4 are more highly *p*-doped, with lower Γ_{2D} values, indicating the least broadening of the corresponding *2D* peaks from charge fluctuations.

4.2 Electrodeposition of Gold Nanoparticles (AuNPs)

Nobel metal NPs like gold are chosen for modification because of their strong localized surface plasmon resonance (LSPR) absorption in the visible range of the electromagnetic spectrum,[128,164] as well as their catalytic and sensing properties. The LSPR effect is useful in Raman spectroscopy as it leads to enhancement in the Raman signal of graphene through the SERS effect,[65,166] which has been observed earlier on graphene after deposition of AuNPs.[50,64,65] Au is preferred over other metals because its electrodeposition does not require any additional growth control agent (such as poly(vinylpyrrolidone) which is needed in case of electrodeposition of other metals (silver).[49] The extra growth agent may interfere with the Raman signals. It is also easier to control the deposition of Au in comparison to Ag.

Figure 4.3 demonstrates the electrodeposition of metal NPs on graphene via the reduction of metal precursor salt by the incoming electrons from the graphene through the

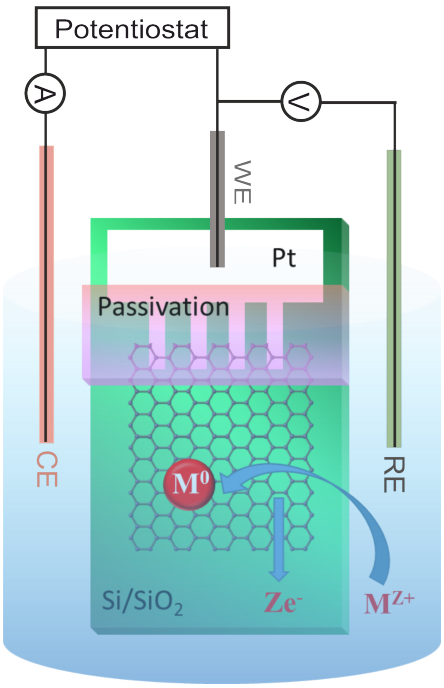

Figure 4.3: Reaction schematic for the reduction of metal ions to form the metal NPs at graphene surface by ECM.

heterogeneous electron transfer (HET), which follows: $M^{Z+} + Ze^- \longrightarrow M^0$, where M is the metal, and M^{z+} is its ionic form.

Functionalization and Characterization For AuNPs, a Au salt ($KAuCl_4$) in 0.1 M $LiClO_4$ (electrolyte) is reduced at double potential steps (vs Ag/AgCl) of -0.5 V, 5 s and 0.4 V, 15 s using chronoamperometry (figure 4.4a). The double potential step approach is a well-known method to control the size, density, and size distribution of the particles in a reproducible manner.[143,145]

The AFM images (figure 4.4b,c) captured at the same area before and after modification clearly shows the formation of AuNPs on graphene after electrodeposition. The formation of particles rather than a continuous film of Au is attributed to a spatial variation in the reactivity of graphene surface arising due to various factors such as defects, domains, etc.[127,201] This leads to local nucleation sites resulting in the formation of small metallic islands or particles.[5] The line profiles along the dashed-lines (black) in the corresponding AFM images are shown in figure 4.4d. It clearly shows the height of around 1 nm for bare graphene, while for Graphene-AuNPs, the height of particles is in the range of 50-60 nm on the basal plane and $\sim$ 120 nm at the edges. The edges are more prone to functionalization due to the presence of a large number of defect sites (increasing their reactivity),[6] and higher diffusion (due to edge effects).[202,203] This leads to higher density and size of the particles at the

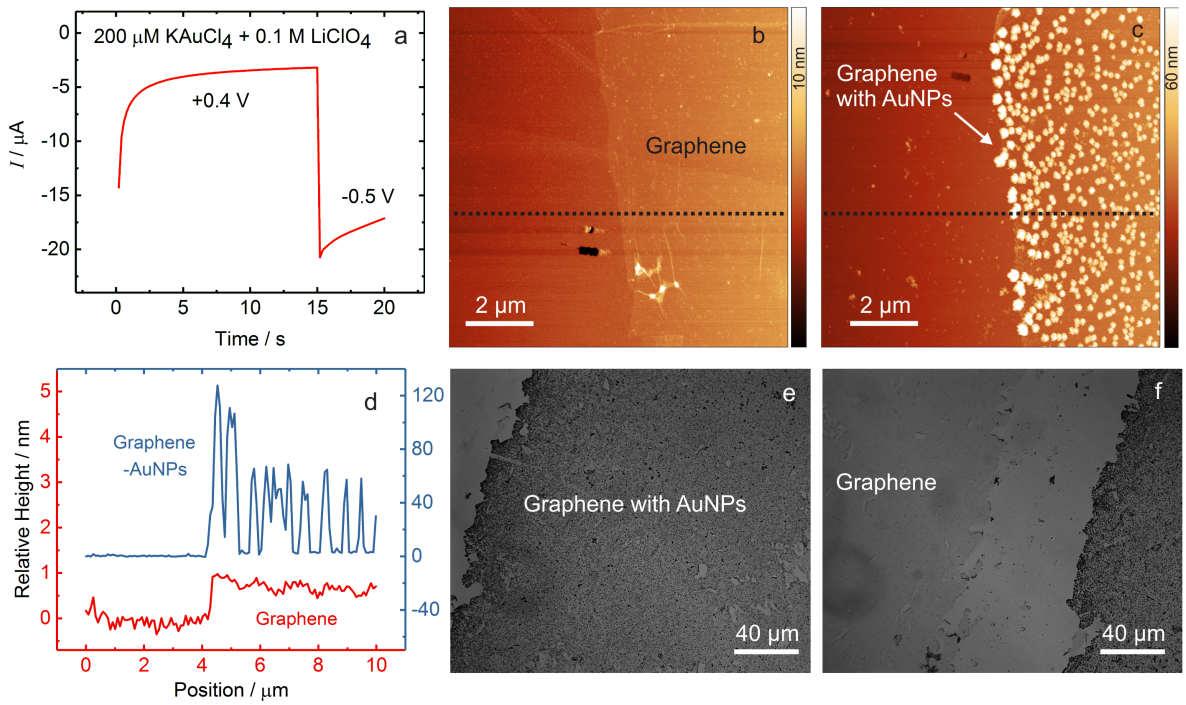

Figure 4.4: (a) A chronoamperometric profile for the deposition of AuNPs at graphene surface. (b,c) are AFM images of the (b) pristine graphene and (c) AuNPs functionalized graphene. (d) The corresponding line profiles (at the locations shown with black dotted lines in (b,c) comparing the height before and after AuNPs deposition. (e,f) are optical images captured after the deposition of AuNPs.

edges. The optical image in figure 4.4e clearly shows the particles grown everywhere on the graphene sheet. In figure 4.4f, there are two regions of graphene, with particles (right side) and without particles (left side), separated by a huge gap (or break) in between the two regions. The left side graphene is not in contact, therefore, no particles were obtained there.

UV-vis Absorption Next, the UV-vis absorption of unmodified graphene and AuNPs modified graphene were obtained on a quartz slide (substrate) in the air in transmission mode (figure 4.5a). The absorption spectrum of pristine graphene (red curve) shows an asymmetric peak at shorter wavelengths ($\sim$ 270 nm) and a flat absorption at higher wavelengths. The asymmetric peak in the UV region is attributed to a excitonic Fano resonance that forms near the Van Hove singularity at the saddle point of the band structure.[204] The limiting value of absorption is close to the theoretical value of $\sim$ 2.3 % (an integer multiple of $\pi\alpha$) in agreement with the previous observations ($\alpha = 1/137$ is a fine structure constant in vacuum).[205,206] The multiple of one to $\pi\alpha$ confirms a single layer of graphene. After modification with AuNPs, the additional absorption bands appear in the range of 500 - 700 nm, which can be attributed to the LSPR bands of the AuNPs. The AuNP-modified graphene sample measured in the air has a peak at $\sim$ 600 nm, which shifts to $\sim$ 660 nm in water and 0.1 M KCl solution (figure 4.5b). A large red shift of $\sim$ 60 nm is observed in the LSPR of AuNPs on graphene when the refractive index was varied from 1.00 (air) to 1.33 (water) and 1.35 (0.1 M KCl). A very small shift ($\sim$ 2 nm) is observed between water and 0.1 M KCl, due to a very small difference in their refractive indices. The maximum absorption wavelength of metal NPs is greatly influenced by the solvents.[207]

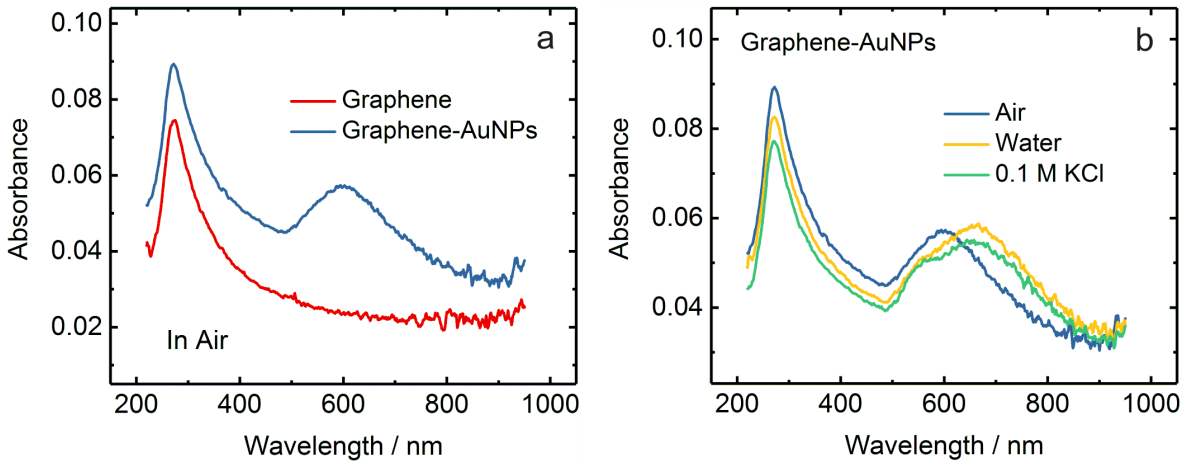

Figure 4.5: (a) Absorption spectra of bare graphene and Graphene-AuNPs. The spectra were obtained in air after transferring graphene on a quartz slide and subsequent electrodeposition step. (b) Absorption spectra of Graphene-AuNPs in different media (Air, water and 0.1 M KCl)

Raman Spectroscopy Figure 4.6a collects Raman spectra at the same location, at pristine graphene before ECM steps, and on AuNPs functionalized graphene, at each ECM step. The size of the particles increases with each ECM step, thereby increasing the intensity of the Raman peaks as well as the fluorescence coming from the particles. The SERS spectra after the ECMs display a number of new features: enhancement of the Raman peaks, a clear background coming from the AuNPs, a slight shift in the position of the peaks, and the increase in the intensity ratio of the *G* to *2D* peaks towards one. The phenomenon of fluorescence background (which is otherwise almost zero in the case of pristine graphene) is characteristic of Au particles (size less than 150 nm) and occurs due to the radiative recombination of electrons from the 6*sp*-band close to the Fermi level with holes in the 5*d*-band.[208–210] Therefore, it is attributed to the fluorescence of deposited AuNPs on graphene, which is in agreement with the previous observations on graphene- (or CNT-) NP hybrids.[50,148] The position of the *G* and *2D* peaks (obtained by fitting Lorentzian) shift from 1588 cm^{-1} and 2678 cm^{-1} (for bare graphene) to 1580 cm^{-1} and 2662 cm^{-1} after the ECM 3. Furthermore the FWHM of both *G* and *2D* increases from $\sim$ 18 cm^{-1} and $\sim$ 33 cm^{-1} (for bare graphene) to $\sim$ 49 cm^{-1} and $\sim$ 55 cm^{-1}. The changes in peak properties after the ECMs are clearly indicative of doping or some kind of chemical interaction (charge transfer) between the AuNPs and graphene.[57] Hence, the fluorescence, the Raman enhancement, and the doping feature, all can be correlated to the attachment of AuNPs, attributed either to the plasmonic resonances[210–212] or to charge transfer properties.[57]

Figure 4.6b shows the enhancement factor (EF) for the main Raman modes as a function of ECM steps. EF is calculated by taking the direct intensity (without baseline subtraction) of each peak after every ECM step and then dividing it by the intensity of the corresponding peak at the bare graphene. It is apparent that the degree of enhancement is slightly different for all the graphene modes and becomes weaker after each ECM. The EF also decreases slightly with an increase in the frequency of the vibrational mode (*G* has higher enhancement than *2D*). From these observations, it can be concluded that increasing particle size mainly

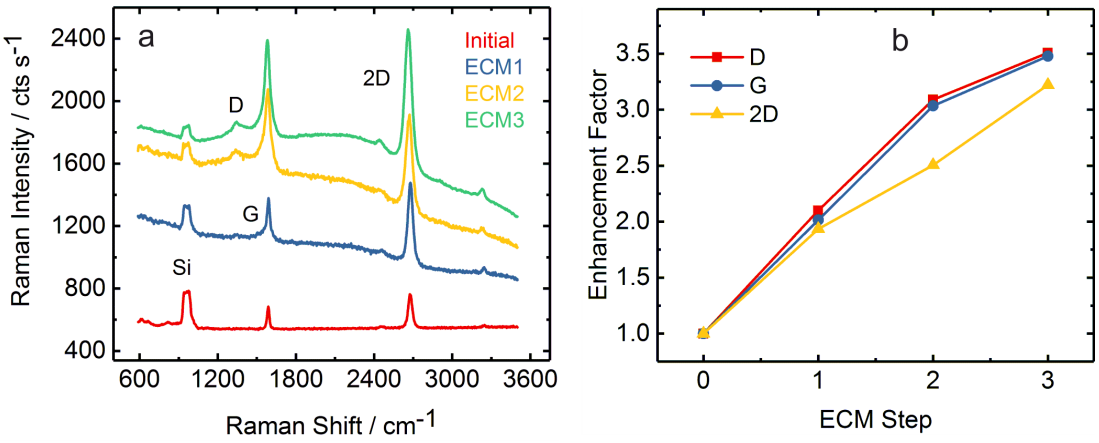

Figure 4.6: Raman spectra of pristine graphene (red), after ECM 1 (blue), ECM 2 (yellow) and ECM 3 (green). (λ_{ex}: 532 nm, 3.4 mW, 2 $\times$ 2 s)

leads to an increase in the fluorescence background and enhancement in the intensity of the observed Raman peaks. The effect of the size, shape, and density of the AuNPs on the extent of Raman enhancement has been studied in detail by Balasubramanian *et al.* previously.[50] The authors have shown systematically that the Raman intensity appears to depend on the interfacial surface area between the AuNPs and graphene, and deposition of smaller particles at high density is the most efficient route to obtain maximal SERS effect with a less fluorescence background.

4.3 Electropolymerization (Non-Covalent)

Electropolymerization is a well-known approach to modify carbon electrodes,[151–154] and has been demonstrated for coating the individual CNTs and graphene sheets non-covalently with the polymeric layers.[49,51] For this, a required monomer is oxidized by applying positive potentials via CV, which generates the active species or the cation radical through the HET with the graphene. The active species tend to react further with the precursor or to self-polymerize resulting in the formation of the polymer coating on the WE. The polymerization mechanism (for aromatic amine) is shown in the schematic in figure 4.7.

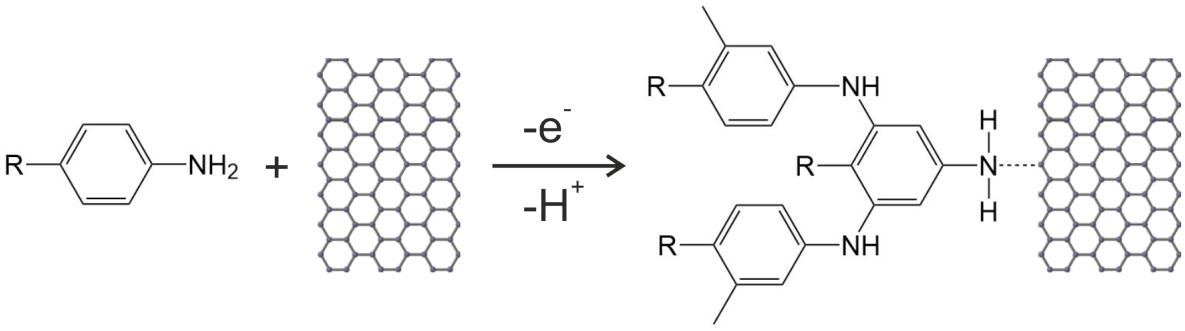

Figure 4.7: Reaction scheme for the oxidative ECM with the broken line indicating the formation of electropolymerized layers of aromatic amine on the graphene without the creation of a chemical bond. Adapted from reference [213].

Functionalization and Characterization The polymerization of 4-aminobenzylamine (ABA) on the graphene surface was performed using CV by applying potential in the range of -0.2 to 0.8 V (vs Ag/AgCl), in a solution of 1 mM ABA (in 0.1 M $LiClO_4$). The CV (red curve) shown in figure 4.8a exhibits an anodic peak at around 0.6 V for 4-ABA oxidation. In literature, this anodic peak corresponds to the irreversible oxidation of the amine group leading to the formation of the corresponding radical, which self reacts to form a polymer layer containing oligomers of varying chain lengths.[214–216] Therefore, the electrochemical oxidation of ABA initiates the polymerization by the generation of ABA radical, which further reacts with another ABA molecule to form poly-4-aminobenzylamine (pABA). Consequently, it could lead to the attachment of pABA layer onto the graphene surface. Figure 4.8c,d

shows AFM images of graphene surface before and after electropolymerization of 4-ABA. From the line profile in figure 4.8b, the inferred thickness of pABA layer is around 1 nm. The thickness of the polymer layer can be systematically controlled by adjusting either of the following electropolymerization parameters: monomer concentration, deposition time, and potential. As an example, the concentration of ABA was increased to 10 mM, which clearly shows the increase in current (because of the increase in active species) in the CV (blue curve) (figure 4.8a) and also the increase in thickness of pABA layer ($\sim$ 3 nm) as evident by the AFM images (figure 4.8e,f) and line profiles (figure 4.8b).

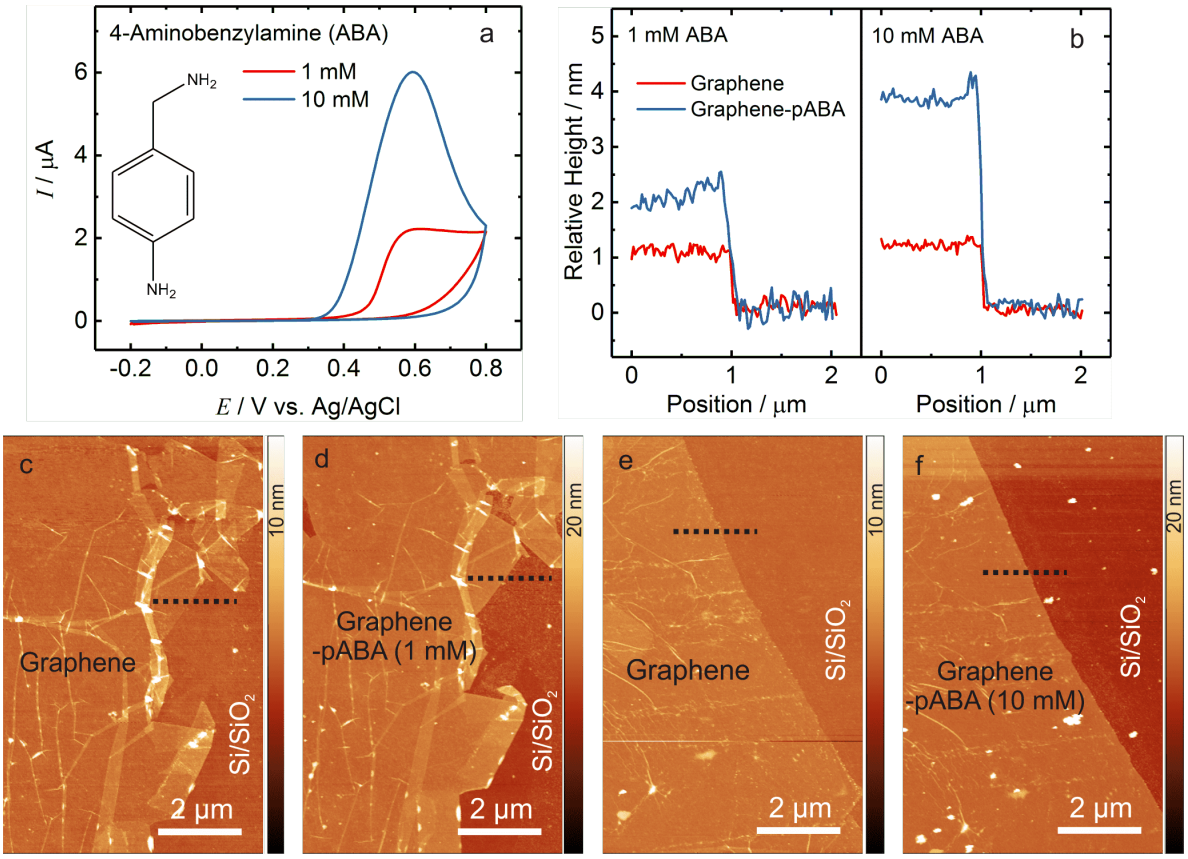

Figure 4.8: Electropolymerization of 4-aminobenzylamine (ABA) on graphene. (a) CVs at a graphene electrode with the precursor ABA at two concentrations: 1 mM (red curve) and 10 mM (blue curve) in an aqueous solution with 0.1 M $LiClO_4$. The scan rate is 20 mV s^{-1}. Inset shows the molecular structure of ABA. (b) Line profiles along the black dotted lines in (c-f) before and after pABA modification. (c,d) AFM images for 1mM ABA, before (c) and after electropolymerization with pABA (d). (e,f) AFM images for 10 mM ABA, before (e) and after electropolymerization with pABA (f)

Raman Spectroscopy Further, the Raman spectra of both the pristine (red) and pABA modified graphene (blue) shows the signature *G* and *2D* peaks (figure 4.9). The absence of *D* peak in Graphene-pABA spectrum confirms the non-covalent nature of the modification, which is in agreement with the previous studies.[51,216] The minimum changes in intensity ratio and FWHM of the Raman peaks is suggestive of negligible doping on the graphene sheet

through pABA layer. Therefore, the non-covalent attachment of pABA preserves the favorable electronic properties of graphene, which are essential to realize graphene electrodes.

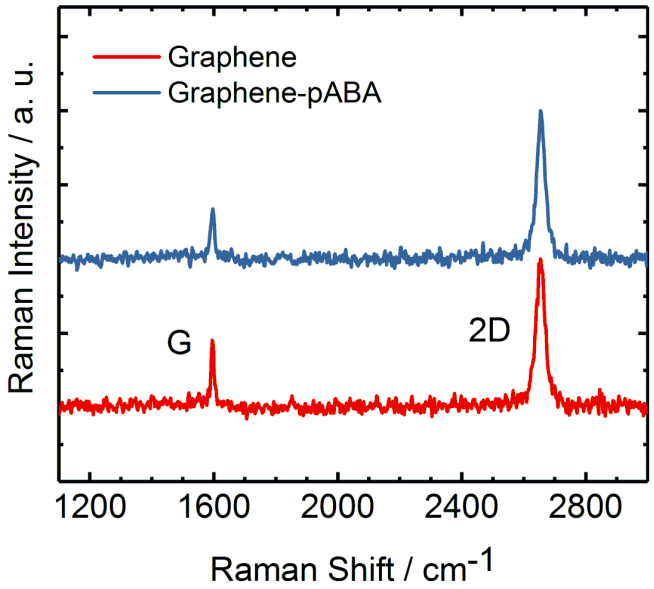

Figure 4.9: Raman spectra of pristine (red) and pABA functionalized graphene (blue). (λ_{ex}: 633 nm, 0.9 mW, 1 $\times$ 1 s)

4.4 Diazonium Chemistry (Covalent Modification)

The covalent modification of graphene is broadly classified into: (a) oxidative approach, which is used mostly for graphene oxide, and results in the generation of groups like ketones, quinones, and/or carboxylic acids, and (b) reductive approach, which is widely used for graphene and results in the formation of covalent bonds between free radicals or dienophiles and sp^2 hybridized carbon atoms of pristine graphene.[110,127] The reductive strategy has been used for the surface modification of materials including gold,[217] HOPG,[218], CNTs,[213,219] glassy carbon,[220] and graphene.[6,127] The substrate (graphene) acts as an electron donor to an aryl diazonium ion on the application of a reductive potential, generating an aryl radical after the elimination of nitrogen gas (as shown in the schematic in figure 4.10a). Consequently, the phenyl moiety forms a covalent bond with graphene. Raman spectroscopy is an easy method to characterize the modified graphene, due to the activation of the defect-related peaks, attributed to disruption of the π conjugated network after the covalent bond formation.

This section demonstrates the electrochemical grafting of groups like benzoic acid and 4-nitrobenzene on monolayer graphene using their respective diazonium salts. Further, Raman spectroscopy has been used for the characterization and quantification of the introduced defects. Later the deposition of AuNPs was carried out on covalently modified graphene to enhance the Raman signals of the grafted functional groups by virtue of the SERS effect, and to identify these groups by vibrational fingerprinting.

4.4.1 Quantification of Defects (Graphene - Benzoic Acid (BA))

Functionalization and Characterization The chemical functionalization of graphene was carried out with benzoic acid (BA) to create the defects by means of covalent binding to the graphene surface. For this, initially, BA diazonium ions were prepared by the reaction of aminobenzoic acid with nitrous acid (generated *in situ* using $NaNO_2$ and H_2SO_4) as shown by the schematic in figure 4.10a. This was followed by the electroreduction of the BA diazonium ions by application of a potential (figure 4.10b). The reduction of the diazonium salt by graphene to form the aryl radical is the rate-limiting step in the reaction of diazonium salts with graphene. The rate depends on the overlap between the electronic DOS of the graphene and the diazonium reactants in solution, and the electron transfer occurs between any occupied state of the graphene that is matched in energy with an unoccupied state of the diazonium. The applied potential increases the energy levels of the DOS of graphene resulting in an overlap of the HOMO of graphene with the LUMO of the aryl radical.[127] The first cycle (red) in CV shows an irreversible reduction wave with a current peak at around -0.25 V (vs Ag/AgCl), which leads to the generation of BA radical units after the displacement of the N_2 groups of the diazonium ion. The BA radical attacks the

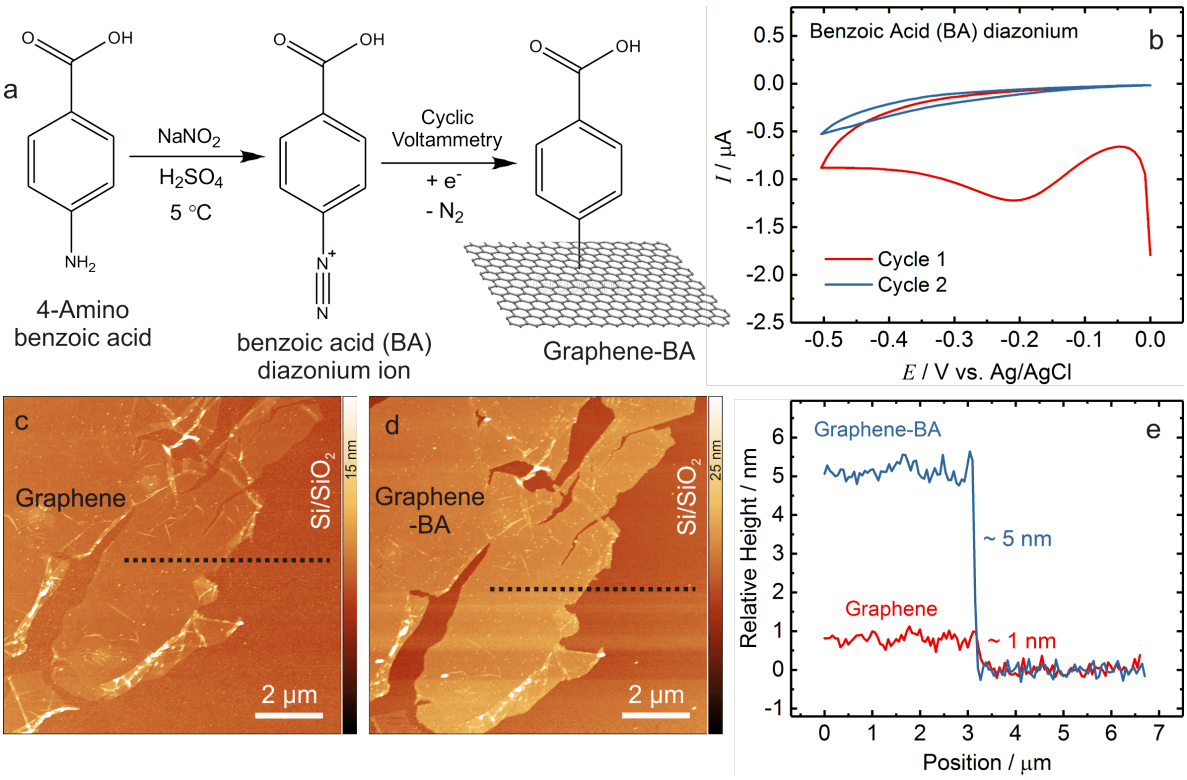

Figure 4.10: Covalent functionalization of graphene with benzoic acid (BA). (a) Reaction scheme for the formation of BA diazonium ions and subsequent diazotization of graphene. (b) CV showing the reduction of BA diazonium ions at graphene electrode. (scan rate: 20 mVs^{-1}) AFM images of (c) pristine graphene and (d) BA functionalized graphene (Graphene-BA). (e) Line profiles of graphene and Graphene-BA, for the corresponding AFM images in (c,d).

double bonds in graphene to form a covalent bond. Subsequently, the second cycle does not show any faradaic processes at this potential (blue), indicating the apparent saturation of the surface with the BA functionalization performed during the first voltage sweep.[220] The voltammetric data can also provide an estimate of the surface coverage (Γ), using the following equation:

$$\Gamma = \frac{Q}{nFA}$$

where the Faradaic charge (Q) can be obtained by integrating the cathodic peak, after removing the contributions from capacitive currents. n=1 is the number of electrons involved in the electrochemical reaction (according to the reaction depicted in figure 4.10a), F is the Faraday constant, and A is the area of the graphene electrode. The coverage of anchored BA units per unit area on the graphene electrode is estimated to be 9.1 $\times$ 10^{-11} mol cm^{-2}), similar to those reported for bulk graphite electrodes.[221]

The AFM images (figure 4.10c,d) clearly show the increase in height after the functionalization process. The line profile (figure 4.10e) of the bare graphene sheet and modified graphene shows an average height of $\sim$ 1 nm and $\sim$ 5 nm, respectively, corresponding to a significant increase in thickness of around 4 nm. This is consistent with the coloumetric information from CV indicating the high surface coverage. Further evidence for covalent attachment is obtained from Raman spectra measured before and after functionalization as shown in figure 4.11. The pristine graphene sheet (red) shows as expected only the *G* (1593 cm^{-1}) and *2D* (2652 cm^{-1}) peaks, whereas after functionalization, the defect-related *D* (1328 cm^{-1}) and *D'* (1620 cm^{-1}) peaks appear with strong intensity confirming a covalent attachment of the functional group BA.[60] Raman map of the ratio of peak intensities (I_D/I_G) before and after functionalization shows the increase in I_D/I_G values from 0.5 - 0.7 to 3 - 4 for the selected area of measurement.

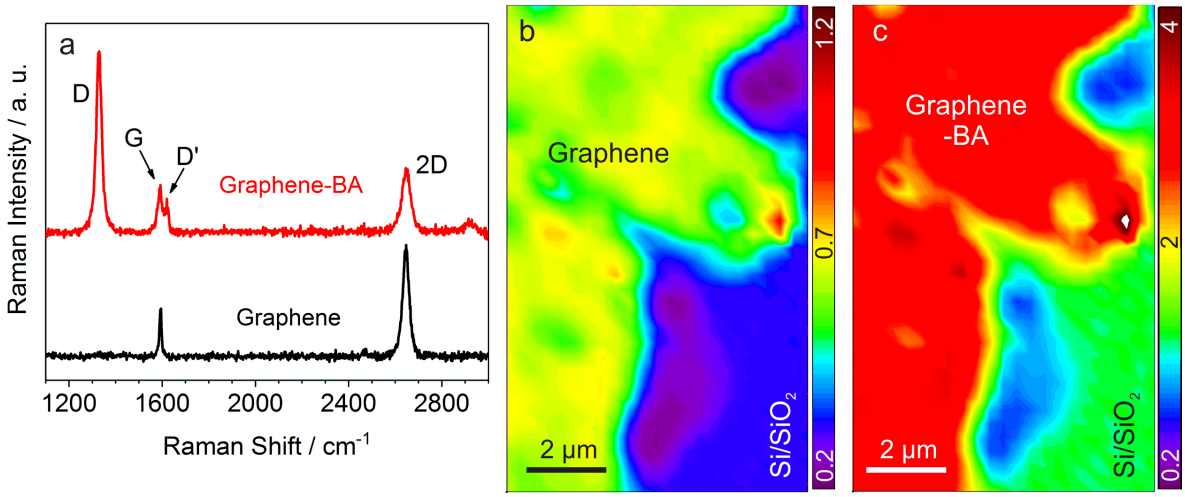

Figure 4.11: (a) Raman spectra of pristine and benzoic acid (BA) functionalized graphene. (b,c) are Raman maps of the ratio of peak intensities (I_D/I_G) for (b) pristine graphene and (c) BA functionalized graphene. (λ_{ex}: 633 nm, 0.9 mW, 1 $\times$ 1 s)

Defect Density Calculation Quantification of defects in *sp²* carbon based nanostructures such as graphene is crucial to understand their fundamental properties like its mobility.[222] There has been significant efforts to quantify defects using Raman spectroscopy for all type carbon materials, namely: nanographites,[57,159,223] amorphous carbons,[223] carbon nanotubes,[224,225] and graphene.[56,57,61,226] According to Ferrari and Robertson [223], Raman spectra of carbons along the amorphization trajectory from graphite to tetrahedral amorphous carbons has been divided in three stages: graphite to nanocrystalline graphite, nanocrystalline graphite to low *sp³* amorphous carbon and low *sp³* amorphous carbon to high *sp³* (tetrahedral) amorphous carbon. Stage 1 and stage 2, relevant to graphene are presented in more detail below :

- Stage 1: For graphene - D appears, I_D/I_G increases, *D'* appears, and all peaks broaden. For graphite, *D* and *2D* lose their doublet structure, *D + D'* appears. At the end of stage 1, *G* and *D'* start to overlap with ω_G at $\sim$ 1600 cm^{-1}.
- Stage 2: ω_G decreases from $\sim$ 1600 cm^{-1} toward $\sim$ 1510 cm^{-1}; I_D/I_G approaches toward 0; no well-defined second-order peaks, broad feature from $\sim$ 2300 to $\sim$ 3200 cm^{-1} modulated by the *2D*, *D + D'*, and *2D'* bands.

Table 4.1: Integrated intensity for each peak in the Raman spectra and their ratio for calculating the defect density.

Sample	I_D	I_G	I_D/I_G	Γ_D	Γ_G
Pristine Graphene	4.99	21.6	0.23	-	12.4
Graphene-Diazonium	165	34.7	4.76	23.4	18.8

The group of Ferrari & co-workers[63] presented a simple equation based on the phenomenological model by Jolin & co-workers[226] to determine the point defect density in graphene using Raman spectroscopy. For this, the graphene samples were bombarded with Ar^+ ions systematically to create controlled amount of defects followed by the Raman measurement. The Raman peaks of both the pristine and BA functionalized graphene (in figure 4.11a) are fitted with the Lorentzian function, and the extracted parameters are presented in table 4.1. Later, the extracted band parameters (I_D/I_G) from the Raman spectra were fitted with the following equation adapted from the reference [63]:

$$\frac{I_D}{I_G} = C_A \left(\frac{{r_a}^2 - {r_s}^2}{{r_a}^2 - 2{r_s}^2} \right) \left[e^{-\pi . {r_s}^2/{L_D}^2} - e^{-\pi({r_a}^2 - {r_s}^2)/{L_D}^2} \right] + C_S \left[1 - e^{-\pi . {r_s}^2/{L_D}^2} \right] \quad (4.1)$$

where L_D is the distance between defects and is a measure of the amount of disorder; r_S (radius of the structurally disordered area caused by the ion) and r_A (radius of the area surrounding the point defect) are length scales determining the region where the D band scattering occurs. The fit in figure 4.12 is performed considering $r_S = 1$ nm and $r_A = 3.1$ nm, in agreement with the values obtained in earlier reports.[226,227]. The equation

considers both an activated area, weighted by the parameter C_A and structurally defective area, weighted by the parameter C_S. Therefore, for each I_D/I_G value, two L_D values will be obtained, on either side of the maximum one in each stage. The left side of the maximum is the second stage and the right side is the first stage. According to the obtained fit, if $L_D > 3.2$ it is stage 1, and if $L_D < 3.2$ it is stage 2.

At $I_D/I_G = 4$, the L_D values obtained from the graph in figure 4.12 (marked with the red dotted lines) are 1.7 and 7 nm. The amorphization stage after the covalent functionalization of graphene with BA was predicted from the Raman spectra in figure 4.11 based on the following parameters: the appearance of *D* and *D'* peaks; increase in I_D/I_G; no change in ω_G; a slight increase in Γ_G and Γ_{2D}; maintaining the sharp second-order features. These features confirm stage 2 of amorphization. Therefore, L_D will be around 7 nm. Defect density n_D (in cm^{-2}) can be calculated by the following equation, $n_D = 10^{14}/\pi {L_D}^2$ which gives $n_D = 6.5 \times 10^{11}$ cm^{-2}. The defect density was converted to 1.1×10^{-12} mol cm^{-2} units to provide a direct comparison with the electrochemical data. The coloumetric information from CV, is found to have a higher defect density (9.1×10^{-11} mol cm^{-2}) than observed through Raman spectroscopy (1.1×10^{-12} mol cm^{-2}).

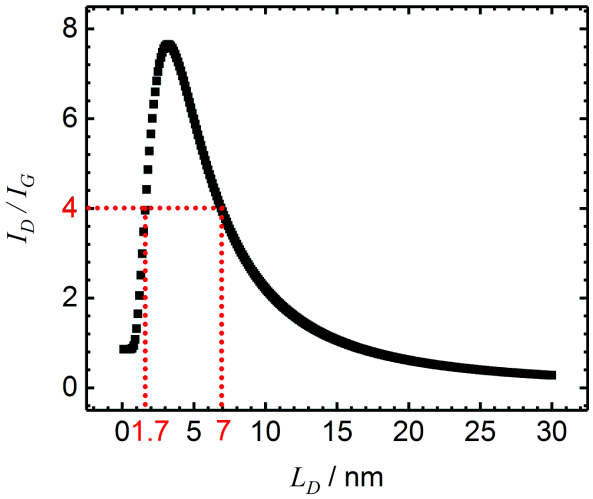

Figure 4.12: A plot of I_D/I_G (black-dash curve) as a function of the average distance between the defects (L_D), generated from equation 4.1 (adapted from reference [63]). I_D/I_G obtained from the data in figure 4.11 gives two values of L_D (red-dash lines).

4.4.2 Vibrational Fingerprinting by SERS

This section demonstrates a method to obtain the chemical information of the groups attached to a graphene layer based on the detection of their Raman modes, which are almost unobservable due to the submonolayer coverages. The intensities of these Raman modes can be significantly enhanced through the additional attachment of AuNPs by the principle of the SERS process.[50,166] This strategy has been shown previously for the detection of non-covalently attached chemical groups (polyaniline) on graphene surface by Zuccaro *et al.*[51]

However, the detection of covalently attached groups to graphene surface by SERS has not been explored yet. For this, graphene was covalently modified with 4-Nitrobenzenediazonium salt followed by deposition of AuNPs.

Graphene-Nitrobenzene (NB) - Functionalization and Characterization The electrochemical grafting of graphene surface with nitrobenzene was done using CV in an aqueous solution containing 4-nitrobenzenediazonium (NB) ions. The CV curve in figure 4.13a shows the apparent reduction wave centered around -0.2 V attributed to the formation of NB radicals. Further confirmation comes from the AFM images taken before (figure 4.13d) and after (figure 4.13e) the NB modification of graphene, which shows an estimated thickness

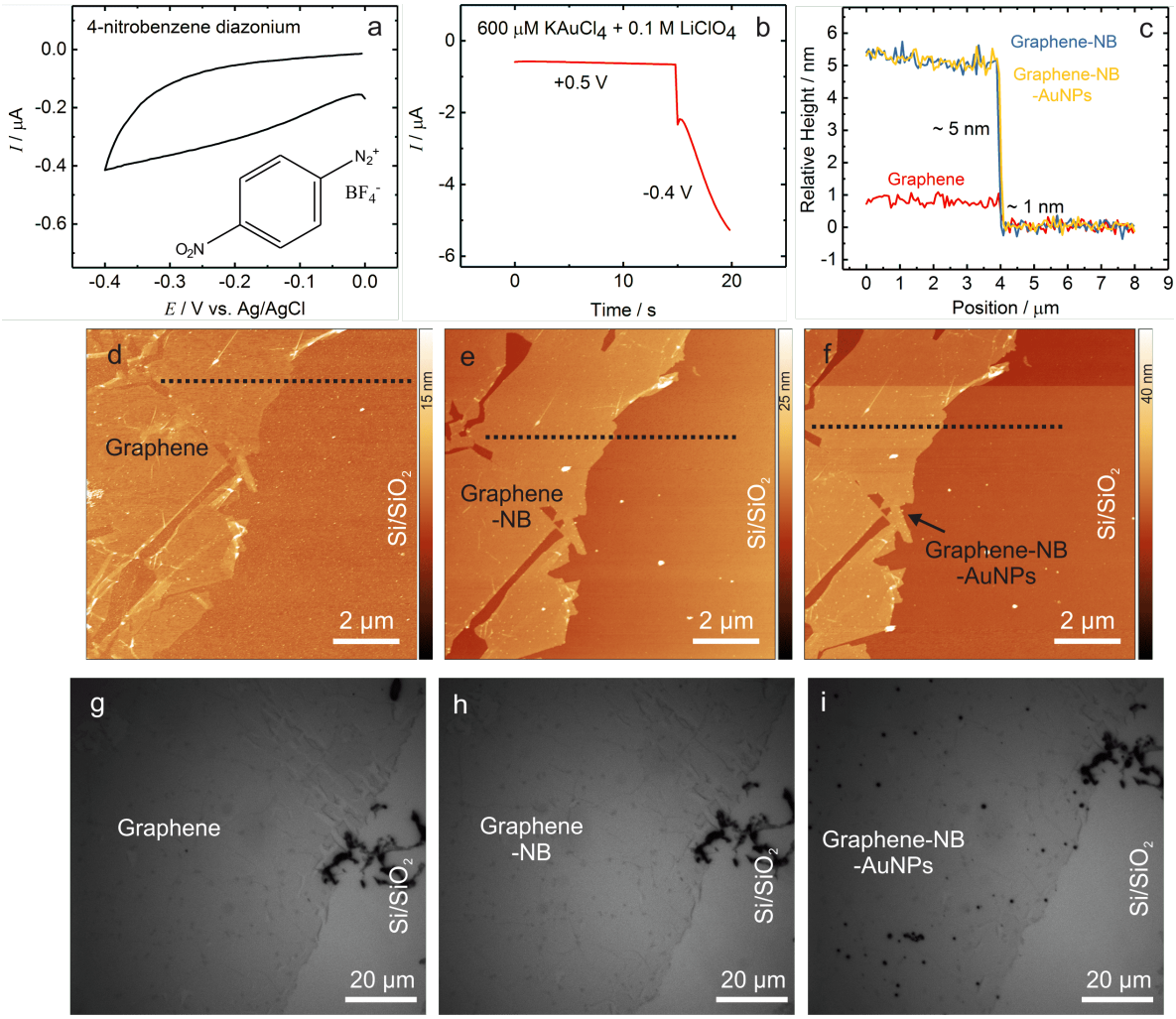

Figure 4.13: Covalent functionalization of graphene with nitrobenzene (NB). (a) CV showing the reduction of 0.1 mM 4-NB diazonium ions (chemical structure in inset) at the graphene electrode in 0.1 M $LiClO_4$ at 20 mVs^{-1}. (b) Chronoamperometric profile for the further deposition of AuNPs. (c) Comparison between the height profile of the pristine graphene, Graphene-NB, and Graphene-NB-AuNPs obtained from the respective AFM images in (d-f). (d,e,f) shows AFM images of pristine graphene, Graphene-NB, and Graphene-NB-AuNPs, respectively. (g,h,i) presents optical images of pristine graphene, Graphene-NB and Graphene-NB-AuNPs, respectively.

of 4 nm of the NB layer extracted from the corresponding height profiles (figure 4.13c). The pristine and NB-modified graphene are referred to as Graphene and Graphene-NB, respectively. The next step involves the deposition of AuNPs on the NB modified graphene surface and is the central part of the vibrational fingerprinting method. The ECM strategy remains the same as described for deposition of particles on pristine graphene in section 4.2, and was performed by chronoamperometry (figure 4.13b). The comparison of AFM images (figure 4.13e,f) for Graphene-NB and Graphene-NB after its modification with AuNPs (Graphene-NB-AuNPs) shows similar images with no AuNPs in the latter case for the same region. The AFM was performed on a smaller area (10 µm × 10 µm), relatively. Although, the optical images taken over the large area of 100 µm × 100 µm show the formed nanoparticles (black spots), indicating the electrodeposition, however, with very low density.

The covalent functionalization of graphene is known to alter the electrochemical and electronic performance, mainly due to the disruption of the conjugated sp^2-hybridized structure which is responsible for the high electronic mobility. This in turn can directly affect the HET occurring at the graphene/electrolyte interface. The ET was investigated by comparing the electroreduction of Au^{3+} on both pristine and NB functionalized graphene in similar experimental conditions. It is apparent from the optical images (figure 4.14a,b) that the pristine graphene has a higher density of AuNPs on its surface than the Graphene-NB. The lower density of particles in Graphene-NB-AuNPs can be because of the NB (organic) layer, which possibly limits the ET between Au^{3+} species and Graphene-NB electrode. This is because the organic layer acts as an insulator hampering the charge transfer, which is in agreement with previous reports. In a similar study, Macedo *et al.* observed higher electrochemical impedance (charge-transfer resistance to interconvert a redox probe on the surface of the electrode) on 4-carboxyphenyl functionalized graphene in comparison to pristine graphene for the redox probe $Fe(CN)_6^{3-/4-}$, indicating a decreased charge-transfer ability of the functionalized graphene.[70]

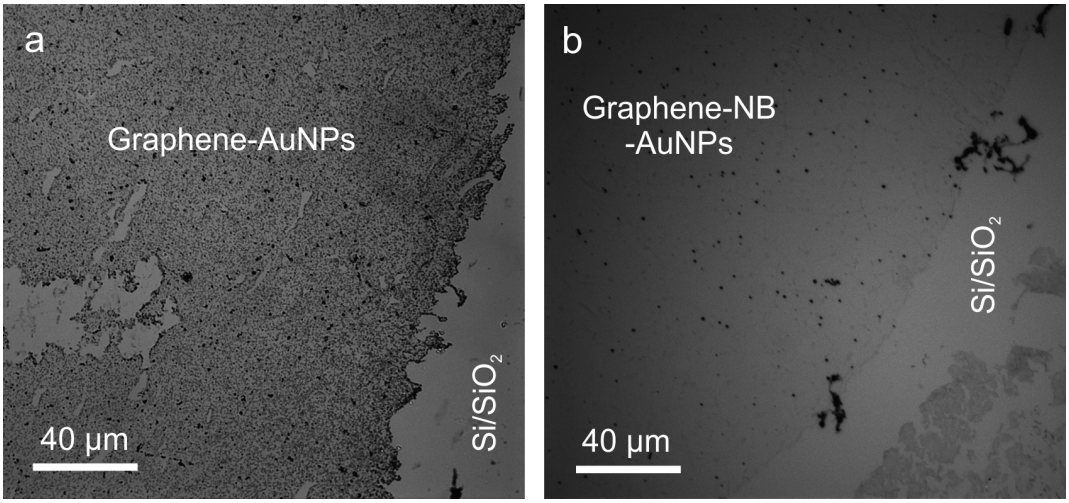

Figure 4.14: Optical images after AuNPs deposition using the same electrodeposition parameters on (a) pristine graphene (b) nitrobenzene modified graphene.

Raman Spectroscopy The Raman spectra obtained for graphene surface at the initial stage, after NB electrografting, and after deposition of AuNPs are compared in figure 4.15. The unmodified graphene shows the typical *G*- and *2D*-peaks of graphene in addition to the substrate-related peaks (at 620 and 940 cm^{-1}). The graphene modified with NB shows strong defect-related peaks *D* and *D'*, consistent with the covalent attachment on graphene. However, there is no observation of the additional peaks of NB. The deposition of AuNPs leads to the appearance of new peaks, whose origin is attributed to the presence of NB, and the SERS effect from the particles. The peak frequencies (represented by $\star$) are labeled with various modes of the NB in table 4.2. These peaks are not observed when AuNPs are deposited in the absence of the NB layer on pristine graphene (see figure 4.6 in section 4.2).

Raman map (area under peak) of NO_2 stretching mode (1358 cm^{-1}) shows the presence of NB peaks only where the particles are present. The varying peak intensity in the selected map region is because of the difference in size and number of the particles in the vicinity of

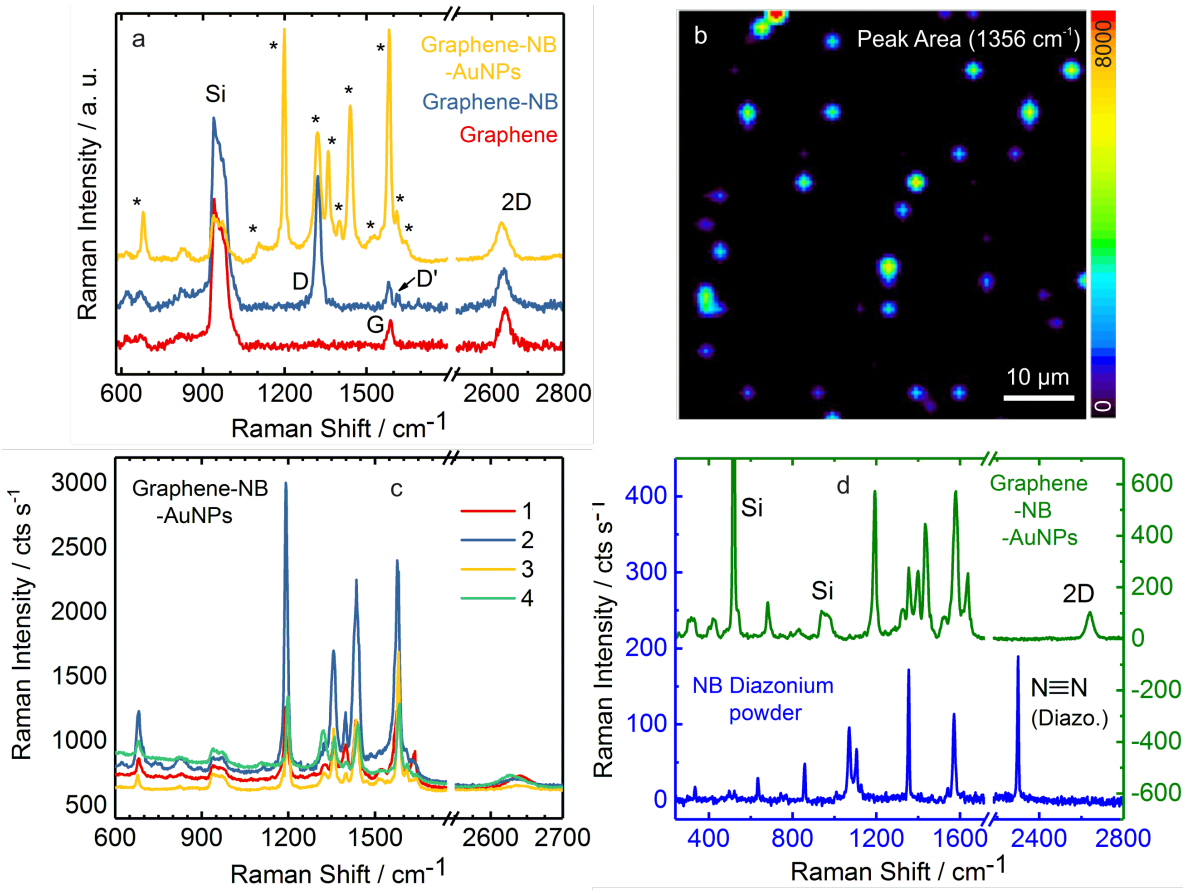

Figure 4.15: (a) Comparison of Raman spectra at different stages of graphene functionalization: Graphene, Graphene-NB and Graphene-NB-AuNPs. The peaks marked by $\star$ are attributed to the NB layer on graphene. (b) Raman map of the NO_2 stretching mode (1356 cm^{-1}), 30 $\times$ 30 data points with an interval of 2 µm. (b) Raman spectra of Graphene-NB-AuNPs at 4 different positions. (d) Comparison of NB Raman signals obtained from Graphene-NB-AuNPs and NB diazonium salt (powder form). (λ_{ex}: 633 nm, 13.6 mW, 1 $\times$ 1 s for Graphene and Graphene-NB; λ_{ex}: 633 nm, 3.4 mW, 2 $\times$ 2 s for Graphene-NB-AuNPs).

the laser spot during the measurement and is shown by collecting spectra from 4 different positions of the map in figure 4.15c. Figure 4.15d contains the Raman spectra of the Graphene-NB-AuNPs as well as the normal Raman spectrum of NB diazonium powder. The spectrum of the Graphene-NB-AuNPs is significantly enhanced and features numerous bands that are consistent with those observed in the NB diazonium powder spectrum. In addition, the presence of *2D* band in the SERS spectrum indicates the presence of a graphene layer beneath the NB layer.

All the band assignments[217,228] of NB are listed in table 4.2. Some of the differences observed between the two spectra are the following. First, a strong band at 2300 cm^{-1}, which corresponds to the N≡N stretch of the diazonium group is observed only in the powder spectrum,[229] and not in the SERS spectrum of Graphene-NB-AuNPs. The band at 1127 cm^{-1} in the NB diazonium powder spectrum also involves the diazonium moiety, which is not observed in the SERS spectrum of Graphene-NB-AuNPs. These observations also provide a strong evidence for the reduction of the diazonium cation to the aryl radical. A second difference is a band at 1199 cm^{-1}, which may be attributed to the multilayer nature of the NB film on graphene. Despite these differences, the relative intensities and vibrational frequencies of some of the prominent bands in the SERS spectrum agree well with that in the NB diazonium powder spectrum, such as ring, NO_2 and C−N stretching modes. In this way, Raman spectroscopy provides a way through vibrational fingerprinting to identify the nitrobenzene group attached to graphene via SERS.

Table 4.2: Assignment of peaks in the spectra of Graphene-NB-AuNPs to the vibrational modes of nitrobenzene.

Assigned Peaks	*NB Diazonium*	*Graphene-NB-AuNPs*
N≡N stretch	2300	-
C=N or C=C stretch	-	1645
ring stretch	-	1610
ring stretch	1572	1579
asymmetric NO_2 stretch	1545	-
symmetric C−N stretch	-	1435
symmetric NO_2 stretch	1354	1356, 1322
C−H bend	-	1199
C−N_2 stretch + ring stretch	1127	-
C−N + ring stretch	1107	1108
C−H in plane bend	1070	-
ring breathing	1009	-
ONO scissor + ring stretch	856	-
ring deformation	637	678

4.5 Summary

In conclusion, this chapter presented various functionalization strategies to modify the graphene surface, and subsequently the characterization methods. The use of electrochemical modification (ECM) provides examples to modify graphene through electrodeposition of nanoparticles, and non-covalent as well as covalent attachment of organic groups. For non-covalent functionalization, graphene was modified with polymeric aryl amino group (aminobenzylamine). Diazonium chemistry was used for the covalent modification, with substituted aromatic groups such as aminobenzoic acid and nitrobenzene. The combination of Raman spectroscopy and AFM was used to characterize the functionalized graphene. The LSPR of gold nanoparticles (SERS) was used to identify the functional groups attached to the graphene surface via vibrational fingerprinting. The functionalization and characterization techniques discussed here in this chapter will enable to understand and characterize the graphene edge electrodes in the next chapters.

5

Fabrication of Isolated Graphene Edge

The results of the experiments presented here were published in the following manuscript: A Yadav, R M Iost, T J Neubert, S Baylan, T Schmid and K Balasubramanian, Selective Electrochemical Functionalization of the Graphene Edge. *Chem. Sci., 2019, 10, 936-942*.

There have been several approaches undertaken to realize graphene edges either in GNRs, nanopores or quantum dots, which contain edge-rich regions or in bulk form (using multilayers of graphene sheets).[25,38,80,230–232] The realization of an isolated graphene edge on the other hand is not that straightforward, since it is important to isolate the effect of the basal plane completely while simultaneously having the capability to address a single sheet. The isolated graphene edge may be considered as an ideal 1D system with the thinnest wire electrode[28,29] that one could realize. There are a few demonstrations of devices realized based on isolated graphene edge or a monolayer graphene edge.[12,33,40,233] However, a great majority of the published work in the graphene edges field emphasize GNRs and other kinds of edges, and not on the importance of exclusive or isolated edges. This chapter presents a photolithographic method to realize nanometer-thick 'isolated graphene edge (GrEdge)' devices by appropriate passivation of the basal plane and reactive ion etching. Further, the exclusive availability of the edge is proved using electrochemistry.

5.1 Methods in Literature

One of the very common methods to fabricate nanoelectrodes is the partial passivation or insulation of electrode/substrate (using materials like photoresist,[234] Teflon,[235] and electrophoretic paint[183], etc.), followed by the removal of the insulation from a small portion to expose the tip/edge part of the electrode which serve as a nanoelectrode. White and co-workers prepared nanoband electrodes in the 1980s. This method has been used to produce nanoelectrodes based on metal and carbon materials commonly . In carbon materials, the first reports were of nanoelectrodes based on CNTs and SWNTs by the groups of Crooks,[236] Dekker[34] and Macpherson.[237]

Graphene Edges There are very few reports available in the literature, which demonstrate the fabrication of isolated graphene edge electrodes. Yuan and co-workers were the first to report a method to fabricate isolated graphene edges, by passivating the regions of the monolayer graphene sheet selectively with an insulating thin film (e.g., epoxy resin (ER)) to prepare both the isolated edge and basal plane (not containing the edges).[12] For fabricating the edge electrode, the entire graphene sheet was embedded in ER and then vertically cut to expose its cross-section. Later, Li and co-workers also used a similar method to fabricate graphene edge nanoelectrode using the multilayer graphene sheet.[39] Other method includes fabricating graphene edge in nanopore like structure, but the fabrication requires elaborate and complicated processes like the deposition of the insulating layers and forming holes with focused ion-beam milling (FIB) and deep reactive-ion etching (DRIE).[40]

The common theme in all the above methods is to first embed or passivate the monolayer graphene sheet partially with an insulating material, and then create the edge by cutting appropriately or drilling holes in the graphene containing stacked layers with FIB and DRIE. It is important to use non-conducting materials like resists, resins or polymers because they do not interfere with the intrinsic properties of graphene. However, one of the main drawbacks of this method is the mechanical cutting step. This type of cutting can easily result in a lift-up of sealed polymer slightly at the cross-section which can expose a small part of the basal plane. Due to this, the edge properties (for example, electrochemical properties) show some contributions from the basal plane area, as indicated by absence of (quasi)-steady-state voltammetric behavior, a characteristic of nanosized electrodes. Second, it is not a clean process as it can result in small trace impurities (from the substrate) at the edge. The cutting or drilling process also requires expensive tools like microtome (or ultramicrotome), FIB and DRIE.

5.2 Fabrication Concept

In this thesis, a different strategy is used, where the transferred graphene monolayer is partially insulated by a non-conducting polymer, and instead of mechanical cutting or drilling hole using electron beam, reactive ion etching is used to remove the uncovered graphene to expose or create the graphene edge (GrEdge). Therefore, it can be divided into two broad steps: passivation/insulation and reactive ion etching. These two steps when combined forms the basis of lithographic patterning. Lithography is a fundamental process in microfabrication, combining patterning and etching. Lithographic patterning is widely used for narrowing down the graphene to GNRs of $\sim$ 5 - 10 nm width, although using very elaborate techniques such as block copolymer lithography, electron-beam lithography, nanosphere lithography, nano-imprint lithography, and scanning tunneling microscope lithography.[18,36,98,99,109] However, in this thesis, a simple form of lithography is used since a large part of graphene sheet (1 - 2 mm^2) remains passivated and is not narrowed down to few nanometers. Only one end of the sheet is exposed to create the edge. For lithography, the key material is the photoresist (PR) coating on top of the substrate (graphene), which is exposed to light, e.g., through a mask or a without a mask (using the spatial light modulator (SLM) - which serves as a programmable mask). A pattern is formed by exposure and development of the PR. Subsequently, reactive ion etching is used to selectively etch unprotected areas (of graphene). The most commonly used lithography technique today uses UV light and is known as photolithography (in opposition to e-beam lithography). The general procedure including the above mentioned steps is illustrated in the figure 5.1.

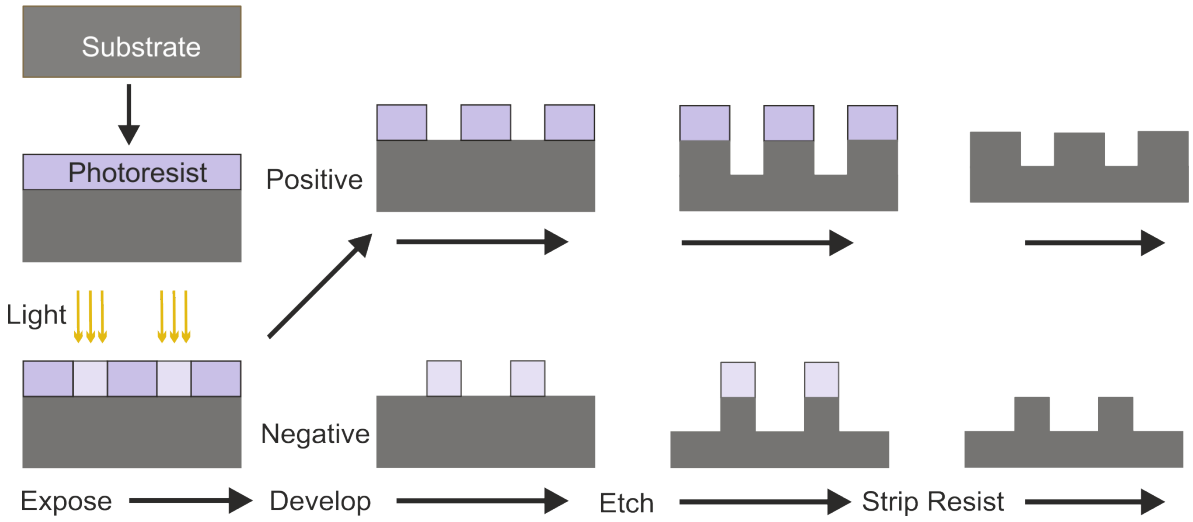

Figure 5.1: General schematic of a photolithography process: application of PR on substrate; followed by its exposure to light, e.g., through a mask or maskless aligner; developing of the PR; etching the exposed areas of the substrate, and stripping the remaining PR off.

5.2.1 Passivation/Insulation

The significant part of the graphene edge fabrication is the selective passivation of the graphene sheet using an insulating material (resist/polymer), which can provide robust and strong passivation with proper adhesion on graphene and Si/SiO_2. This is the first step after graphene transfer where the required area of graphene is covered selectively by resist to set the location of the edge. The passivation layer protects the covered graphene (basal plane) area from coming in contact with different solvents, etchants and also from reaction with highly reactive ions when using plasma etching. The passivation can be done either by drop-casting (with polystyrene) or lithographic patterning (with photoresists).

Photoresists (PRs) PRs are the fundamental materials used in photolithography to form a patterned coating on a substrate. They are light-sensitive and composed of a polymeric resin, a sensitizer and a solvent. They serve as masking materials for the transfer of images into an underlying substrate via etching processes. PRs are coated on a substrate (graphene in this thesis), on top of which a patterned (or programmable in case of maskless aligner) mask is applied such that light will be projected onto the substrate according to the pattern. The resist changes its structure when it is exposed to light or radiation. The solvent, called developer allows the PR to be spun while spin coating and removes PR that is exposed. Finally, the sensitizer controls the photochemical reaction in the polymer phase. PRs can be classified as positive (+) and negative (-) depending on its exposure with light:

- *Positive (+)*: Exposure to light weakens the polymer, making it more soluble to the developer, so the positive pattern (an exact copy of the pattern) is achieved on the substrate, as a stencil for subsequent processing. The advantages of (+) PR are better resolution and thermal stability. The commonly used (+) PRs are novolac resins (phenol-formaldehyde copolymer) and diazoquinones (diazonaphthoquinone).[238] In this thesis, a (+) PR called S1805 (figure 5.2), which consists of photoactive naphtha-diazoquinone derivatives and Novolak, a phenol-formaldehyde condensation polymer has been used for preparation of GrEdge samples, and later for GrEdge functionalization (chapter 6).

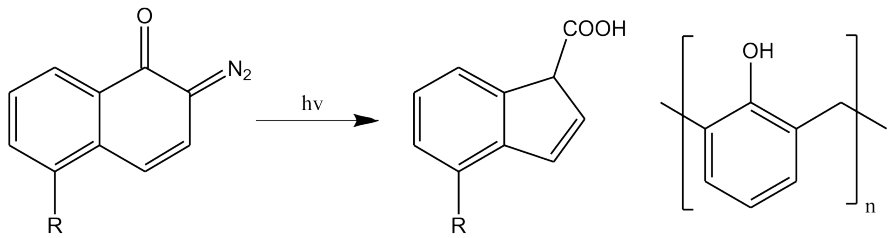

Figure 5.2: Chemical structure of (+) PR S1805, which consists of photoactive naphtha-diazoquinone derivatives and Novolak, a phenol-formaldehyde condensation polymer. (Adapted from ref. [238])

- *Negative (-)*: Exposure to light causes the polymerization of the PR, so the PR remains on the surface of the substrate where it is exposed, and the developer solution removes only the unexposed areas. Therefore, it contains the inverse or photographic 'negative' of the pattern which is to be transferred. The advantages of (-) PRs are: higher durability in presence of water and good adhesion to silicon. One common (-) PR is SU-8 (figure 5.3), an epoxy-based polymer,[239] and it has been used for the preparation of edge samples for electrochemistry measurements (chapters 7 and 8).

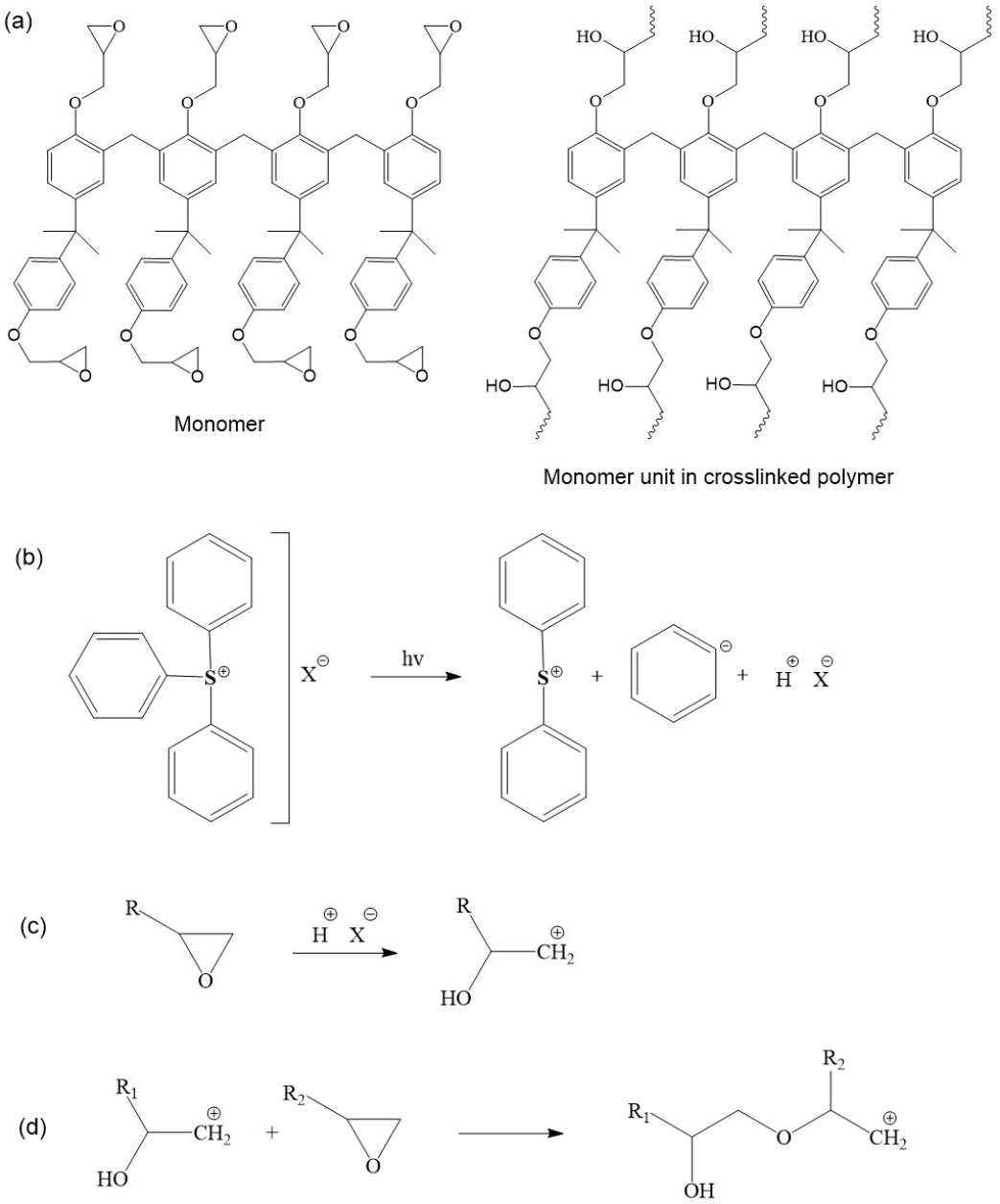

Figure 5.3: (a) Chemical structure of epoxy based (-) PR SU-8: The single molecule / monomer (left) and the monomer unit in the crosslinked polymer (right). (b) Generation of acid upon UV exposure as a result of protolysis of triarylsulfonium, the cationic photoinitiator. (c) Initiation and cationic opening of the epoxy group. (d) Chain propagation of the crosslinking process. (Adapted from ref. [239])

5.2.2 Reactive Ion Etching

Reactive ion etching (RIE), is used to remove the uncovered part of graphene, and create the exposed edge. RIE is a plasma-based etching process where the highly reactive species can interact mechanically and/or chemically with the substrate or thin films. The plasma is generated using controlled conditions in the O_2 atmosphere inside the gas chamber: pressure = 0.6 mbar, power = 100 mW for 12 s). Mild conditions were used to prevent the oxidation of the edge (more detailed discussion in Chapter 6). The plasma interacts with the uncovered graphene and etches (or removes) it, but not the passivated graphene. This process leads to the breaking of the periodic lattice of sp^2 carbons of graphene and consequently, creates the neat and straight graphene edge (GrEdge) consisting of a line of carbon atoms exposed below the sharp edge of the PR.

5.2.3 Fabrication Approach

Figure 5.4a presents the schematic of the general fabrication method to prepare GrEdge electrodes, divided into three main steps:

1. Graphene transfer to the pre-patterned Si/SiO_2 substrate with Pt contacts using a wet transfer process.

2. Patterning (lithographic) - Passivating or covering the required area of graphene with polymeric layer. The passivation material should be non-conducting in nature.

3. Reactive ion etching in O_2 plasma to remove the uncovered part of graphene, and expose the carbon atoms constituting the edge at the graphene-resist boundary.

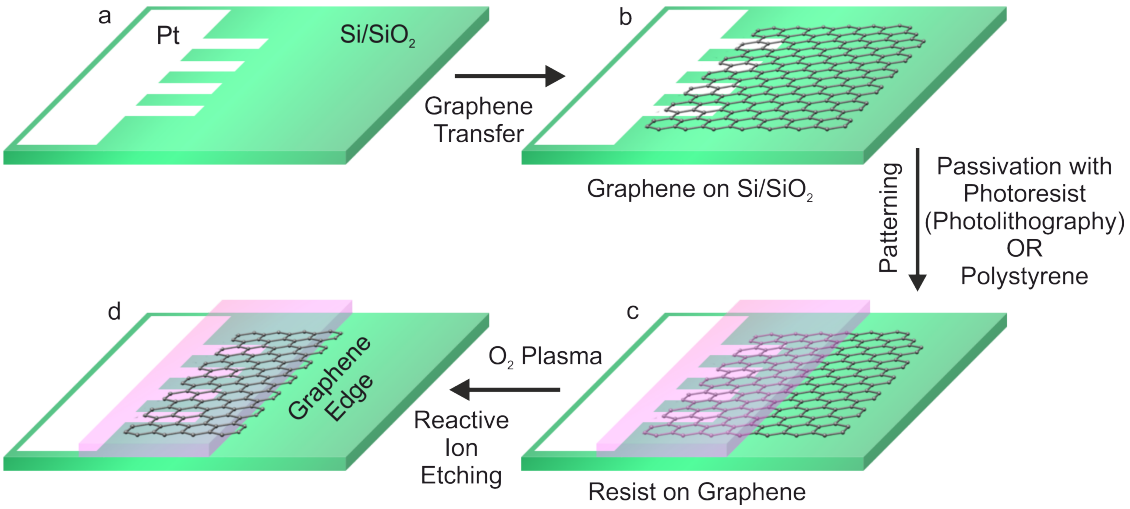

Figure 5.4: Schematic of a graphene edge electrode fabrication process: (a) A pre-patterned Si/SiO_2 substrate with Pt contacts, (b) Graphene transferred Si/SiO_2 (c) Patterned graphene with resist applied in the required region, and (d) A typical graphene edge sample with the exposed edge after plasma etching in O_2 plasma.

5.3 Graphene Edge Fabrication and Characterization

Figure 5.5, shows the optical images of the typical Si/SiO_2 substrate after each step involved in the fabrication of the GrEdge electrode: (a) graphene (in contact with Pt electrode lines) on Si/SiO_2 substrate after wet transfer step; (b) the layer of PR after the passivation step, showing both covered and uncovered regions of graphene; (c) the GrEdge sample after etching in O_2 plasma, with no presence of graphene in the region where PR is not applied. The exposed linear GrEdge along the left end of the PR consists of a line of carbon atoms at the cross-section under the PR layer shown by the pointed arrow. The graphene under the PR remains intact, and act as a contact between the GrEdge and Pt lines.

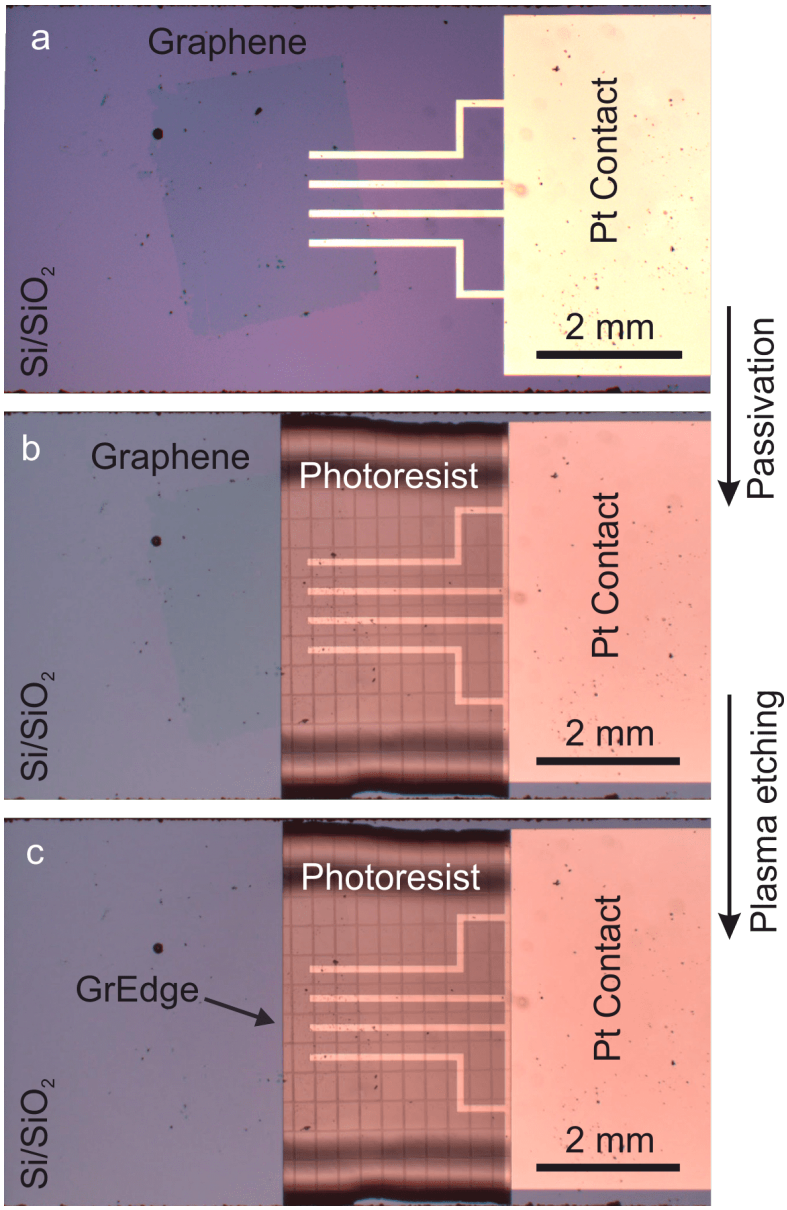

Figure 5.5: GrEdge preparation. Optical images of (a) graphene transferred Si/SiO_2 substrate (b) graphene on Si/SiO_2 after appropriate passivation and (c) graphene dge (GrEdge) sample after etching the uncovered part of graphene in O_2 plasma.

5.3.1 Preparation of GrEdge with PR S1805 (+)

The passivation with PR S1805 (Microposit) on graphene was done by spin coating. The sample was dried at 90°C for 2.5 min on a precision hot plate. Then, the inverse of the desired passivation layout was illuminated (95 mJ/cm^2, 365 nm LED). Later the PR was developed in MF-319 developer (Microposit) for 30 s, washed with water and blow-dried with air. The performed experimental steps are shown in the figure 5.1 This results in a $\sim$ 500 nm thick layer of the PR S1805 on top of graphene. The optical images in figure 5.6a1,b1 show the covered (right) and uncovered regions of the graphene sheet. The graphene below the S1805 layer is clearly visible and intact. In the middle of the image, the line-type structure (one end of PR) forms the location of the GrEdge. After plasma etching (figure 5.6a2,b2), there is no evidence of graphene to the left of the PR layer, which was left uncovered. The etching of the uncovered graphene creates the GrEdge along the sharp edge of S1805.

S1805 can be removed from the graphene without damaging it. This feature was essential to characterize the pristine edge (or functionalized functionalized), as the analytical measurements (such as AFM, Raman and EDX) cannot be done without removing the PR.

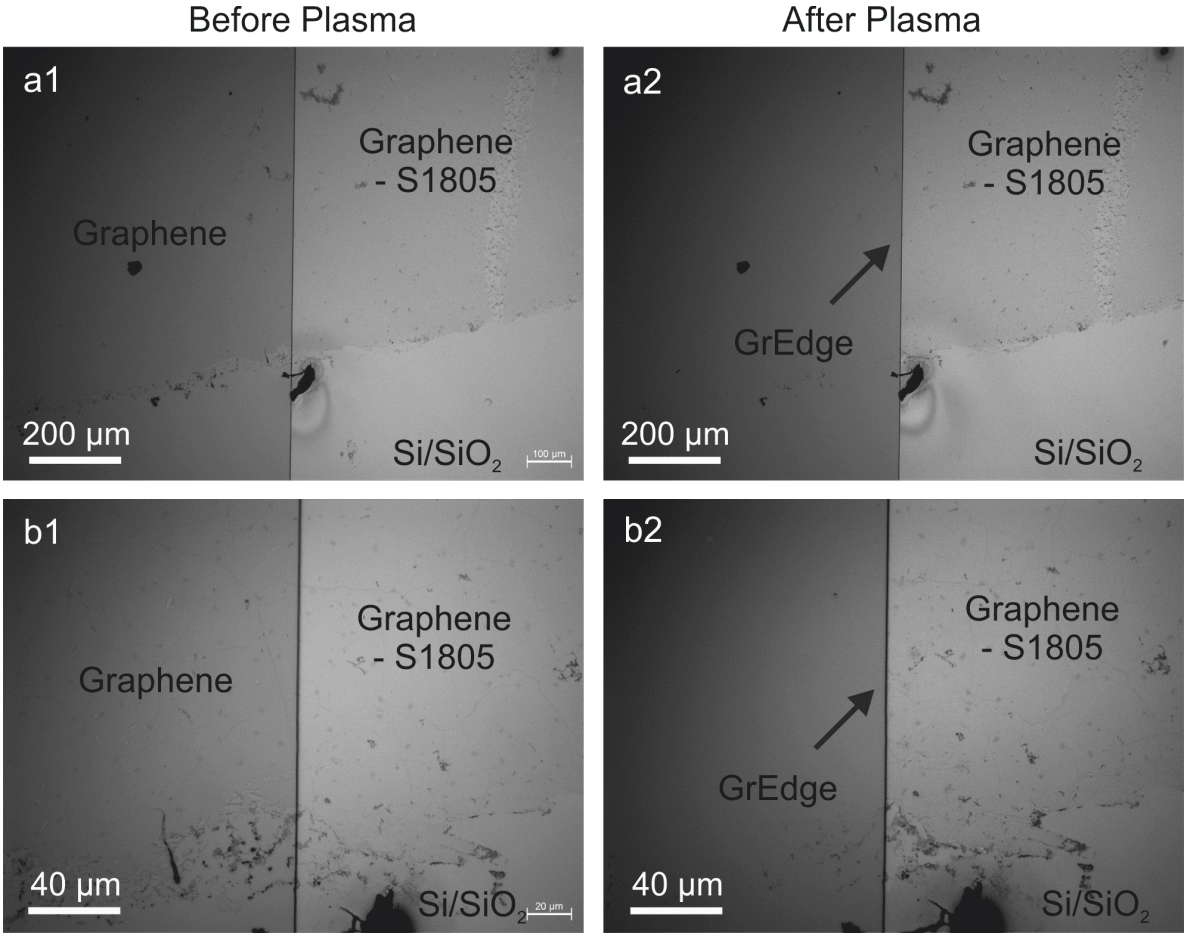

Figure 5.6: Optical images of the (+) PR S805 covered graphene on Si/SiO_2, (a1,b1) before and (a2,b2) after O_2 plasma etching at two different positions. Si/SiO_2 substrate.

5.3.2 Preparation of GrEdge with PR SU-8 (-)

SU-8 (10) was also applied by spin coating and pre-baked at 65°C (2 min) and 95°C (5 min). Then, the layout of the passivation was illuminated (330 mJ/cm^2, 365 nm LED) as shown in figure 5.1 and the samples were post-baked at 65°C (1 min) and 95°C (2 min). Afterwards, the samples were developed in mr-Dev 600 developer (MicroResist Technology), washed with isopropanol and blow-dried in air. In this way, a 10 µm thick layer of cross-linked SU-8 polymer is deposited on top of graphene. The optical images shown in figure 5.7a1,b1 confirms the successful passivation by SU-8 as shown by the coating on top of graphene. The grid visible on the PR is originating from the maskless aligner. The exposure is performed stepwise. Each rectangle represents one step of exposure. In case of S1805, this is not visible, since the exposed regions are removed during development. The remaining uncoated graphene was removed by the plasma etching process, generating the GrEdge along the SU-8 edge as shown in figure 5.7a2,b2. The graphene visible under SU-8 remains intact after plasma etching. The negative PR SU-8 (10) (MicroChem) yields more robust and thick passivation with better adhesion and slower ageing of the edge samples. However, it acts as a permanent resist, and cannot be removed without damaging the graphene beneath.

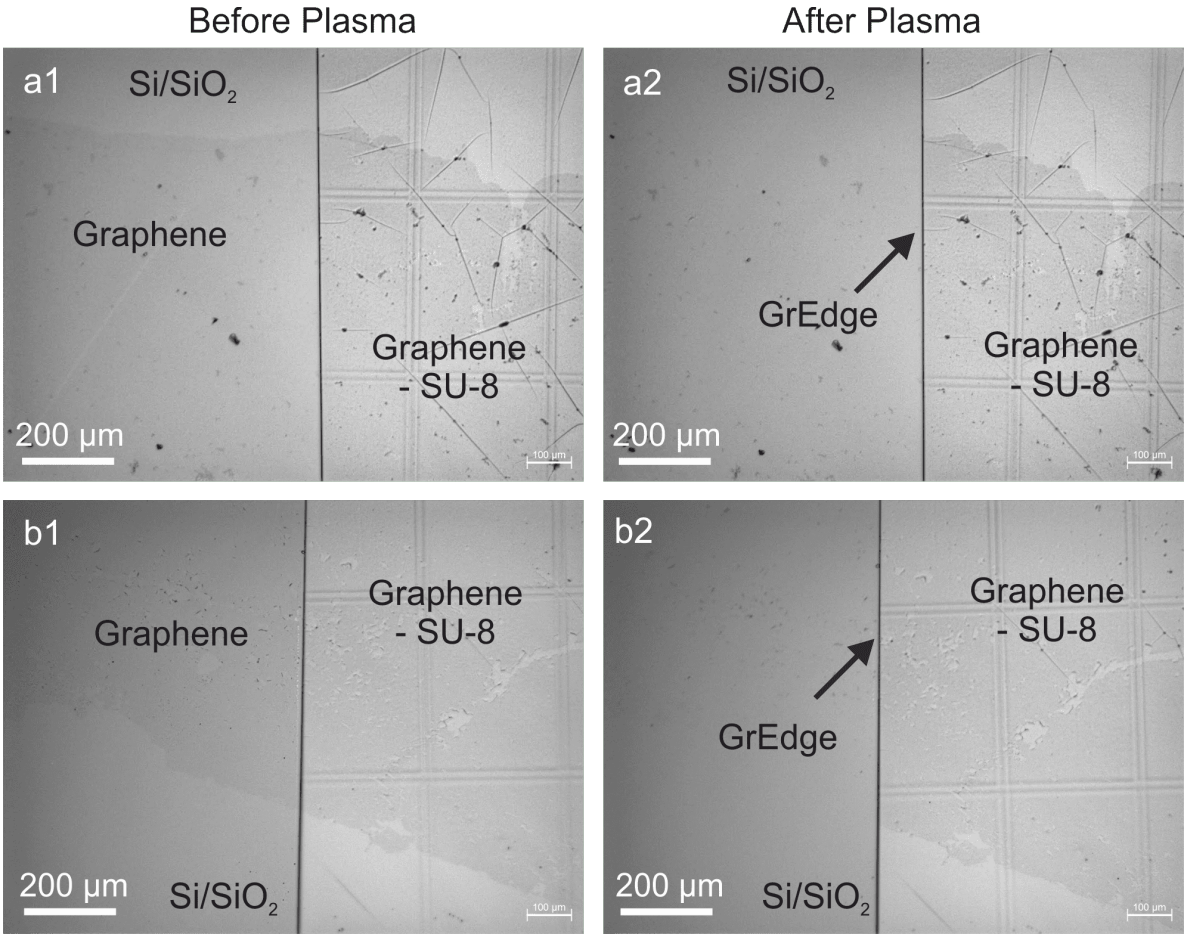

Figure 5.7: Optical images of the (-) PR SU-8 covered graphene on Si/SiO_2, (a1,b1) before and (a2,b2) after O_2 plasma etching at two different positions.

5.3.3 Preparation of GrEdge with Polystyrene (PS)

PS is already used in two procedures in the lab: 1. PS-assisted wet transfer of graphene (see section 3.1.1), and 2. passivation (which is same as here in this case) of the graphene contacts on Si/SiO_2 for the electrochemistry experiments (see section 3.2.7). The passivation of the graphene sheet was done by drop-casting the PS solution (two styrene beads dissolved in 100 µl toluene) on top of the graphene sheet. The sample was then dried overnight in the hood to dry the PS, insulating the required part of the graphene sheet including the electrodes in contact with it as shown in figure 5.8a. The sharp end of the PS layer eventually forms the location of the edge. The optical images after PS passivation

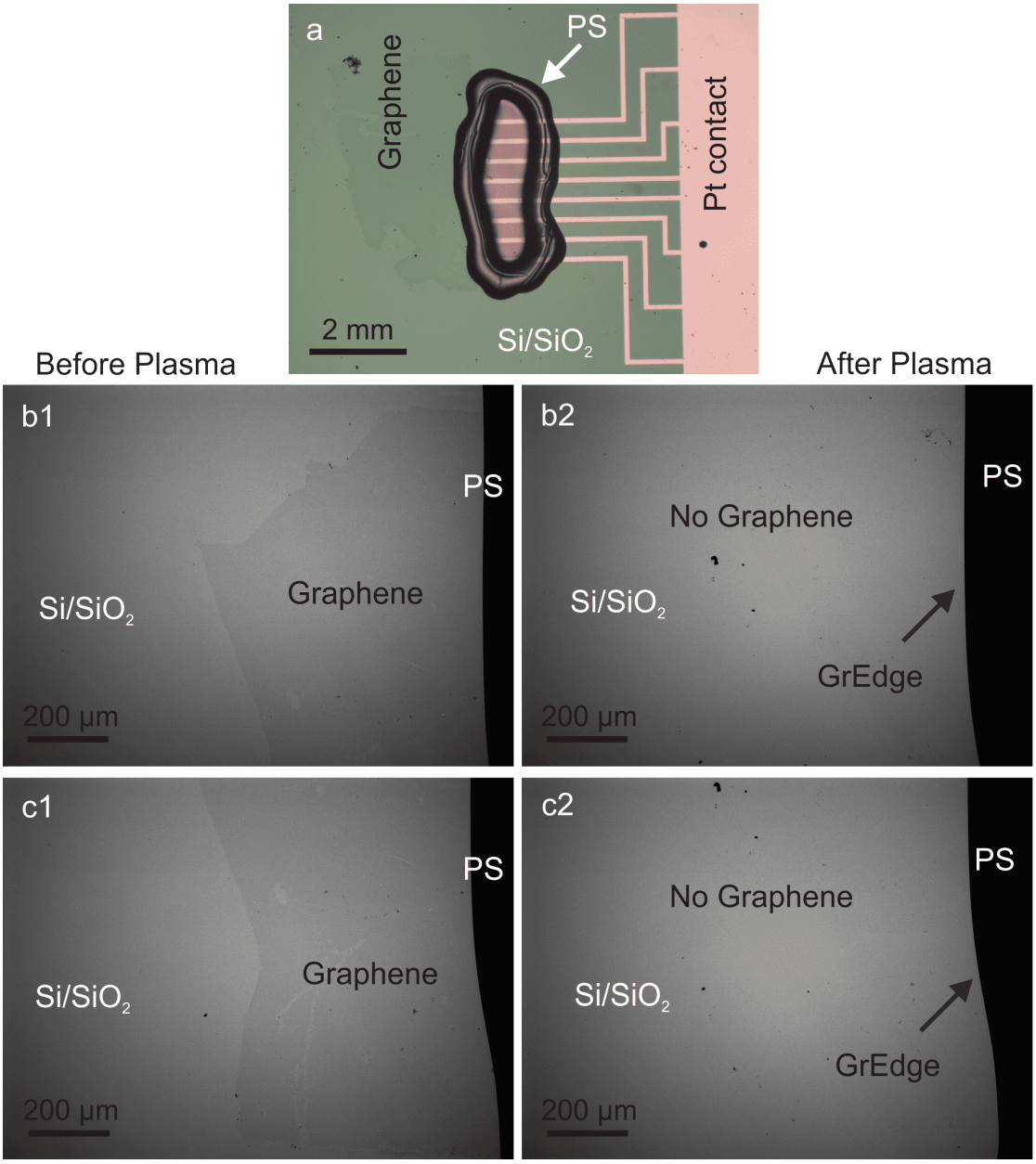

Figure 5.8: Optical images of (a) the PS covered graphene on Si/SiO_2. (b1, b2) are optical images before (b1) and after O_2 plasma etching (b2), and same for (c1, c2) at another position.

show the partially insulated graphene sheet (figure 5.8b1,c1). The graphene sheet under the PS is not visible under the microscope because of the high thickness of the PS layer. After the plasma etching (figure 5.8b2,c2), uncovered graphene sheet is etched away to form the GrEdge. However, in the thesis, the edge electrodes prepared using PS are not used, due to less durabilty and quick ageing of the samples during the electrochemistry experiments.

5.3.4 Characterization

As mentioned earlier, it is difficult to get the sufficient spatial resolution of the graphene edges using the conventional spectroscopic and microscopy characterization techniques due to the high thickness and insulating layer of polymer above the edges. Below are the few ways of characterizing the fabricated GrEdge using electrochemical methods, and after removing the PR:

- The PR S1805 can be removed to investigate the edge region using AFM and Raman spectroscopy. However, the data obtained from the GrEdge will consist of contributions from the basal plane region too (for example in Raman spectroscopy, because of the big spot size ($\sim$ 500 µm) of the laser). The PR S1805 was removed by dissolving it in acetone.

- Electrochemistry can be used to probe the edge without removing the PR layer. The conductive nature of graphene can be utilized to probe the exposed edge. Since it is the only conductive component of the hybrid structure, thus, as long as the line of carbon atoms constituting the edge is exposed below the surface of the polymer, it can come in contact with the solvents and probed using electrochemistry.

- Another approach is to functionalize the GrEdge and then subsequently removing the S1805 PR. This can be done by the electrochemical modification (ECM) method. The electrodeposition to attach nanoparticles (NPs) is performed with the basal plane still protected by the PR. The PR makes the GrEdge selective towards functionalization. In this way, if only the GrEdge is functionalized on the whole graphene surface, then the GrEdge was successfully created.

AFM This was performed in order to check the height of the PR layer and to characterize the fabricated GrEdge. The AFM images in figure 5.9a,b confirm the presence of the layer of S1805 on top of graphene, with the line profiles showing the thickness of $\sim$ 500 nm for S1805. The AFM images captured after the S1805 removal (in figure 5.9c,d) shows a well-defined and straight edge along with the basal plane region. The line profile at the edge shows height as 1 nm, indicating that graphene used in this study is in single layer form. AFM measurement was not possible in the case of SU-8 (where the supposed height is 10 µm) because of the limiting Z range (5 µm) of the instrument.

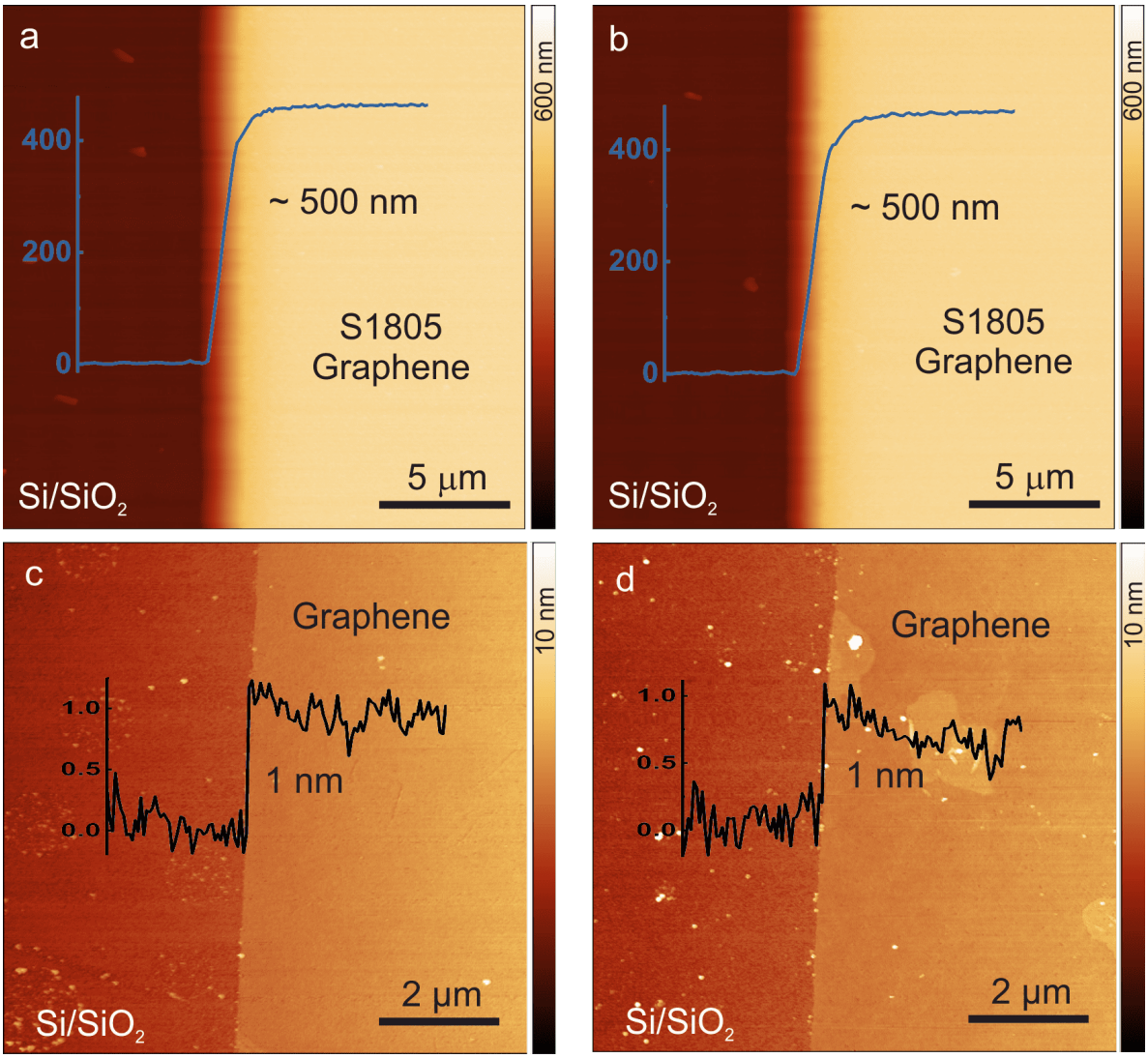

Figure 5.9: (a,b) AFM images of the PR S1805 on top of graphene sheet after reactive ion etching on two different samples, with the respective height profiles. (c,d) AFM images of the GrEdge after removal of PR S1805 on two different samples, along with line profile showing the height at the edge.

Raman Spectroscopy Figure 5.10a,b presents background-subtracted Raman spectra obtained at the basal plane and at the GrEdge (after removing the PR S1805). For a better characterization of the edge, incident polarization was kept parallel to the edge, because the D-peak intensity strongly depends on the angle between incident polarization and edge, it is maximum when the angle is zero.[61] The spectrum of the basal plane (red curve) shows as expected *G* and *2D* peaks,[60] indicative of the fact that plasma etching treatment did not damage the basal plane of graphene which was covered under PR. The GrEdge spectrum (blue curve) shows additionally a small *D* peak and a minuscule shoulder (*D'*-peak, $\sim$ 1620 cm^{-1}) next to the *G*-peak, attributed to the presence of sp^3-carbons. This is because of the creation of edges after the etching process, disrupting the honeycomb lattice by breaking the C=C bonds and consequently, leading to an increase in the disorder-related *D* and *D'* peaks of graphene.[56,58,161,162] The Raman spectra obtained at the GrEdge is consistent with previous observations on graphene edges, where the *D'* peak has been observed on H-terminated zigzag graphene edges[61,157,240] and in hydrogenated graphene called graphane.[241–243]

Another important information obtained from the Raman spectrum of graphene is the sensitivity of *G* and *2D* peaks to doping, where a blue- and red-shift of the *G* and *2D* peaks occurs upon *p*- and *n*-type doping, respectively.[59] There is no significant difference in the ω_G and ω_{2D} of both basal plane and GrEdge, however, there is a slight increase in Γ_G and Γ_{2D} for GrEdge. The intensity ratio I_{2D}/I_G was also found to bethe same for both cases.

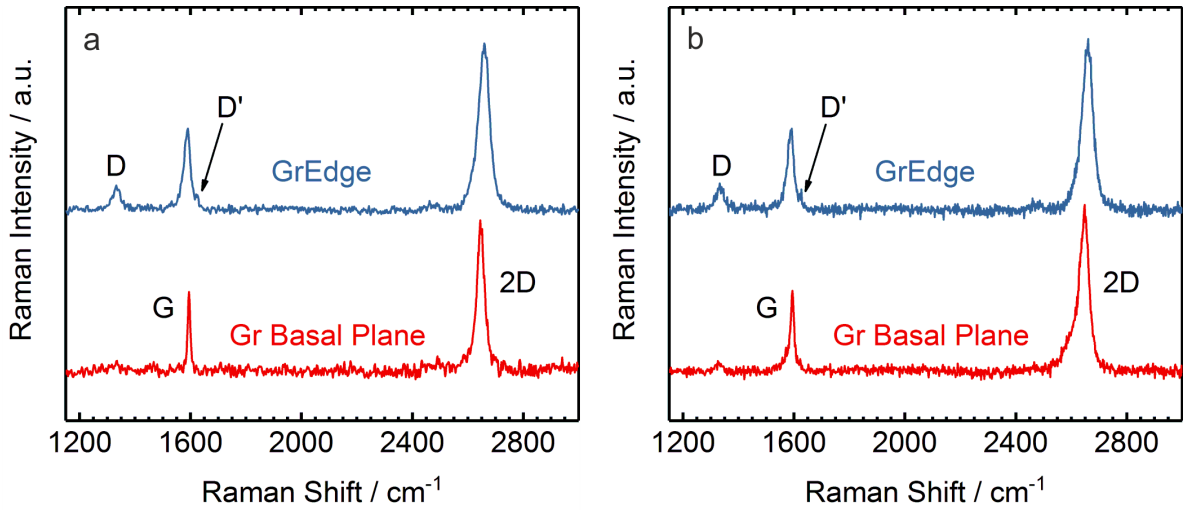

Figure 5.10: (a,b) Raman spectra comparing the the graphene basal plane and graphene edge at two different positions. (λ_{ex}: 633 nm, 4.5 mW, 1 $\times$ 1 s)

5.3.5 Steady-State Voltammetry of Nanoelectrodes

A simple electrochemical technique of cyclic voltammetry can be used to distinguish electrodes of different dimensions based on the magnitude and voltammetric behaviour of the current response. The electrodes with at least one of the dimensions of the order of micrometer or nanometer are referred to as nanoelectrodes or ultramicroelectrodes (UMEs), and they display characteristic properties different from that of the normal-sized conventional or macroelectrodes. By the nanoelectrode definition, the GrEdge electrode fabricated from a single graphene sheet of thickness 1 nm, should behave as a nanoelectrode, if only the edge of the graphene sheet (thickness $\sim$ 1 nm) is exposed to the solution during the electrochemical measurement. At nanoelectrodes, the obtained current response show sigmoidal-shaped steady-state voltammograms with low currents of the order of pA to nA. The current densities are high because of their small electrode area. At conventional macroelectrodes, the currents are in the range of µA to mA, with the typical wave-shaped voltammogram

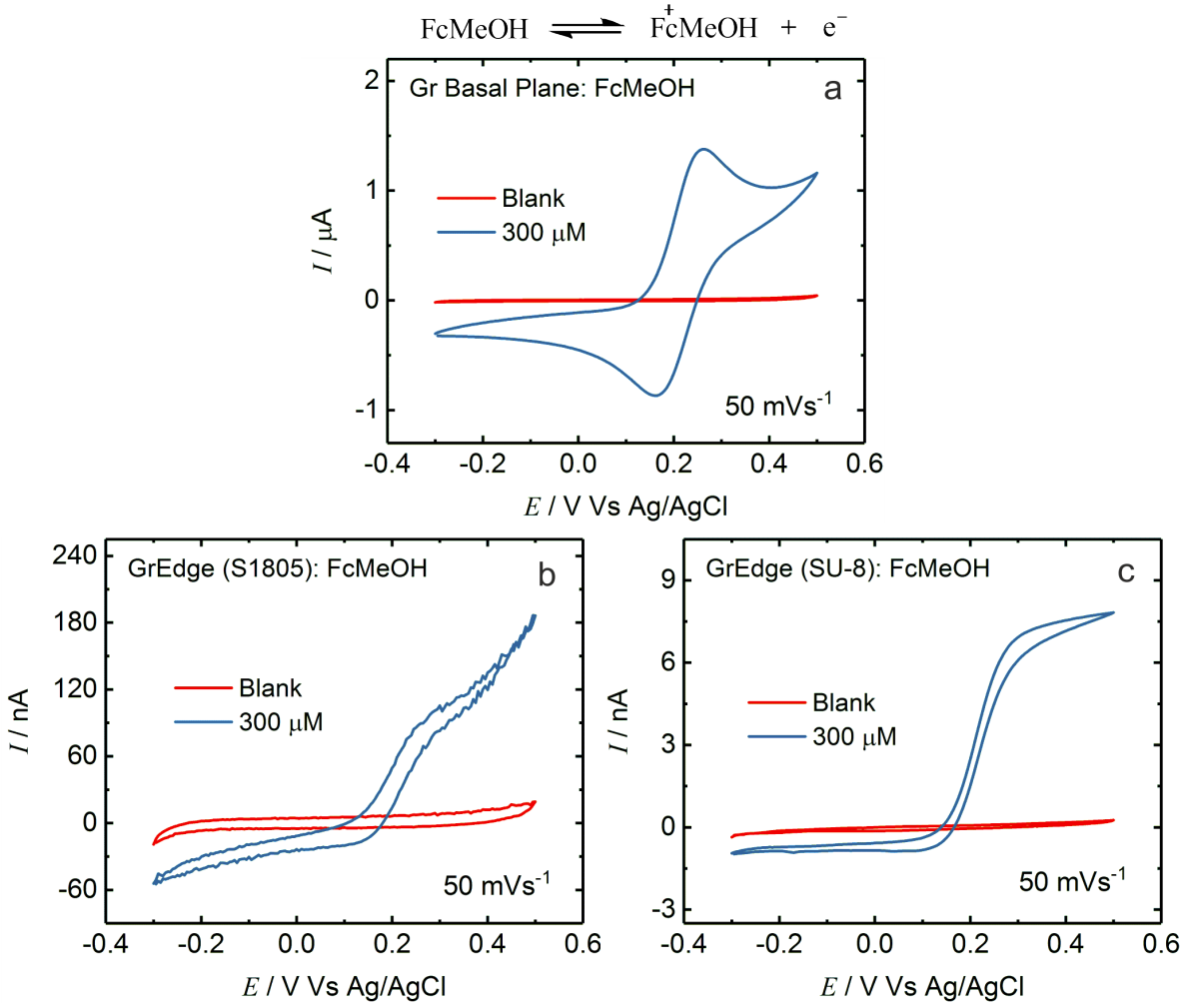

Figure 5.11: CVs for the oxidation of 300 µM FcMeOH at: (a) Graphene basal plane electrode, (b) GrEdge electrodes prepared using S1805 PR (c) GrEdge electrodes prepared using SU-8 PR. (Supporting electrolyte: 0.5 M KCl)

consisting of oxidation and reduction peaks. The graphene basal plane electrode with its dimensions in few millimeters can be considered as a macroelectrode. Both the graphene basal plane and the GrEdge (prepared using both the PRs: S1805 and SU-8) electrodes were characterized using ferrocenemethanol (FcMeOH), which is a common one-electron outer-sphere redox probe, and are shown in figure 5.11.

For graphene basal plane, shown in figure 5.11a, a typical peak shaped voltammogram is observed for the oxidation of FcMeOH (300 µM), which can be referred to as a planar/macroelectrode behaviour. The blank solution (electrolyte) here is 0.5 M KCl, which shows minimum or close to zero current. While for GrEdge, figure 5.11b,c shows a sigmoidal-shaped voltammogram indicating a steady-state current (constant plateau, independent of the time) behaviour, along with very low currents in nA range. This proves that the electrode is in nanometer dimensions (resembling a nanowire shape) and hence, only the edge part of the electrode is exposed. The steady-state response is an indication of an electrode with nanoscale dimensions and is consistent with previous measurements at nanosized electrodes (Pt and CNT UMEs).[35,71,244] The electrochemistry at the GrEdge electrodes is further discussed in detail in chapter 7.

Damaged PR at the edge In many cases, where the graphene is often protected by a PR layer, there is a possibility of the solution entering the region between the PR and the graphene sheet. This can be due to holes in the polymer or lift-off of the polymer at the edge, which usually comes from the photolithography process, in case it has not been done properly or PR is not sealed at their edges. Therefore, it is very important to check the fabricated edge for defective/leaking passivation at the edges of the PR sample under an optical microscope. In case, the PR is not sealed, then some portion of the basal plane will be exposed to the solution, resulting in the observation of electrochemical currents that are not characteristic of nanoelectrodes.[245] This is demonstrated in figure 5.12. Figure 5.12a,b shows the optical images of the PR with good and damaged quality passivation at their edges, respectively. The voltammograms in figure 5.12c for FcMeOH show typical oxidation and reduction peak-like features, indicative of the behaviour more towards the macroelectrode instead of the sigmoidal voltammogram as expected for the GrEdge nanoelectrode. The macroelectrode behaviour is attributed to the increase in graphene area exposed to the solution, and it confirms that in addition to the GrEdge, some part of the basal plane is exposed to the solution when the PR is not sealed or it is damaged at the edge, thereby contributing to the electrochemical current response at the edge. Therefore, it is important to note that such lift-off or damage of PR should be minimized significantly with passivation of high quality in the fabricated edge devices as shown by the optical images (figure 5.6 and 5.7) and characteristic voltammetric responses (figure 5.11c).

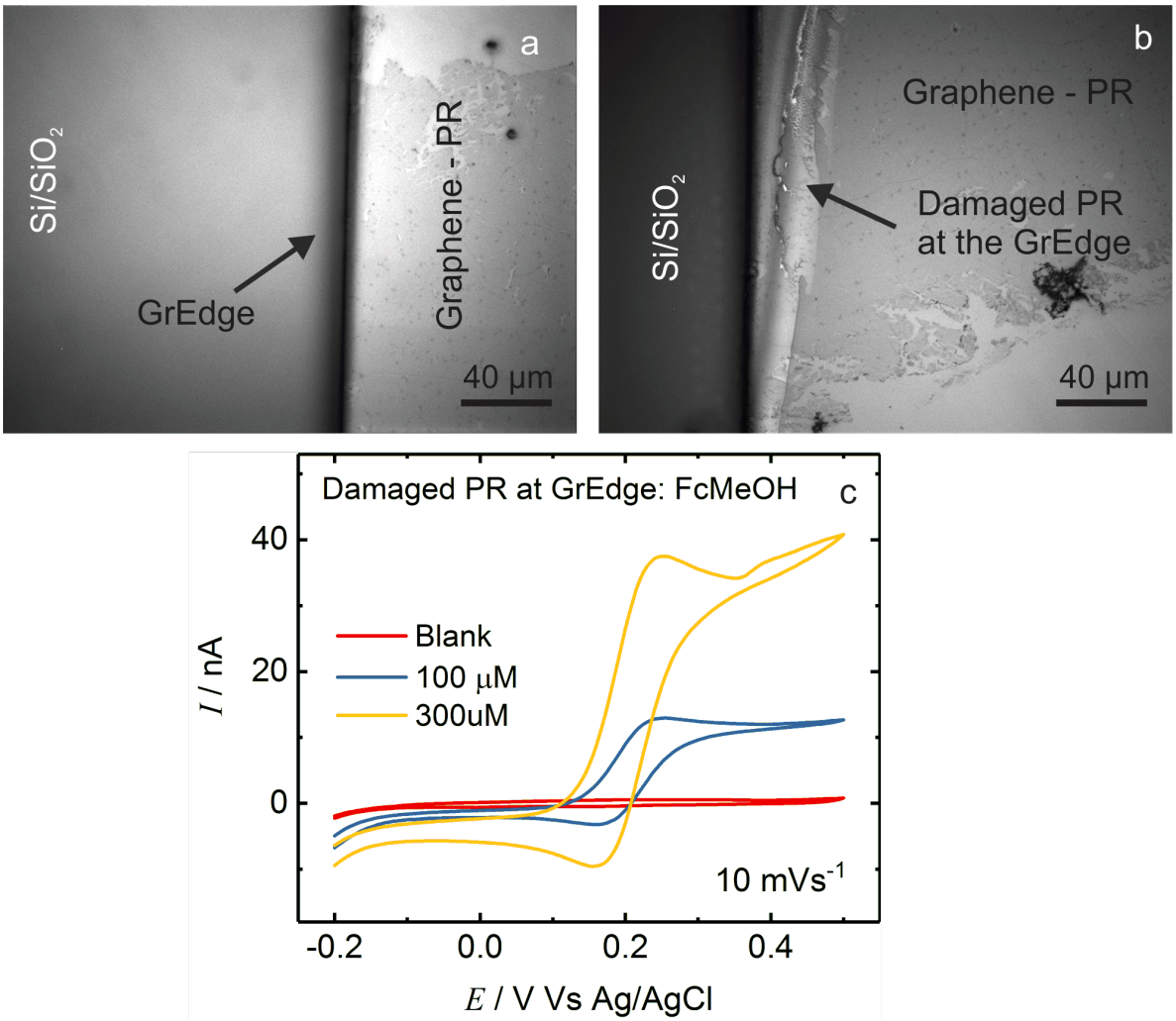

Figure 5.12: Optical images of the (a) GrEdge with good quality of PR passivation at the edge. (b) GrEdge with damaged PR, resulting in the exposure of some part of the basal plane along with the edge. (c) CV of FcMeOH oxidation for different concentrations showing deviation from nanoelectrode behavior at the damaged PR electrode. (Supporting electrolyte: 0.5 M KCl and scan rate in both cases was 10 mVs^{-1})

5.3.6 Electrochemical Modification of the Edge

Another method by which it can be proved that only the edge part of graphene is exposed, and not the basal plane, is the electrochemical modification (ECM) of graphene. The objective is that the modification will occur only at the part of graphene which is exposed to the electrolyte solution during the electrochemistry, and the basal plane part will remain protected by the PR.

For this purpose, gold nanoparticles (AuNPs) were deposited through electrochemical reduction of a gold salt ($KAuCl_4$), at the edge samples prepared using PR S1805 (removable). On an application of a cathodic potential (at stage d in figure 5.4), the heterogeneous electron transfer between the Au^{3+} species in solution and the GrEdge electrode leads to the deposition of Au at the edge. The particles at GrEdge cannot be spatially resolved

from the thick S1805 layer, using optical microscopy or AFM. Therefore, the S1805 layer is removed after Au deposition step, in order to characterize the modified edge region and visualize the particles. Figure 5.13a shows the optical image of the graphene sample partially covered with S1805. Figure 5.13b,c shows the optical images after functionalization and removal of S1805. It illustrates the formation of particles at the GrEdge, in the form of a linear nanowire structure. The presence of this nanowire kind of structure exclusively at the GrEdge confirms that only the edge part of graphene was exposed to the solution during the ECM process.

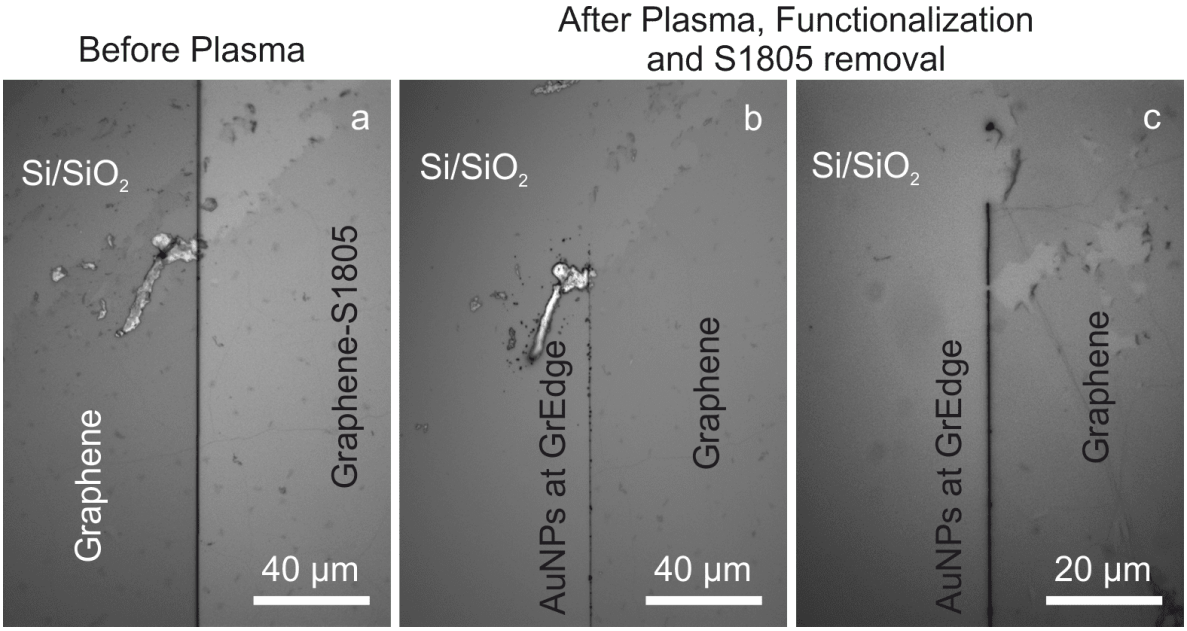

Figure 5.13: Optical images of (a) graphene after partial insulation with S1805. (b,c) functionalized graphene edge with NPs after removal of the S1805 PR.(Note: images a-c are captured at the same location).

However, in case the PR is broken or not sealed properly at the edge, the particles can form even under the PR near the edge. This is shown in figure 5.14 in the presence of a PR, where the small particles as pointed by black arrows are apparent at the location slightly right of the edge line. This is another reason why passivation should be of high quality in the fabricated edge devices. The functionalization of the edge with the particles also results in the modification of its chemistry, and it is discussed in detail in the next chapter 6 of the thesis.

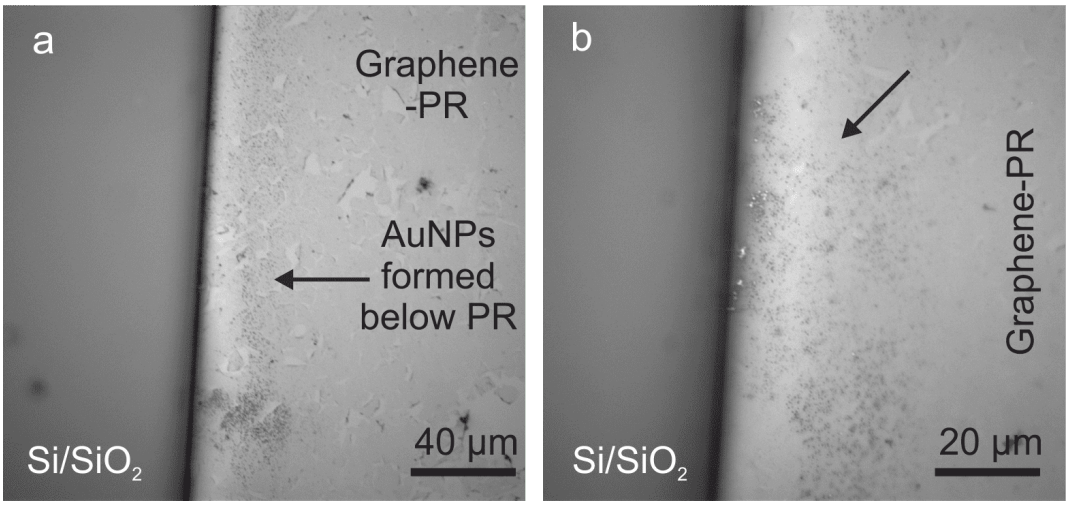

Figure 5.14: Optical images of Au nanoparticles functionalized graphene edge with PR broken at the edge at two different scales. (Note: both the images are captured at the same location)

5.4 Summary

In conclusion, electrodes based on isolated graphene edge (GrEdge) have been fabricated for the first time by region-specific passivation (with photoresists) of CVD-grown monolayer graphene sheet, followed by plasma etching. The exclusive availability of the isolated graphene edge is proved by the steady-state voltammetric behavior as well as the electrochemical modification. The fabricated nanometer-thick GrEdge is important to separate the basal plane- and edge-specific graphene properties. For example, in electrochemical studies, the edge electrode shows a nanoelectrode (in a nanowire form) behaviour in contrast to the basal plane electrode having characteristics of a macroelectrode. The protection of the basal plane also guarantees the selective functionalization of only the edge and not the basal plane.

6

Selective Functionalization of Graphene Edge

The results of the experiments presented here were published in the following manuscript: A Yadav, R M Iost, T J Neubert, S Baylan, T Schmid and K Balasubramanian, Selective Electrochemical Functionalization of the Graphene Edge. *Chem. Sci., 2019, 10, 936-942*.

The aim of the selective functionalization of the graphene edge is to modify only the carbon atoms present on the edge and at the same time preserving the constituting sp^2 carbon atoms of the basal plane.[26,75] This allows to tune the chemistry of only the edge region of graphene. and in addition provides the proof of the successful creation of the isolated edge. Until now, most of the edge functionalization methods have been used on graphene flakes dispersed in solution, where a single object control and observation is not possible.[10,41–43,121] The selective modification has been hardly explored under ambient conditions and relied often on bulk methods such as ball-milling, reactive plasma etching (under H_2, O_2, NH_3, etc.), organic synthesis by polymerizing edge functionalized polycyclic aromatic hydrocarbon monomers.[120,246] However, in all the above-mentioned methods, there is no direct attachment of the functional group to the edge, instead, these are intrinsic and extrinsic modifications such as atomic-scale defects, structural distortions, and unintended chemical functionalization. This is due to the higher reactivity of the carbon atoms at the graphene edge than the relatively inert basal plane. Therefore, most of the fabrication processes (lithography, oxidative unzipping, and catalytic etching with metal) result in highly defective, non-uniform, and inhomogeneous edge structures. Hence, one other reason to modify the graphene edge is to tailor its chemistry in a controlled and systematic manner, in order to obtain a homogeneous and continuous edge. In the gas phase, there exists two reports where: tetrapyrroles were fused covalently to a graphene edge using surface assisted

coupling,[122] and individual tetrafluoro-tetracyanoquinodimethane molecules were fixed on the graphene edge by using an electronically inert molecular anchor.[123] However, in both cases, the edge was modified only partially, with a single molecule by using an elaborate and indirect methodology in ultrahigh vacuum at low temperatures.

This chapter presents a strategy for the selective homogeneous modification of the edge of a single graphene sheet under ambient conditions with chemical moieties such as metal nanoparticles (NPs), polymeric amino groups, and diazonium salts. The attachment of metal NPs gives an added advantage of surface-enhanced Raman scattering (SERS), to gather spectroscopic information and to identify the chemistry of the functional groups present or formed at the edges.

6.1 Functionalization Strategy

The general schematic for the selective functionalization of the GrEdge (figure 6.1) illustrates all the steps needed to functionalize the edge electrode: the GrEdge sample prepared using positive PR S1805 (same as demonstrated in chapter 5); functionalization - ECM using an appropriate precursor/ monomer (e.g. $KAuCl_4$ salt for modification with AuNPs) at the exposed GrEdge; removal of PR for the characterization. The presence of the PR on the basal plane during the functionalization or ECM step will selectively promote the electrochemistry reaction to occur only at the exposed GrEdge, and not at the whole surface of graphene. In the end, the PR is removed in order to characterize the functionalized edge. The GrEdge was functionalized with the following chemical moieties:

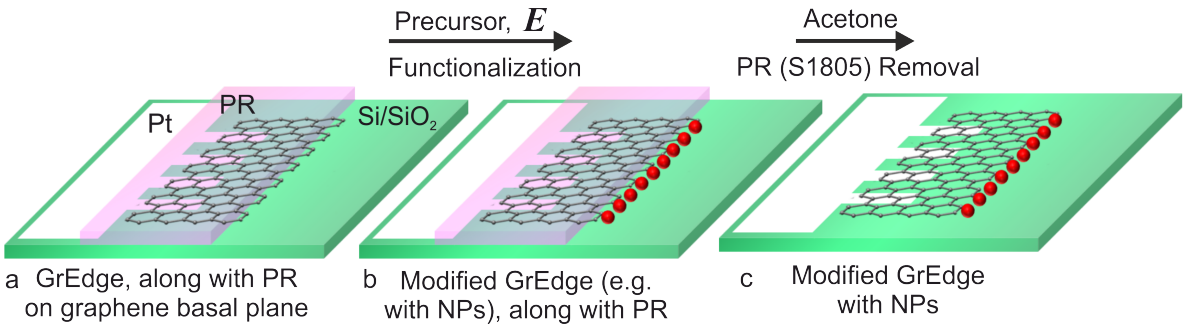

Figure 6.1: Schematic of the procedure for functionalization of a graphene edge. (a) GrEdge sample prepared using positive PR S1805, (b) Selectively modified GrEdge (e.g., with NPs) through ECM by application of a potential E at the exposed GrEdge using the required precursor. (c) Modified GrEdge after the removal of PR S1805 in acetone.

- Electrodeposition of metal NPs (Au, Pd, Pt).
- Non-covalent attachment of polymeric amino acid group (poly-4-aminobenzylamine) using electropolymerization, followed by deposition of AuNPs.
- Covalent attachment using diazonium chemistry.

6.2 Electrodeposition with AuNPs

6.2.1 AuNPs Deposition and Characterization

The AuNPs electrodeposition was performed using chronoamperometry in a three-electrode arrangement (GrEdge acts as a WE, a Pt wire as CE, and an Ag/AgCl wire as RE) where the deposition potential (cathodic) was applied in two-time pulses (double potential step approach) to control the size, density, and distribution of the particles in a reproducible manner.[143,145,247]

Figure 6.2 shows a typical chronoamperometric profile recorded at the GrEdge electrode in the presence of 10 µM $KAuCl_4$ in 0.1 M $LiClO_4$ (supporting electrolyte) solution. The potentials of -0.4 V (nucleation), 5 s and +0.4 V (growth), 15 s is applied for two cycles at the stage 'a' in figure 6.1) in a solution of $KAuCl_4$ in 0.1 M $LiClO_4$. The deposition is driven by the HET between the gold species in solution ($AuCl_4^-$) and the GrEdge electrode, which leads to the electrochemical reduction of Au^{3+} to Au^0, and subsequently, its deposition at the GrEdge electrode. Later the PR layer is removed by dissolving it in acetone for the characterization of the functionalized GrEdge-AuNP device.

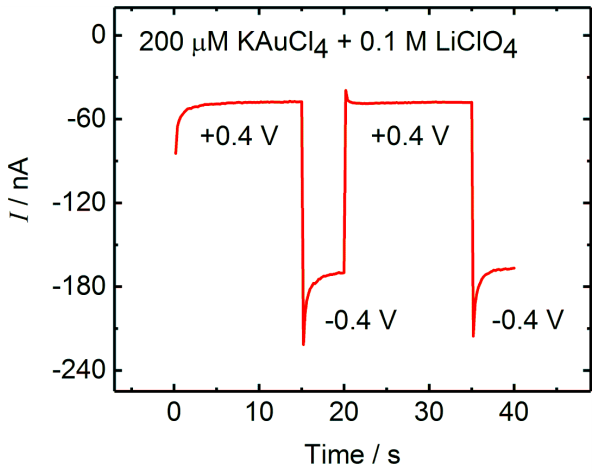

Figure 6.2: A typical chronoamperometric profile for the potentiostatic deposition of AuNPs at a GrEdge electrode (device in figure 6.3), with 200 µM $KAuCl_4$ in 0.1 M $LiClO_4$ (supporting electrolyte).

Figure 6.3a shows an AFM image of the free GrEdge after the PR removal as a control without any functionalization. The unmodified sample shows a clean graphene surface (with a height of around 1 nm as shown by the line profile). The AFM and backscattered electron SEM images in figure 6.3b,c show the edge with the NPs (GrEdge-AuNPs) after the functionalization and confirms that a chain of particles (similar to a nanowire) is generated exclusively at the graphene edge in the case of the GrEdge-AuNPs sample. It also shows that the functionalization is continuous, with the homogeneous size of the particles at all places on the edge. The line profile shows an average height of 70 nm for the particles.

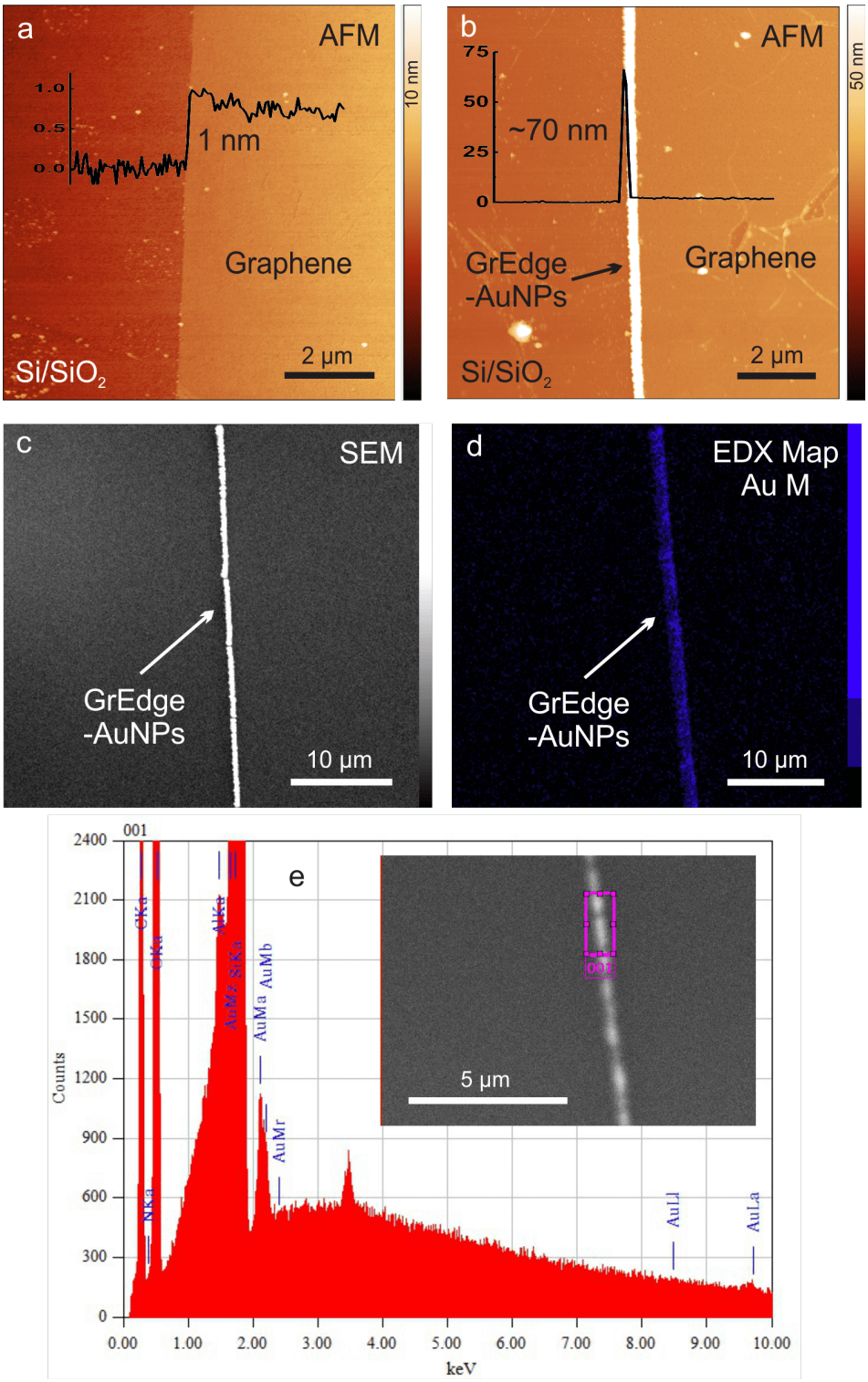

Figure 6.3: (a,b) AFM images (along with respective line profiles showing the height at the edge) of the (a) free GrEdge, and (b) modified GrEdge-AuNPs. (c) SEM image of the GrEdge decorated with AuNPs. (d) Au EDX map (obtained by integrating intensity of Au Mα line) of the sample, showing AuNPs only at the edge. (e) EDX spectrum showing the Au peaks marked as such. The image in the inset is a secondary electron SEM image, while the small rectangular area along the aligned NPs was selected on a backscattered electron image for accumulation of the EDX spectrum. Note: the PR has been removed in a-e to obtain the AFM, SEM and EDX images.

The SEM image visualizes the distribution of different chemical elements, also referred to as material contrast (on the basis of conductivity and electron yield), which is clearly different at the GrEdge (figure 6.3c) due to the deposited NPs. The energy dispersive X-ray (EDX) map gives an account of the spatial distributions of chemical elements as the sample atoms that absorb can emit X-ray spectra containing element-specific emission. The EDX map (figure 6.3d), obtained over the same selected area as of SEM image, shows the selected peak intensities (coming from the M electron shell of Au) only at the edge. The EDX spectrum (figure 6.3e) obtained directly from the deposited AuNPs at the edge shows the characteristic peak at 2.12 keV corresponding to the emission line from the M shell of Au. Therefore, EDX provides support that the particles are of gold. The selective modification of the edge of graphene with AuNPs was reported for the first time in this work.

In order to demonstrate the need for the PR coverage for achieving NP attachment exclusively at the edge, a control experiment was carried out, where the electrodeposition procedure with the same parameters (as in figure 6.3b) was repeated at a graphene electrode that was not covered by the PR. As shown in figure 6.4a,b, when the basal plane is not protected, it is clear that the particles grow everywhere on graphene. Further details of basal plane modification can be found in the chapter 4, as well as in the previous publications by Balasubramanian *et al.* in references [50] and [51].

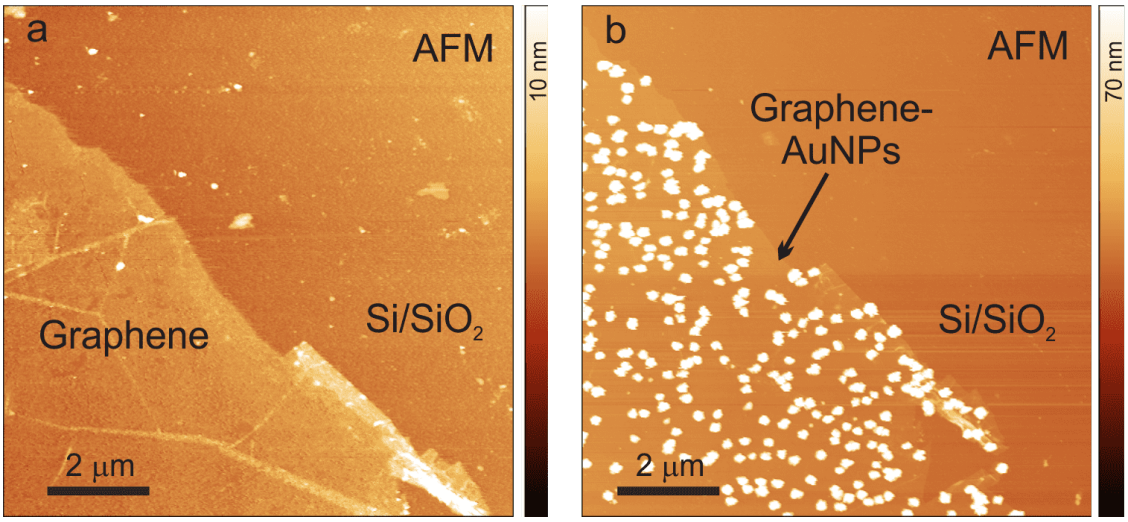

Figure 6.4: AFM images of typical graphene basal plane sample when it is not covered with PR layer (a) pristine form (b) after modification with AuNPs. Note: the PR has been removed in a-d to obtain the AFM, SEM and EDX images.

Further, it was shown that the particle size at the edge can be varied by using different electrodeposition parameters (the cathodic potential, duration of the pulse, and the concentration of the metal salt ($KAuCl_4$ in this case) accordingly. In all the GrEdge devices shown in figure 6.5, the size of deposited AuNPs is different, attributed to different $KAuCl_4$ concentrations and deposition times. At $KAuCl_4$ concentrations of 35 µM, 100 µM and 200 µM

(time and potential remain constant), the respective AuNP sizes obtained in figure 6.5a,b,c are $\sim$ 40-50 nm, $\sim$ 100 nm and $\sim$ 250 nm, respectively. On increasing the deposition time from 10 s to 20 sec (concentration and potential remain constant) in figure 6.5c,d, the size of AuNPs increases from $\sim$ 200 nm to $\sim$ 450 nm.

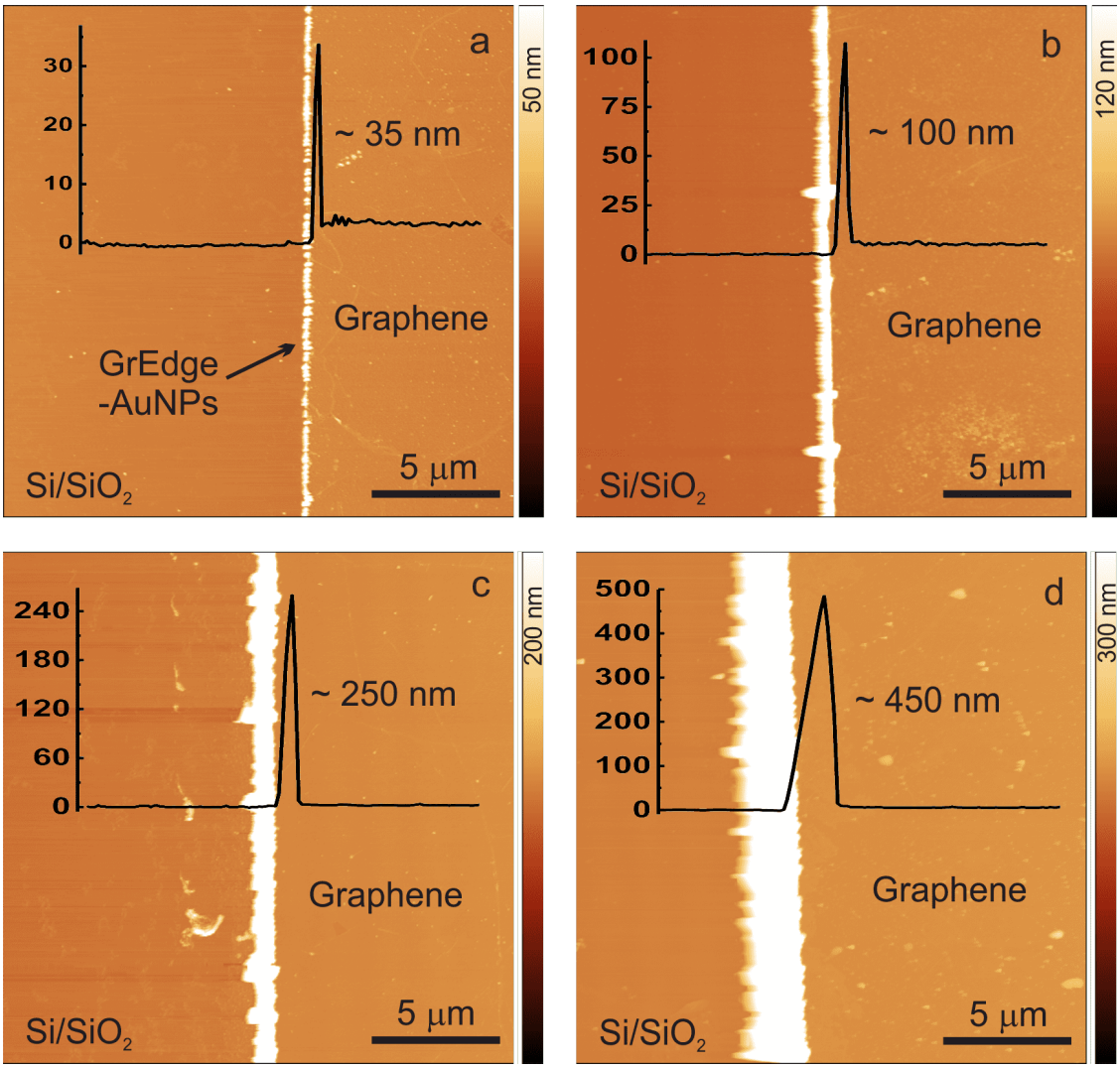

Figure 6.5: AFM images of GrEdge devices functionalized with AuNPs of varying size, obtained by using different electrodeposition parameters. The parameters ($KAuCl_4$ concentration, deposition potential, time) in the same order are: (a) 35 µM, -0.5 V, 10 s (b) 100 µM, -0.4 V, 10 s (c) 200 µM, -0.4 V, 10 s (d) 200 µM, -0.4 V, 20 s.

6.2.2 Raman and SERS Effect at the Edge

AuNPs exhibit strong LSPR absorption in the visible range of the electromagnetic spectrum,[128,164] creating highly localized regions of intense local field enhancement called hot spots, leading to enhancement of Raman and Rayleigh scattering. In other words, the surface-enhanced Raman scattering (SERS) exploits surface plasmons induced by the incident field in metallic nanostructures to enhance the Raman intensity,[65,166] as also shown in chapter 4. There is significant Raman enhancement at an excitation wavelength of 633 nm, due to its resonance with the surface plasmons of Au particles.[64] The enhancement in the intensities of the Raman-active modes by SERS can facilitate in determining the chemistry at the GrEdge through the detection of extra-functional groups (in case they are introduced by the mild O_2 plasma treatment leading to oxidation of the GrEdge). Therefore, the deposition of AuNPs serves a threefold purpose:

- The presence of AuNPs exclusively at the edge of graphene and not on the basal plane confirms that only the edge part of graphene was exposed to the solution.
- Functionalization/modification of the edge, where the exclusive deposition of particles at the edge can be confirmed by surface characterization.
- The presence of AuNPs at the edge allows us to perform selective spectroscopic characterization of the chemistry exclusively at the edge through surface-enhanced Raman scattering (SERS).

Comparison of Individual Raman spectra Figure 6.6 presents the comparison between Raman spectra obtained at the basal plane, the bare (unmodified) GrEdge, and the AuNPs modified GrEdge. The Raman measurement at the modified GrEdge was carried out after the removal of PR S1805. All the spectra are plotted after their background subtraction.[51] The basal plane Raman spectrum (black curve) shows only *G* (1584 cm^{-1}) and *2D* (2631 cm^{-1}) peaks, and the absence of a *D* peak indicates that the graphene sheet is of high quality mostly free of defects. The ratio I_{2D}/I_G of $\sim$ 2 further confirms the single layer of the graphene sheet.[60] The bare GrEdge spectrum without AuNPs (red curve) shows as expected the disordered related peaks in addition to the typical *G* and *2D* peaks: a weak *D*-peak (at around 1330 cm^{-1}) and a very small shoulder (*D'*-peak, $\sim$ 1620 cm^{-1}) next to the *G*-peak.[233] These extra signals are due to the breaking of C=C bonds during the etching process, which introduce the sp^3-carbon atoms perturbing the honeycomb lattice.[56,58,161,162]

Interestingly, in the Raman spectrum of GrEdge-AuNPs (SERS spectrum), the same 4 peaks are observed, with differences in the relative intensities and peak positions. The most notable change is an increase in the intensity of *D*-peak, and clearly visible *D'* peaks, unlike before the attachment of NPs.[233] It is worth mentioning that when AuNPs are deposited on the pristine basal plane (chapter 4), the *D'*-peak does not appear.[50] Also, the *2D*- and

G-peak shift slightly towards lower frequency after the deposition of AuNPs. Furthermore, the intensity ratio of the *D*- to *G*-peaks (I_D/I_G) has increased and is now close to one. Qualitatively similar behavior is also observed for other locations as shown in figure 6.7a. The above-mentioned changes after deposition of AuNPs are indicative of a chemical interaction (doping or charge transfer) between the AuNPs and GrEdge (or graphene). About the nature of bonding between the GrEdge and AuNPs, one can safely assume that the NPs are deposited on the surface without any covalent bond, based on the previous Raman and electrical measurements performed on graphene (or CNTs) - AuNP hybrids.[49,50] At the frequency of the *D* mode, resonant enhancement by plasmonic absorption of AuNPs is strong, which is not the case for the frequency of the *2D* mode.[212] Therefore, the strong *D* mode can be explained by the enhancement and is not a clear indication of covalent attachment. Furthermore, the *D* mode (being representative of defects in the *2D* lattice of graphene) is expected to be stronger at the edge, which is also visible in its Raman spectrum (red curve). As the edge is decorated with the particles, its significant features are enhanced stronger in the Raman spectrum. Therefore, the previously weak *D*-mode originating from the edge is now enhanced. However, the intensity of the *2D* mode remains at a constant level without any enhancement, which underlines that there is no covalent modification by the AuNPs. The decrease of the *2D* mode intensity would be indicative of covalent modification. Therefore, the particles are deposited at the edge without the formation of a covalent bond. The enhancement factor of the bands is discussed in the latter part of this section.

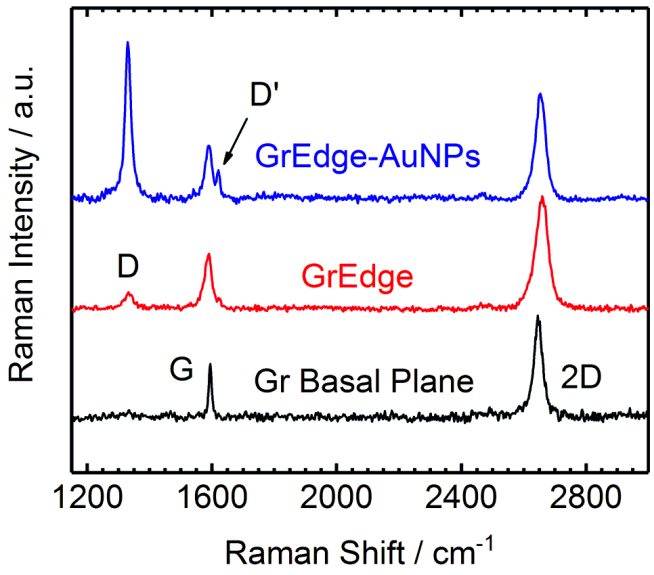

Figure 6.6: Comparison of Raman spectra from the graphene basal plane (black curve), the graphene edge (red curve) and the graphene edge with AuNPs (blue curve). The spectra are shifted for clarity. (λ_{ex}: 633 nm, 4.5 mW, 1 × 1 s)

Additionally, a control experiment has been performed without the gold species in 0.1 M $LiClO_4$ solution using the same electrodeposition parameters (as used with the Au^{3+} in

solution). The Raman spectra at 4 different positions of the GrEdge after this procedure is shown in figure 6.7b, which is similar to the unmodified GrEdge spectrum shown in figure 6.6 (black curve). There is no *D'* peak present as well as there is no enhancement in the *D* peak. This further strengthens the point that the enhancement/change in the Raman spectrum occurs if only the AuNPs are deposited.

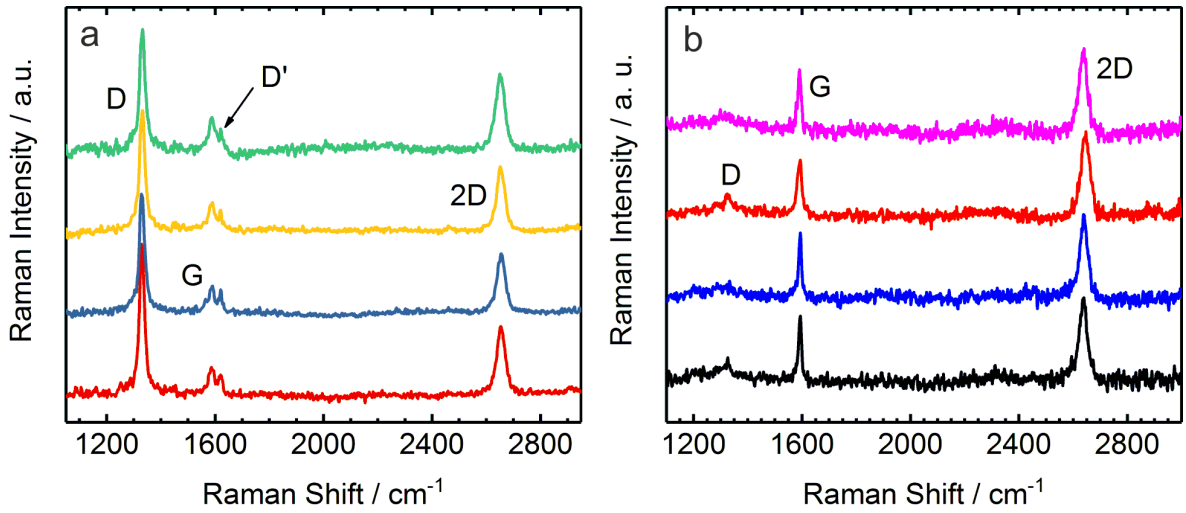

Figure 6.7: (a) Raman spectra of GrEdge-AuNPs from 4 different locations demonstrating the reproducibility of the peaks and the absence of other modes. (b) Raman spectra of GrEdge after chronoamperometry in background electrolyte 0.1 M $LiClO_4$ in the absence of the precursor $KAuCl_4$ salt for 4 different positions, indicating that the edge remains unmodified in the absence of the gold species. The spectra are shifted for clarity. (λ_{ex}: 633 nm, 4.5 mW, 1 $\times$ 1 s)

Raman (or SERS) Maps Figure 6.8a,b presents the chronoamperometric profile for AuNPs deposition at GrEdge (with conditions optimized to get the size of AuNPs favorable for SERS effect), and an AFM image of the prepared GrEdge-AuNPs sample. The particles show an average height of 50 $\pm$ 7 nm, calculated from the line profile obtained from AFM at several locations on the edge (figure 6.8c shows a line profile at one location). Raman intensity maps (measured in the region shown by the dotted (black) rectangle in the AFM image) of the corresponding graphene bands are shown in figure 6.8d. In the AFM image, one position (below the black arrow) shows no AuNPs at the GrEdge. This can be attributed to the absence of the exposed GrEdge (because of the hole in the graphene sheet) at that position, where the deposition of particles doesn't take place due to absence of the electron transfer. The same position (or hole) is also visible in the Raman maps of $I_{D'}$ and I_{2D}. The Raman maps (4 µm $\times$ 20 µm, with each spectrum measured at an interval of 200 nm) were mainly obtained to investigate the spatial variation of the Raman enhancement, where the spectra were acquired as a function of position. It is apparent from the I_{2D}, $I_{D'}$ and I_D/I_G maps that the intensities of the Raman bands have significantly increased along the GrEdge after ECM (indicative of SERS enhancement) with exclusive observation of the disorder at

the edge. In this way, it is clear that the presence of particles at the GrEdge results in a surface enhancement exclusively at the edge and in this manner, the observed SERS signals can be associated as coming predominantly from the edge. On the other hand, the intensity of the Raman peaks (or the enhancement) is slightly different at locations along the edge. This is attributed to the small difference in size and density of the AuNPs (also evident in the AFM image) formed along the edge, since it strongly controls the degree of enhancement.

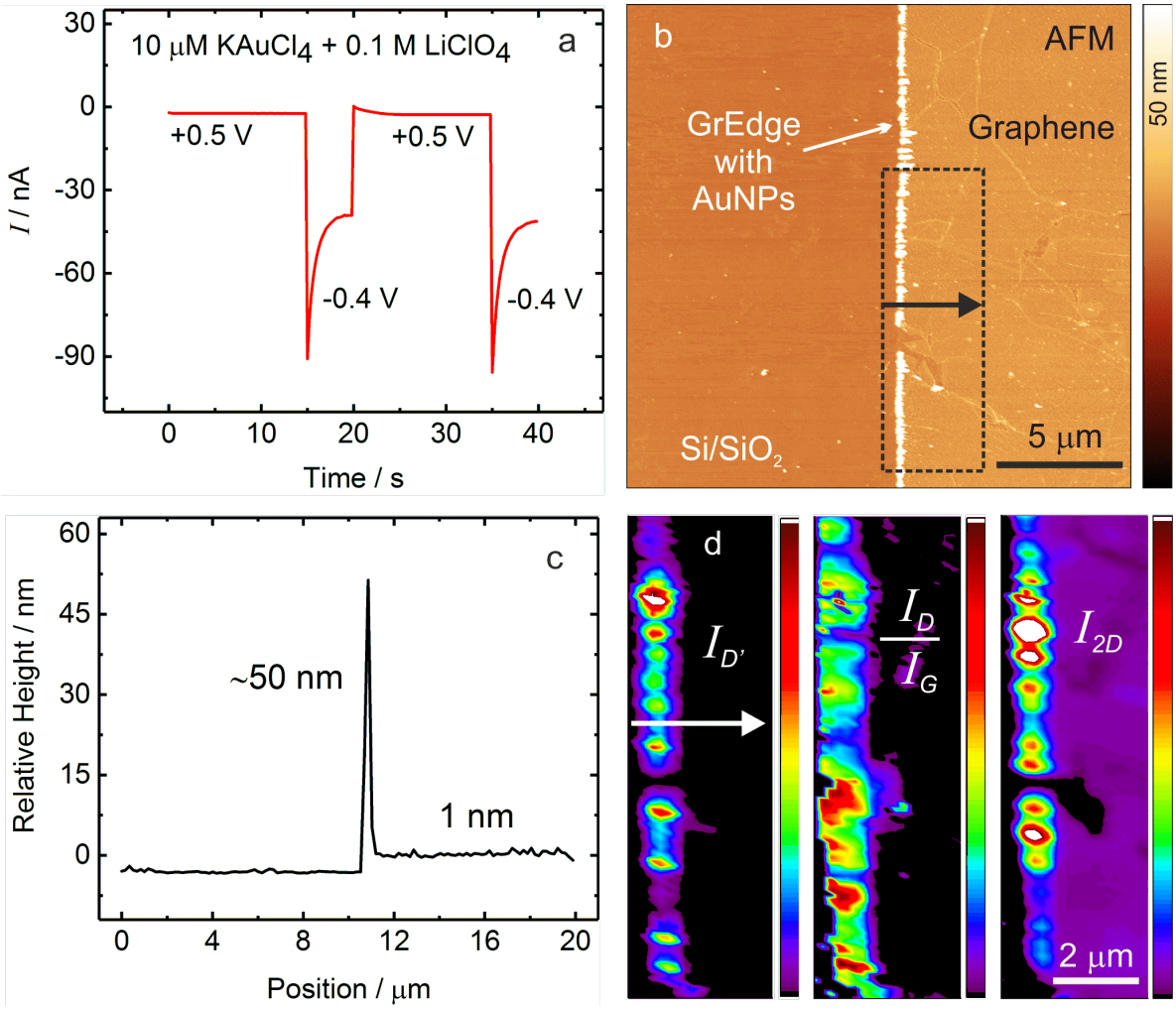

Figure 6.8: (a) A chronoamperometric profile for the AuNPs deposition at the edge. (b) AFM image of the free and modified edge with AuNPs after removal of PR. (c) Line profiles showing the average height at the edge. (d) The corresponding Raman maps of *D'* (1620 cm^{-1}), *D* (1330 cm^{-1}), relative to *G* (1587 cm^{-1}), and *2D* (2653 cm^{-1}) intensities at the same location shown by the box in AFM image (b) (λ_{ex}: 633 nm, 4.5 mW, 1 × 1 s)

Fluorescence of AuNPs One of the characteristics of AuNPs is the emission of fluorescence, which arises due to recombination of photoexcited electrons (from the 6*sp*-band) with holes (in the 5*d*-band) at the band edges of the L- and X-points (in reciprocal space).[208–210,248] This was investigated by plotting all the Raman spectra (1-19) from one horizontal line of the map (position and direction shown by the black and white arrows in

the AFM image and Raman map in the previous figure 6.8) without background subtraction in figure 6.9a (they are further divided into three separate graphs, figure 6.9c-d). There are total 19 spectra (measurement points) with a step size of 200 nm between them. The measurement starts from left to right as shown by the direction of the arrow in the AFM image (figure 6.8). The left end is only the Si/SiO_2 substrate, and does not show any graphene bands as confirmed by the spectra 1 and 2. Then comes the edge with AuNPs indicated by the AFM and high intensity of the Raman peaks contributing to the spectra 3 to 13. In addition to the enhancement of the Raman peaks, there is a clear background, in all these spectra in the vicinity of the AuNPs at the GrEdge, which is otherwise almost zero on bare edge and bare basal plane. This is in accordance with the background observed earlier on AuNPs modified graphene basal plane in chapter 4,[50,148] and can be assigned to the characteristic fluorescence of AuNPs deposited at the edge.[210,248] The fluorescence background increases gradually from spectra 3 onwards, and is strongest at spectra 8. From spectra 9, it is apparent that the fluorescence becomes weaker gradually, and decreases until spectra

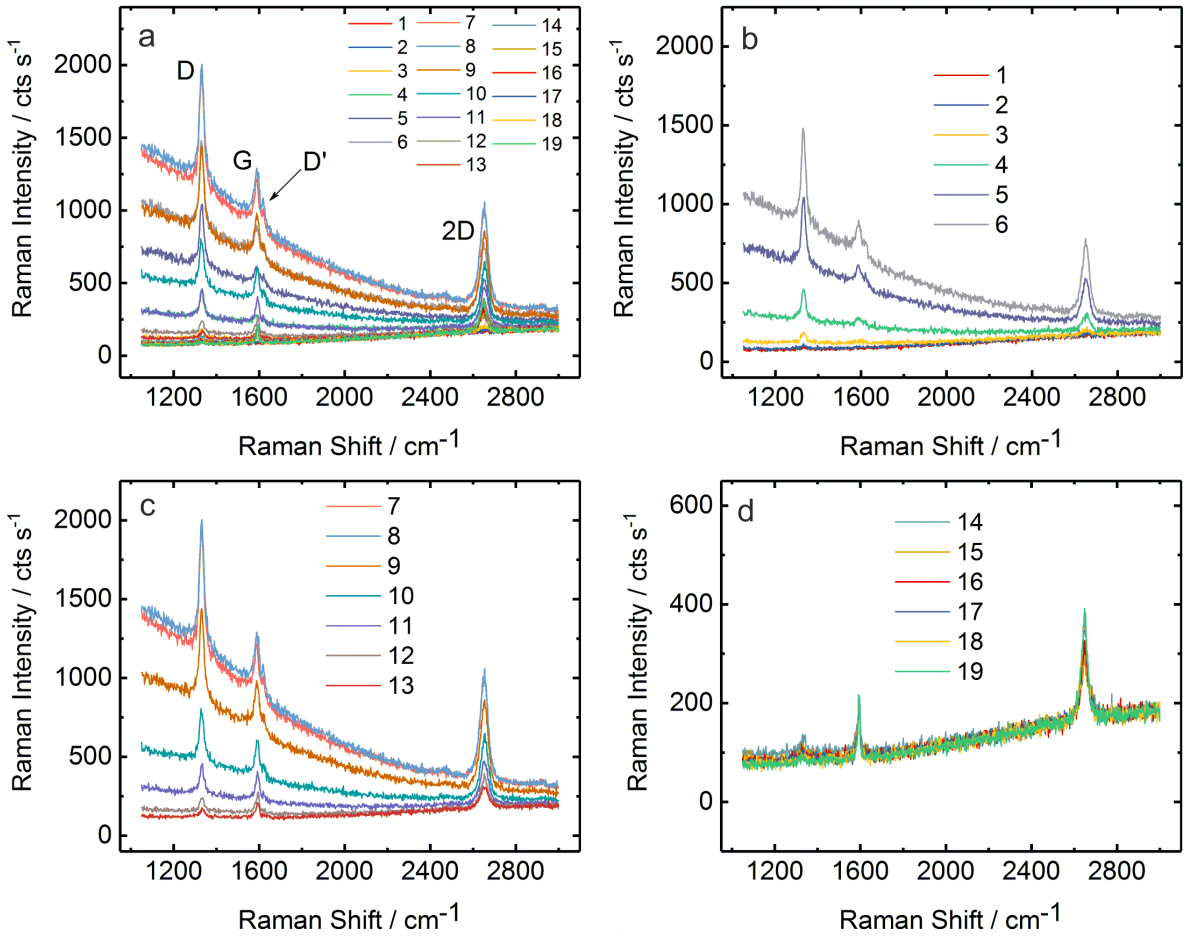

Figure 6.9: (a) Raman spectra from the graphene basal plane (black curve), the graphene edge (red curve) and the graphene edge with AuNPs (blue curve). (b) Raman spectra of GrEdge-AuNPs from 4 different devices demonstrating the reproducibility of the peaks and the absence of other modes. (The spectra are shifted for clarity) (λ_{ex}: 633 nm, 4.5 mW, 1 × 1 s)

13, indicative of moving away of the measurement point from the GrEdge and particles. The right side of GrEdge-AuNPs is the pristine basal plane region as shown by the uniform intensity of the graphene Raman peaks without any fluorescence background (spectra 14-19). From these observations it can be concluded that there is a clear correlation between the observed Raman signals and obtained fluorescence from the AuNPs at the GrEdge.

Enhancement Factor The Raman enhancement factor for the main Raman modes is calculated by taking the direct intensity without baseline subtraction of each peak after the GrEdge modification, and then dividing them by the intensity of their corresponding peak obtained from the unmodified GrEdge. The enhancement factor for *D*, *G* and *2D* peaks are shown in the table 6.1. It is apparent from figure 6.9 that the degree of enhancement is significantly different for all the graphene modes and becomes weaker with the increase in frequency of the vibrational mode. *D* band has higher enhancement than *G* and *2D*, while *G* band has higher enhancement than *2D*. The highest EF for the *D* band can be explained by taking into account the plasmonic resonances, since it is strongest near the *D* band region and weakest in the *2D* band region. Theoretically, the maximum SERS enhancement occur when the LSPR λ_{max} (600 - 650 nm) lies between λ_{ex} and λ_{vib}.[212]

Table 6.1: Raman enhancement factors for the intensity of graphene bands after the functionalization of the GrEdge with AuNPs. (Calculated by taking the spectra at 5 different positions)

Raman Band	Enhancement Factor
D	18.64 ($\pm$1.43)
G	6.12 ($\pm$0.15)
2D	2.94 ($\pm$0.40)

Figure 6.10 presents the positions of the *D*, *G* and *2D*-peaks (in nm, measured at $\lambda_{ex} =$ 633 nm) along with the absorption spectra of AuNPs deposited on graphene. In addition, the optical extinction spectra of differently sized AuNPs (calculated by using the Mie theory) are presented for comparison (Adapted from reference [148]). It is apparent that the extinction coefficient decreases as the Raman vibrational frequency increases, with *D* peak (691.3 nm) overlapping at the highest extinction coefficient, followed by *G* (703.8 nm) and *2D* (761.1 nm). This can be directly correlated with the decrease in Raman EFs as a function of the vibrational frequency. Therefore, resonant enhancement by plasmonic absorption of AuNPs is strongest at the energy of the *D* mode, followed by *G* and *D'*, and lowest for the energy region of the *2D* mode.

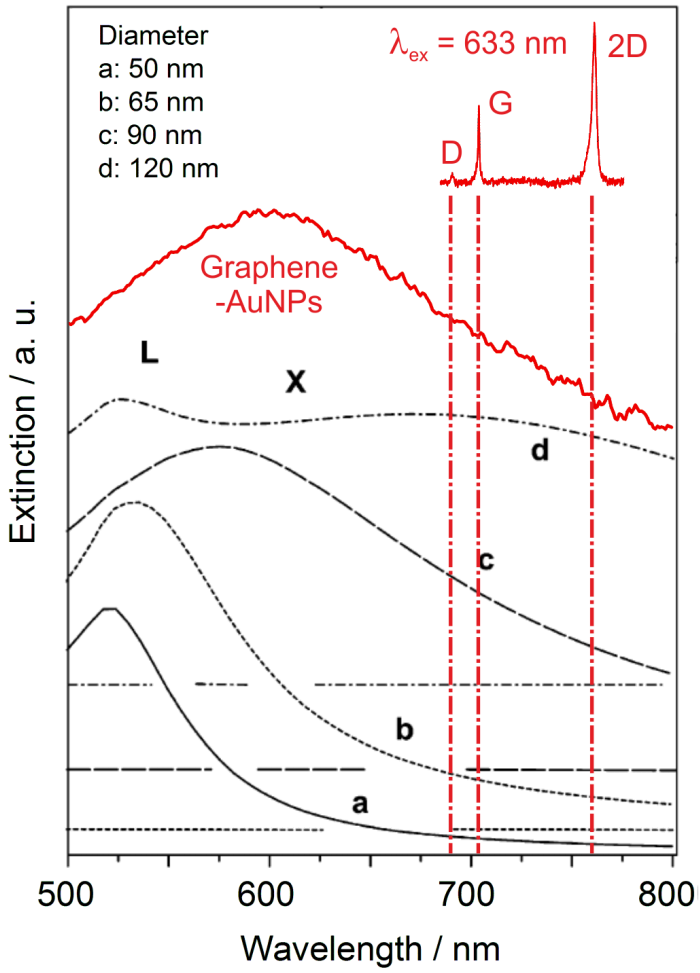

Figure 6.10: Optical extinction spectra of AuNPs of varying size calculated according to Mie theory. (Adapted with permission from ref. [148]). The wavelengths corresponding to the positions of the L- and X-points in the reciprocal space are indicated as well. The additional experimental UV-vis absorption spectra of AuNPs deposited on monolayer graphene is shown in red. The Raman spectra with positions of the *D*, *G* and *2D*-peaks are marked in red. (λ_{ex}: 633 nm, 4.5 mW, 1 $\times$ 1 s)

Doping/Chemical Interaction between GrEdge and AuNPs To study the nature of chemical interaction and charge transfer doping between the AuNPs and GrEdge (or graphene), different Raman maps are obtained from the data of various peak parameters of the graphene basal plane, GrEdge and GrEdge-AuNPs (similar to as presented in figure 6.11). The maps were recorded at the same selected area as shown in figure 6.8.

Figure 6.11a-d, shows the intensity maps of all the graphene modes, with higher intensity at the edges due to the Raman enhancement. The I_D and $I_{D'}$ as expected has almost negligible values in the basal plane region. The maps of intensity ratio are plotted in figure 6.11e-h. The maps of I_D/I_G, I_D/I_{2D}, $I_{D'}/I_{2D}$ further indicates the negligible defects in the basal plane region, while higher and exclusively observable defects with enhancement due to AuNPs at the edges. The I_G/I_{2D} increases at the edge in comparison to basal plane, since enhancement in *G* peak is greater than the *2D* peak due to SERS as shown in table 6.1.

The peak position maps of ω_G and ω_{2D} are plotted in figure 6.11i,j to distinguish between *n*- and *p*-type doping. The decrease in ω_G by $\sim$ 8 cm^{-1} and ω_{2D} by $\sim$ 15 cm^{-1} for GrEdge-AuNPs (w.r.t basal plane), are consistent with ET from the AuNPs to graphene.[50]

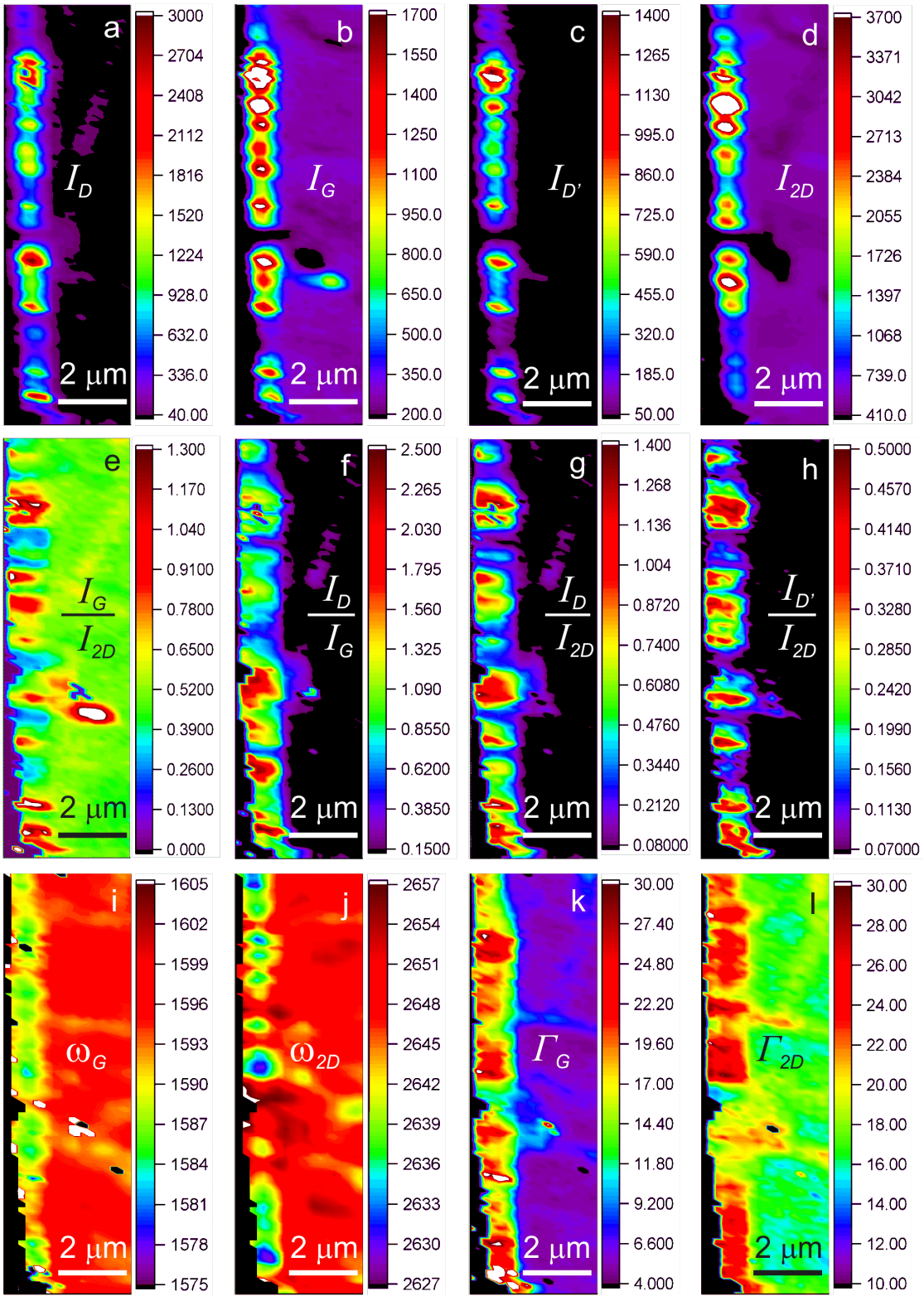

Figure 6.11: Raman Maps of the intensity (I), intensity ratio, mode frequency or peak position (ω) and FWHM (Γ) of the various graphene bands for the sample in Figure 6.8. (λ_{ex}: 633 nm, 4.5 mW, 1 $\times$ 1 s)

The FWHM maps Γ_G and Γ_{2D} are shown in figure 6.11k,l. The increase in both the Γ_G and Γ_{2D} after AuNPs deposition, indicates more charge fluctuations at the GrEdge due to the presence of Au. The interfacial contact area between AuNPs and the edge is considerably smaller, explaining the comparatively weak charge transfer between the particles and graphene. These observations are consistent with the claim that the particles are exclusively attached to the edge of the graphene sheet. Further, all the observations in the Raman maps are also tabulated in table 6.2.

Table 6.2: Mode parameters of graphene-related peaks in the Raman spectra of basal plane, GrEdge and GrEdge-AuNPs.

$\pm$ cm^{-1}	Basal plane	GrEdge	GrEdge-AuNPs
ω_D	-	1328.4($\pm$0.81)	1329.1 ($\pm$3.9)
ω_G	1595.5($\pm$0.87)	1592.8($\pm$1.8)	1588.9 ($\pm$2.5)
$\omega_{D'}$	-	-	1621.0 ($\pm$1.2)
ω_{2D}	2649.0($\pm$1.1)	2650.5($\pm$1.9)	2639.9 ($\pm$5.4)
Γ_G	5.5($\pm$0.42)	13.2($\pm$2.7)	20.0 ($\pm$2.0)
Γ_{2D}	16.5($\pm$0.84)	20.6($\pm$1.2)	22.7 ($\pm$2.2)
I_{2D}/I_G	2.06($\pm$0.13)	2.5($\pm$0.48)	1.9 ($\pm$0.8)
I_{2D}/I_G	2.06($\pm$0.13)	2.5($\pm$0.48)	1.9 ($\pm$0.8)

Chemistry at the Graphene Edge Another important advantage of using AuNPs is that it allows for local vibrational fingerprinting by SERS, which has been used earlier to obtain information about functional groups on the graphene surface (chapter 4).[51] The edges created after the breaking of C=C bonds consists of many defects with unstable dangling bonds, and are prone to possible termination by oxygen containing groups or adsorption of other reactive species from the electrolyte solution.[79] Reactive plasma etching treatment during the GrEdge fabrication can be a possible source of oxidation at the GrEdge.[97] The combination of GrEdge and AuNPs can be directly used to investigate the presence or absence of functional groups at the patterned GrEdge. However, for the fabricated GrEdge samples, even after the deposition of AuNPs, no additional peaks were observed in the Raman spectra (figure 6.6). Although SERS is known to be sensitive down to the single molecule level, in all the Raman spectra (figure 6.7b and 6.2) that were measured on the pristine GrEdge with varying particle sizes, there was no observation of oxygenated carbon groups. In order to further verify the sensitivity of the SERS method to detect the functional groups at the GrEdge, the GrEdge was deliberately oxidized through electrochemical oxidation to increase the density of such groups, followed by AuNPs deposition. In this case, the additional oxygen-related peaks were clearly observed in the SERS spectra (figure 10.2a). Such oxygen-related peaks are however absent in the SERS spectra of the pristine GrEdge (figure 6.6) suggesting that we have a rather low density of oxygen-related functional groups here. This is most likely due to the very mild plasma conditions used. Stronger plasma conditions

are not suited since this would affect the photoresist adversely. The absence of oxygen-related groups at the edge has also been reported in other occasions, e.g. at the graphene edge under inert high vacuum conditions. Hence, it can be concluded that the patterned edge is most likely predominantly hydrogen terminated, with a rather low density of other functionalities.

6.3 Electrodeposition with Pt and Pd NPs

Graphene edge with platinum NPs (GrEdge-PtNPs) For PtNPs, the precursor salt $H_2(PtCl_6)$ (0.1 mM) containing Pt^{2+} ions in 0.1 M $LiClO_4$ electrolyte solution was used. Similar to AuNPs deposition, the PtNPs are also deposited via chronoamperometry, where the Pt^{4+} ions are reduced to Pt^0 at GrEdge by application of constant potential of -0.4 V for two 10 s pulses as shown in figure 6.12a. The presence of the deposited Pt particles exclusively at the GrEdge is confirmed by the AFM, optical and backscattered electron SEM images. AFM height map shows the increased relative height only at the edge. From the line profile, the size/height of the particles at the edge was found to be $\sim$ 90 nm and the relative height in graphene basal plane region is $\sim$ 1 nm Si/SiO_2 confirming the single sheet of graphene. The optical images are acquired for larger areas, and shows the nanowire like structure with continuous and homogeneous particles all along the edge, while in the basal plane region, the graphene cracks and domains are clearly visible. The clear contrast at the edge in the backscattered electron SEM image is due to PtNPs at the edge. Further the EDX map shows the selected Pt M specific intensities only at the edge location (blue line).

Graphene edge with Palladium NPs (GrEdge-PdNPs:) For PdNPs, chronoamperometry was used with 100 µM $Na_2(PdCl_4)$ precursor salt containing Pd^{2+} ions in 0.1 M $LiClO_4$. The Pd^{2+} ions are reduced to Pd^0 by the application of -0.2 V potential (for 15 s), resulting in deposition of PdNPs at the GrEdge. The modified GrEdge was later characterized by AFM and optical microscopy (figure 6.13), confirming the presence of the PdNPs at the GrEdge.

The above two examples of PtNPs and PdNPs, confirms the versatality of the approach. Both GrEdge-PtNPs and GrEdge-PdNPs electrodes, given the excellent catalytic properties of Pt and Pd, will be pursued for further studies on their electrocatalytic properties in future.

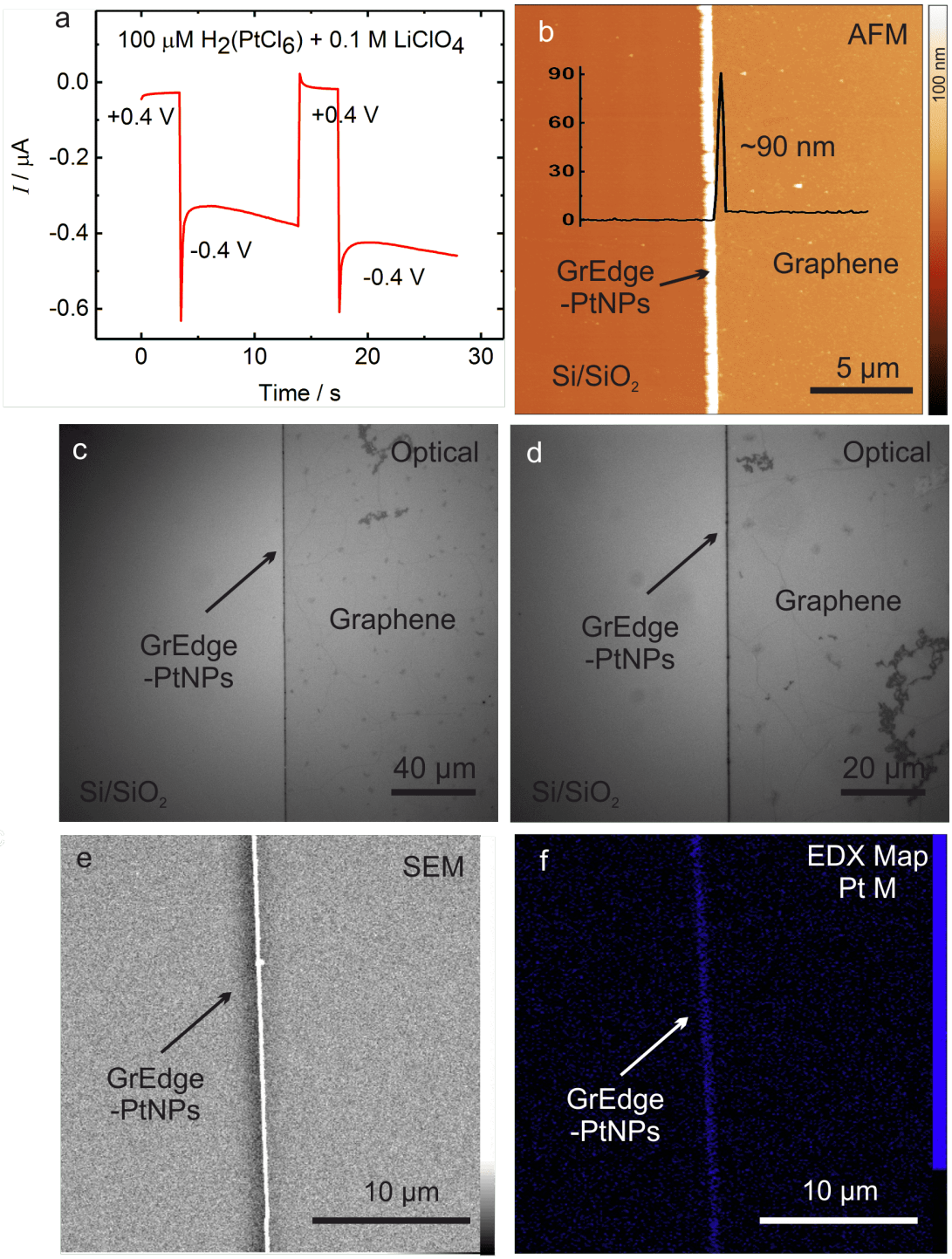

Figure 6.12: (a) Chronoamperometric profile for the potentiostatic deposition of Pt-NPs at a GrEdge electrode with 100 µM $H_2(PtCl_6)$ (Supporting electrolyte: 0.1 M $LiClO_4$). (b) AFM images of the free and modified edge with AuNPs after removal of PR, along with line profiles showing the height at the edge. (c,d) Optical images showing the GrEdge decorated with AuNPs.(e) SEM image showing the modified GrEdge with AuNPs. (f) Au EDX map (obtained by integrating intensity of Au Mα line) of the sample, showing AuNPs only at the edge. Note: the PR has been removed in b-f to obtain the AFM, optical, SEM and EDX images.

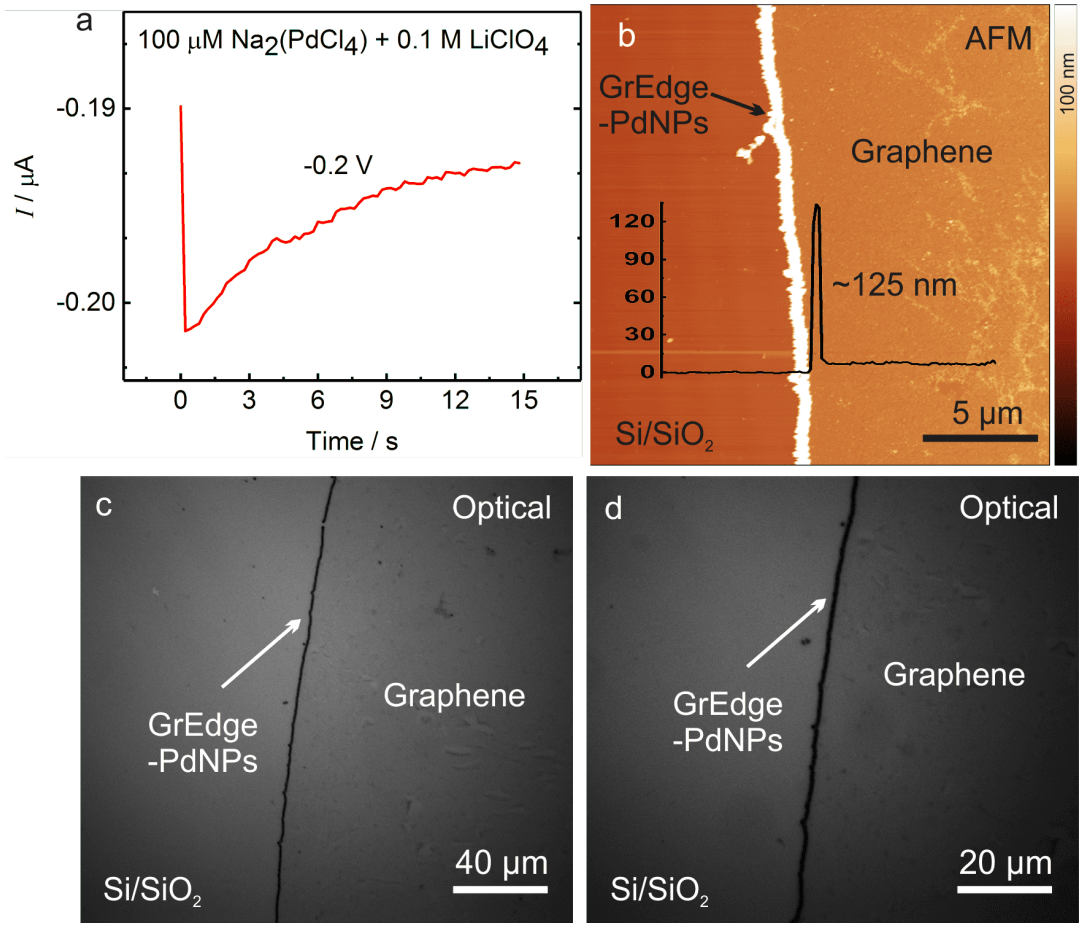

Figure 6.13: (a) Chronoamperometric profile for the potentiostatic deposition of PdNPs at a GrEdge electrode with 100 µM $Na_2(PdCl_4)$ (Supporting electrolyte: 0.1 M $LiClO_4$). (b) AFM image of the modified edge with PdNPs after removal of PR, along with line profiles showing the height at the edge. (c,d) Optical images showing the GrEdge decorated with AuNPs. Note: the PR has been removed in b-d to obtain the AFM and optical images.

6.4 Electropolymerization (Non-Covalent)

A primary challenge after functionalization is the identification of the chemical nature of the attached moieties at the nanoscale level. It was shown earlier in this thesis for two examples (to identify NB groups on graphene modified with NB groups in section 4.4.2, as well as oxygenated carbon groups at oxidized edges of graphene in section 10.1) that the attachment of AuNPs on modified graphene or GrEdge can result in identification of characteristic vibrational modes of the molecules via SERS effect (AuNPs act as local hotspots to enhance the intensity of Raman signals). In this section, a similar strategy of vibrational fingerprinting of functional groups that are attached exclusively to GrEdge was employed by decorating modified GrEdge with AuNPs.

GrEdge-pABA-AuNPs: GrEdge modified with aminobenzylamine, followed by AuNPs For this purpose, the GrEdge was functionalized with 4-aminobenzylamine (4-ABA) through oxidative electropolymerization, followed by the deposition of the AuNPs.[233] 4-AbA is a common functional moiety and have been used very often in functionalization of graphene (see section 4.3) and CNTs.[49,213,216] The poly-4-aminobenzylamine (pABA) modified edge is referred to as GrEdge-pABA electrode, and the final edge after the subsequent deposition of AuNPs is referred as GrEdge-pABA-AuNP. The deposition of 4-ABA is driven by HET reaction between the 4-ABA species in solution and GrEdge electrode, which promotes the irreversible oxidation of 4-ABA. This leads to formation of a polymer pABA containing oligomers of varying chain length[214] at the GrEdge. The stepwise functionalization approach for the preparation of GrEdge-pABA-AuNP electrode is demonstrated in the schematic in figure 6.14a. Figure 6.14b illustrates the chemical structure of the 4-ABA (monomer) and its polymeric form pABA.

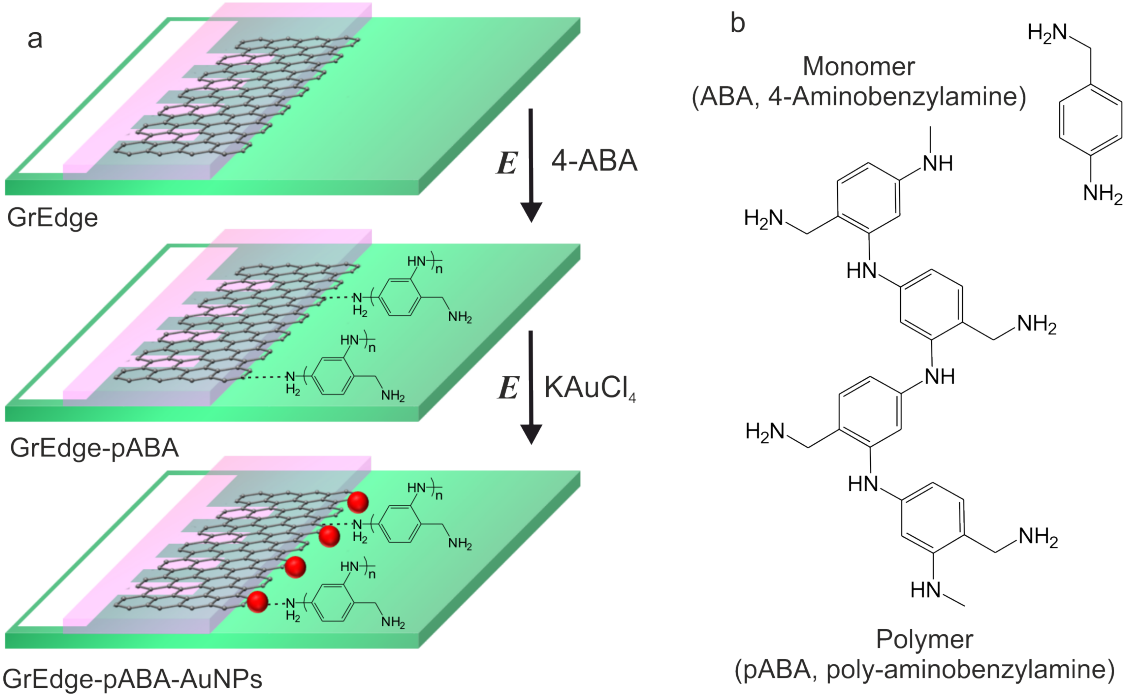

Figure 6.14: (a) Stepwise schematic of the pABA and subsequent AuNP functionalization at the GrEdge electrode. (b) The chemical structures of: 4-aminobenzylamine (ABA) monomer and poly-4-aminobenzylamine (pABA) polymer.

To prepare the desired electrode, the bare GrEdge electrode was subjected to electropolymerization of 4-ABA through oxidative coupling approach (similar to basal plane electrodes in section 4.3). For this, the potential was applied in range of -0.2 to 0.8 V (Vs Ag/AgCl) at the GrEdge (WE) in an aqueous solution of 5 mM 4-ABA in 0.1 M $LiClO_4$ (figure 6.15a). The decrease in current in the 2nd cycle in comparison to 1st cycle of CV may be attributed to the slight increase in charge transfer resistance. The passivation with an organic layer tends to decrease the catalytic activity of the GrEdge, thereby, increasing the resistance as seen in 2nd cycle of CV. This is indicative of the presence of the pABA coating at the

GrEdge. The AFM (figure 6.15b) image along with the line profile measured after the modification and removal of the PR clearly shows the increase in thickness of $\sim$ 2 - 3 nm at the GrEdge. Further, in order to characterize the attached pABA functional groups using SERS, the GrEdge-pABA is modified with AuNPs.

The deposition of AuNPs at pABA modified GrEdge is possible since the polymer layer does not block ET completely between the electrode and the solution.[51] Therefore, it is still feasible to functionalize the already modified GrEdge-pABA, by reducing the Au^{3+} species in solution. Figure 6.15c shows a typical double step potential chronoamperometric profile, for the deposition of AuNPs at the GrEdge-pABA electrode. The presence of particles is confirmed by the AFM image of GrEdge-pABA-AuNPs sample along with the line profile as illustrated in figure 6.15d. The AuNPs size at the GrEdge-pABA-AuNP electrode is found to be bigger than at the GrEdge-AuNP electrode (for the same deposition parameters). This can be because of some kind of interaction between the Au^{3+} ions in the solution and NH_2 groups at the GrEdge, facilitating the deposition. The deposition of AuNPs will enhance the Raman signals of the pABA attached at the edge through surface enhancement.

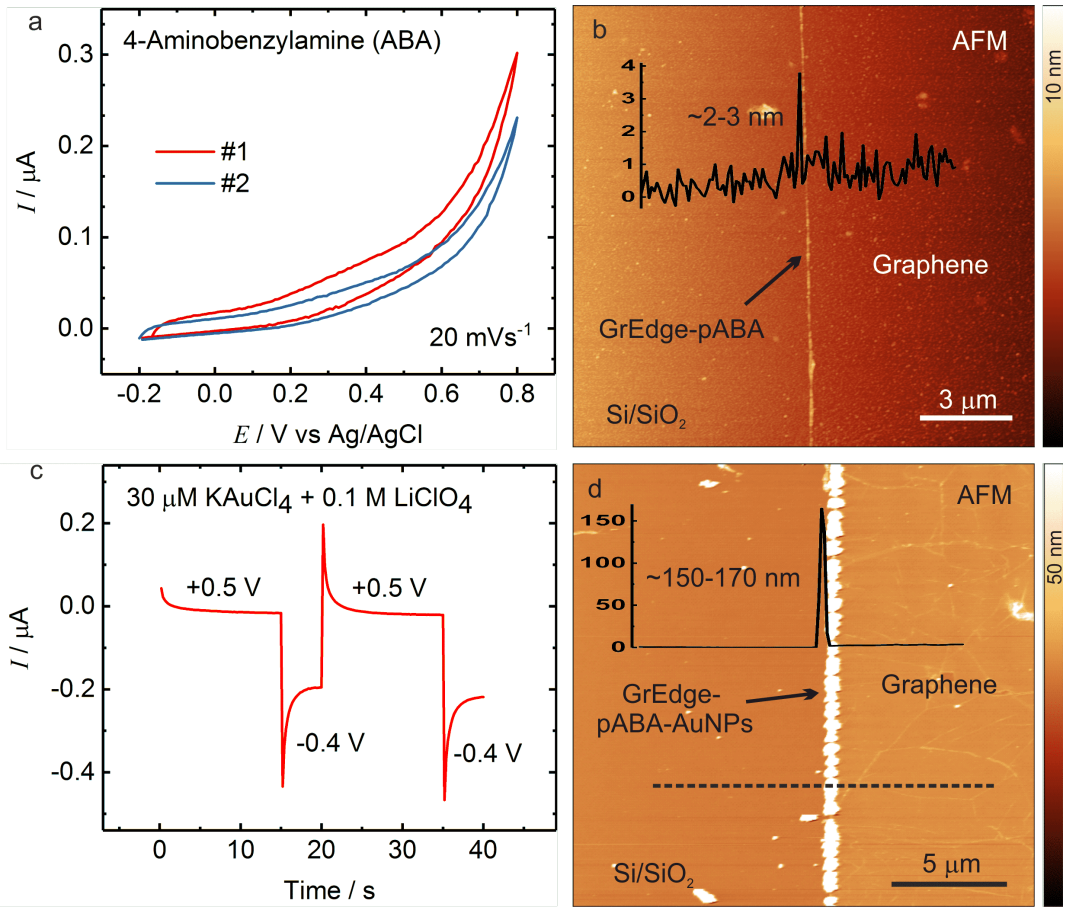

Figure 6.15: (a) CV of 5 mM ABA in 0.1 M $LiClO_4$ at the GrEdge elctrode. (b) AFM image of the edge after its functionalization with pABA, (GrEdge-pABA) (c) Chronoamperometric profile for the deposition of AuNPs at pABA modified edge. (d) AFM image of a GrEdge functionalized with pABA and AuNPs, referred to as GrEdge-pABA-AuNPs.

Raman Spectroscopy Figure 6.16a presents typical Raman spectra at the functionalized GrEdge before (red curve) and after (blue curve) attachment of AuNPs. The spectrum of GrEdge-pABA-AuNPs shows new peaks in addition to the graphene-related peaks, which are assigned to the vibrational fingerprint of the pABA layer. The negligible change in *D*-peak intensity in the red spectrum indicates that pABA is non-covalently attached to GrEdge, consistent with reports on the oxidative coupling of substituted anilines (such as ABA) on CNTs,[49,213] and the graphene basal plane (chapter 4).[51,216] This is also supported by the subsequent ability of the GrEdge-pABA to undergo ET to obtain the AuNPs.

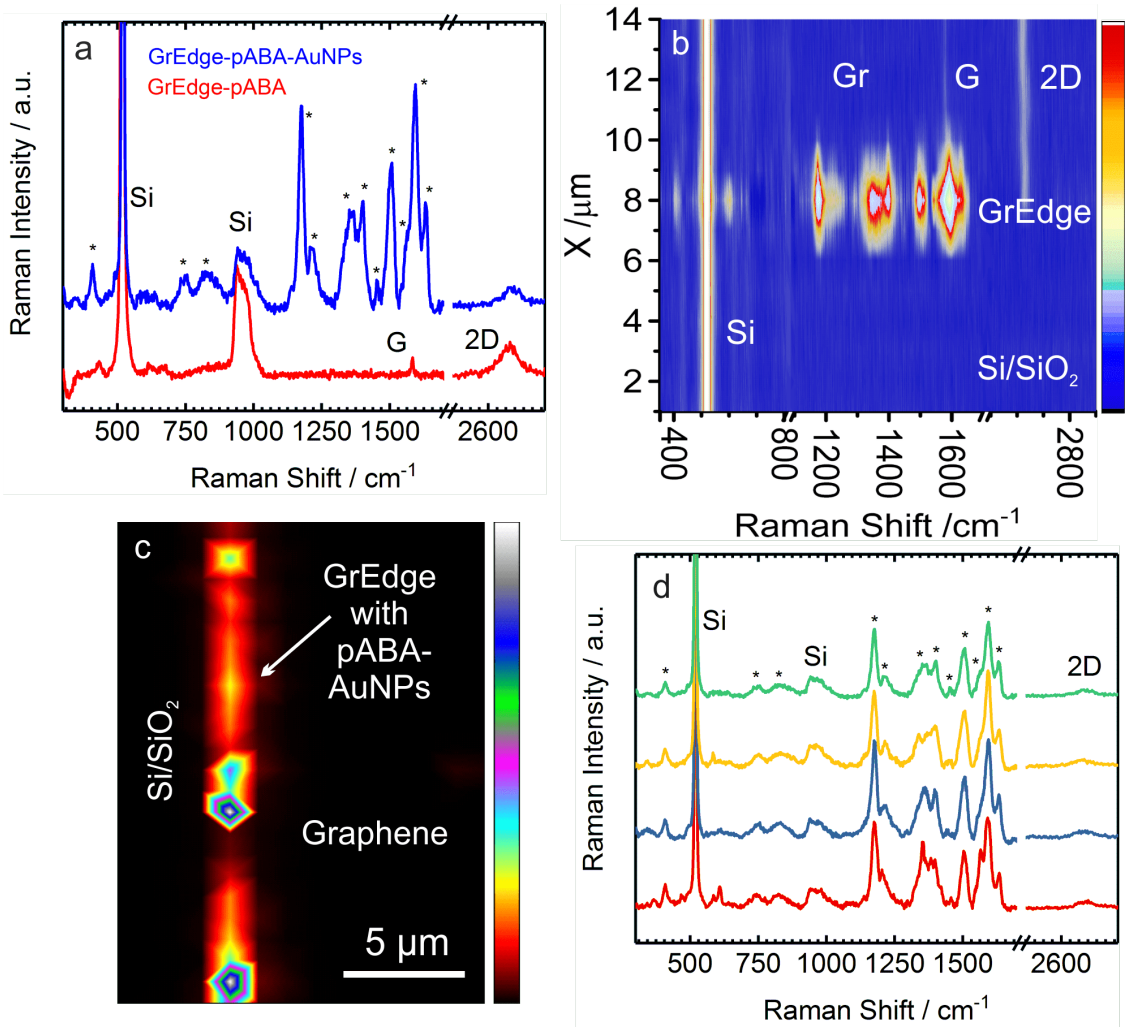

Figure 6.16: (a) Comparison of the Raman spectra at GrEdge-pABA (red curve) and GrEdge-pABA-AuNPs (blue curve). (b) Raman map along the line shown in figure 6.15d. (c) Map of the C−N stretching mode (1358 cm^{-1}) of the same region as in figure 6.15d. (d) Raman spectra at GrEdge-pABA-AuNPs for four different electrodes. (λ_{ex}: 633 nm, 3.4 mW, 2 × 1 s)

Table 6.3 presents the assigned Raman modes for the peaks observed commonly in the spectra recorded at many positions on several samples (figure 6.16). The Raman modes of pABA have some similarity with that of polyaniline due to the similarity in their chemical structure.[51,249,250] The mode at 1632 cm^{-1} is assigned to NH_2 deformation characteristic of

primary amine group,[251] while the modes at 1593 and 1566 cm^{-1} are due to C−C/C=C ring stretching of the benzenoid form.[252] The two bands at 1358 and 1399 cm^{-1} is attributed to C−N stretch.[253] The mode at 1175 cm^{-1} is due to C−H bending. The band at around 1504 cm^{-1}, arises from aromatic C−C stretching and a mode in low frequency region at 409 cm^{-1} is assigned to C−N−C bending of amines. The remaining modes at 1137 and 1214 cm^{-1}, which are assigned to C−N stretch and C−C−N bending, may arise due to the free NH_2 group, which is not participating in polymerization reaction.[251] These characteristics of the Raman spectra of pABA confirm its formation at the GrEdge. A Raman map along a cross-section across the edge is shown in figure 6.16c, where it is apparent that the pABA modes are found exclusively at the edge. This is further confirmed by the Raman map of the C−N stretching mode, as shown in figure 6.16d. The spots corresponding to the vibrational modes of the pABA layer appears to be elongated since the signals are convoluted by the diffraction-limited spot and the size of the AuNPs.

Table 6.3: Assignment of peaks in the spectra of GrEdge-pABA-AuNPs to the vibrational modes of poly-4-aminobenzylamine.

Raman shift, (± 2 cm^{-1})	Assigned peaks
1632	NH_2 deformation
1593	C=C ring stretch
1566	C−C ring stretch
1504	C−C ring stretch
1453	CH_2 scissor vibration
1400	C−N stretch
1358	C−N stretch
1214	C−C−N bending
1175	C−H bending
1137	C−N stretch
825	C−H wag
744	C−N out of plane deformation
409	C−N−C bending

6.5 Diazonium Chemistry (Covalent)

The chemical functionalization of graphene using diazonium chemistry is the most common way for the covalent attachment of a range of chemical moieties on graphene basal plane (chapter 4).[6,127] This section demonstrates the capability of modifying the GrEdge electrodes using covalent functionalization via ECM. It further investigates the influence of the aryl groups introduced by such functionalization on ET at the GrEdge electrode. For this, 4-nitrobenzene (NB) diazonium tetrafluoroborate was chosen as a diazonium salt for electrografting at the GrEdge.

GrEdge functionalization with 4-nitrobenzene: GrEdge-NB A schematic of the ECM strategy is shown in figure 6.17a. The electrografting of 4-nitrobenzene (NB) at the GrEdge (WE) was carried out using 1 mM 4-NB diazonium tetrafluoroborate salt dissolved in a solution of 0.1 M $LiClO_4$. The NB aryl radicals were generated through the electroreduction of NB diazonium ions at bare GrEdge electrode, by applying potential in a given voltage range through CV (figure 6.17b). It is expected that, consequently, the NB aryl radicals bind selectively to the edges of graphene in a covalent manner, since the basal plane surface of graphene remains passivated by PR. Next, the functionalization of the GrEdge electrode is investigated using Raman spectroscopy in figure 6.17b. The GrEdge

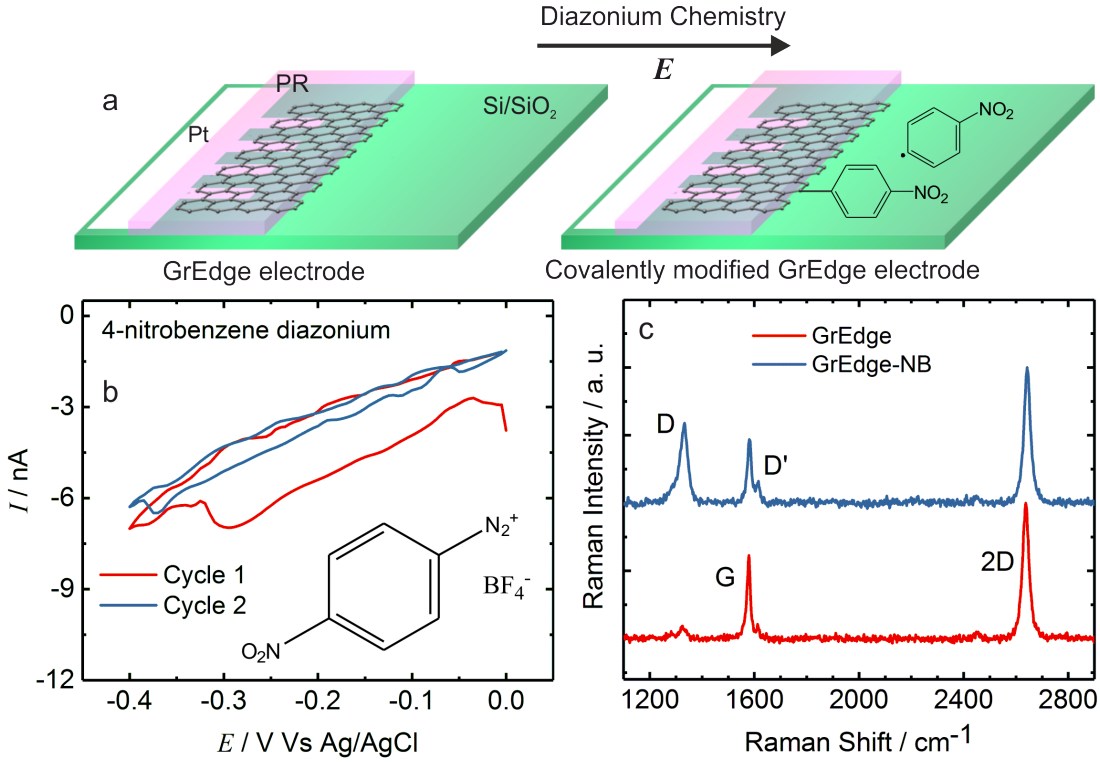

Figure 6.17: (a) A schematic of the ECM strategy for the covalent functionalization of the edge of graphene. (b) CV of the GrEdge electrode in 4-nitrobenzene diazonium in 0.1 M $LiClO_4$ at 20 mV/s. Inset shows the chemical structure of the diazonium salt used. (b) Comparison between the Raman spectra of the GrEdge before (red) and after (blue) electrografting of nitrobenzene (GrEdge-NB). (λ_{ex}: 633 nm, 3.4 mW, 2 × 2 s)

spectra (red) presents a small *D* peak, a signature peak coming from the breakdown of the periodic lattice of graphene by the edges. Upon NB attachment, the *D* peak intensity increases, with the I_D/I_G ratio rising to slightly over 1. The increase in I_D/I_G ratio indicates to higher density and the modification of the sp^3 centers, confirming the covalent functionalization of the GrEdge.

Influence of NB passivation on ET at GrEdge electrode The covalent modification of GrEdge with NB introduces NO_2 moieties at the edge, which can influence the ET at GrEdge electrodes. To study this, an experiment to deposit AuNPs on GrEdge-NB electrode

was performed using chronoamperometry. A typical current profile for AuNPs deposition is shown in inset (top right) of figure 6.18a. The optical, SEM and EDAX map images (figure 6.18a-c) show almost no particles at the GrEdge-NB, with exception of few indicated by the arrows at the edge. This can be explained by taking into account the ET, which may be hampered between the Au^{3+} species and modified GrEdge-NB by attached NB groups at GrEdge electrode, and thereby resulting in no electrodeposition. This is consistent with the results obtained with covalently modified Graphene-NB (Chapter 4), but in contrast to the results acquired in case of GrEdge-AuNPs (bare or non-covalently modified edge) electrode.

For the confirmation of the inhibition of ET, figure 6.18d compares the CV response at the GrEdge electrode in presence of 1 mM FcMeOH in 0.5 M KCl performed before (red curve) and after (blue curve) the electrografting of the NB aryl-radicals. A sigmoidal

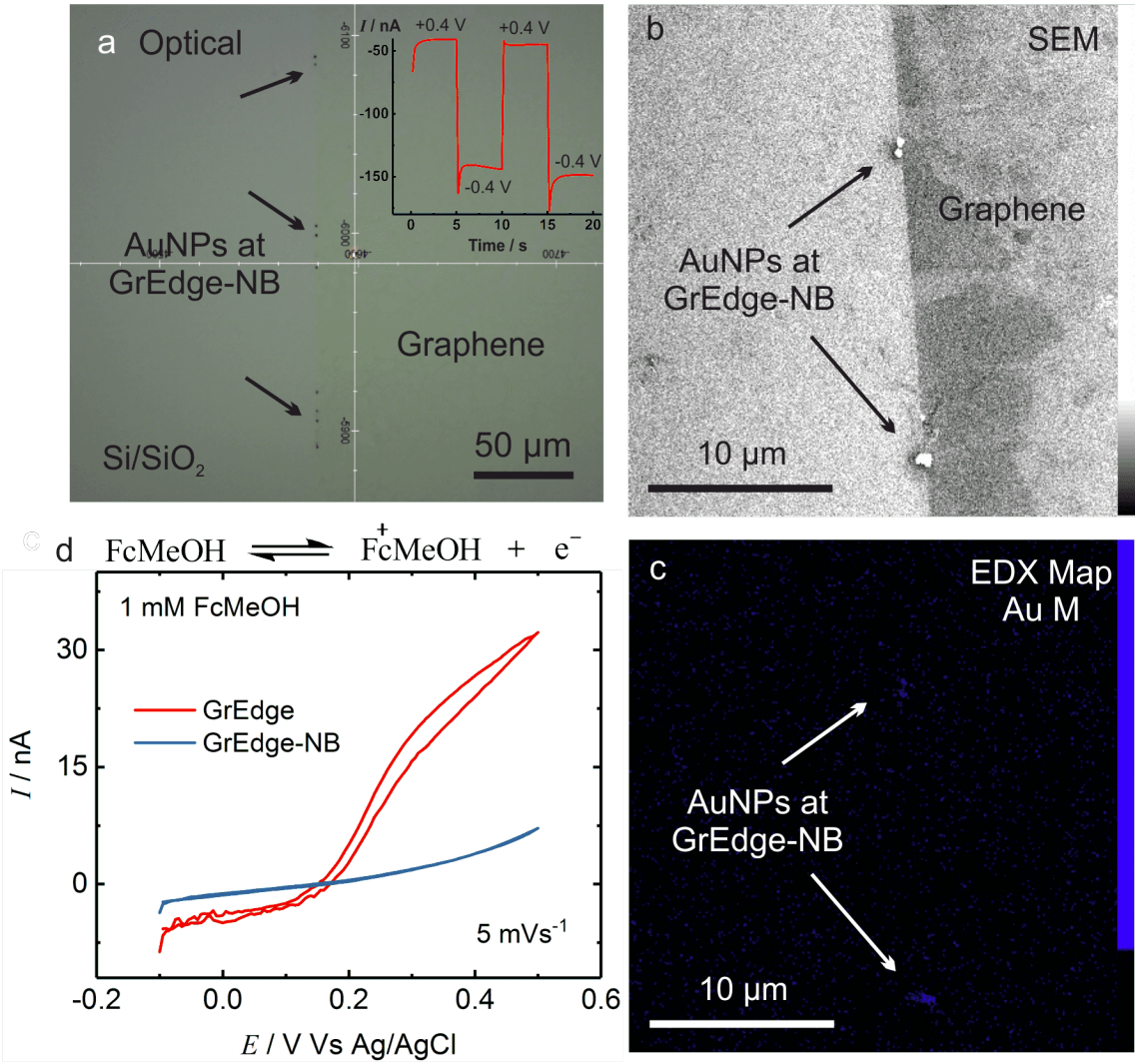

Figure 6.18: (a) Optical image of a GrEdge functionalized with nitrobenzene and AuNPs with arrows pointing to few AuNPs at the NB functionalized GrEdge (inset shows the chronoamperometric profile for Au deposition is shown in the top right corner). (b) and (c) are SEM and Au EDX map (obtained by integrating intensity of Au Mα line) images of GrEdge-NB functionalized with AuNPs. (d) CV for the oxidation of 1 mM FcMeOH (in 0.5 M KCl) at GrEdge (red) and GrEdge-NB (blue) electrodes.

response and quasi-steady-state ($E > +0.3$ V), characteristic of nanoelectrodes (or UMEs), with very little hysteresis is observed for the bare GrEdge electrode. While for the GrEdge-NB electrode, the current decreases with no presence of quasi-steady-state. This is a direct evidence of the suppression of the ET and confirms the presence of an insulating NB passivation layer at the GrEdge.

6.6 Summary

In conclusion, selectively functionalized monolayer graphene edges were realized for the first time, using the strategy of electrochemical modification with different chemical moieties: metal nanoparticles (Au, Pt, and Pd) by electrodeposition, aromatic amino groups by electropolymerization (non-covalent), and aryl groups by diazonium chemistry (covalent). The identification of the chemical groups attached at the modified GrEdge was corroborated by local vibrational fingerprinting using surface-enhanced Raman scattering (SERS) after the attchment of gold nanoparticles. The attachment of different chemical moieties can be helpful in tuning the nanoscale interface and systematically studying its effect on the ensuing physical and chemical properties. The metal nanoparticle deposition enhances the catalytic properties of the edge and have implications in electrocatalysis. The functional groups may also serve as anchor molecules or layers for the subsequent coupling of suitable receptor molecules specific for a certain analyte in sensing devices based on graphene edges.

7

Electrochemistry at the Graphene Edge Nanoelectrodes

The results of the experiments presented here were published in the following manuscript: A Yadav, M Wehrhold, T J Neubert, R M Iost and K Balasubramanian Fast Electron Transfer Kinetics at an Isolated Graphene Edge Nanoelectrode with and without Nanoparticles: Implications for Sensing Electroactive Species. *ACS Appl. Nano Mater. 2020, 3, 12, 11725*.

The electrochemistry of monolayer graphene electrodes has been studied in detail on several occasions earlier.[8,70,167] A good understanding of the electron transfer (ET) properties at the graphene-electrolyte interface in detail, is essential in order for its use in research areas of sensors, batteries, fuel cells, etc. It has often been observed that the ET kinetics at CVD-grown monolayer graphene electrodes[11,158,167,176] were similar to or worse than that of HOPG,[9,38,80] which has often been explained by the comparatively low density of states at graphene.[169,170] The presence of edge-plane sites was found to increase the ET rates.[1,9,10,66,69] However, scanning electrochemical measurements have shown that high ET rates can also be achieved at the basal plane for inner/outer-sphere redox probes.[171,254] The measured ET rates are very sensitive to the type of graphene, surface chemistry, the preparation method used, aging, and solution pH.[158,170,171,176] More work on the investigation of electrochemistry at an isolated graphene edge may help provide further clarification on the comparative heterogeneous electron transfer (HET) behavior between the edge and the basal plane.

Another motivation for realizing isolated graphene edge electrodes is a possible application to study fast ET kinetics, as has been demonstrated with other nanoelectrodes such as single nanotubes and nanoparticles.[30–32] Nanoscale electrochemistry is critically important in many key research areas, such as catalysis, sensor development, and energy conversion and

storage because of their advantages in providing unique information which is unattainable using traditional methods. For example, the development of new kinds of nanoelectrodes may accelerate the study of fast ET processes that are often too fast to investigate with conventional electrodes and electrochemistry in poorly conducting organic solvents.[71,72] The graphene edge may be considered as an ideal one-dimensional system and is the thinnest wire electrode[28,29] that one could realize. Hence, it may be expected that the electrochemistry at such electrodes is unique. However, in many of the reports until now, the observed CV profiles have shown diffusion-limited response without indication of (quasi)-steady-state behavior.[12,33] Moreover, there is still no report about values of ET rates at an isolated graphene edge. By comparison, at one-dimensional electrodes, namely at individual carbon nanotubes the electrochemistry was found to be kinetically limited,[34,35] with a high mass transport rate and has allowed the probing of fast electrode kinetics (ET rate more than 1 cm/s for a ferrocene species).[30]

In this chapter, electrochemistry at an isolated graphene edge is investigated systematically, with carefully prepared devices. The following aspects of graphene edges (unmodified and modified with AuNPs) are presented: properties in terms of current response, capacitance, change in the critical size of graphene edge and their comparison to graphene basal plane electrodes; theory and experiments to extract the kinetic parameters (standard heterogeneous rate constant k^0 and transfer coefficient α), for better understanding of electron and mass transfer at such nanoelectrodes.

Another important area of interest is the effect of modification of the graphene edge on its electrochemical properties. Nanoparticles have been shown to impart electrocatalytic properties to different kinds of carbon electrodes.[30,129,130] Until now, there is only one demonstration of the electrochemistry of modified single graphene edge electrodes with nanoparticles, which showed a lower onset potential for the reduction of oxygen and could be used for realizing glucose sensors.[149] In chapter 6, metal nanoparticle decoration is demonstrated to prove the availability of a pristine graphene edge, which also allows for surface-enhanced Raman spectroscopic investigation of chemical functionalities at the edge.[233] The analysis of the voltammetric behavior at the GrEdge-AuNP electrode provides a better understanding of the unique HET behavior observed at unmodified GrEdge electrodes.

7.1 Properties of Edge Electrodes

The isolated edge electrodes for electrochemical studies are prepared as demonstrated in chapters 5 and 6. However, instead of S1805, only a negative PR SU-8 is used in the fabrication process, because the passivation obtained with SU-8 is more robust, with better adhesion and slower aging of the GrEdge samples in comparison to S1805 (see figure 5.11 in section 5.3.5). Firstly, the electrochemical behavior at single-layer graphene-based electrodes is studied, comparing the graphene basal plane to its edge. After this, the bare edge was modified with AuNPs, and in this manner, two different classes of edge electrodes are obtained:

- Free / unmodified graphene edge called 'GrEdge'
- Gold nanoparticles modified graphene edge called 'GrEdge-AuNPs'

The characterization of deposited Au at the edge was done using an electrochemical method, without the removal of the PR. In the further sections, studies such as capacitance, the influence of supporting electrolyte concentration, scan rate dependence, HET rates have been carried out at both the GrEdge and GrEdge-AuNP electrodes.

7.1.1 Graphene Edge Vs Graphene Basal Plane

The electrochemical behavior at graphene basal plane is believed to be different from that at its edge due to the differences in their chemical structure. For this, the electrochemical properties of the GrEdge (1 nm $\times$ 2 mm) and basal plane electrode (2 mm $\times$ 2 mm) interfaces were investigated using different standard redox probes: FeMeOH, $Ru(NH_3)_6^{3+}$, $Fe(CN)_6^{3-}$, and $IrCl_6^{2-}$, with differing potentials.

Graphene Basal Plane Figure 7.1 compares the CV curves for the oxidation of FcMeOH in 0.5 M KCl measured at the edge and basal plane electrodes. The basal plane electrode (figure 7.1a) shows a wave-shaped voltammogram with the oxidation and reduction peaks of FcMeOH. This behavior can be explained by considering the basal plane electrode as a conventional electrode, because of its millimeter-scale dimensions. The shape of voltammograms is defined by the rate of mass transport (diffusion). The diffusion layer thickness is much bigger for macroelectrode, therefore, the mass transport occurs perpendicular to the electrode surface, known as planar or linear diffusion. At the electrode interface, the concentration of redox species also changes with the HET. The redox species take a longer time to diffuse, hence, the current changes with time, and typical peak-shaped voltammograms are obtained. The oxidation (E_{pa}, anodic potential) and reduction peaks (E_{pc}, cathodic potential) are at 0.26 V and 0.16 V, respectively. The peak-to-peak separation or peak spacing (ΔE_{pp}) value is $\sim$ 100 mV. The obtained values are in agreement with previous

observations at graphene basal plane electrodes.[158] For a typical reversible redox process, the peak current at a planar electrode follows Randles-Ševčík equation given by,[180]

$$i_p = (2.69 \times 10^5) n^{3/2} C^* D^{1/2} v^{1/2} \tag{7.1}$$

where i_p is the peak current density (A/cm^2), n is the number of electrons transferred in the redox reaction, D is the diffusion coefficient (cm^2/s) of the electroactive species, C^* is the the bulk concentration of the electroactive species and v is the scan rate (V/s). Therefore, the peak current varies linearly with the concentration, as shown in figure 7.1c.

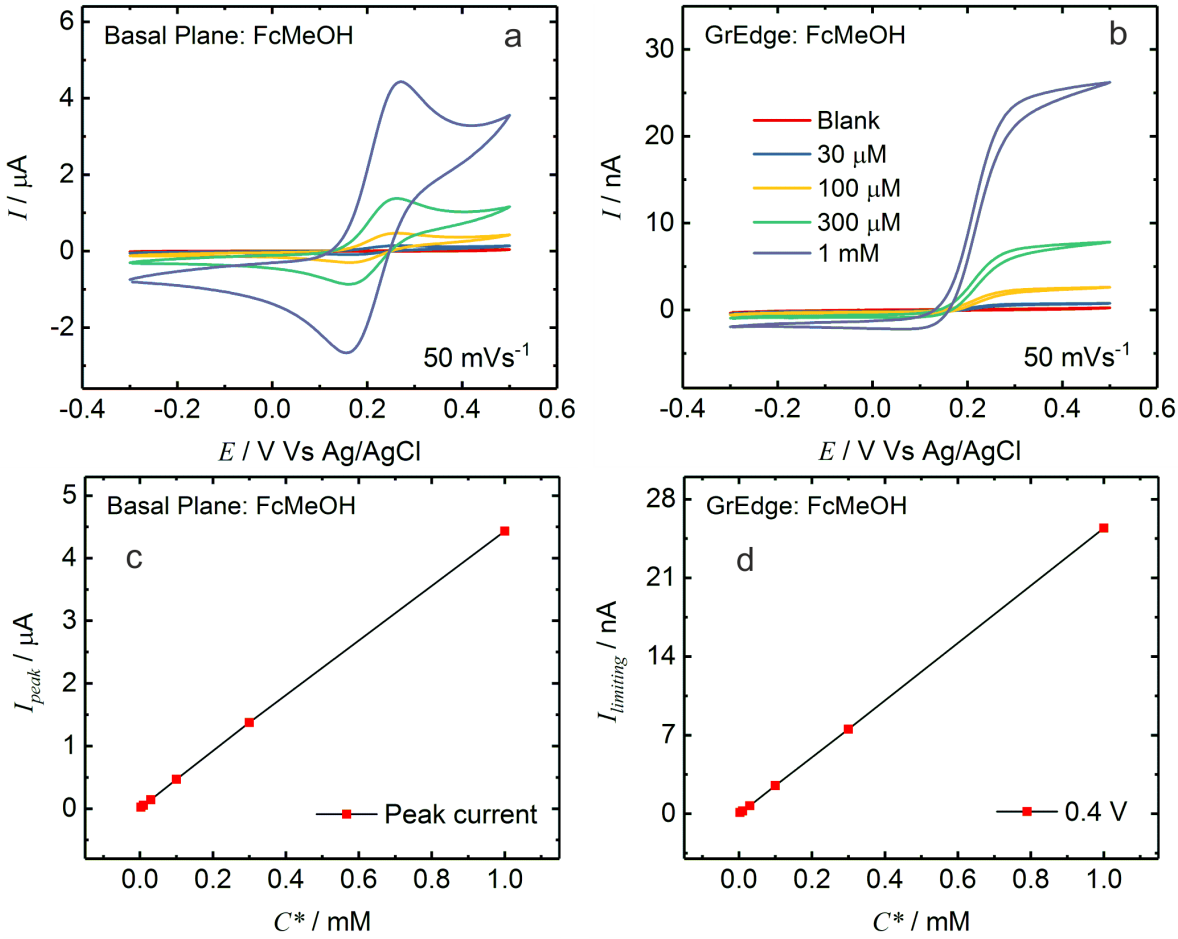

Figure 7.1: (a,b) CVs for the oxidation of FcMeOH (with different concentrations) at the (a) graphene basal plane, and (b) edge electrodes. (c) Plot of peak current currents vs concentration obtained from (a) showing a linear dependence. (d) Plot of limiting currents vs concentration obtained from (b) showing a linear dependence. (Supporting electrolyte: 0.5 M KCl)

Graphene Edge On the other hand, in the case of the GrEdge electrode, a well-defined sigmoidal-shaped voltammogram is obtained for FcMeOH oxidation in figure 7.1b. This type of CV curve is characteristic of steady-state behavior at nanoelectrodes (and UMEs),[180] and can be attributed to the convergent diffusion at the electrode. This diffusion can be

assumed of a hemicylindrical form, because of the quarter-cylindrical geometry of the edge electrode.[255] The convergent diffusion results in faster mass transport, and finally leads to a time-independent process, where the obtained current reaches a plateau. The current obtained at the plateau is called steady-state current (i_{ss}) or limiting current. The small hysteresis (shift in half-wave potential) between the forward and reverse waves are indicative of a slight departure from a true steady-state response and can be due to the high scan rate of 50 mVs^{-1}. However, the electrode in this case, exhibits a sigmoidal shape even at a high scan rate of 50 mVs^{-1}. A slow scan rate (such as 5 mVs^{-1}) is preferred for this behavior since a convergent diffusion mode is dominating at slow scan rates.[256] The diffusion-controlled steady-state or limiting current, i_{ss} or $i_{limiting}$, at a nanoelectrode and UME for any geometry is given by:

$$i_{ss} = nFAmC^* \tag{7.2}$$

where F is Faraday constant, A is area of the electrode, m is mass transport coefficient whose functional form depends on the geometry of the electrode and C^* is the concentration of the redox probe. For a cylindrical geometry, the above equation be re-written as:

$$i_{cylinder} = \frac{2nFADC^*}{r \ln \tau}$$

where $\tau = 4Dt/r^2$ and r is the radius of the cylinder. By this equation, current depends on time, and the steady-state deviates from the true steady state. However, time dependence appears only as an inverse logarithmic function, and current declines rather slowly in the long time limit. Therefore, the current obtained can still be used experimentally in the same way as nanoelectrodes of other geometries such as a sphere or a disk, which provide a perfect steady-state. In literature, this case of steady-state is referred to as quasi-steady-state. The time dependence also explains the obtained non-ideal steady-state for the GrEdge electrode, as the current in the plateau region ($E > +0.3$ V) is not constant and varies slightly as a function of the applied potential. This is also suggestive of a cylindrical-type geometry of the edge. This quasi-steady-state response is an indication for an electrode with nanoscale dimensions, which is consistent with previous measurements at nanosized electrodes and scanning electrochemical microscopy data.[35,244] The linear dependence between quasi-steady-state current and concentration is apparent in figure 7.1d.

Similar behaviour is obtained for other redox probes at the basal plane and edge electrodes with the exception of $Fe(CN)_6^{3-}$ at the edge electrode as shown in figure 7.2. For the basal plane, the reduction of $Ru(NH_3)_6^{3+}$, $IrCl_6^{2-}$ and $Fe(CN)_6^{3-}$, show peak-shaped voltammograms, which can be attributed to the planar electrode behaviour. The redox peaks of $Ru(NH_3)_6^{3+}$ are at -0.245 and 0.105 V (ΔE_{pp} of 140 mV); $IrCl_6^{2-}$ are 0.69 and 0.795 V (ΔE_{pp} of $\sim$ 100 mV); and $Fe(CN)_6^{3-}$ are at 0.215 and 0.3 V (ΔE_{pp} of 85 mV). For GrEdge electrode, the reduction of $Ru(NH_3)_6^{3+}$ and $IrCl_6^{2-}$ shows a clear quasi-steady-state in $E <$

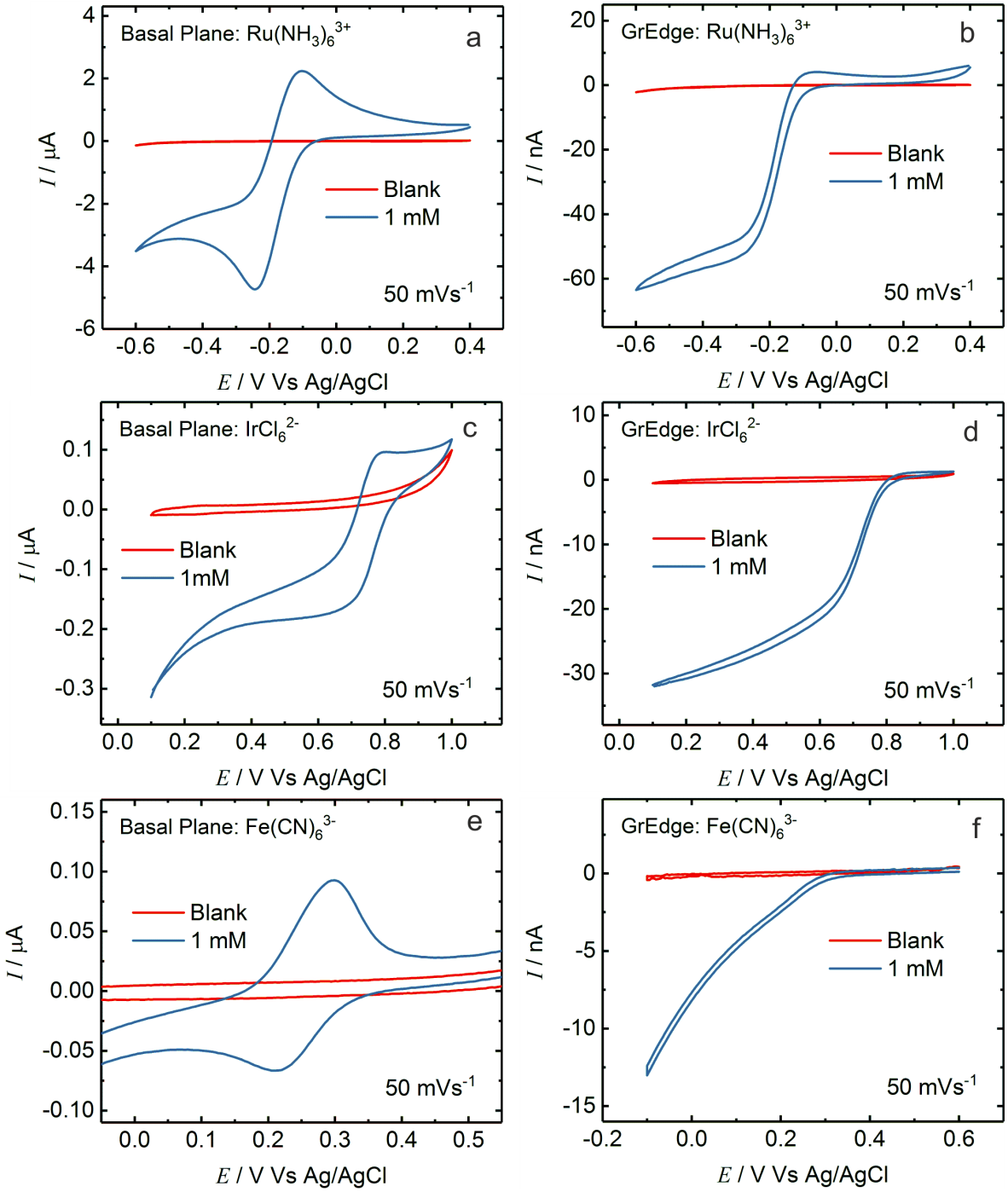

Figure 7.2: CVs for different redox probes:$Ru(NH_3)_6^{3+}$ reduction (a,b); $IrCl_6^{2-}$ (c,d); $Fe(CN)_6^{3-}$ (e,f) at the graphene basal plane (a,c,e) and edge (b,d,f) electrodes. Supporting electrolyte is 0.5 M KCl for all the redox probes.

-0.2 V and $E < +0.7$ V regions, respectively, which are suggestive of the nanoelectrode behaviour. The reduction of $Fe(CN)_6^{3-}$ at GrEdge electrode shows a different behavior with the cathodic current increasing monotonously with the applied potential ($E < +0.3$ V). The absence of a steady-state current for $Fe(CN)_6^{3-}$ is in accordance with the observations at individual CNTs.[34]

7.1.2 Redox Behavior of AuNPs Deposited at the GrEdge

Further, the GrEdge was functionalized with AuNPs to fabricate the GrEdge-AuNPs electrode (chapter 6). However, for its characterization, the techniques such as AFM and SEM cannot be used since SU-8 is a permanent PR, and cannot be removed, without damaging the graphene beneath. Therefore, CV was employed to show the presence of the AuNPs deposited at the edge. For this, CV is performed at GrEdge-AuNP electrode in 1 M H_2SO_4, along with a similar control experiment at the free GrEdge. H_2SO_4 is a common electrolyte to study the anodic behavior of deposited metals such as Au, Pd, Pt, etc.[257] Figure 7.3 shows the comparison of the CV curves obtained at GrEdge and GrEdge-AuNPs. The bottom CV in figure 7.3b at the GrEdge-AuNP electrode shows two regions (A and B) and a reduction peak C, observed in the potential range of 0 to 1.6 V. Region A (0.2 - 0.6 V) of the CV corresponds only to the double layer charging, while region B (0.6 - 1.35 V) is the so-called pre-oxide region after Au oxidation. The shoulder at around 1.4 V corresponds to the formation of Au_2O_3. The cathodic peak at 0.9 V in the reverse scan is from the reduction of Au_2O_3 to Au.[258,259] The observed CV is characteristic for a gold surface and hence confirms the presence of gold at the GrEdge.

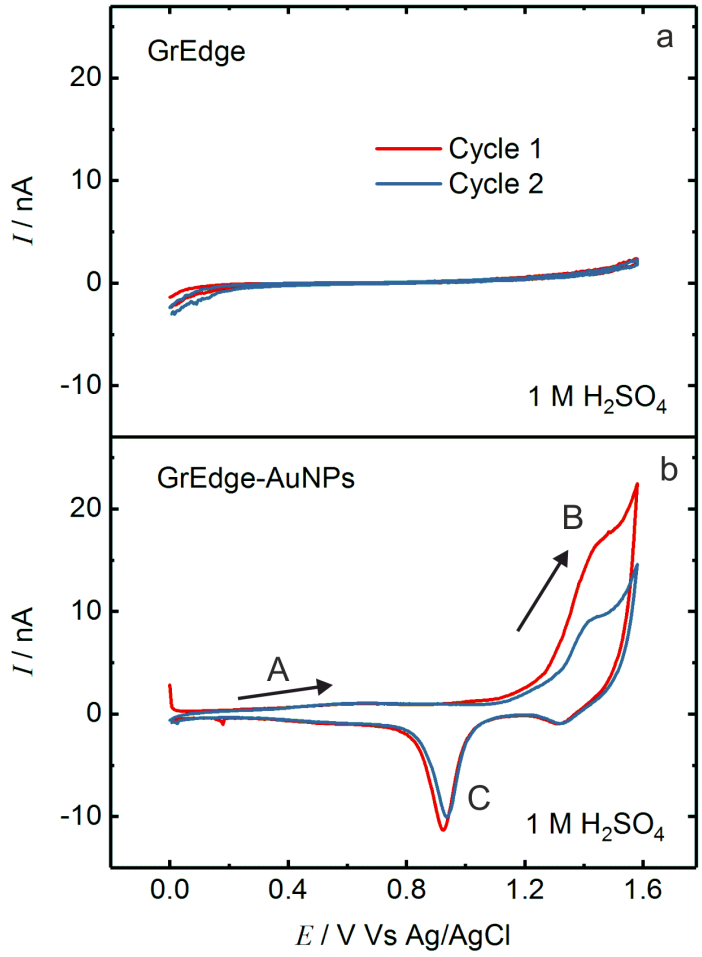

Figure 7.3: CV for the electrochemistry of (a) free GrEdge and (b) GrEdge-AuNPs electrodes in 1 M H_2SO_4.

Area calculation of the graphene basal plane electrodes For graphene basal plane, the area is given according to the geometrical shape of transferred graphene. In most cases, it is in a rectangular form, hence,

$$Area = l \times b$$

where l and b are the length and width of the piece of graphene. Usually, both l and b are somewhere between 0.1 and 0.3 cm. For example, area for a 0.2 cm $\times$ 0.3 cm graphene piece is 0.06 cm^2.

Area calculation of the edge electrodes In order to explain the voltammetric response of both types of nanoelectrodes, the closest models which can be considered are microband and cylinder. However, in the case of a microband model, it is assumed that the band electrode lying on a surface is exposed to the entire solution region above the band. By contrast, the GrEdge is protected on one side (along the length of the edge) by the thick PR layer and hence the microband models cannot be directly applied for this situation. Therefore, the best geometric model which suits the GrEdge electrode geometry is a quarter-cylinder.[255] Hence, a quarter-cylinder is assumed with an apparent radius r, which is $h/4$, where h is the graphene height or thickness (1 nm) for GrEdge electrodes and average NP height for the GrEdge-AuNP electrodes. l is the length of GrEdge. The height of the AuNPs and the length of the edge are obtained from calibrated AFM (as shown in figure 6.5 of chapter 6) and optical images respectively.

$$Area = 2\times\pi\times r\times l = \frac{2\times\pi\times h\times l}{4} \tag{7.3}$$

For example, area of the GrEdge and GrEge-AuNP electrodes with l = 0.23 cm and height of AuNPs, h = 70 nm is:

$$Area(GrEdge) = \frac{2\times\pi\times1\times10^{-7}\times0.23}{4} = 3.61\times10^{-8}\ cm^2$$

$$Area(GrEdge - AuNPs) = \frac{2\times\pi\times70\times10^{-7}\times0.23}{4} = 2.52\times10^{-6}\ cm^2$$

7.1.3 Capacitive Current

When the applied potential is changed, the resulting current flows to charge the double layer capacitance, C_{dl} (electrochemical double layer behaves like an electrolytic capacitor). This process affects the potential at the interface as it does not attain the applied potential value until the charging is complete. Also, the charging and Faradaic currents are not separate at short times. Therefore, it is important to fasten the whole charging process. For an electrode in supporting electrolyte solution that does not contain any electroactive species, a charging current (i_c), required to charge the double layer of capacitance C flows through a total cell resistance R, and their product RC represents the cell time constant. i_c decreases exponentially with time (t) at a rate dictated by RC for a single potential step (ΔE),[180]

$$i_c \propto -exp(-t/RC)$$

This implies that smaller the time constant RC for charging the double layer, faster the process. $R \propto 1/r$, and the capacitance is proportional to the electrode area (or r^2) where r is the size (or radius r) of electrode such that,

$$RC \propto r$$

Therefore, the product RC decreases with decreasing electrode size 'r'. The smaller RC cell time constant of nanoelectrodes means that they respond more rapidly to changes in the applied potential than their macroscopic counterparts. Therefore, the graphene edge electrodes due to their nano-dimensions have an advantage of small capacitance values.

The capacitance of the edge and the basal plane electrodes was studied by CV in an aqueous solution of 0.5 M KCl (pure electrolyte) in the absence of any redox-active species in figure 7.4. At GrEdge electrode, the charging current density value is over 4 orders of magnitude higher than that of the basal plane electrode and 1 order higher than that of

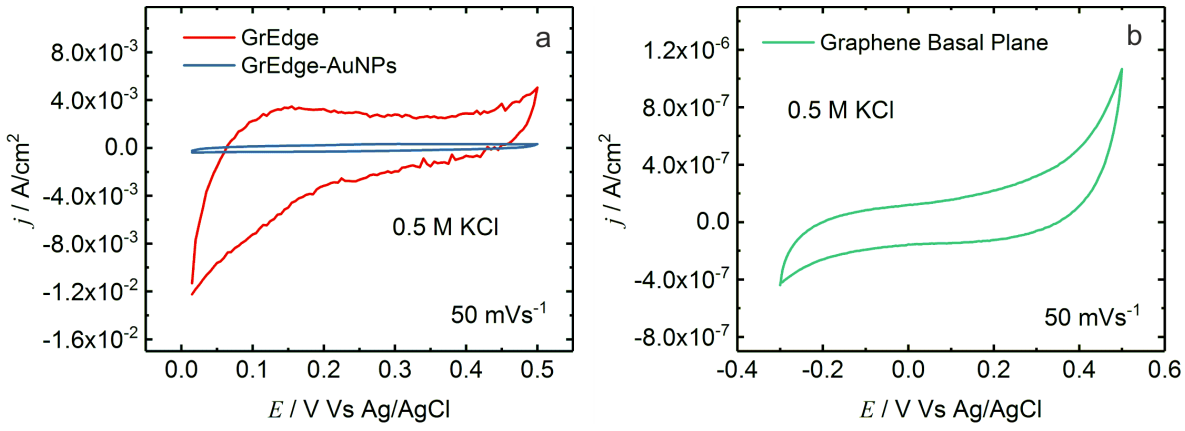

Figure 7.4: Comparison of capacitive current density at graphene edge and basal plane electrodes. (a, b,c) CVs of the GrEdge (a), GrEdge-AuNPs (b) and basal plane (b) electrodes in 0.5 M KCl.

GrEdge-AuNPs electrode. A decrease in size of the macroelectrode (basal plane) from a few millimeter to nanoelectrode (free edge), leads to consequent decrease in the magnitude of the charging current. The approximated specific capacitance (calculated using the charge values obtained by integrating the area under the CV curves) of bare GrEdge, GrEdge-AuNP and basal plane electrodes are 5.4 $\times$ 10^4, 4.4 $\times$ 10^3 and 2.2 µF cm^{-2}, respectively. The high specific capacitance of the edge can be due to the accumulation of ions at the defects to form electrochemical double layer.[260]

Further, the CV experiments containing mainly the charging current i_c were performed in a narrow potential range of 0.0 to 0.2 V in 0.5 M KCl, to compare the same edge with and without AuNPs. The average height of AuNPs at the modified GrEdge is $\sim$ 70 nm,

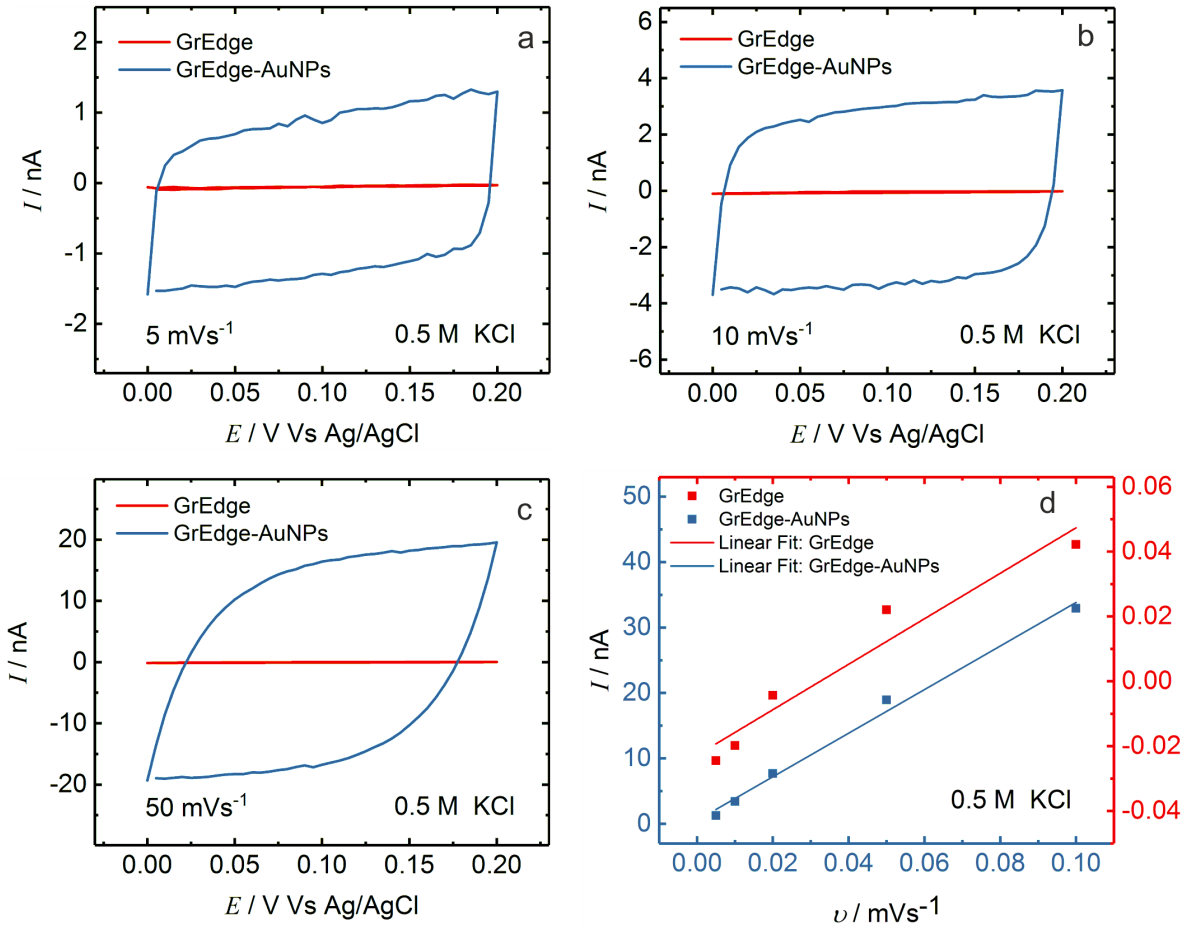

Figure 7.5: (a-c) CVs showing the capacitive charging current in 0.5 M KCl in the absence of any redox active species at three scan rates. (d) A plot of the capactive current at 0.1 V vs. Ag/AgCl as a function of scan rate showing a linear dependence. The slope gives an idea of the interfacial capacitance. red curves: GrEdge, blue Curves: GrEdge-AuNP electrodes

assumed by the calibrated PR S1805 passivated GrEdge-AuNPs sample prepared at the same electrodeposition parameters (AFM images in chapter 6). The rectangular-shaped CVs for both electrodes indicate a pure capacitive behavior as shown in figure 7.5a-c with different scan rates. The value of C_{dl} for GrEdge or GrEdge-AuNP electrodes can be estimated by

the charging current dependence with scan rate ν, given by

$$i_c = C_{dl}\nu$$

where a linear response is expected for an ideal capacitor.[180,261] The assumption of a linear relation between i_c and ν, gives an estimate of C_{dl} (slope) for the two types of electrodes (figure 7.5d). A capacitance value of 0.3 nF and 0.7 µF is extracted for GrEdge and GrEdge-AuNP electrodes, respectively. The low values of C_{dl} for both types of electrodes imply smaller RC cell time constants which means that they respond more rapidly to changes in the applied potential than their macroscopic counterparts like graphene basal plane electrode. This ability to respond to changes in the applied potential at short timescales also makes GrEdge nanoelectrodes attractive for investigating fast ET reactions (section 7.2). The background capacitive current values in the CV curve also give an estimate about the electrochemically active area of the participating electrode.[180,261] Therefore, the increase in absolute values of C_{dl} after the attachment of NPs clearly confirms the increase in surface area of the edge electrodes. Hence, the graphene edge electrodes due to their nano-dimensions have an advantage of small capacitance values.

7.1.4 Steady-State Voltammetry at GrEdge and GrEdge-AuNPs

This section discusses the voltammetric response at the same GrEdge without and with AuNPs using two redox probes, FcMeOH (outer-sphere) and $Fe(CN)_6^{3-}$ (inner-sphere), at a slow scan rate of 5 mVs^{-1} as shown in figure 7.6. To understand the material electrochemically, it is better to employ both the outer- and inner-sphere ET processes, which differ according to the sensitivity of their ET kinetics to the surface chemistry of the electrode. The electrode surface can have defects, impurities, or adsorption sites, which may affect the ET process at their interface.[158] In short, outer-sphere redox probes are not influenced by the surface state, while the inner-sphere probes are influenced by the state of the surface. The GrEdge-AuNPs electrode also provides an aspect to investigate the obtained steady-state voltammograms by varying the size of the AuNPs.

FcMeOH The unmodified GrEdge electrode (figure 7.6a) shows an expected sigmoidal response, characteristic of UMEs and nanoelectrodes, with very little hysteresis for FcMeOH oxidation. The steady-state ($E > +0.3$ V) is not perfectly constant and varies slightly as a function of the applied potential leading to a quasi-steady-state as discussed before. iR-drop and solution resistance effects can be excluded since the magnitude of the current are quite low for such effects to introduce a distortion in the CVs.[35,71] These effects are discussed in the section 7.1.7 under the heading 'ohmic effects'.

For the case of the GrEdge-AuNP electrode (figure 7.6b), a Nernstian (reversible) response with a constant steady-state current is clearly observed, which is in contrast to the

quasi-steady-state obtained at the GrEdge electrode. The limiting current has also increased from 33 nA to 52 nA (taken at -0.4 V) and can be explained by the increase in the area of the edge electrode due to AuNPs deposition. The conditions to the formation of the steady-state differ accordingly due to the change in the critical size of the electrode. For the GrEdge electrode size of 1 nm, the mass transport is very high, due to which the current observed exhibits a quasi-steady-state or a dominantly kinetic response. The increase in critical size at the GrEdge-AuNPs electrode decreases the mass transport of the FcMeOH species, shifting the ET towards a diffusion-controlled process.

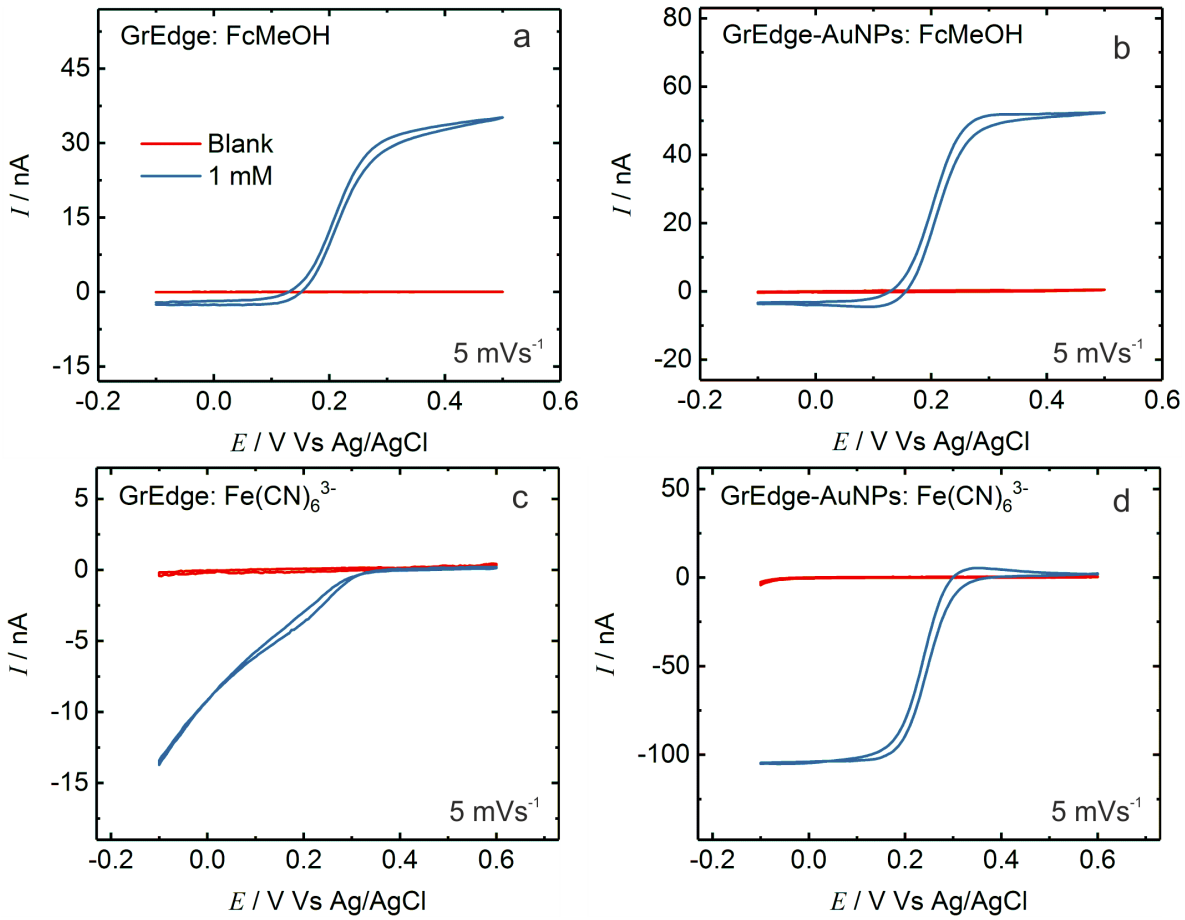

Figure 7.6: CV at a low scan rate of 5 mVs^{-1} at (a, c) GrEdge and (b, d) GrEdge-AuNP electrodes for the redox probes (blue curves): (a, b) 1 mM FcMeOH (oxidation) and (c, d) 1 mM $Fe(CN)_6^{3-}$ (reduction). (Supporting electrolyte: 0.5 M KCl)

$Fe(CN)_6^{3-}$ Figure 7.6c,d shows the voltammetric response for $Fe(CN)_6^{3-}$ reduction at an unmodified GrEdge and a GrEdge-AuNPs electrode, respectively. In a potential range of -0.1 to -0.6 V, the AuNP-modified GrEdge shows a sigmoidal response with a clear steady-state (figure 7.6d), while the unmodified GrEdge shows a peculiar behavior with the cathodic current increasing monotonously with the applied potential ($E < +0.3$ V) (figure 7.6c). A similar response is always observed for $Fe(CN)_6^{3-}$ at other unmodified GrEdge electrodes (in figures 7.2f, 7.7b and 7.11). This kind of distinct behavior for $Fe(CN)_6^{3-}$ reduction at

a similar unmodified GrEdge also shows that the rate of ET across the electrode / solution interface is influenced by the identity of the redox couple. The absence of a steady-state current plateau at the unmodified GrEdge suggests that there is no diffusion limitation and that the ET occurs under kinetic control, analogous to observations at individual CNTs.[34] The small critical dimension of the GrEdge leads to very high rate of mass transport, which may have become larger than the rate of ET, resulting in a deviation from the thermodynamic equilibrium between oxidized and reduced species at the GrEdge electrode surface, thereby departing from the Nernstian limit as seen in 7.6c. Upon addition of AuNPs, the electrode area increases manifold and the behavior becomes similar to that of a UME.[71,72] The voltammetric behaviour at both the electrodes for FcMeOH oxidation and $Fe(CN)_6^{3-}$ reduction are explained in detail in the section 7.2 discussing HET.

7.1.5 Influence of Critical Size on Steady-State Voltammograms

The critical size of the electrode is the most important parameter that distinguishes the nanoelectrode or UME from the conventional sized electrode as has been shown in section 7.1.1. However, the change in critical size at the nanoscale also plays an essential role in the steady-state behavior or shapes of the voltammetric curves as seen in the previous figure 7.6 (section 7.1.4) at nanoelectrodes. Figure 7.7 presents the dependence of the steady-state current and shape characteristics of the voltammetric curve on the critical size (i.e., the height of the GrEdge by varying the size of the AuNPs) for both the redox probes. To avoid the effects of other parameters, an unmodified GrEdge electrode, along with two subsequent modifications with AuNPs are carried out at the same GrEdge electrode. In this way, three different sizes were obtained at the same sample systematically by keeping other parameters (like the length of the edge) constant. For FcMeOH, all the three sizes ($\sim$ 1 nm, $\sim$ 50 nm, and $\sim$ 80 nm) show either a quasi-steady-state or steady-state behavior, with slight changes in the sigmoidal shape. The unmodified GrEdge having 1 nm critical size has the

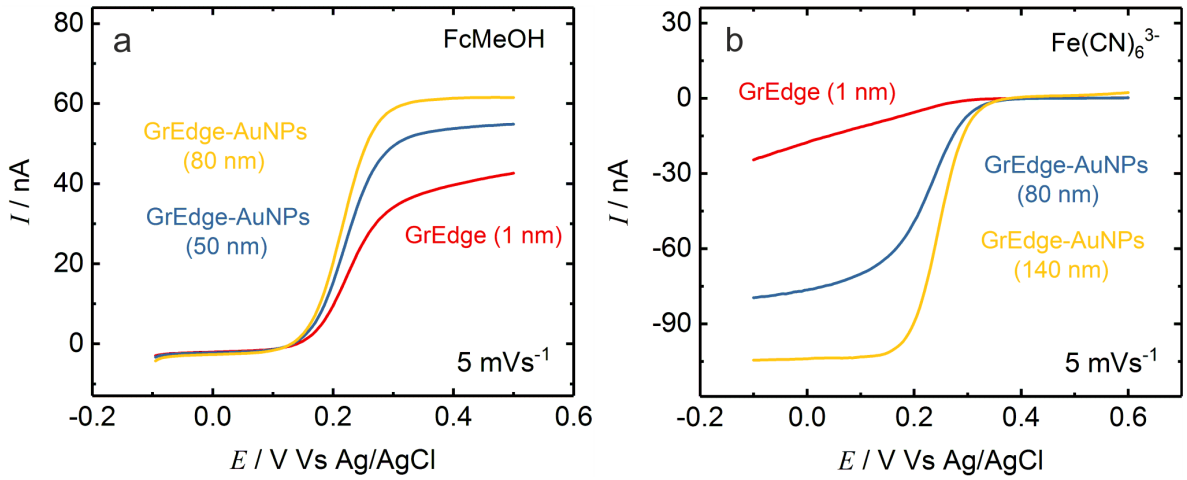

Figure 7.7: CVs obtained at GrEdge electrodes of varying critical sizes for: (a) FcMeOH oxidation and (b) $Fe(CN)_6^{3-}$ reduction. (Supporting electrolyte: 0.5 M KCl)

lowest steady-state current (at 0.4 V) of 37 nA. As expected, the current at steady-state increases with an increase in the critical size of the edge after deposition of the particles: 53 nA and 64 nA at $\sim$ 50 nm- and $\sim$ 80 nm-sized GrEdge-AuNPs, respectively. This increase is in line with the data shown in section 7.1.4, attributed to an increment in the area of the GrEdge. The change in the shape of the sigmoidal curve from quasi-steady-state ($\sim$ 1 nm) to perfect steady-state ($\sim$ 80 nm) is also apparent, with $\sim$ 50 nm having an intermediate shape between them. On the other hand, in case of $Fe(CN)_6^{3-}$, a similar trend is observed, except that there is no steady-state observed at unmodified GrEdge. With the increase in size, a quasi-steady-state and a perfect steady-state are obtained at $\sim$ 70 nm and $\sim$ 120 nm, respectively. The cathodic currents at -0.1 V are: 27 nA at GrEdge ($\sim$ 1 nm); 78 nA at GrEdge-AuNPs ($\sim$ 70 nm); and 116 nA at GrEdge-AuNPs ($\sim$ 120 nm).

One important property that changes with the size/radius of the electrode is the mass transport rate or coefficient (m) of the electroactive species. According to equation7.2, $m \propto 1/A$, therefore, it increases with a decrease in size. It means very high m at unmodified GrEdge, and mass transport process can take place as fast or even faster than the ET, thereby resulting in ET or kinetic limited process. The decrease in m at GrEdge-AuNPs electrode can lead to a mass transport limited process, shifting the current response more towards the reversible or Nernstian. Therefore, the (quasi)-sigmoidal shapes recorded in figure 7.7a indicate that the mass transport rates to the edge electrodes were comparable (GrEdge) to or larger (GrEdge-AuNPs, 80 nm) than the ET rate from FcMeOH. However in figure 7.7a, the mass transport rates are either smaller (GrEdge) or comparable (GrEdge-AuNPs, 70 nm) / larger (GrEdge-AuNPs, 120 nm) than the ET rate from $Fe(CN)_6^{3-}$. The difference in the shape of the voltammetric response at unmodified GrEdge for these two species can be due to a lower ET rate for $Fe(CN)_6^{3-}$ than for FcMeOH. Therefore, the change in the size of the nanoelectrodes and UMEs at the nanoscale is an important parameter to obtain different kinetic regimes or processes at the electrode interface. The observed systematic change in the voltammetric behavior is explained in the HET section 7.2 by using two different models.

Length Dependence Theoretically, the steady-state current for cylindrical geometry is linearly dependent on its length and is proven by measuring CV for 1 mM FcMeOH oxidation at GrEdge electrodes of different edge lengths. Figure 7.8a,b presents the forward cycle of CVs acquired from three GrEdge and three GrEdge-AuNP devices of different edge lengths. All the free GrEdge devices show quasi-steady-state behavior while the modified GrEdge-AuNPs devices show constant steady-state behavior with an increase in the magnitude of the steady-state or limiting current with the length of the edges. The steady-state currents are plotted 7.8a,b and a similar response is observed for $Fe(CN)_6^{3-}$ at both kinds of edge electrodes, with different edge lengths (as shown in figures 7.2f, 7.7b and 7.11).

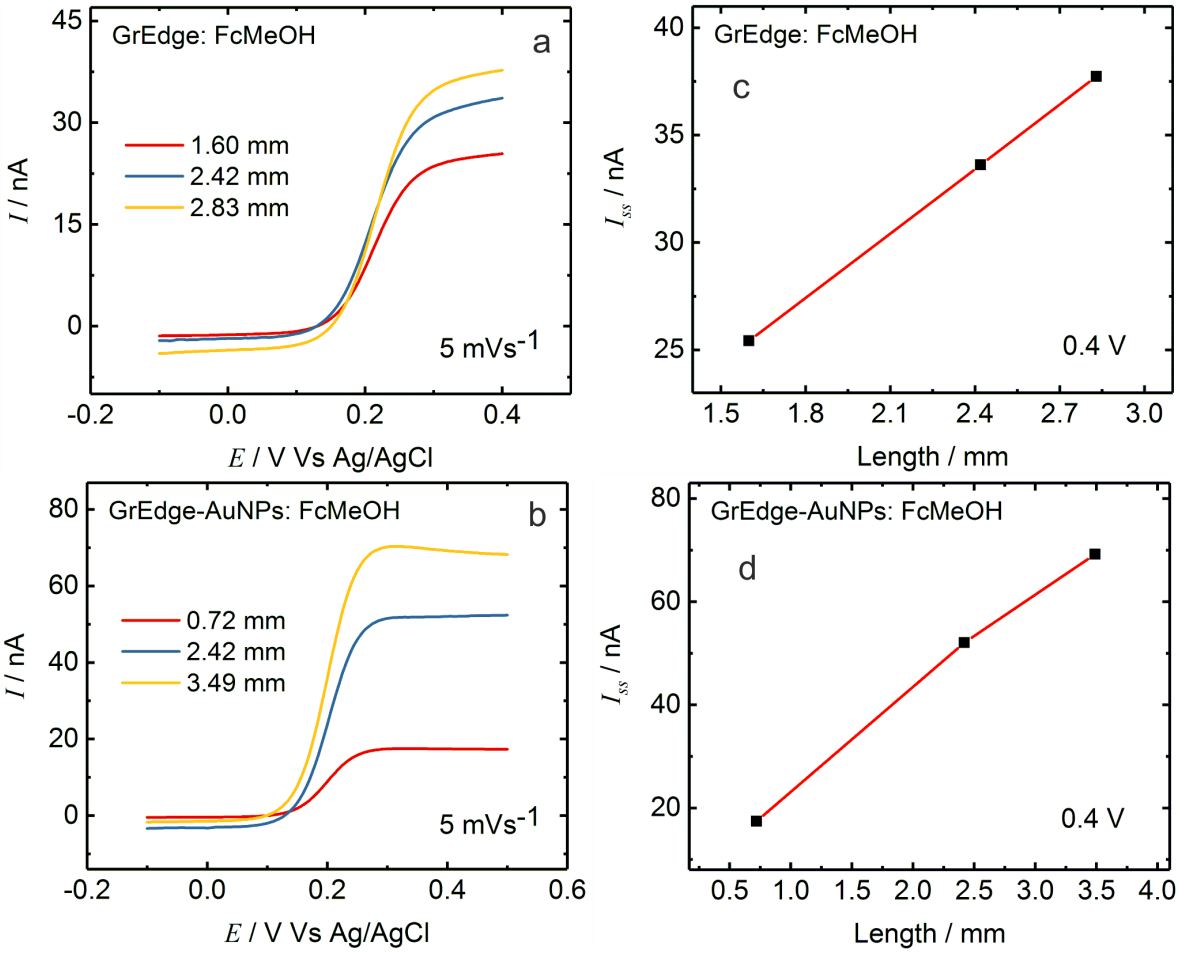

Figure 7.8: CV of 1 mM FcMeOH oxidation obtained at electrodes of varying edge length: (a) GrEdge and (b) GrEdge-AuNP electrodes. (c,d) Plots of limiting current as a function of electrode length. The length values of the electrodes are quoted in the legend. (Supporting electrolyte: 0.5 M KCl)

7.1.6 Scan Rate Dependence

Another parameter on which the shape of the voltammograms obtained at a nanoelectrode (or UME)depends is the scan rate. In this section, the transition from steady-state to peak-shaped voltammograms is demonstrated by varying the scan rates from 5 mVs^{-1} to 100 mVs^{-1} at both the free GrEdge and AuNPs modified GrEdge, for the FcMeOH and $Fe(CN)_6^{3-}$ redox probes. The experimental time scale of the CV experiment is related to the scan rate by $\nu = \Delta E/\Delta t$, where ν is the scan rate, ΔE is a potential step, and Δt is the time taken to complete one potential step. Therefore, the higher the scan rate, the lower is the experimental time scale.

FcMeOH For the GrEdge electrode, the sigmoidal shape with the quasi-steady-state is present for the scan rates from 5 mVs^{-1} to 200 mVs^{-1} (figure 7.9a-f), indicating similar convergent diffusion (hemicylindrical diffusion) as shown in 7.6a. However, there is a slight increase in hysteresis with every increase in scan rate. At very high scan rates of 500 and 1000 mVs^{-1} (in figure 7.9g,h), the peak shaped features are slightly visible with potential separated anodic and cathodic waves, indicative of the transition from nanoelectrode to macroelectrode behavior. This can be explained by considering the diffusion layer. At short experimental timescales (very fast scan rates), the thickness of the diffusion layer that is depleted of electroactive species is much smaller than the critical size of the electrode (thickness of GrEdge). The species from the edge of the diffusion layer approach the cylindrical GrEdge electrode perpendicularly (planar diffusion) as in the case of normal-sized electrodes. These are called edge effects and are noticeable at higher scan rates.[202,203] The mass transport process at higher scan rates, therefore, is dominated by linear diffusion to the GrEdge electrode. For the GrEdge-AuNPs electrode, a constant steady-state current plateau is maintained at the initial scan rates from 5 to 50 mVs^{-1} (figure 7.10a-d). At higher scan rates of 100 mVs^{-1} and above in figure 7.10e-h, there is a gradual increase in peak features, with a very clear observation of the oxidation (0.27 V) and reduction peaks (0.17 V) particularly at 500 and 1000 mVs^{-1}.

Since the observed steady-state responses also depend on the critical dimension of the electrode, the time scales (scan rates) for obtaining steady-state are different in the case of GrEdge and GrEdge-AuNP electrodes. For the GrEdge electrode having the critical size of 1 nm, the steady-state is maintained until scan rates of 200 mVs^{-1}, while in the case of GrEdge-AuNP, the critical size of $\sim$ 70 nm leads to true steady-state only until 50 mVs^{-1}. This is because of the interdependence of the electrode size and experimental time scales, which means that the transition from the peak-shaped to the steady-state voltammograms can be achieved by reducing the scan rate, and smaller the characteristic critical size of the electrode, faster the transition, or vice-versa. Therefore, at 1 nm size-sized GrEdge electrodes, the transition to (quasi)-steady-state occurs at 200 mVs^{-1}, while at $\sim$ 70 nm-sized GrEdge-AuNP electrodes, it occurs at around 50 - 100 mVs^{-1}.

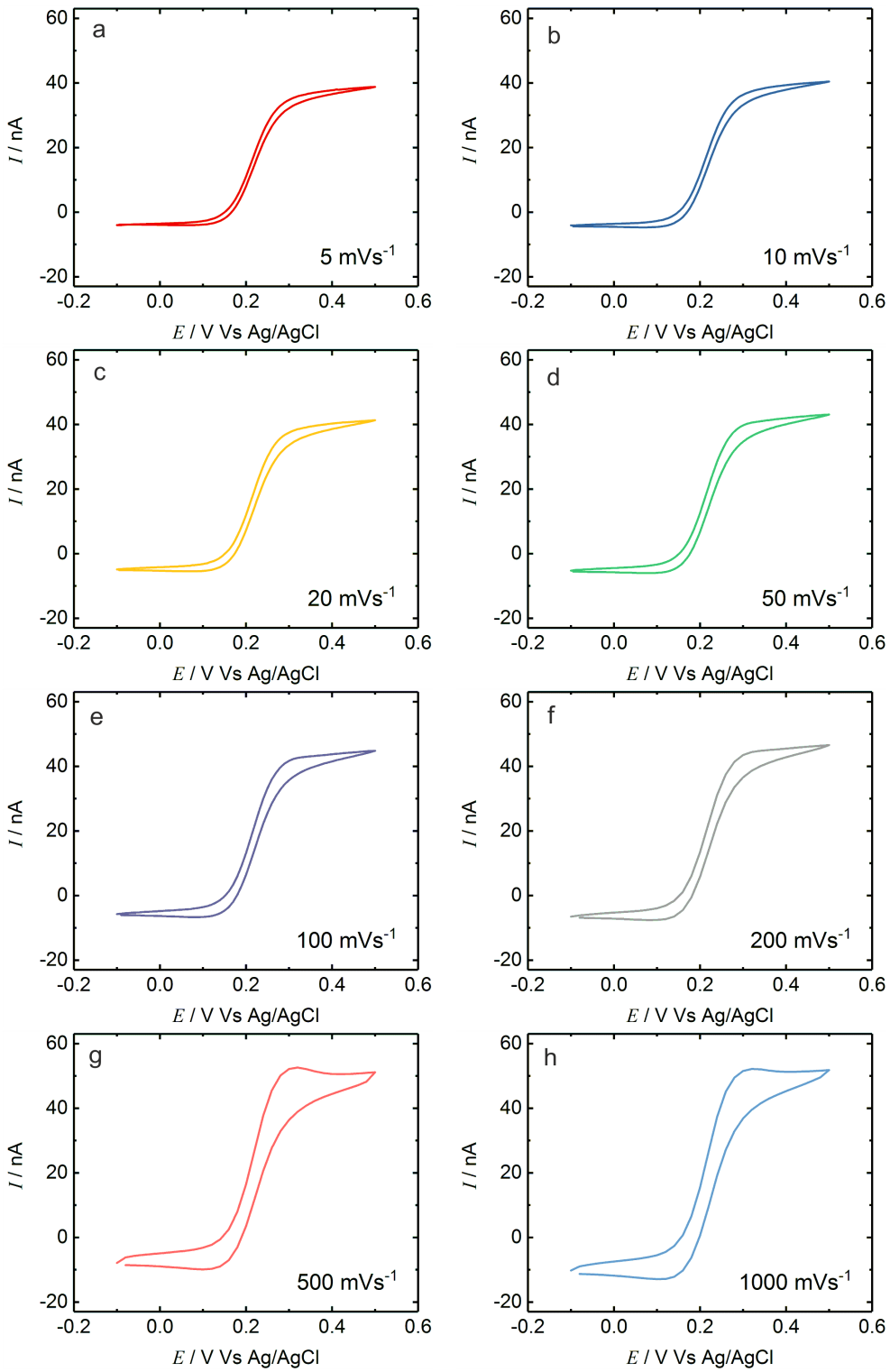

Figure 7.9: CVs for the oxidation of 1 mM FcMeOH at GrEdge electrode, measured by varying the scan rate. (Supporting electrolyte: 0.5 M KCl)

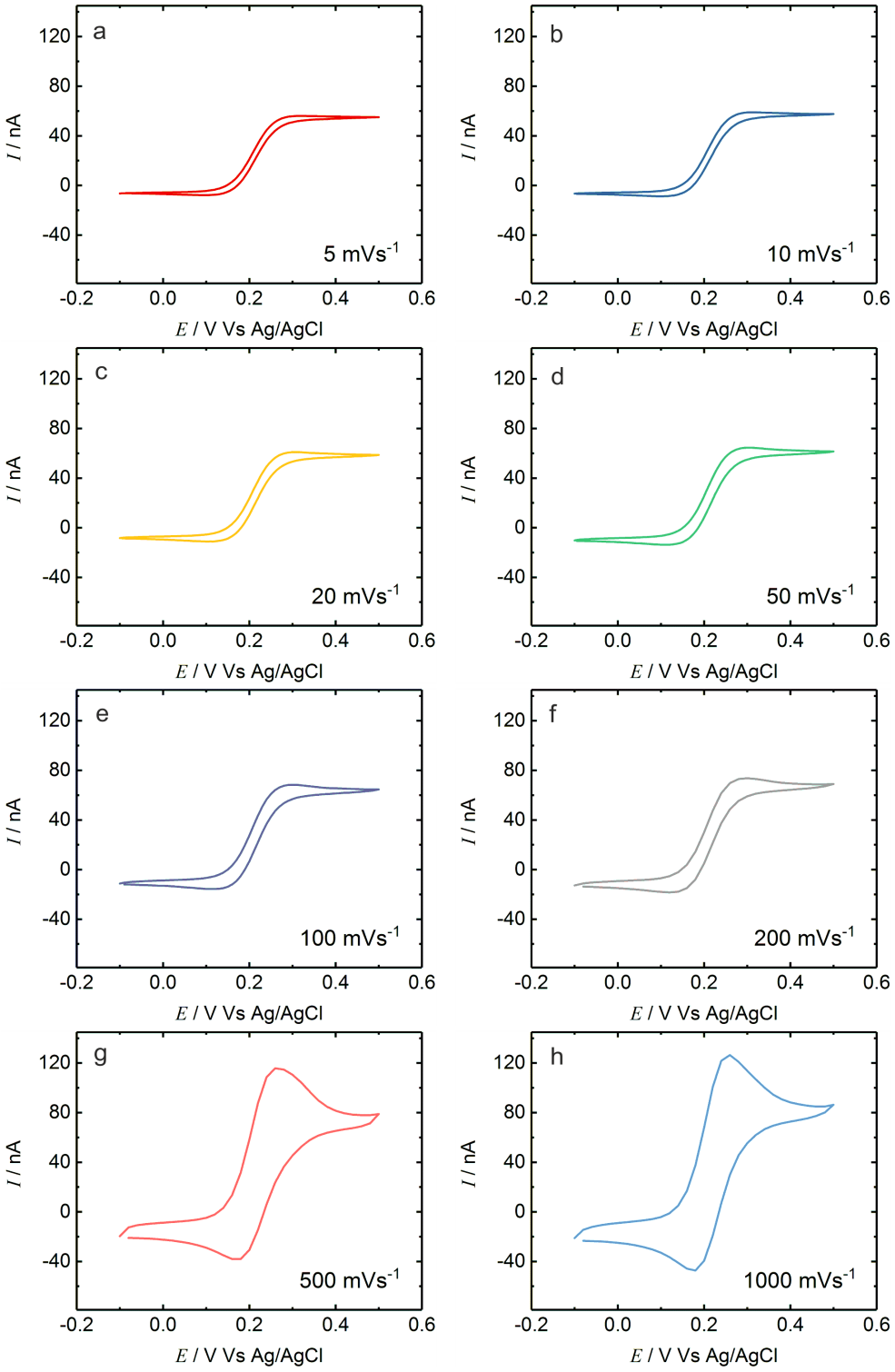

Figure 7.10: CVs for the oxidation of 1 mM FcMeOH at GrEdge-AuNPs electrode, measured by varying the scan rate. (Supporting electrolyte: 0.5 M KCl)

$Fe(CN)_6^{3-}$ Figures 7.11, and 7.12, shows CVs at varying scan rates obtained at the free and AuNPs modified GrEdge for $Fe(CN)_6^{3-}$. For the unmodified GrEdge, the monotonous increase in cathodic current for $E < +0.3$ V is seen for all scan rates, along with a gradual increase in hysteresis with increase in scan rate. However, at very high scan rates of 500

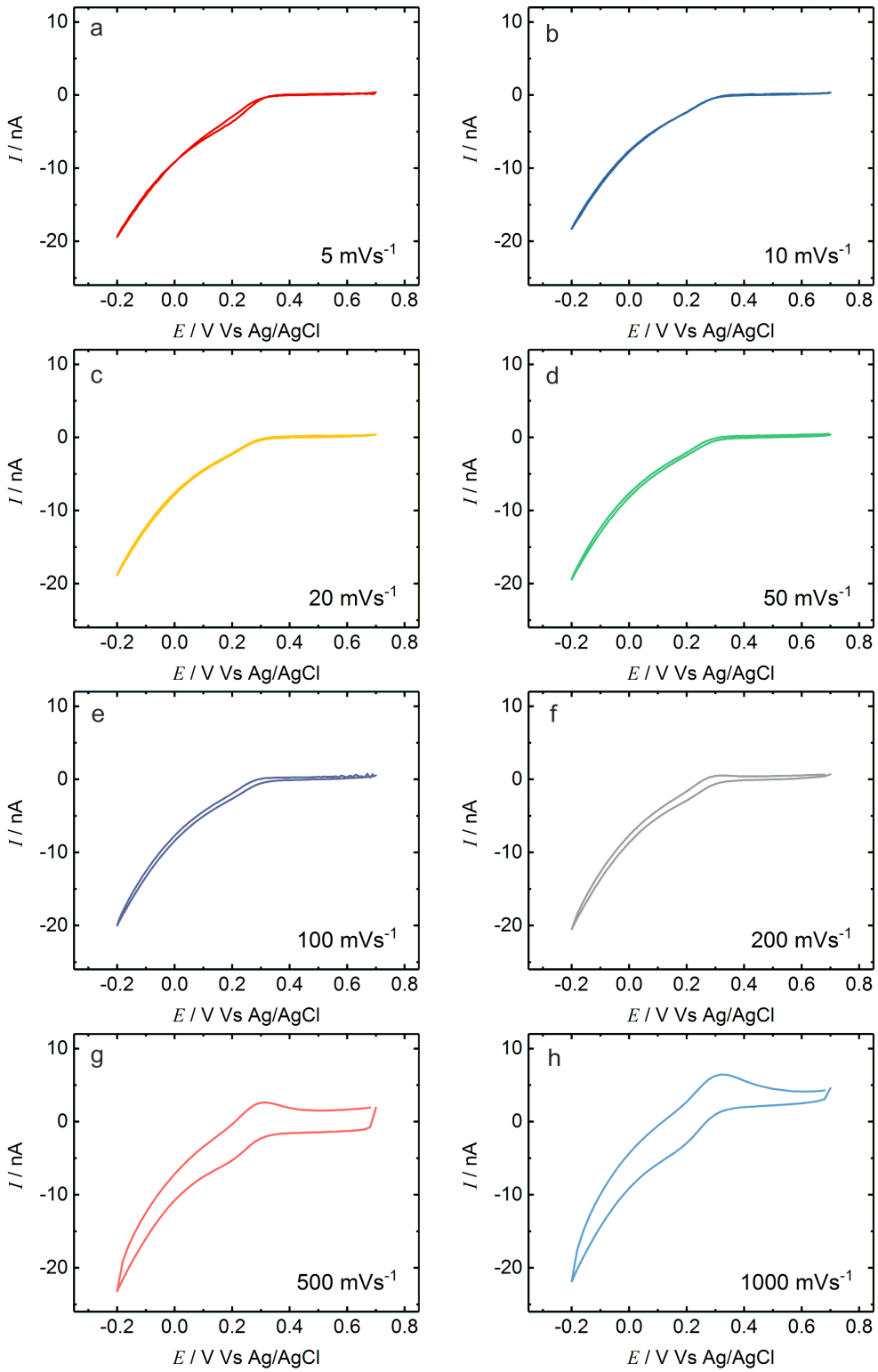

Figure 7.11: CVs for the reduction of 1 mM $Fe(CN)_6^{3-}$ at GrEdge electrode, measured by varying the scan rate. (Supporting electrolyte: 0.5 M KCl)

and 1000 mVs^{-1}, the redox peaks of $Fe(CN)_6^{3-}$ are visible. For the GrEdge-AuNPs electrode, a voltammetric trend similar to FcMeOH is observed. From 5 to 50 mVs^{-1}, a steady-state is maintained, while from 100 mVs^{-1}, the peak features start to appear, and become very prominent at 500 and 1000 mVs^{-1} with peaks at 0.32 V (oxidation) and 0.16 V (reduction).

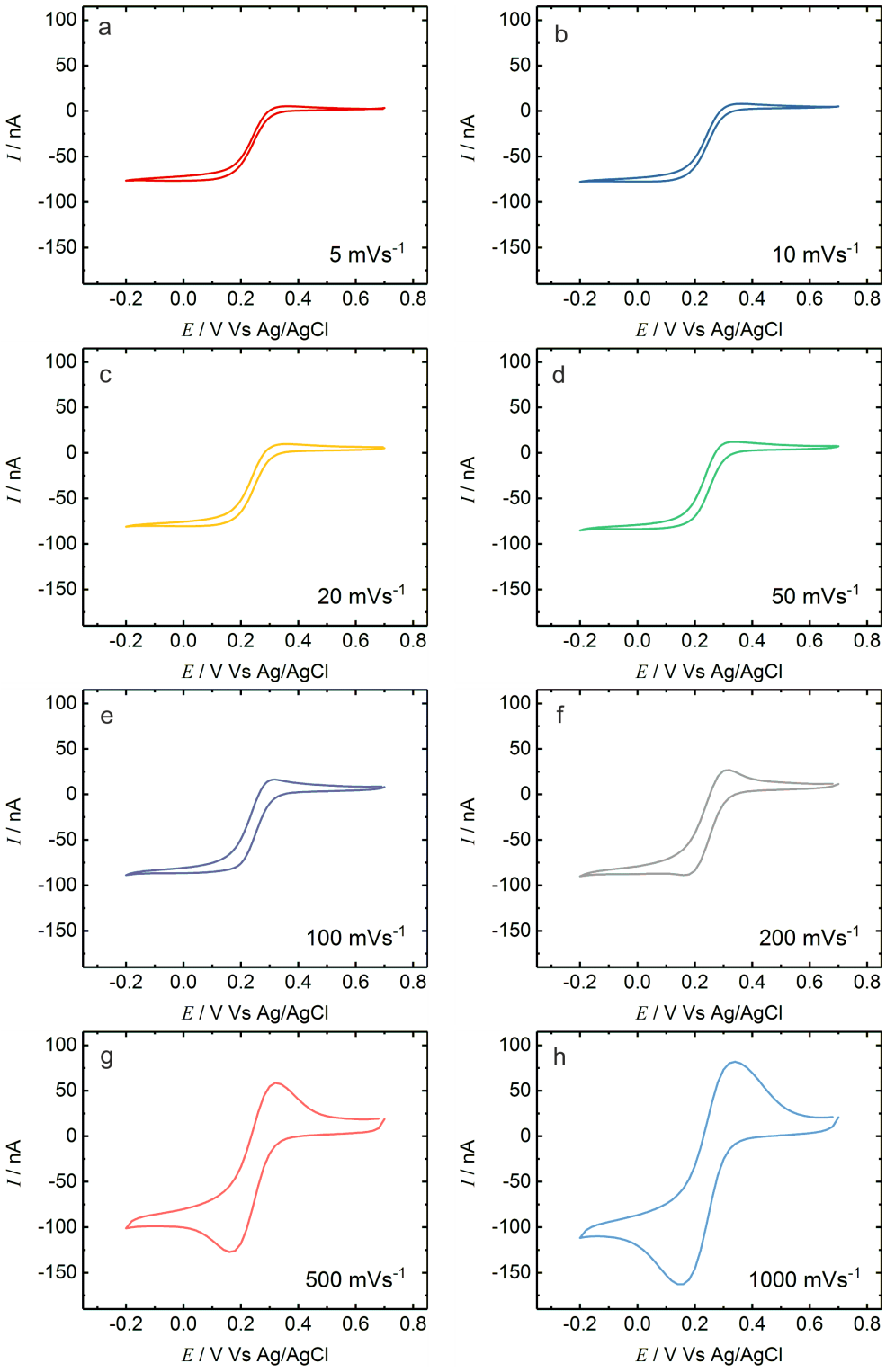

Figure 7.12: CVs for the reduction of 1 mM $Fe(CN)_6^{3-}$ at GrEdge-AuNPs electrode, measured by varying the scan rate. (Supporting electrolyte: 0.5 M KCl)

Limiting Current Vs Scan Rate The plot of limiting current versus scan rate (ν) for FcMeOH oxidation and $Fe(CN)_6^{3-}$ reduction at GrEdge and GrEdge-AuNPs electrodes shows that limiting current is rather independent of scan rate up to 200 mVs^{-1} for free edge and 50-100 mVs^{-1} for AuNPs modified edge. For the case of planar diffusion, the current is directly proportional to the square root of the scan rate, according to equation 7.1 (Randles-Ševčík), therefore it should vary as a function of $\nu^{1/2}$, which is not observed here. Although at higher scan rates, it varies as $\nu^{1/2}$. The observation of a steady-state for low to high scan rates, and redox peak features (reminiscent of planar diffusion) only at very high scan rates, is a characteristic signature of nanoelectrodes and UMEs. Therefore, low scan rates and the smaller critical size of the electrode favor the typical nanoelectrode and UME behavior.

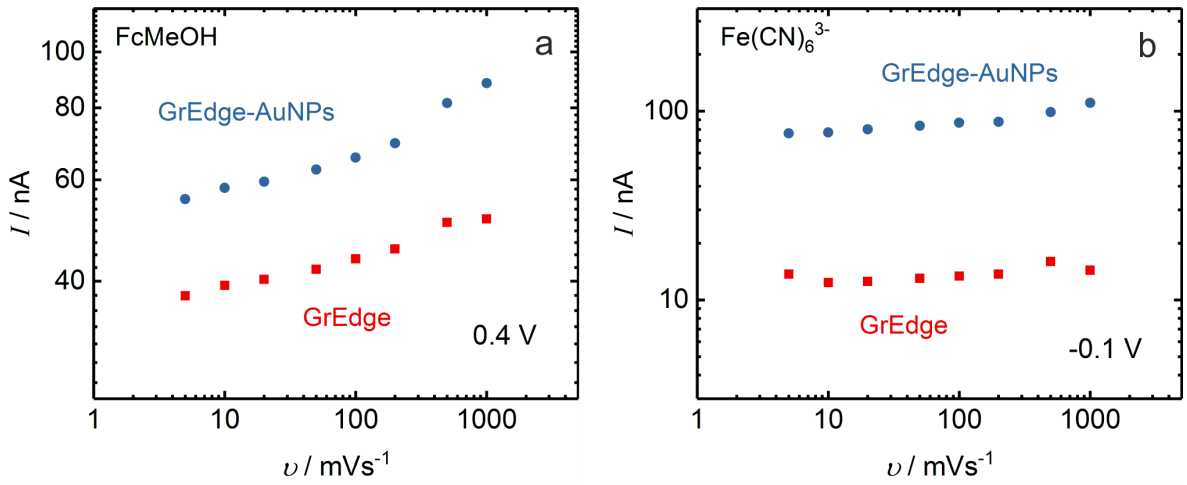

Figure 7.13: Log-Log plot of limiting current versus scan rate for (a) 1mM FcMeOH oxidation and (b) 1mM $Fe(CN)_6^{3-}$ reduction at GrEdge (red) and GrEdge-AuNPs (blue) electrodes. Supporting electrolyte: 0.5 M KCl. Note that there is no true limiting current for the reduction of $Fe(CN)_6^{3-}$ at the free GrEdge, therefore, the current at -0.1 V is plotted here.

7.1.7 Ohmic Effects: Electrolyte Concentration Dependence

Ohmic effects (or ohmic drop) are generated when the Faradaic and charging currents flow through a solution, due to the development of a potential that weakens the applied potential by an amount iR, where i is the total current, and R is the cell resistance. Any applied potential at the electrode will be incorrect because of the ohmic potential drop given by:

$$E_{Working} = E_{applied} - iR$$

The ohmic effects can lead to severe distortions in current responses and shift in peak potentials, particularly in resistive media and at high scan rates. The Faradaic currents depend on the electrode area. This sensitivity to the area means that the currents observed at nanoelectrodes or UMEs are typically three to four orders of magnitude smaller than

those observed at macroelectrodes. Therefore, the small currents at nanoelectrodes can significantly reduce these effects of solution resistance and can often eliminate iR problems. Typically supporting electrolyte is used in large excess in comparison to the electroactive species, to compensate for the ohmic drop by increasing the ionic conduction in solution. Thus, in the present study, it is of interest to quantitatively examine the electrochemical behavior of GrEdge and GrEdge-AuNPs electrodes as a function of the concentration of supporting electrolyte ions. The objectives are to determine whether there is any difference between the voltammetric measurements in terms of current and potential in low and high ionic strength solutions.

Figure 7.14 shows the voltammetric response for the oxidation of 1 mM FcMeOH in supporting electrolyte KCl, with different concentrations of 10 mM, 100 mM, 500 mM, and 1000 mM, at GrEdge and GrEdge-AuNP electrodes. The limiting or steady-state current for the oxidation of the neutral species FcMeOH is unaffected by the ionic strength of the KCl solution. The other main parameter, $E_{1/2}$ for the oxidation of FcMeOH, shifts negligibly with a change in KCl electrolyte concentration.

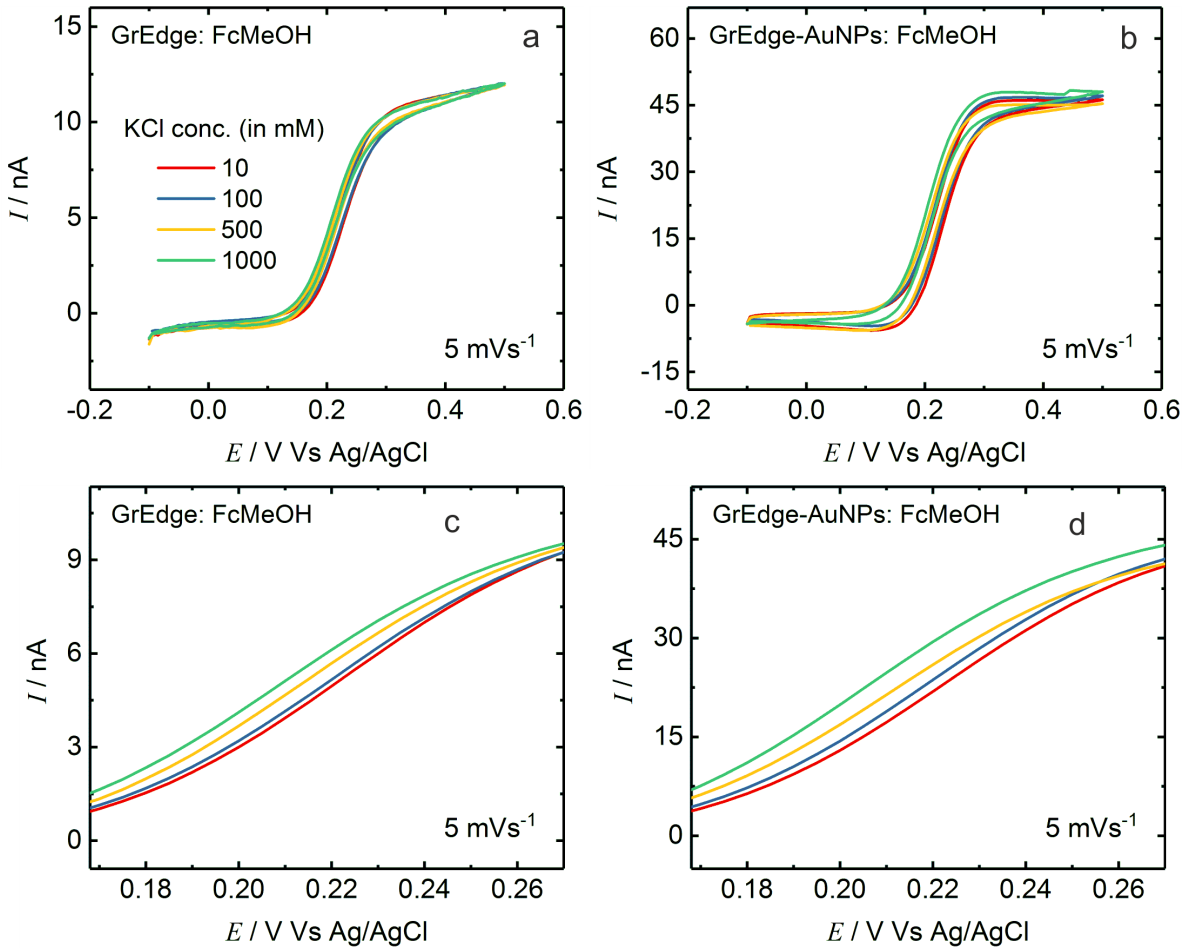

Figure 7.14: CVs for the oxidation of FcMeOH redox probe (1 mM) in different supporting electrolyte (KCl) concentrations (10, 100, 500 and 1000 mM) at (a) GrEdge electrode and (b) GrEdge-AuNPs electrode. (c,d) shows the forward cycle data of CV for the respective electrodes in a smaller potential range.

To investigate closely, the forward cycles of the CV were plotted for narrow potential range, showing the minimal shifts of $\sim$ 3 mV and $\sim$ 5 mV in $E_{1/2}$ for GrEdge and GrEdge-AuNPs electrodes, respectively, with increasing KCl concentration. This minuscule shift could also be due to the potential of the reference electrode which depends on the KCl concentration as well. However, overall there is no significant change in the voltammetric curves measured by increasing the supporting electrolyte concentration. Therefore, the nanoelectrode behavior and the low currents observed at the edge electrodes in a way protect the electrochemical measurements from the distorted current responses and shifted peak potentials, and hence, reduce the ohmic effects.

7.2 Heterogeneous Electron Transfer (HET) Kinetics

A typical electrochemical process comprises at least three consecutive steps: diffusion of the reactant to the electrode surface, HET, and diffusion of the product into the bulk solution. This section is concerned with measurements of kinetic parameters of HET processes (i.e., standard heterogeneous rate constant k^0 and transfer coefficient α).

As discussed in the earlier sections, the responses observed at nanoelectrodes and UMEs are significantly less distorted by charging and ohmic effects than macroelectrodes, and the applied potential is realized at much shorter time scales. This allows one to probe faster ET kinetics. The fast mass-transport rate of nanoelectrodes and UMEs is essential to study the kinetic parameters of electrochemical reactions by using steady-state voltammetry.[181–185] The kinetic parameters of nanoelectrodes are similar to those of UMEs. Aoki & Matsuda,[186] Fleischmann & Pons,[187] Oldham & Zoski,[188] and Mirkin & Bard[189] have provided several approaches for analyzing and modelling the experimental current-voltage curves at simple UMEs such as spherical, microband and disc electrodes. The voltammetric data obtained from the (modified) GrEdge electrodes cannot be analyzed with existing models based on the geometry. The closest to GrEdge geometry is the microband model, however, it is assumed that the band electrode lying on a surface is exposed to the entire solution region above the band. By contrast, the GrEdge is protected on one side (along the length of the edge) by the thick PR layer and hence these models cannot be directly applied for the GrEdge situation. In principle, both GrEdge and GrEdge-AuNP electrodes may be considered as a variant of (hemi) cylindrical electrodes.

In this work, three different available approaches are considered for estimating values of k_0 from the voltammetric data. The first two methods assume that the electrode is uniformly accessible (i.e., the surface concentration of reduced/oxidized species is uniform along the entire graphene edge), while the third method (adapted Koutecký-Levich method) is more general and has been recently successfully applied for ultramicroelectrodes and nanoelectrodes of different shapes. A brief description of all the three methods is as follows:

- The first method (section 7.2.1) is one of the most general approaches applicable for uniformly accessible nanoelectrodes and UMEs of all shapes and is based on the fitting of the sigmoidal voltammetric curves of the transient and steady-state currents to a specific kinetic model (based on Butler-Volmer kinetics). Based on the kinetic parameters extracted from the fitting, the analytical model can predict and simulate various kinetic regimes.

- A second possibility is the method of Mirkin & Bard [189], where kinetic parameters of simple quasi-reversible ET reactions can be determined by using only the quartile potentials ($E_{1/4}$, $E_{1/2}$ and $E_{3/4}$), i.e. the values of the potential at which the magnitudes of the current are $i_{ss}/4$, $i_{ss}/2$ and $3i_{ss}/4$ respectively, from a single steady-state voltammogram. The parameters α, $E^{0'}$ and k^0 can then be obtained by calculating the difference potentials $\Delta E_{1/4} = |E_{1/2} - E_{1/4}|$ & $\Delta E_{3/4} = |E_{1/2} - E_{3/4}|$, and looking up the corresponding values in the reference table available for uniformly accessible electrodes of arbitrary shape. However, the table only provides information about the spherical, hemispherical, and disc-shaped UMEs, and this method is only applicable to quasi-reversible processes, for which $\Delta E_{1/4} \geq 30.5$ mV and $\Delta E_{3/4} \geq 31$ mV. If the difference potentials are higher, the voltammogram is Nernstian, in which case it is not possible to determine k_0. Therefore, this method cannot be applied to the voltammograms obtained at GrEdge and GrEdge-AuNP electrodes.

- The third approach is the adapted Koutecký-Levich (K-L) method (section 7.2.2) by Kim & Bard [262] where kinetic information is obtained by analyzing a plot of the inverse current density against the inverse of mass transport coefficient at various sizes. The mass transport rate changes on the basis of electrode size and geometry by as much as two orders of magnitude, with little effect on the heterogeneous rate constant, and is estimated from the steady-state currents measured at various concentrations using a linear relation (equation 7.2) between them.

The kinetic regimes or parameters are defined partly by experimental conditions such as the shape and size of the electrode and scan rate. In this work, the time scale is important, since the sizes of both the edge electrodes are already different. Therefore, the scan rate is maintained at 5 mVs^{-1} for both the probes at GrEdge and GrEdge-AuNP electrodes. In the next two subsections, both the Butler-Volmer kinetics based and K-L models are discussed in detail along with the quantitative and qualitative analysis of the voltammograms and extraction of the rate constants.

7.2.1 Analytical Model Based on Butler-Volmer Kinetics

One way to determine kinetic parameters is to fit an experimental i/i_{ss} vs overpotential (η) dependence using α, and $E^{0'}$ as adjustable parameters.

7.2.1.1 Theory and Model

Theory Equation 7.4 describes the shape of a steady-state CV curve at any uniformly accessible UME (i.e., when the surface concentrations and diffusion fluxes of redox species are uniform over the entire electrode surface) of an arbitrary shape.[188,263]

$$i = \frac{i_{ss}}{\theta + 1/\kappa} \tag{7.4}$$

where i is the electrochemical current and i_{ss} is the steady-state current, given by the equation 7.2:

$$i_{ss} = nFAmC^*$$

i_{ss} is proportional to the bulk concentration (C^*), $n = 1$ (one-electron process), m (mass transport coefficient), F (Faraday constant) and A (area of the electrode). θ and κ are given by[188,263]

$$\theta = 1 + exp[nF(E - E^{0'})/RT]m_O/m_R$$

$$\kappa = k^0 exp[-\alpha nF(E - E^{0'})/RT]/m_O$$

where $\eta = E - E^{0'}$ is the overpotential, α is the transfer coefficient, R is the universal gas constant and T is the temperature. Furthermore, $m = m_O$ and $C^* = C_O^*$ for reduction, $m = m_R$ and $C^* = C_R^*$ for oxidation, with the O and R subscripts referring to oxidized and reduced species respectively. $E^{0'}$ is the formal potential of the redox species. On substituting $\eta = E - E^{0'}$ and $f = F/(RT)$, the current given by the above equation 7.4 can be re-written for a one-electron oxidation process as:

$$i_{ox} = \frac{i_{ss}}{1 + \frac{m_R}{m_O}e^{-f\eta} + \frac{m_R}{k^0}e^{-(1-\alpha)f\eta}} \tag{7.5}$$

where i_{ox} is the electrochemical current (positive for oxidation) as a function of the applied potential E and the bulk concentration of the redox active species (C^*). Similarly, for an one-electron reduction, the current (i_{red}) is given by:

$$i_{red} = \frac{i_{ss}}{1 + \frac{m_O}{m_R}e^{f\eta} + \frac{m_O}{k^0}e^{\alpha f\eta}} \tag{7.6}$$

Model The overall kinetics of redox processes is determined by its slow step whose rate can be measured experimentally. In other words, the lower of the two rates (the mass transport rate m and the ET rate k^0) dictates the shape of the obtained voltammetric curves. For the discussion, the ratio of the mass transport coefficients (m_O/m_R) is assumed to be 1. The third term ($\frac{m_O}{k^0}e^{-(1-\alpha)f\eta}$) of the three terms in the denominator, of the equations 7.5 and 7.6, involves both m and k^0 and is essential to explain the behavior of the voltammograms. A model, shown schematically in figure 7.15 is developed where the normalized current for oxidation i_{ox}/i_{ss} from equation 7.5 is plotted as a function of the m_R/k^0 ratio and the overpotential η. The map in Figure 7.15a shows a black contour corresponding to half-wave potential $E_{1/2}$ (where $i_{ox}/i_{ss} = 0.5$). According to this model, the shape (or kinetic regime) of the voltammetric responses can be empirically divided into three different categories:

- **Case 1**, $m/k^0 \leq 0.1$: When the ratio of m to k^0 is very small (or alternatively, in the absence of the third term in the denominator), the normalized current (i/i_{ss}) is given by an ideal sigmoid function $(1/(1+e^{\pm f\eta}))$ with a clear steady state. This means that in this regime, mass transport coefficient m dominates the voltammetric response, or in other words, m is low enough and the voltammetric response is mass transport limited. $E_{1/2} = E^{0'}$ ($E = E^{0'}$ at $\eta = 0$, in figure 7.15a) and the current response is sigmoidal with a clear steady state for the black and red curves in figure 7.15b at $m/k^0 = 0.05$ and 0.1.

- **Case 2**, $m/k^0 > 0.1$: When m becomes sizeable or comparable to k^0 then a deviation from the ideal sigmoidal behavior is expected as shown in figure 7.15a. $E_{1/2}$ starts to deviate from $E^{0'}$ and the current response does not present a perfect steady-state, instead an intermediate behavior is observed. This regime is referred as quasi-steady-state. For $m/k^0 = 1$ (blue curve) shows the quasi-steady-state behaviour in figure 7.15b.

- **Case 3**, $m >> k^0$: When m becomes much larger than k^0 (i.e., $(m/k^0 > 10)$, $E_{1/2}$ deviates from $E^{0'}$ by more than 0.2 V. In this regime, the response is dominated by the lower rate k^0, hence, kinetics of ET and the voltammetric curve becomes more akin to a Butler-Volmer kind of response (kinetic limitation).

Often at UMEs the mass transport rate is lower than the ET rate, i.e. $m/k^0 < 0.1$ (case 1). For nanoscale electrodes, however, the mass transport is vigorously favored, due to which a regime is reached where the mass transport rate can be comparable to or higher than the ET rate. In such a situation, a clear deviation from the ideal steady-state is expected and the current observed may exhibit a quasi-steady-state (case 2) or a dominantly kinetic response (case 3).

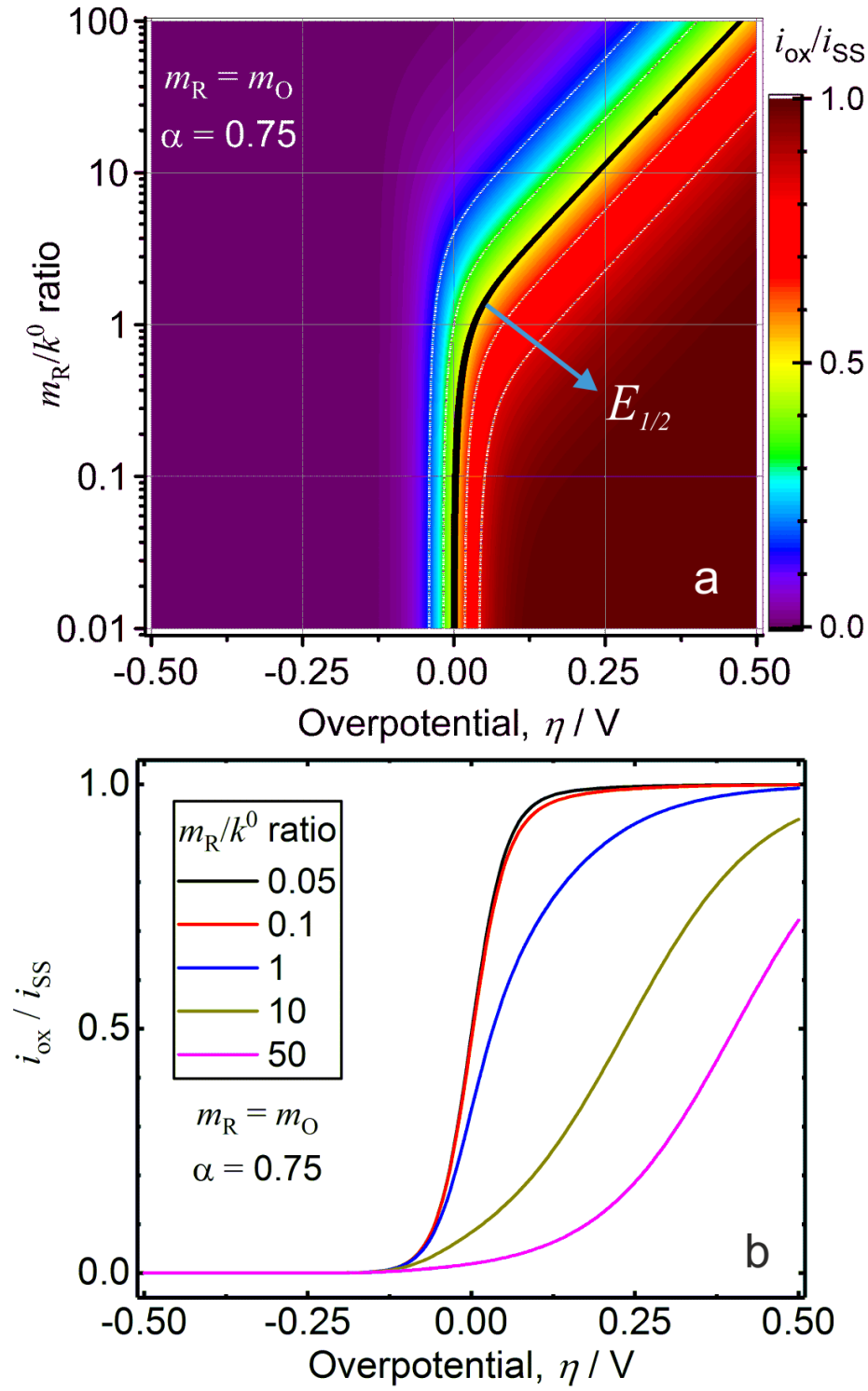

Figure 7.15: (a) Map showing the (theoretical) normalized voltammetric response i_{ox}/i_{ss} (in eq. 7.5) as a function of m_R/k^0 ratio and the overpotential $\eta = E$ - E^0 for one-electron oxidation at a UME of arbitrary shape. The black contour corresponds to the situation where $i_{ox}/i_{ss} = 0.5$ and corresponds to $E_{1/2}$. (b) Selected CVs at the indicated values of m_R/k^0 ratios, using eq. 7.5. For both the plots, $\alpha = 0.75$ and $m_R = m_O$. It is apparent that a deviation from an ideal steady state is seen for values of $m_R/k^0 > 0.1$, signified both by the deviation of $E_{1/2}$ from E^0 ($E = E^0$ at $\eta = 0$) visible in (a) as well as by the shape of the CV in (b).

Explanation of the voltammograms in figure 7.6 Applying this knowledge to the data in figure 7.6, a couple of predictions can be made for the explanation of the voltammetric curves. For a given electrode size and shape, the mass transport coefficient is expected to be similar for both FcMeOH and $Fe(CN)_6^{3-}$ since the diffusion coefficients have similar values.[66,158,264] The difference in the shape of the current response at unmodified GrEdge for these two species can thus be traced back to an apparently lower k^0 for $Fe(CN)_6^{3-}$ than for FcMeOH. Moreover, it can be said that the value of k^0 must be comparable to m_R for FcMeOH, whereas it must be at least an order of magnitude lower than m_O for $Fe(CN)_6^{3-}$, signifying that the ET with $Fe(CN)_6^{3-}$ at the unmodified GrEdge is kinetically limited. For GrEdge-AuNPs, it can be said that the mass transport rate gets lower because of the increase in the area brought about by the AuNPs according to i_{ss} equation. As a result, the m/k^0 ratio gets smaller because of which the ideal sigmoidal response with a proper steady-state is recovered.

7.2.1.2 Application: Extraction of Kinetic Parameters

To gather quantitative information about the mass and ET rates, the voltammetric response at several concentrations was measured at both types of electrodes. The value of m_R or m_O alone is obtained by equation 7.4 for oxidation or reduction, respectively from the experimental data using the linear dependence between steady-state current i_{ss} and concentration C^* of the redox probe. The equation 7.2 can be further re-written as

$$m = \frac{i_{ss}}{C^* F A} = \frac{slope}{FA}$$

The linear plot gives the slope i_{ss}/C^*, for all the 4 cases in figures 7.16c,d and 7.17c,d. For the area A, the electrodes are modeled as quarter-cylinders for both the unmodified or modified GrEdge electrodes, respectively as shown in equation 7.3. This is justified[265] by considering that the (modified) GrEdge electrodes are expected to behave as nanowires, protected on one side by the PR. The lengths of the electrodes were in the range of 0.5 - 3.8 mm. The area for both types of electrodes was calculated accordingly using equation 7.3. The mass transfer coefficients can also be determined theoretically assuming uniform diffusion, and literature values of diffusion coefficients (D): 7.4 $\times$ 10 $^{-6}$ cm^2/s for FcMeOH and 6 $\times$ 10 $^{-6}$ cm^2/s for $Fe(CN)_6^{3-}$.[66,264] m (theory or calculated) for cylindrical geometry is given by:

$$m = \frac{2D}{r \ln \tau} \tag{7.7}$$

$\tau = 4Dt/r^2$, $t = RT/F\nu$ and ν is scan rate. For fitting, theoretically calculated m values were used, since m cannot be obtained for $Fe(CN)_6^{3-}$ at unmodified GrEdge electrodes due to the absence of steady-state. A constrained global fit of the model to equations 7.5 or 7.6) is performed to the voltammetric data including at least three different concentrations (30, 100, and 300 µM), to extract the fitting parameters (i_{ss}, α, $E^{0'}$, and k^0). The fitting was

done in Mathematica 12 using the NonlinearModelFit routine with the NMinimize algorithm to obtain a global minimum.

GrEdge electrodes Figures 7.16a,b present a typical example of the measured data along with the fitting results for the oxidation of FcMeOH and the reduction of $Fe(CN)_6^{3-}$ at unmodified GrEdge electrodes, where a very good fit for all three concentrations is apparent. This is also attested by a statistical analysis of the model fit yielding very low P-values along with all the fitting parameters in table 7.1. The P-values are typically $< 10^{-5}$, or close to zero, and are adjusted until the required accuracy to get a good fit of the model. Figure 7.16c show the linear fit between i_{ss} and concentration, and m value of 16 cm/s was extracted for FcMeOH oxidation at unmodified GrEdge electrode. This is in close agreement with the

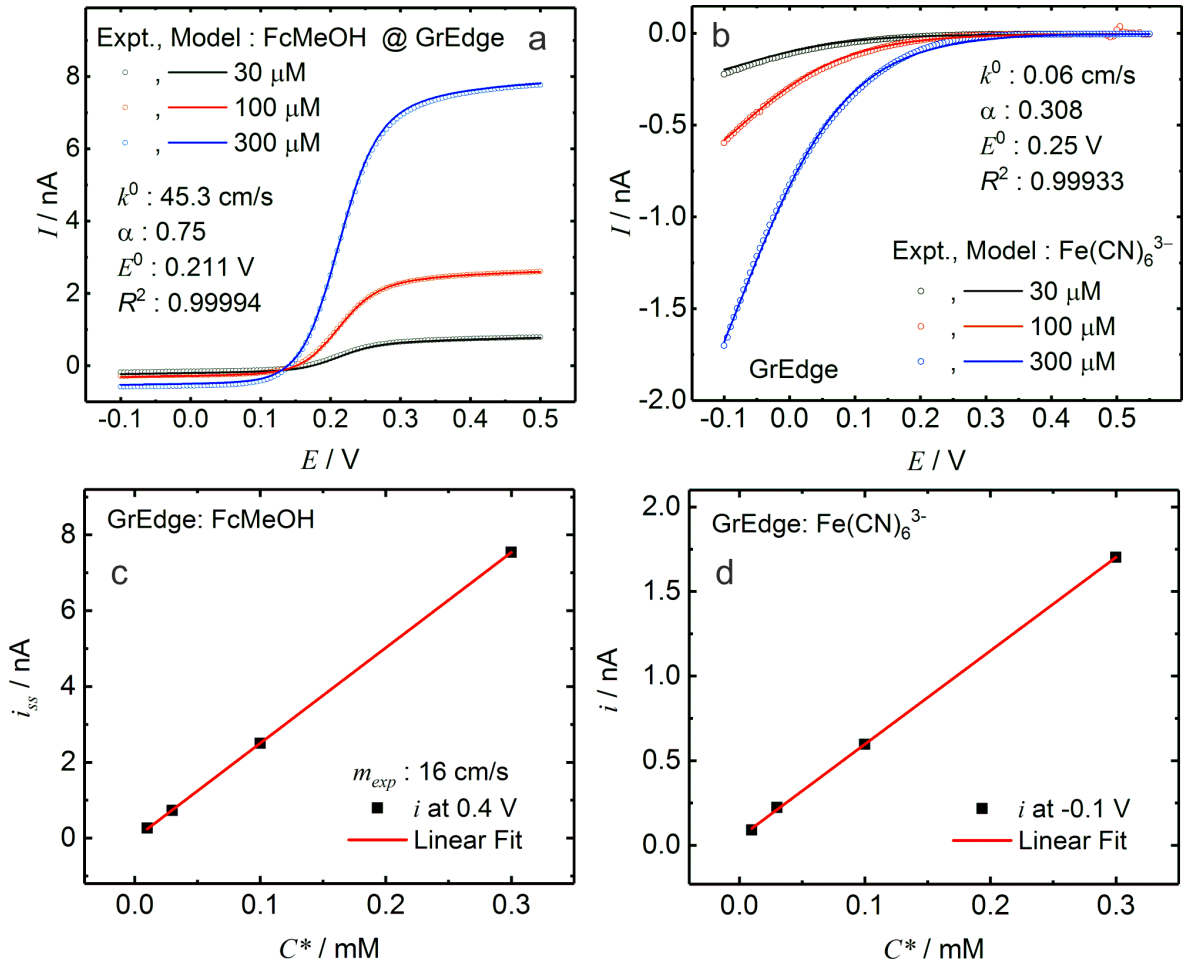

Figure 7.16: Curve-fitting at GrEdge electrodes. (a,b) Experimental (open markers, Expt.) and the fitted (solid lines, Model) voltammetric responses for: (a) FcMeOH oxidation, (b) $Fe(CN)_6^{3-}$ reduction. The model parameters were obtained by fitting the experimental response to equations 7.5 and 7.6. A very good fit ($R^2 \approx 1$) is apparent between the experimental data and the model. Statistical information about the quality of fit can be found in table 7.16. (c,d) Dependence of the steady-state current on concentration for: (c) FcMeOH oxidation (at 0.4 V), (d) $Fe(CN)_6^{3-}$ reduction (at -0.1 V). (scan rate: 5 mVs^{-1}, supporting electrolyte: 0.5 M KCl).

calculated m value of 22.6 cm/s. For $Fe(CN)_6^{3-}$ reduction, the calculated m is 18.5 cm/s. The reliability of the k^0 values is further improved by measurements on several electrodes, which provide similar values, as tabulated in 7.3.

Table 7.1: Results of the fitting in figure 7.16a,b with statistical information for: FcMeOH oxidation and $Fe(CN)_6^{3-}$ reduction at GrEdge (electrode height: 1 nm).

Parameter	*Estimate*	*Standard Error*
FcMeOH: GrEdge (1 nm)		
$E^{0'}$ (V)	0.21098	2.26259×10^{-4}
k^0 (cm/s)	45.318	1.046
i_{ss} (A) / 1 mM	2.62154×10^{-8}	6.19773×10^{-11}
α	0.75	0.01092
C_O^*/C_R^*	0.05682	5.76109×10^{-4}
$Fe(CN)_6^{3-}$: GrEdge (1 nm)		
$E^{0'}$ (V)	0.25	0.01776
k^0 (cm/s)	0.0596608	1.28916×10^{-2}
i_{ss} (1 mM) / A	$9.86448 \times 10^{-9} \times 10^{-8}$	1.64368×10^{-10}
α	0.30811	0.00241

Overall, the values of k^0 and m for GrEdge electrodes are in very good agreement with the qualitative predictions discussed above in section 7.2.1.1. At unmodified GrEdge, the obtained k^0 values are in the range of 14 - 46 cm/s (45.3 cm/s for electrode in figure 7.16a) for FcMeOH. The ratio m/k^0 lies in 0.4 - 2.03 (0.49 cm/s for electrode in figure 7.16a) and clearly belongs to case 2 ($m/k^0 > 0.1$) kinetic regime of the model, in accordance with the quasi-steady-state voltammograms of figure 7.16a. Despite the very high k^0, the occurrence of a quasi-steady-state response can be explained by observing that the mass transfer coefficient is very high, which is around 16 cm/s, typical for nanoscale electrodes.

For $Fe(CN)_6^{3-}$, k^0 values are in the range of 0.06 - 1.6 cm/s (0.06 cm/s for the electrode in figure 7.16b), and varied considerably from one device to another. The larger variation in k^0 for $Fe(CN)_6^{3-}$ at the unmodified GrEdge is explained by the inner-sphere nature of HET of $Fe(CN)_6^{3-}$ with graphene electrodes and by the sensitivity to the local chemistry at the nanoscale edge. By comparing with the calculated mass transport coefficients (around 18 cm/s), the ratio m/k^0 is in the range of 11.6 - 370 (308 for the electrode in figure 7.16b), and comes under case 3 ($m >> k^0$) kinetic regime. It is apparent from the ratio values and the voltammograms, that for $Fe(CN)_6^{3-}$ a mass transport limitation is seldom attained, and hence, the HET is kinetically controlled. This is due to the very small electrode area of the unmodified GrEdge combined with the low k^0 value resulting in low conversion or depletion rates in comparison to the diffusional rate. The ET rates for $Fe(CN)_6^{3-}$ at the CVD-graphene edge are higher than the rates that have been reported at the basal plane of CVD-graphene.[158] However, high ET for this species has also been reported at the basal plane of highly oriented pyrolytic graphite (HOPG).[254] The differences in ET may be attributed to the difference in the origin of the graphene sheets (CVD vs HOPG) and due to varying

preparation procedures. While the high ET at the basal plane of HOPG was observed mainly at a freshly cleaved surface, the aging of the electrode and exposure to various chemicals led to a deterioration of the ET rate at the basal plane.[171] The CVD GrEdge, on the other hand, appears to be less prone to aging effects or exposure to chemicals, probably due to chemical and processing conditions such as O_2 plasma treatment used here.

GrEdge-AuNPs An important consequence of equations 7.5 or 7.6 is that when k^0 becomes large in comparison to m (case 1) or the ET becomes reversible, a Nernstian response (see figure 7.6b,d) is observed in the voltammetric curves. In such a case, it is not possible to obtain k^0 using the above fitting procedure. This is because the third term in the denominator (which is the only term that contains k^0) does not significantly affect the voltammetric response anymore. For the GrEdge-AuNPs, the increase in the surface area leads to a significant decrease in the m value. Hence, a Nernstian response is observed on several edge devices with large NPs, suggesting that ET is quite reversible at such electrodes. Therefore, to be able to extract k^0 from voltammetric profiles, it is necessary to increase m sufficiently such that its value gets comparable to k^0. This can be achieved at smaller particle sizes. Typically, a quasi-steady-state behavior is observed when the particle size is around 60 nm or less for FcMeOH and when it is 120 nm or less for $Fe(CN)_6^{3-}$, while for particles larger than these sizes, the response is essentially Nernstian for respective redox probes (see figure 7.6b,d) and hence a k^0 value cannot be extracted for such electrodes. For example, the current responses depending on particle sizes in figure 7.7 (see section 7.1.5) shows that for FcMeOH, a response near to perfect steady-state at 80 nm and a quasi-steady state response at 50 nm is obtained; and for $Fe(CN)_6^{3-}$, a perfect steady-state at 140 nm and a quasi-steady-state response at 80 nm is obtained.

For this, CVs were measured at GrEdge-AuNP electrodes with smaller particles (50 nm), and a reliable fit was obtained for three different concentrations of both the redox probes as shown in figure 7.17a,b in order to extract the fitting parameters. All the fitting parameters along with their statistical information are displayed in table 7.2. The linear fit between i_{ss} and concentration is apparent in figure 7.16c,d. The decoration of the GrEdge with AuNPs leads to an increase in the surface area, as confirmed by an analysis of background capacitive currents in supporting electrolyte KCl in the absence of the redox-active species (see capacitance analysis in figure 7.5 in section 7.1.3). Assuming again a quarter-cylinder (analogous to nanoparticle-modified CNTs[30,34,35] or similar to a metallic nanowire),[266,267] the surface area increases roughly by 2 orders of magnitude for particles of size around $\sim$ 50 nm (in comparison to an unmodified edge height of 1 nm). This leads to a reduction in the mass transport rate by more than 1 order of magnitude as seen for both experimentally extracted as well as calculated values in the same order: 0.93 and 0.64 cm/s for FcMeOH oxidation; 0.49 and 0.53 cm/s for $Fe(CN)_6^{3-}$ reduction.

For FcMeOH, k^0 is in the range of 2 - 3 cm/s (2.05 cm/s for the electrode in figure 7.17a). The reason for the lower k^0 at GrEdge-AuNP electrodes is not clear. It is worth noting that a range of k^0 values has been reported at various electrodes for FcMeOH.[266] An analogous strategy is pursued in the next section 7.2.2, using the adapted Koutecký–Levich (K-L) method, to obtain k^0 values from the voltammetric response at nanoelectrodes and UMEs.[31,262,266] The k^0 obtained from K-L analysis is 2.9 cm/s (see the section 7.2.2), and is in agreement with the values obtained from the curve-fitting method. With m as 0.64 cm/s, the m/k^0 ratio lies in 0.21 to 0.32 (0.31 for the electrode in figure 7.17a), and belongs to case 2 ($m/k^0 > 0.1$) kinetic regime of the model. This can be explained by taking into account that both m and k^0 have decreased by an order of magnitude after deposition of AuNPs (50 nm). However, m is still lower than k^0. Therefore, the mass transport limited

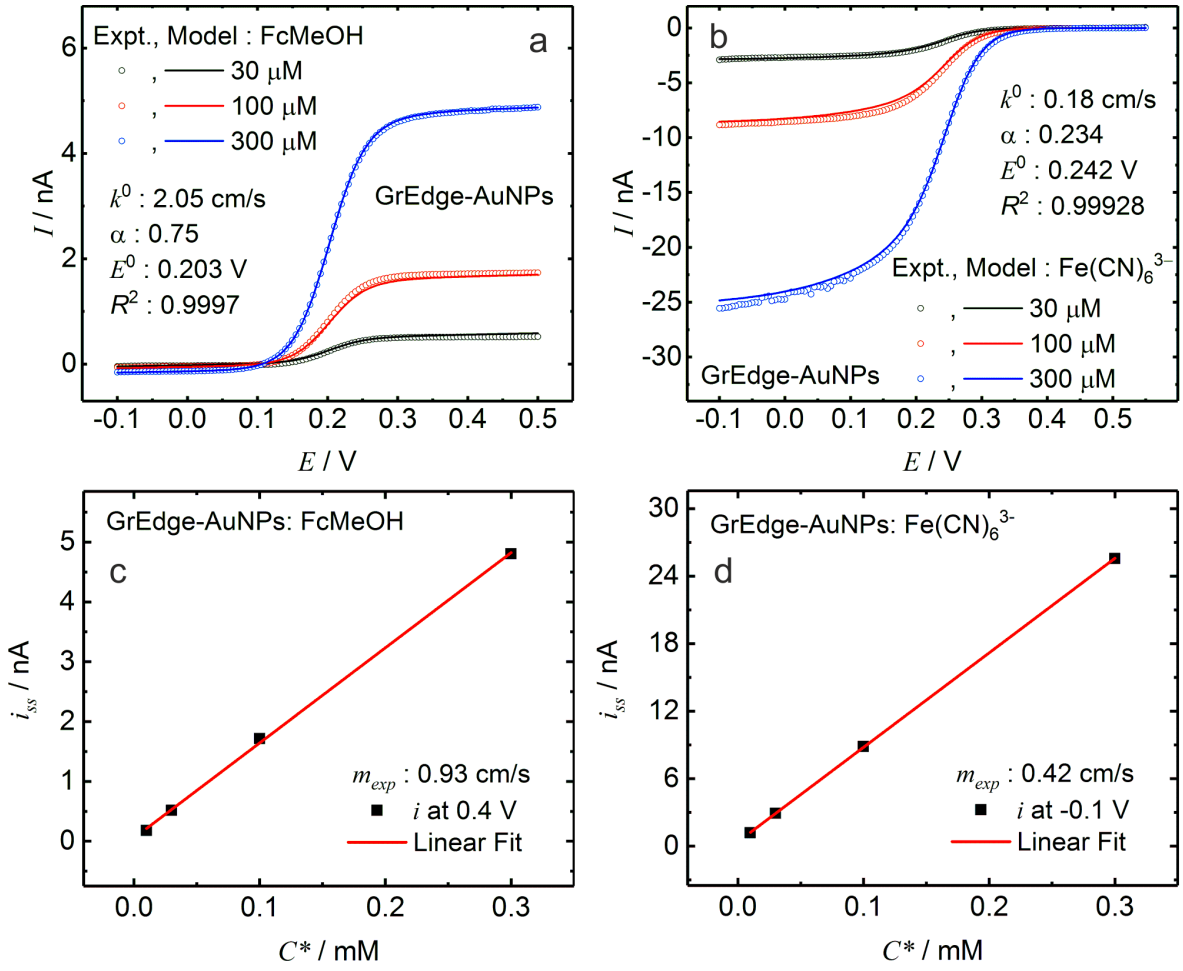

Figure 7.17: Curve-fitting at GrEdge-AuNP electrodes. (a,b) Experimental (open markers, Expt.) and the fitted (solid lines, Model) voltammetric responses for: (a) FcMeOH oxidation; (b) $Fe(CN)_6^{3-}$ reduction. The model parameters were obtained by fitting the experimental response to equations 7.5 and 7.6. A very good fit ($R^2 \approx 1$) is apparent between the experimental data and the model. Statistical information about the quality of the fit can be found in table 7.17. (c,d) Dependence of the steady-state current on concentration for: (c) FcMeOH oxidation (at 0.4 V); (d) $Fe(CN)_6^{3-}$ reduction (at -0.1 V). (scan rate: 5 mVs^{-1}, supporting electrolyte: 0.5 M KCl).

response for FcMeOH is similar to that observed at unmodified GrEdge electrodes, with validation by the observed quasi-steady-state.

Table 7.2: Results of the fitting in figure 7.17a,b with statistical information for: FcMeOH oxidation and $Fe(CN)_6^{3-}$ reduction at GrEdge-AuNPs (electrode height: 50 nm)

Parameter	*Estimate*	*Standard Error*
FcMeOH: GrEdge-AuNPs (50 nm)		
$E^{0'}$ (V)	0.20257	5.12836×10^{-4}
k^0 (cm/s)	2.046	0.354
i_{ss} (1 mM) / A	1.59248×10^{-8}	7.87888×10^{-11}
α	0.75	0.08583
C_O^*/C_R^*	0.02709	0.0013
$Fe(CN)_6^{3-}$: GrEdge-AuNPs (50 nm)		
$E^{0'}$ (V)	0.24175	7.17267×10^{-4}
k^0 (cm/s)	0.185	6.86892×10^{-3}
i_{ss} (A) / 1 mM	$8.32917 \times 10^{-8} \times 10^{-8}$	4.71018×10^{-10}
α	0.23353	0.01297

For $Fe(CN)_6^{3-}$, k^0 values are between 0.17 and 0.35 cm/s (0.18 cm/s for the electrode in figure 7.17b). These values are consistent with the comparatively higher k^0 for $Fe(CN)_6^{3-}$ at gold than at graphene.[158] The m/k^0 ratio is in between 1.5 and 3.1 (2.7 in this case, figure 7.17b), and comes under case 2 ($m/k^0 > 0.1$) kinetic regime of the model due to the higher values of k^0 in comparison to m. This is consistent with the observation of the quasi-steady-state and confirms that the response is mainly limited by mass transport.

Table 7.3 collects the results of the fitting with data from several devices, showing the range of the parameter values of k^0, the mass transfer coefficients (m, experimental or calculated), $E^{0'}$, and α, estimated for all four cases as discussed above (figures 7.16a,b and 7.17a,b).

In previous reports, the graphene edge has been modeled as a band electrode.[12,39,40] The values of k^0 and m obtained by the latter assumption are 1.5 times larger than the case when the (modified) GrEdge is considered as a quarter-cylinder. It can be possible that there is some uncertainty in the use of a certain value of electrode height, since it may vary along the millimeter-long edge electrode. The values of heights used in the fitting routine signify average height along the entire electrode, which is an assumption. The value of estimated k^0 is inversely proportional to the height value. For example, if the electrode height is taken to be twice higher, then k^0 will be reduced by half. The justification of the values of electrode height is provided by AFM images (see GrEdge-AuNP samples prepared using S1805, in figure 6.5, section 6.2). Hence, the m/k^0 ratio is unaffected with respect to either quarter-cylindrical or band electrode model, while the k^0 values obtained here represent a lower limit.[265]

Table 7.3: Table showing the range of parameter values extracted from the voltammetric data measured for at least three devices for each case. Except for the theoretical values of the mass transfer coefficient (m), all values are obtained from experimental curves and fitting according to the discussion for figures 7.16 and 7.17. For $Fe(CN)_6^{3-}$ at the free GrEdge, $m/k^0 > 10$ indicates kinetic control. For all other cases, the ratio is between 0.1 and 10, corresponding to the quasi-steady-state regime. When the particle sizes of the GrEdge-AuNP electrodes become large (not shown in the table), m decreases and the ratio becomes less than 0.1, yielding Nernstian voltammetric profiles.

Redox Probe	*Sample*	$E^{0'}$ (V)	α	k^0 (cm/s)	m (cm/s)		$m^{calc.}/k^0$
					exp.	*calc.*	
FcMeOH	GrEdge	0.20 - 0.22	0.75 - 0.81	14 - 46	9 - 18	22.6	0.62 - 2.03
	GrEdge -AuNPs	0.20 - 0.22	0.67 - 0.80	2 - 3	0.3 - 2.2	0.64 / 50 nm	0.21 - 0.32
$Fe(CN)_6^{3-}$	GrEdge	0.24 - 0.25	0.19 - 0.31	0.06 - 1.6	-	18.5	11.6 - 370
	GrEdge -AuNPs	0.24 - 0.25	0.23 - 0.48	0.17 - 0.35	0.2 - 0.9	0.53 / 50 nm	1.5 - 3.1

7.2.2 Koutecký - Levich (K-L) Model

The classical Koutecký-Levich (K-L) model is a simple method to analyze steady-state voltammograms at the rotating disk electrode (RDE), where the mass transfer coefficient (m) is modulated by varying the rotation rate or angular velocity. However, due to limitations on the attainable angular velocity, the measurable kinetic parameter (k^0) is limited to lower than 0.05 cm/s.[268] Bard and co-workers have developed the adapted K-L model in order to estimate k^0 for the case of fast HET at UMEs. Here, m is modulated by varying the size of the nanoelectrodes and UMEs, instead of angular velocity.[31,262] The slope and y-intercept obtained from a linear plot of 1/current density ($1/j$) vs $1/mC^*$ (at different potentials generated from the steady-state voltammograms) allows for the extraction of kinetic parameters. The K–L model was earlier adapted in the heterogeneous electrochemical kinetic study with UMEs by the Bard group for redox probes: $Fc(MeOH)_2$, $Ru(NH_3)_6^{3+}$.[31,262]

7.2.2.1 Theory & Model

Here, the derivation for the method is presented along the same lines of reference [262], adapted accordingly to the conventions used in this thesis. The overall current density for a quasi-reversible one-step, one-electron oxidation reaction, can be expressed as (positive current for oxidation):

$$j = Fk^0[C_R^S.e^{(1-\alpha)f\eta} - C_O^S.e^{-\alpha f\eta}] \tag{7.8}$$

where $f = F/RT$, $\eta = E - E^{0'}$ and surface concentrations: $C_R^S = C_R^* \left(1 - \frac{j}{j_{ss,ox}}\right)$, $C_O^S = C_O^* \left(1 - \frac{j}{j_{ss,red}}\right)$. j_{ss} is the steady-state/ mass transport limited current for oxidation (ox) or reduction (red), given by $j_{ss,ox} = Fm_R C_R^*$ and $j_{ss,red} = -Fm_O C_O^*$. The exchange

current density is given by

$$j_0 = Fk^0 C_R^* e^{(1-\alpha)f(E_{eq}-E^{0'})} \tag{7.9}$$

where

$$E_{eq} = E^{0'} + \frac{1}{f}\ln\left(\frac{C_O^*}{C_R^*}\right)$$

We define a concentration ratio p as:

$$\frac{C_O^*}{C_R^*} = e^{f(E_{eq}-E^{0'})} = 1/p \tag{7.10}$$

Substituting equation 7.10 in 7.9, j_0 can be re-written as,

$$j_0 = Fk^0 C_R^* p^{-(1-\alpha)} \tag{7.11}$$

We set $m_R m_O = q$, and $u = e^{f\eta}$. Substituting all the above in equation 7.8,

$$\frac{1}{j} = \frac{1}{Fk^0 C_R^*}\left(\frac{pu^\alpha}{pu-1}\right) + \frac{1}{Fm_R C_R^*}\left(\frac{pu+pq}{pu-1}\right) \tag{7.12}$$

A plot of $\frac{1}{j}$ versus $\frac{1}{m_R C_R^*}$ called a K-L plot gives a straight line for a given u (or for a given E), whose slope approaches $\frac{1}{F}$ for large u , large p and $q = 1$. The y-intercept (j_{int}) is given by,

$$j_{int} = \frac{1}{Fk^0 C_R^*}\left(\frac{pu^\alpha}{pu-1}\right)$$

Since there are only reduced species in solution, and the amount of the generated oxidized species can be considered low at the electrode surface, p is assumed to be large. Therefore, the y-intercept can be approximated as:

$$j_{int} = \frac{1}{Fk^0 C_R^*} u^{-(1-\alpha)} \tag{7.13}$$

Hence, the value of the intercept varies as a function of u (or alternatively E). Equation 7.13 can be re-written as:

$$\ln j_{int} = \ln\left(\frac{1}{Fk^0 C_R^*}\right) - (1-\alpha)f\eta$$

$$\ln j_{int} = \ln\left(\frac{1}{Fk^0 C_R^*}\right) - (1-\alpha).\left(\frac{F}{RT}\right).(E-E^{0'}) \tag{7.14}$$

A plot of lnj_{int} versus $(E-E^{0'})$ gives a straight line whose:

$$slope = -(1-\alpha)\frac{F}{RT}$$

and

$$intercept = \ln\left(\frac{1}{Fk^0C_R^*}\right)$$

from where α and k^0 can be extracted.

7.2.2.2 Application

The adapted K-L method is applied on a single GrEdge device, by vary the particle size in four consecutive electrochemical modification steps to modulate m. The height of AuNPs at the GrEdge after each of the 4 ECMs are 20, 35, 50 and 65 nm, respectively, with a constant edge length of 2.3 mm. The GrEdge modified by AuNPs is similar to a nanowire, and has quarter-cylindrical geometry. The mass transfer coefficient m is given for the cylindrical form as: $m = \frac{2D}{r \ln \tau}$ (equation 7.7) where $\tau = \frac{4Dt}{r^2}$, $t = \frac{RT}{F\nu}$, D is the diffusion coefficient of FcMeOH (7.4 $\times$ 10^{-6} cm^2/s), T is temperature (298 K), ν is the scan rate (in mVs^{-1}), r is the apparent radius ($h/4$), and h is the average height of the AuNPs. In the potential range

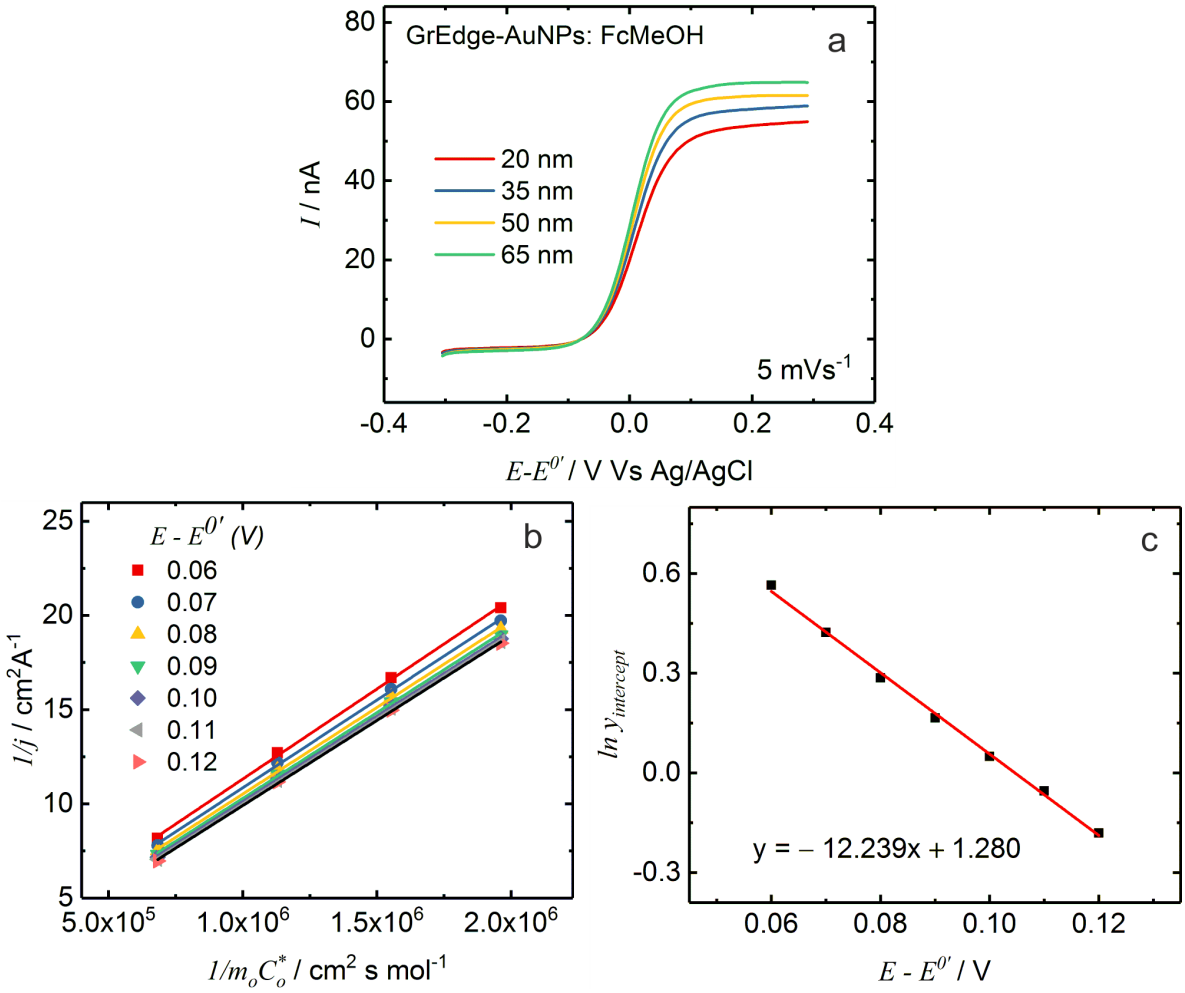

Figure 7.18: Adapted K-L analysis to estimate k^0: (a) CV obtained for oxidation of 1 mM FcMeOH at GrEdge-AuNP electrodes with 20 - 65 nm particle height in 0.5 M KCl. (b) K-L plots generated from CVs in (a). (c) Linear plot of $ln(j_{int})$ vs. $(E - E^{0'})$ obtained from (b).

of $E - E^{0'} \geq$ 0.04 V, u becomes significantly large, thus resulting in the slopes of K–L plots approaching $1/F$. The y-intercepts in the potential range from 0.05 to 0.15 V were obtained using the K-L plots as shown in Figure S12c. By plotting $ln(j_{int})$ versus $(E - E^{0'})$, both α and k^0 were determined from the obtained slope and y-intercept according to the obtained equation (based on the equation 7.14) shown in figure 7.18c as $k^0 =$ 2.9 cm/s and $\alpha =$ 0.69. The k^0 value obtained in this manner is close to the value from the fit in figure 7.17a.

7.3 Summary

In summary, a detailed electrochemical characterization of free and modified (with AuNPs) monolayer graphene edge electrodes using classical redox probes is presented here for the first time. The voltammetric curves strongly indicate that the realized GrEdge and GrEdge-AuNP electrodes behave like a one-dimensional electrode with typical nanoelectrode (or UME) responses, and properties such as (quasi)-steady-state current, reduced capacitance, and absence of ohmic effects. The fitting of the voltammograms to the general theoretical model (based on the Butler-Volmer kinetics) gives high ET rates, $k^0 >$ 14 cm/s for the outer-sphere redox probe FcMeOH, and $k^0 >$ 0.06 cm/s for the inner-sphere redox probe $Fe(CN)_6^{3-}$. A quasi Nernstian and kinetically controlled responses are observed for FcMeOH and $Fe(CN)_6^{3-}$, respectively, at the unmodified GrEdge. After the modification of GrEdge with AuNPs, a mass-transport-limited Nernstian response is observed (due to the decrease in mass transport rates) for both the redox probes. The ET characteristics improves for $Fe(CN)_6^{3-}$, consistent with the superior ET reported for it at AuNPs. The presented graphene edge electrodes enables the availability of a new form of one-dimensional graphene nanoelectrodes with the capability to study fast electron transfer kinetics and when modified with different metals, such electrodes can also be evaluated for applications in electrocatalysis.

8

Analytical Performance of the Graphene Edge Nanoelectrodes

The results of the experiments presented here were published in the following manuscript: A Yadav, M Wehrhold, T J Neubert, R M Iost and K Balasubramanian Fast Electron Transfer Kinetics at an Isolated Graphene Edge Nanoelectrode with and without Nanoparticles: Implications for Sensing Electroactive Species. *ACS Appl. Nano Mater. 2020, 3, 12, 11725*.

The combination of material like graphene and nanoscale dimensions makes graphene edge an ideal electrode material in the field of analytical chemistry to realize microsensors for detecting chemical and biological molecules. The nanoscale dimension is also beneficial for measurements of local concentration profiles and very small sample volumes analysis. Therefore, nanoelectrodes are suitable candidates for detecting electroactive species and hence are promising for the realization of portable electrochemical nanosensors.

There have been few reports suggesting superior electrocatalytic activity for isolated graphene edge than graphene basal plane. In this chapter, the sensing performance of the isolated graphene edge electrodes is evaluated in terms of electrocatalytic activity and detection limit for various redox species. The edge electrodes are tested for the detection of the reduced form of nicotinamide adenine dinucleotide (NADH) and flavin adenine dinucleotide (FAD) as electrochemical sensors. A limit of detection for NADH attained in this work is nearly three orders of magnitude better than previous reports. In several applications, the sensor characteristics could be improved by the introduction of nanoparticles, however, this depends very much on the chemistry of the electrode interface and the actual interaction with the electroactive species of interest. There is only one demonstration of modified single graphene edge electrodes with nanoparticles, which showed a lower onset potential for the reduction of oxygen and could be used for realizing glucose sensors.[149]

8.1 Redox Probes

FcMeOH The concentration dependence at the pristine and modified edge electrodes is presented in figure 8.1a,b. The quasi-Nernstian response at the unmodified GrEdge as well as the steady-state response at the GrEdge-AuNP electrodes is well reproduced for all concentrations for FcMeOH. It is clearly visible that steady-state current increases with an increase in the concentration of FcMeOH. Furthermore, the extracted Faradaic current densities at 1 mM FcMeOH concentration are in the range of 0.1 - 1 and 0.01 - 0.05 A/cm^2 for the free GrEdge and for the GrEdge-AuNPs, respectively, consistent with previous reports.[33,39] The current densities are calculated by normalizing the (quasi)-steady-state current (at 0.4 V) by the geometric area (calculated by assuming the exposed edge a quarter-cylinder with average thickness of 1 nm and 70 nm for unmodified GrEdge and modified GrEdge with AuNPs, respectively, as shown previously in chapter 7) of the corresponding electrode. With nanoparticles, although the measured current increases, the estimated Faradaic current den-

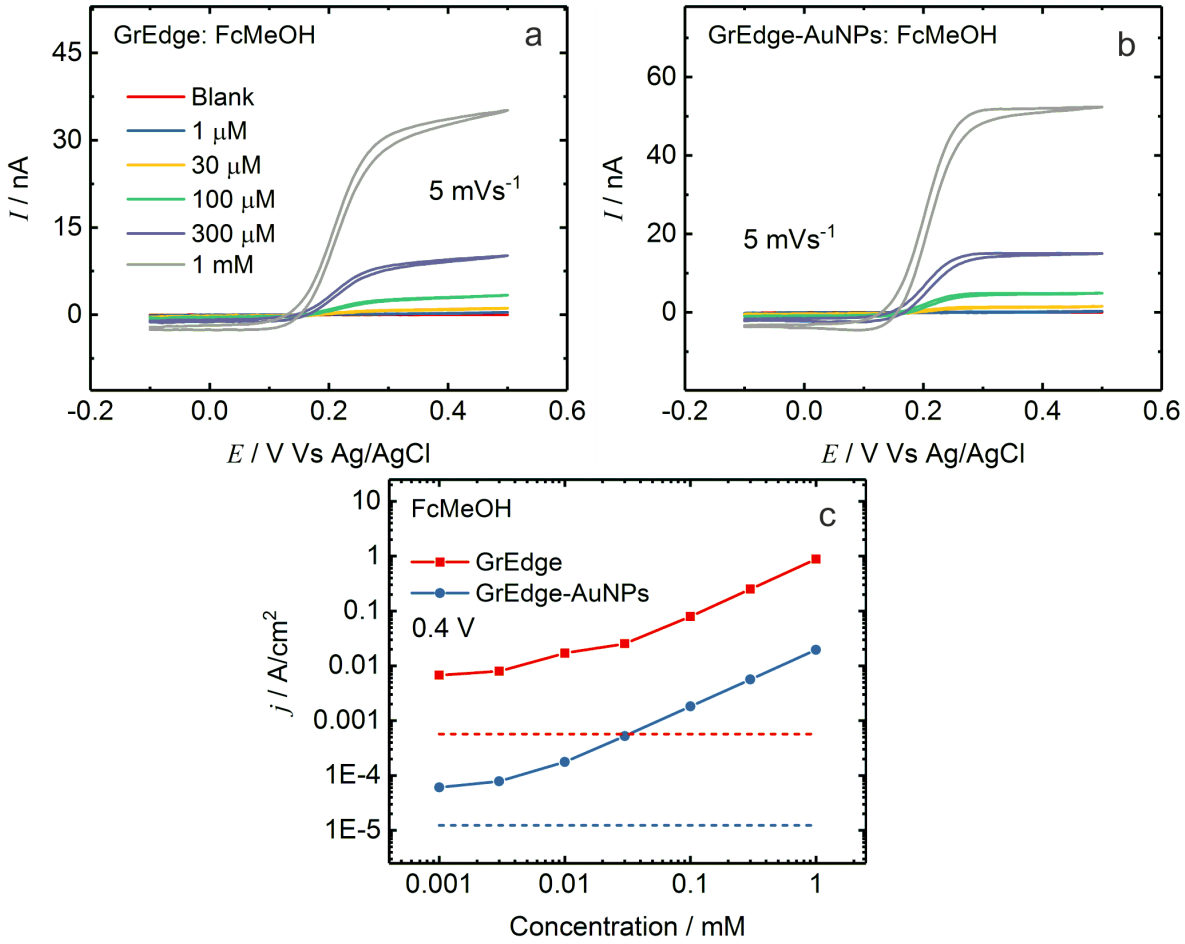

Figure 8.1: (a,b) CVs for the oxidation of different concentrations of FcMeOH at (a) GrEdge (measured at different device, is different from the figure 7.1a, chapter 7), and (b) GrEdge-AuNP electrodes. (c) Concentration dependence of the steady-state current density at 0.4 V. Scan rate: 5 mVs^{-1}, supporting electrolyte: 0.5 M KCl. The dashed line shows the mean background current plus thrice the standard deviation.

sity drops to lower values. The log-log plot of current density against FcMeOH concentration in figure 8.1c, shows that the current density increases with concentration and it is lower for GrEdge-AuNPs for all concentrations. The dashed line shows the mean background current density plus thrice the standard deviation. It is apparent that concentrations as low as 10 µM can be detected even using CV for both the cases and the detection limit with AuNPs is at a similar level as for unmodified GrEdge. The limit of detection (LOD) is estimated as the concentration at which the current (or current density) can be clearly distinguished from the baseline (dashed line in the graphs) and from the response for the next lower concentration.

$Fe(CN)_6^{3-}$ The current response is plotted for different concentrations of $Fe(CN)_6^{3-}$ measured at both the GrEdge and GrEdge-AuNP electrodes in figure 8.2a,b. At unmodified GrEdge, kinetically limited current response is present, while at GrEdge-AuNP electrodes the quasi-steady-state current response is present, for all concentrations of $Fe(CN)_6^{3-}$, and there is a systematic increase in current with concentration. The extracted current densities at 1 mM $Fe(CN)_6^{3-}$ concentration are in the range of 0.3 - 2 and 0.02 - 0.1 A/cm^2 for the

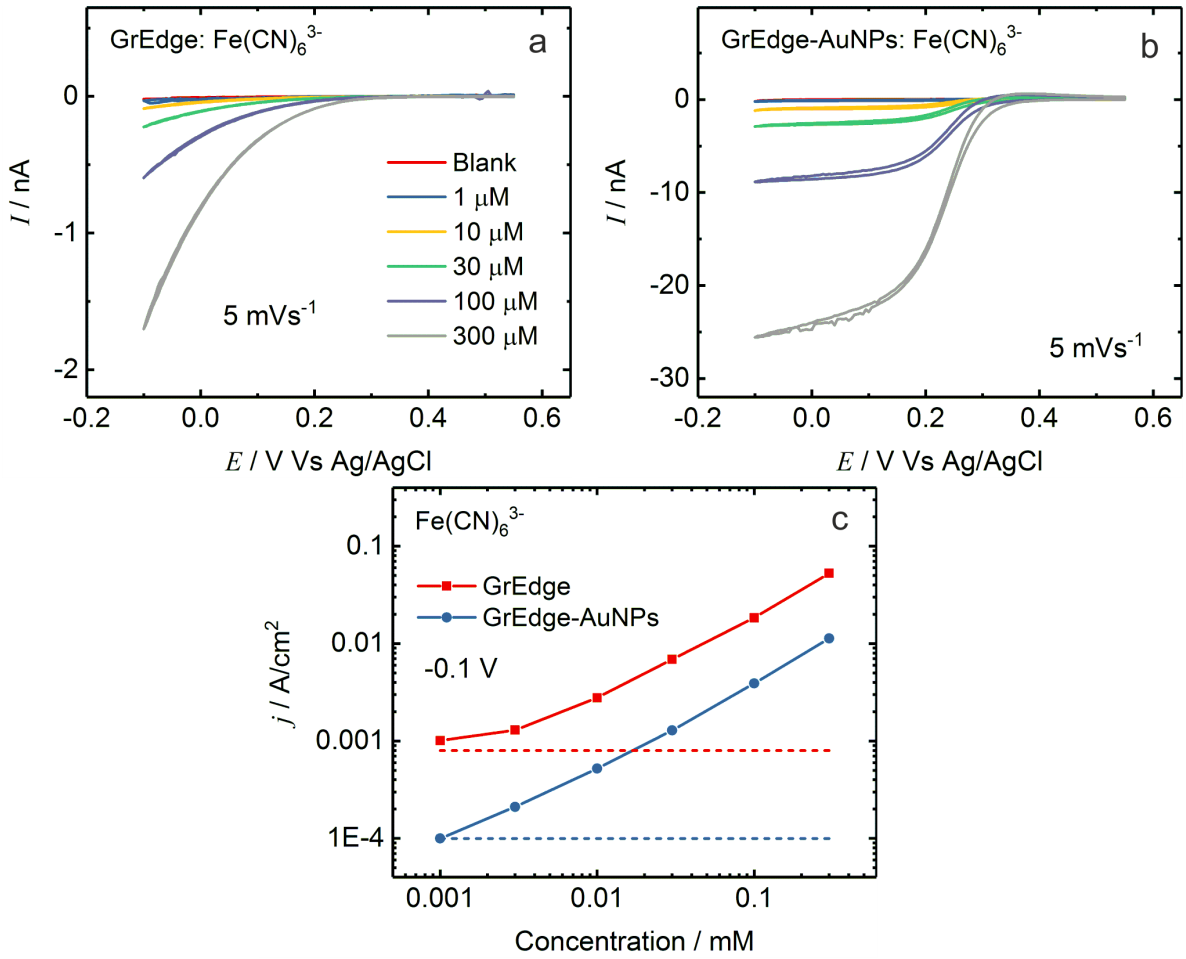

Figure 8.2: (a,b) CVs for the reduction of different concentrations of $Fe(CN)_6^{3-}$ at (a) GrEdge and (b) GrEdge-AuNPs electrodes. (c) Concentration dependence of the current density at -0.1 V. Scan rate: 5 mVs^{-1}, supporting electrolyte: 0.5 M KCl. The dashed line shows the mean background current plus thrice the standard deviation.

free GrEdge and for the GrEdge-AuNPs, respectively. It is apparent from the log-log plot of current density against $Fe(CN)_6^{3-}$ concentration in figure 8.2c that the detection limit for unmodified GrEdge is similar to GrEdge with AuNPs, and the concentrations as low as 3 - 10 µM can be detected using CV for both the cases.

A similar detection limit down to 10 - 30 µM has also been observed for other redox probes such as $Fe(CN)_6^{4-}$, $IrCl_6^{2-}$ and $IrCl_6^{3-}$ in figure 8.3. The obtained detection limits are lower than values at other individual edge electrodes reported in the low millimolar range until now.[12,33,39]

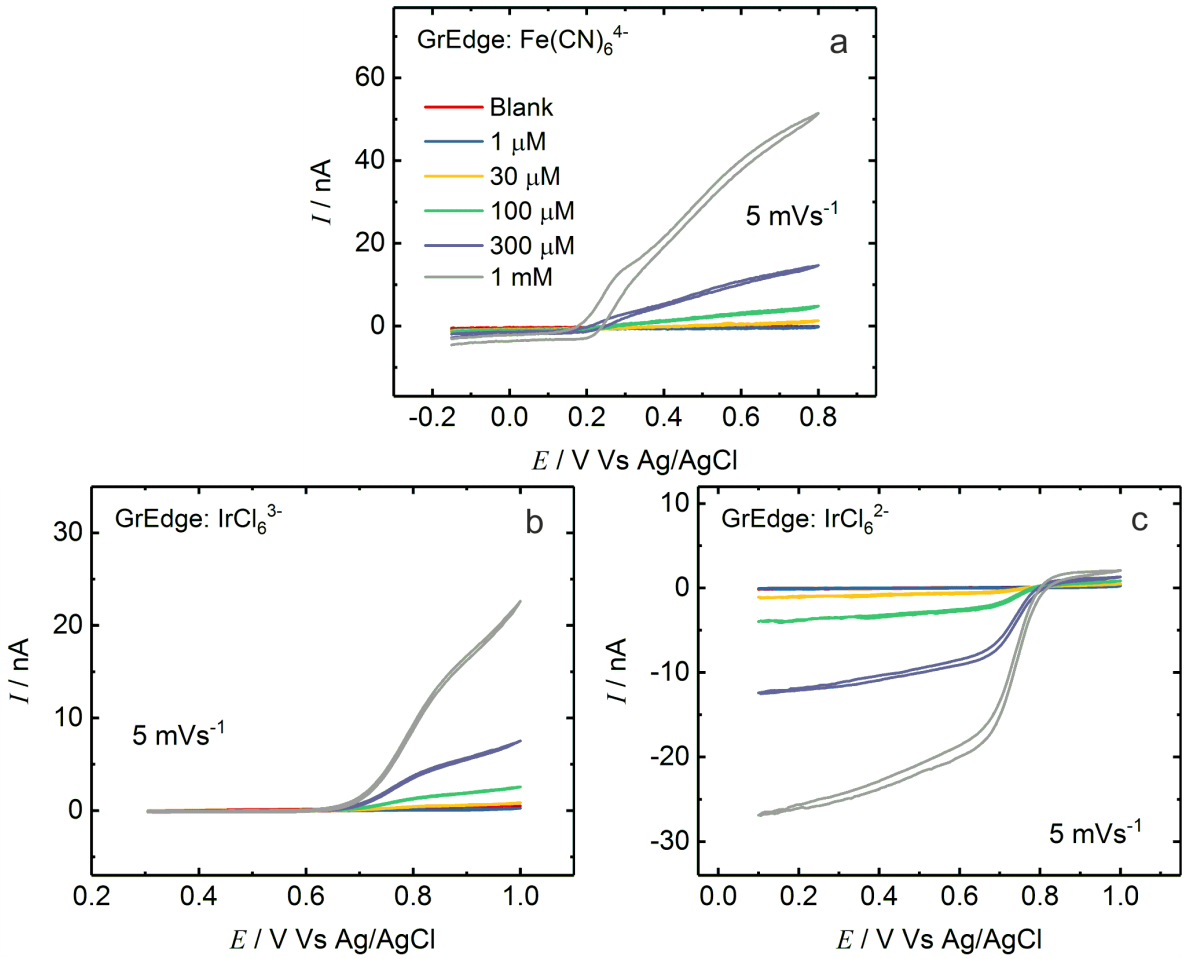

Figure 8.3: (a,b) CVs for the reduction of different concentrations of $Fe(CN)_6^{3-}$ at (a) GrEdge and (b) GrEdge-AuNPs electrodes. (c) Concentration dependence of the current density at -0.1 V. Scan rate: 5 mVs^{-1}, supporting electrolyte: 0.5 M KCl. The dashed line shows the mean background current plus thrice the standard deviation.

8.2 Application as Electrochemical Sensors

One main motivation for investigating GrEdge electrodes is to evaluate their performance for a sensing application. For this, both types of electrodes are evaluated as electrochemical sensors for the detection of the reduced form of nicotinamide adenine dinucleotide (NADH) and flavin adenine dinucleotide (FAD).

8.2.1 NADH

NADH and NAD^+ are important carriers (transferring electrons and protons) in many biosynthetic reactions in living organisms. They are cofactors of several hundreds of enzymes and play major roles in the development of electrochemical enzyme biosensors and biofuel cells, which use dehydrogenase enzymes. NADH transforms to its oxidized form NAD^+ by reducing the substrate. Figure 8.4a presents the molecular structure of NADH. The three-step mechanism (according to ref. [269]) for its oxidation to NAD^+ involves the transfer of two electrons and one proton as shown by the three reactions in figure 8.4b: a HET to form a cation radical $NADH^{\bullet+}$; a deprotonation reaction to form of neutral radical $NAD^{\bullet}$ and a second HET to form NAD^+. Therefore, overall the oxidation of NADH to NAD^+.

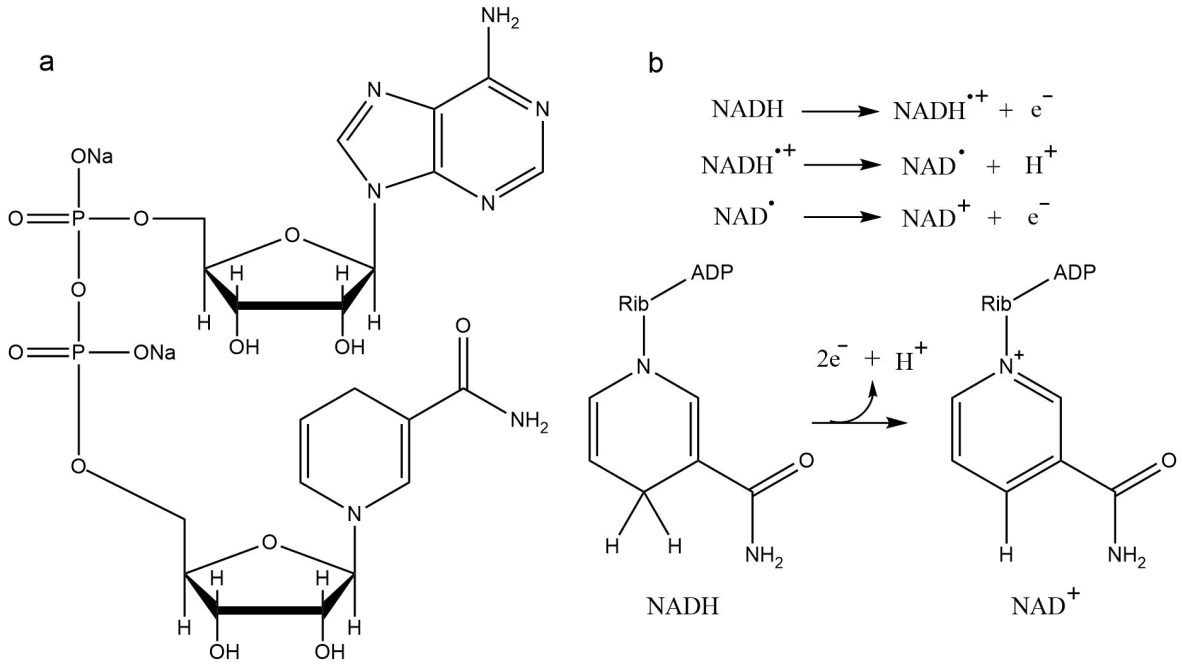

Figure 8.4: (a) Molecular structure of NADH (b) The three step mechanism for oxidation of NADH to NAD^+.

Electrocatalytic Activity Figure 8.5a-c present CVs for the oxidation of NADH at the graphene basal plane and two kinds of edge electrodes at a high scan rate (50 mVs^{-1}). From figure 8.5b,c it is directly clear that the major advantage of using GrEdge (in comparison

to the basal plane) in this case is the improvement in ET as inferred by a much lower onset potential. At the GrEdge electrode, the CV exhibits an oxidation peak centered at 0.38 V for cycle 1 and 0.395 V for cycle 2 (figure 8.5b), while the corresponding peak at the GrEdge-AuNPs electrode is at the same position (0.39 V) for both cycles (figure 8.5b). In comparison, the corresponding the peak at the graphene basal plane electrode is positively shifted to 0.66 V for cycle 1 and 0.67 for cycle 2 (figure 8.5a). This is consistent with previous reports on single edge electrodes.[12] However, the peak currents on cycle 2 are

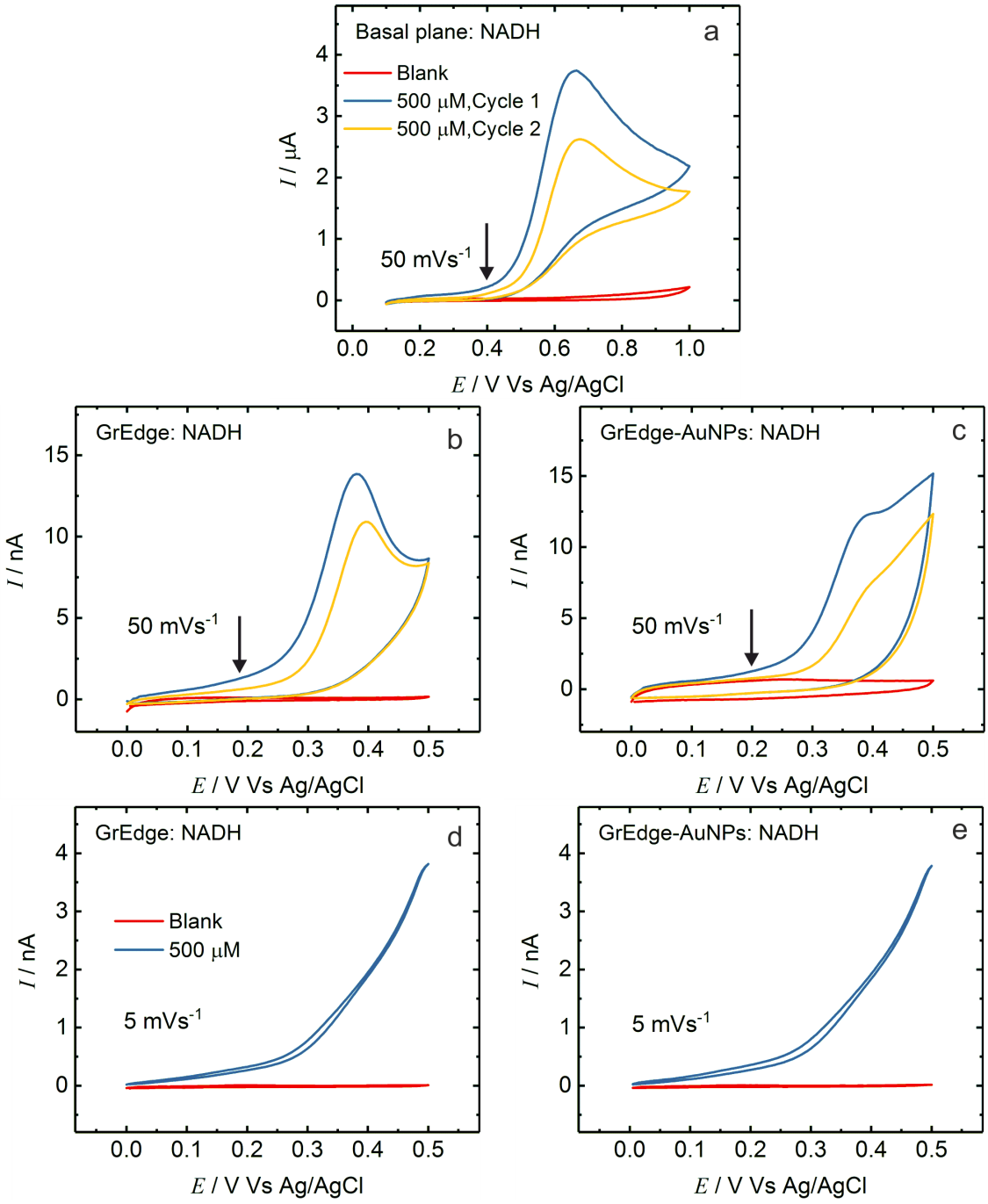

Figure 8.5: CVs for the oxidation of 500 μM NADH in phosphate buffer (pH 7) at (a) the graphene basal plane (50 mVs^{-1}), (b) GrEdge (50 mVs^{-1}), (c) GrEdge-AuNP (50 mVs^{-1}), (d) GrEdge (5 mVs^{-1}), and (e) GrEdge-AuNP (5 mVs^{-1}) electrodes.

observed to be much weaker than that on cycle 1 for all three electrodes. This is because the oxidation of NADH at most electrode materials results in the passivation of the electrodes due to the adsorption of the oxidized product, NAD^+ and thereby decreasing the passing currents.[270] This type of passivation with NAD^+ adsorption has been observed earlier on glassy carbon, CNTs, basal plane (BPPG), and edge plane (EPPG) of HOPG.[173,270,271]

The electrochemical results described above indicate that both types of graphene edges (GrEdge and GrEdge-AuNPs) are much superior to its basal plane on the electrocatalytic oxidation of NADH, and this may be attributed to more defective sites or oxygen-containing groups at the interface of edge electrodes, which reduce the over-potential for NADH oxidation (indicated by the arrows in figure 8.5a-c). On the other hand, the surface of the basal plane electrode has a nearly perfect sp^2 hybridized graphitic lattice. Furthermore, the higher shift of potential in cycle 2 can be explained by stronger passivation at the GrEdge electrode (defects are more prone to the adsorption of NAD^+ ions)[270] in comparison to GrEdge-AuNP and basal plane electrodes. This also means that the electrocatalytic activity of graphene-type nanostructures is directly correlated to the defects on their surfaces.

Another observation to note is that in both the edge electrodes the redox appears to be kinetically limited since there is no steady-state current plateau as shown in figure 8.5e,f. This is consistent with the previous explanation (for the behavior of $Fe(CN)_6^{3-}$ at GrEdge, section 7.2.1 in chapter 7) since the rate for oxidation of NADH is expected to be much lower than that of $Fe(CN)_6^{3-}$, as is also apparent from a relatively high overpotential needed for the oxidation ($E^{0'}$) for NADH is -0.6 V vs. Ag/AgCl. Therefore, NADH oxidation comes under case 3 ($m >> k^0$) of the kinetic regime (according to the proposed model in figure 7.15, section 7.2.1), and hence the ET is kinetically limited.

Limit of Detection Figure 8.6a,b shows the dependence of current response on the concentration of NADH at GrEdge and GrEdge-AuNP electrodes. It is apparent that the current increases with an increase in concentration at both electrodes. The current was further converted to current density by dividing with the geometrical area of both the electrodes and the calculated peak current densities are 0.93 and 0.012 A/cm^2 for 1 mM NADH at GrEdge and GrEdge-AuNP electrodes, respectively. The current densities are plotted against concentration as a log-log plot in figure 8.6a,b. As expected, the current density at each concentration for the GrEdge electrode is higher than the GrEdge-AuNPs. The interesting aspect here is however that for the unmodified GrEdge, a detection limit as low as 10 µM can be reached which is similar to the redox probes (figures 8.1 and 8.2). The LOD at the GrEdge-AuNP electrode is higher by around an order of magnitude. The ratios of the redox current to the background current are as follows: 153.24 for GrEdge, 17.04 for GrEdge-AuNPs, and 8.54 for the basal plane. The highest signal-to-background ratio for the GrEdge electrode amongst all the electrodes measured is in agreement with the low LOD at GrEdge. It is interesting also to note that the LOD for NADH is lower at the unmodified GrEdge than

at the CVD graphene basal plane. It has been observed earlier that the detection limit was better at HOPG than at an edge plane pyrolytic graphite (EPPG) electrode.[171] However, the GrEdge electrode is quite different from the EPPG in terms of both the electrode material as well as the diffusion profile. The unique diffusion regime arising from the nanoscale nature of our GrEdge electrode should play a role in the improved detection limit of the edge in comparison to the basal plane. The EPPG/HOPG is prepared at much higher temperatures than CVD graphene and the history of the electrode and the chemicals they are exposed to have a significant effect on the electrochemical characteristics.[171] Therefore, it is clear that the choice of the redox analyte and its specific interaction with the electrode plays a significant role in the observed electrochemical characteristics.

The addition of nanoparticles to an electrode has very often been shown to improve the performance of electrochemical sensing.[149,272,273] However, for the sensing of NADH at GrEdge, this is not the case. For this, the oxidation of NADH is tested at GrEdge-

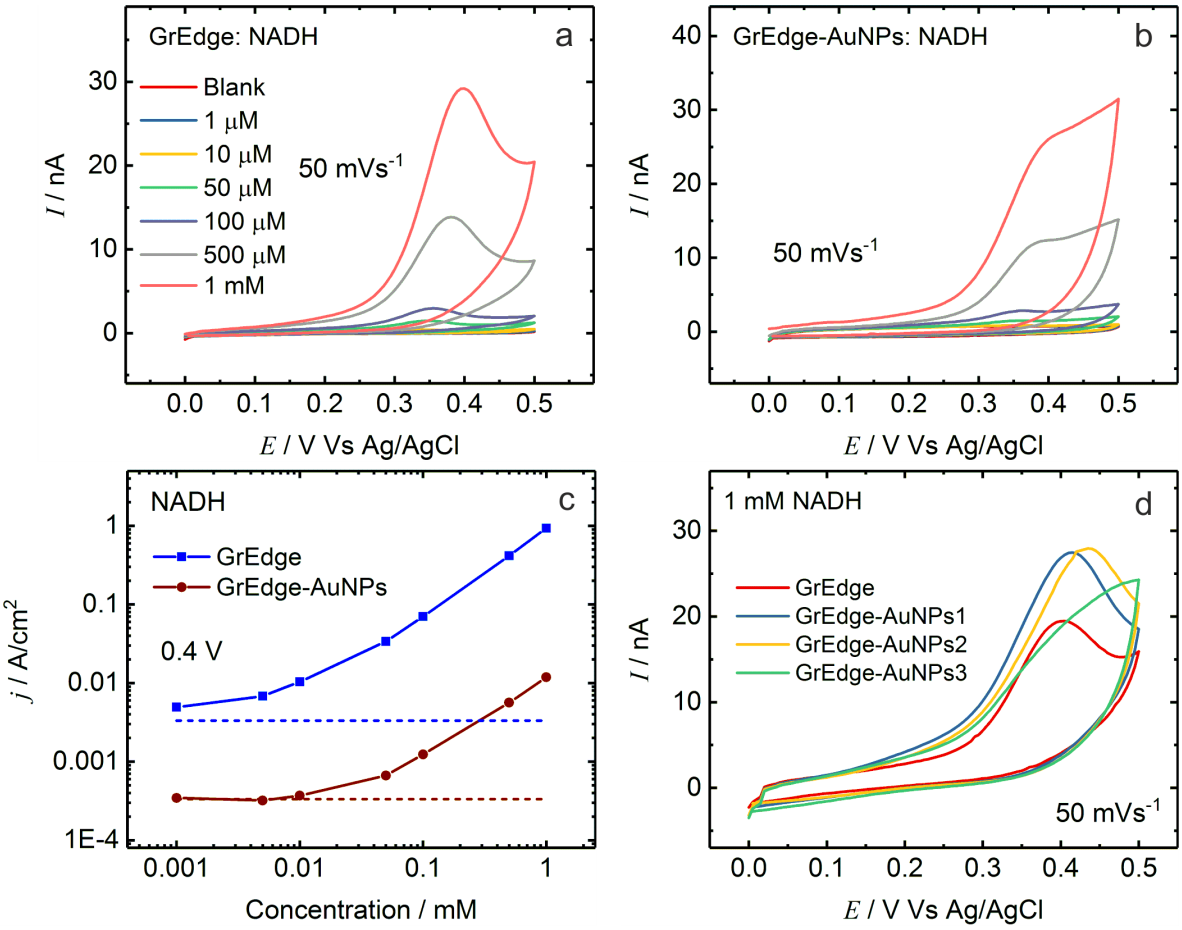

Figure 8.6: (a,b) CVs for the oxidation of different concentrations of NADH in phosphate buffer (pH 7) at (a) GrEdge and (b) GrEdge-AuNPs electrodes. (c) Concentration dependence of the current density at 0.4 V for both electrodes. The dashed line shows the mean background current plus thrice the standard deviation. (d) CVs for the oxidation of 1mM NADH in phosphate buffer (pH 7) at unmodified GrEdge electrode and modified GrEdge-AuNP electrodes after three subsequent ECMs with AuNPs (GrEdge-AuNPs1, GrEdge-AuNPs2, GrEdge-AuNPs3).

AuNP electrodes with different particle sizes (three subsequent ECMs with AuNPs at the same GrEdge electrode) as shown in figure 8.6d. The Faradaic current for NADH oxidation increases slightly after the first modification (for GrEdge-AuNPs1, blue curve), it remains the same after the second modification (for GrEdge-AuNPs2, yellow curve). After, the third modification the current decreases slightly, along with a weak peak-like feature. As a result, there is no significant improvement in the sensing response by the addition of AuNPs. Most likely the interaction of NADH (being an inner sphere probe) with carbon is superior to that of gold as has been reported earlier.[173,271,274] In order to further cross-check this behavior at GrEdge-AuNP electrodes, the sensing of another redox-active biochemically relevant molecule flavine adenine dinucleotide (FAD) is studied in the next section.

8.2.2 FAD

FAD is found in many enzymes and functions often as a cofactor in many enzymatic reactions in metabolism, such as cytochrome-b5 reductase enzyme in flavoproteins.[275] FAD can be reduced to form $FADH_2$ by using electrochemistry. Figure 8.7a presents the molecular structure of FAD, which consists of two portions: the adenine nucleotide in the form of adenosine monophosphate and the flavin mononucleotide (FMN), bonded together through their phosphate groups. The reduction of FAD to $FADH_2$ happens by the addition of two electrons and two protons as shown in Figure 8.7b. Figure 8.8a presents the sensing

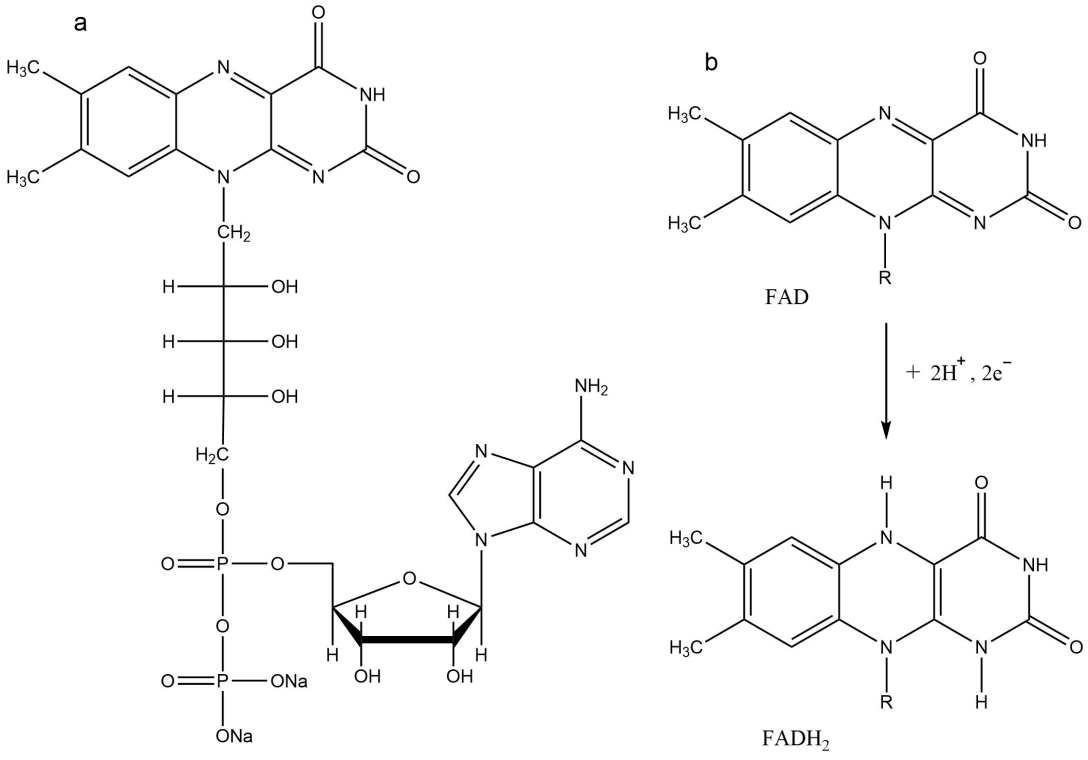

Figure 8.7: (a) Molecular structure of FAD (b) The mechanism for reduction of FAD to $FADH_2$.

response to 1 mM FAD at the same GrEdge without and with AuNPs of two different sizes (two subsequent electrodeposition cycles: GrEdge-AuNPs1, blue curve; and GrEdge-AuNPs2, yellow curves). In contrast to the case of NADH, there is a significant increase in the Faradaic currents due to the redox peaks of FAD upon subsequent addition of AuNPs. With every cycle of nanoparticle addition at the edge, the magnitudes of the oxidation and reduction peak currents are found to increase. The position of the FAD reduction peaks are at: -0.45 V (GrEdge), -0.456 V (GrEdge-AuNPs1), 0.467 V (GrEdge-AuNPs2) and -0.495 (basal plane) for the respective electrodes, with the lowest onset potential observed at the GrEdge electrode. The cyclic voltammograms become more reversible with the subsequent attachment of the Au particles. The peak spacing, or the potential separation between the anodic and cathodic peaks (ΔE_{pp}) is lower for the edge electrodes: 38 mV (GrEdge), 45 mV (GrEdge-AuNPs1), and 57 mV (GrEdge-AuNPs2) than 110 mV for the basal plane electrode. The values below 60 mV may indicate a reversible process and a fast charge exchange,[180] which is consistent with improved ET expected at the edges. These results show clearly that the nature of the interaction between the redox-active analyte and the (modified) graphene edge as well as the interfacial chemistry dictate the improvement in sensor performance attainable at GrEdge electrodes upon modification with AuNPs.

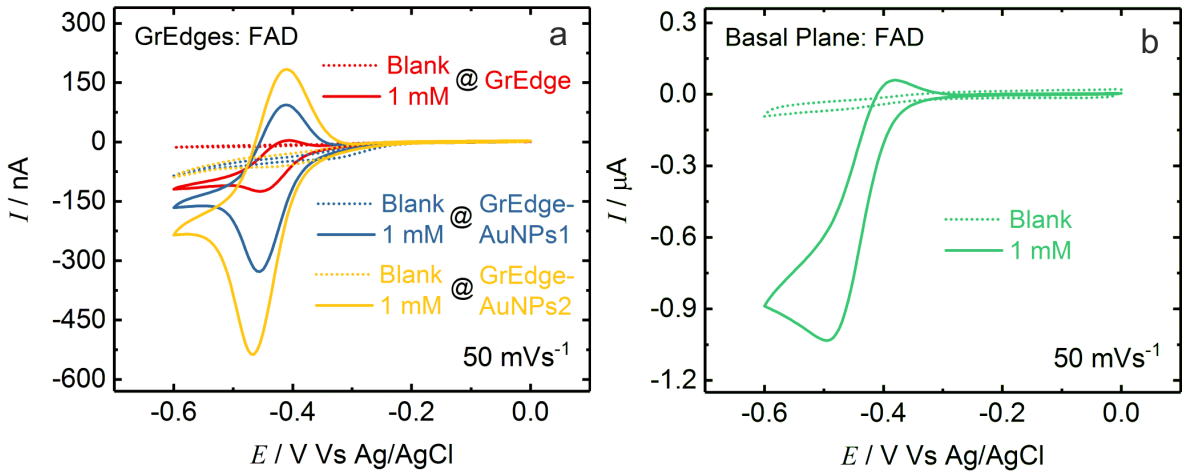

Figure 8.8: CVs showing the redox behavior of 1 mM FAD in phosphate buffer (pH 7) at (a) the same graphene edge electrode without (GrEdge, red curve) and with AuNPs (two subsequent electrodeposition cycles: GrEdge-AuNPs1, blue curve and GrEdge-AuNPs2, yellow curves) (b) the graphene basal plane electrode.

Figure 8.9 shows the dependence of current response on FAD concentration at unmodified and modified graphene edges as well as basal plane electrodes. It is apparent that the current increases with an increase in FAD concentration at all the electrodes in figure 8.9a-d. The calculated current densities for 1 mM FAD are: 3.1826 A/cm^2 (GrEdge), 0.27823 A/cm^2 (GrEdge-AuNPs1), 0.19536 A/cm^2 (GrEdge-AuNPs2) and 6.88 $\times$ 10^{-5} A/cm^2 (graphene basal plane), and it decreases with increase in GrEdge area after subsequent deposition steps, and is lowest at the basal plane electrode. The current densities at each concentration are further plotted as a log-log plot in figure 8.9e. The detection limit

of 50 µM is found at the GrEdge electrode which is higher than at NADH and redox probes. The LOD at the GrEdge-AuNPs1,2 and basal plane electrodes is found to be similar.

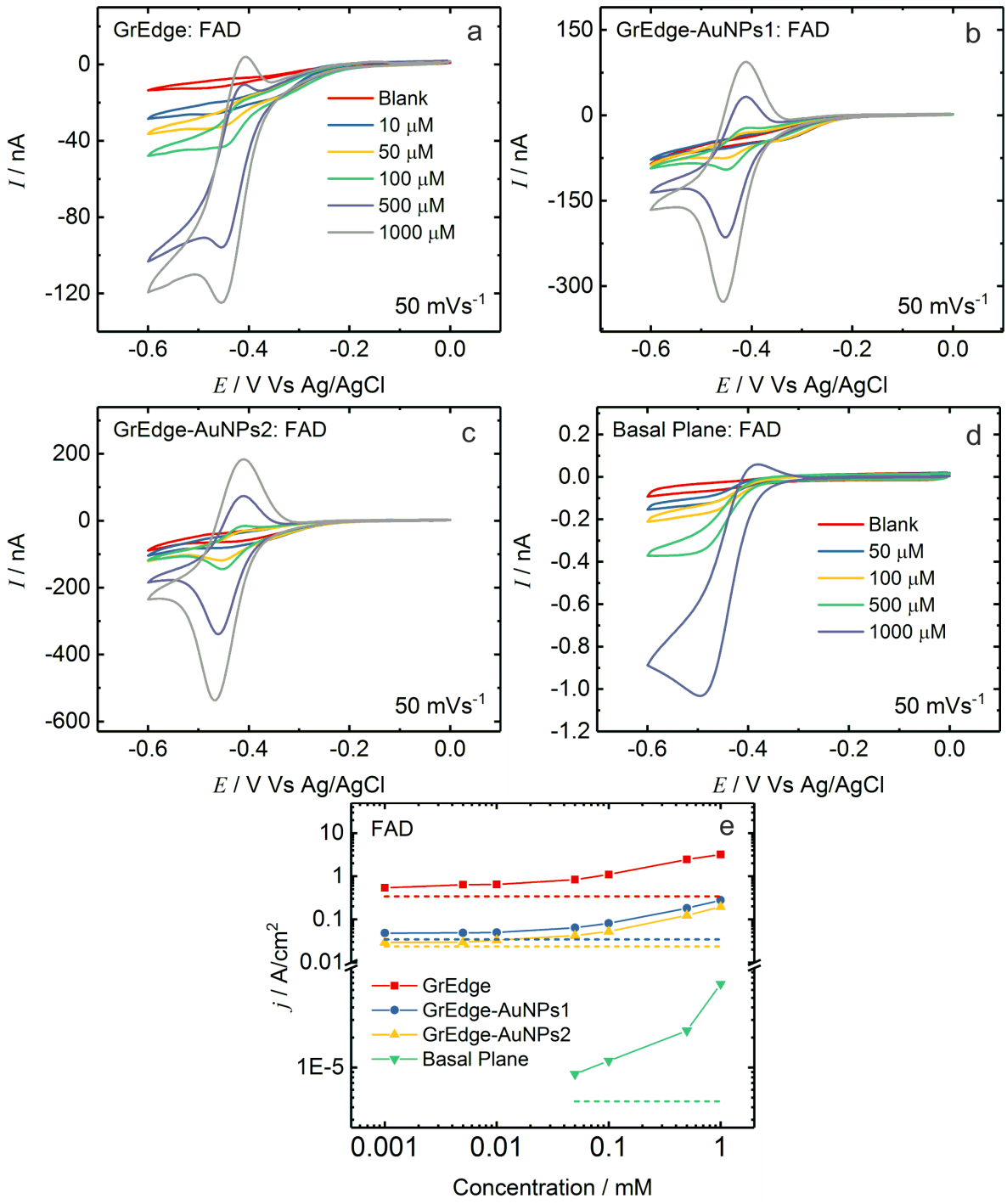

Figure 8.9: (a-d) CVs for the reduction of different concentrations of FAD in phosphate buffer (pH 7) at (a) GrEdge (b) GrEdge-AuNPs1 (after first deposition step) (c) GrEdge-AuNPs2 (after second deposition step) and (d) the graphene basal plane electrode. (e) Concentration dependence of the peak current density for all the electrodes in (a-d). The dashed line shows the background current.

8.3 Summary

For the analytical applications in electrochemical sensing, the unmodified GrEdge electrodes with their nanoscale dimensions exhibit currents with a high signal-to-background ratio enabling the detection of different electroactive analytes such as FcMeOH, $Fe(CN)_6^{3-}$, NADH down to 10 µM using cyclic voltammetry. Graphene edge (with and without AuNPs) also has a much stronger electrocatalytic activity than graphene basal plane, towards the oxidation of NADH and reduction of FAD. Upon the attachment of AuNPs, the sensing performance does not improve for NADH; however, for sensing of FAD, the redox peak characteristics improve along with higher Faradaic currents after the modification. These results indicate that the chemistry of the nanoscale interface needs to be engineered appropriately to maximize the sensing performance of such electrodes for the analyte of interest.

9

Summary and Outlook

The atomic graphene edge have been of great interest due to its superior reactivity and electron transfer (ET) properties in comparison to the relatively inert basal plane. The edge sites of graphene are known to influence the properties (e.g. bandgap, chemical reactivity) of graphene locally, and their role becomes dominant with stronger nanosize effects and consequent boundary conditions when narrowing down graphene sheets to edge-rich structures (e.g. GNRs). However, more details about the physical and chemical properties of the graphene edge remains to be elucidated, mostly due to difficulty in isolating the edges completely from the basal plane. This involves the role of the specific groups at the graphene edges, and the detailed ET properties at the graphene edges themselves. The focus of the thesis was on the isolation of the monolayer graphene edge from the basal plane contribution completely, while at the same time having the capability to address a single sheet.

This thesis demonstrates for the first time, the realization of the isolated graphene edge (GrEdge) nanoelectrodes using CVD-grown monolayer graphene on an insulating substrate, and subsequently the selective functionalization and electrochemical properties of the isolated edge. The isolated GrEdge was fabricated using photolithographic patterning by a simple strategy of insulation and etching (chapter 5). The GrEdge nanoelectrode consists of a line of graphitic carbon atoms (width of $\sim$ 1 nm, in an ideal case) with possibly the thinnest 1D nanowire (very high aspect ratio of 10^6-to-1) structure, realized in a 2D graphene basal plane (which acts as mere support and contact to the edge).

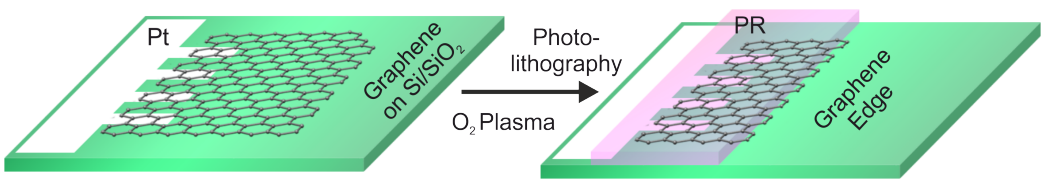

Figure 9.1: Fabrication of an isolated graphene edge electrode using photolithography and plasma etching.

Further, in chapter 6, the use of simple electrochemical modification was demonstrated to selectively and homogeneously attach nanoparticles (Au, Pt, Pd) and organic groups (non-covalently and covalently) at the edge under ambient conditions (summarized in figure 9.2). The deposition of Au nanoparticles provides an added advantage of surface-enhanced Raman spectroscopy (SERS), which was used to investigate the presence of chemical moieties at the pristine and functionalized graphene edges by means of local vibrational fingerprinting. The metal nanoparticles may enhance the catalytic properties of the edge electrodes. The functional groups may also serve as anchor molecules or layers for the subsequent coupling of suitable receptor molecules specific for a certain analyte in sensing devices based on graphene edges.

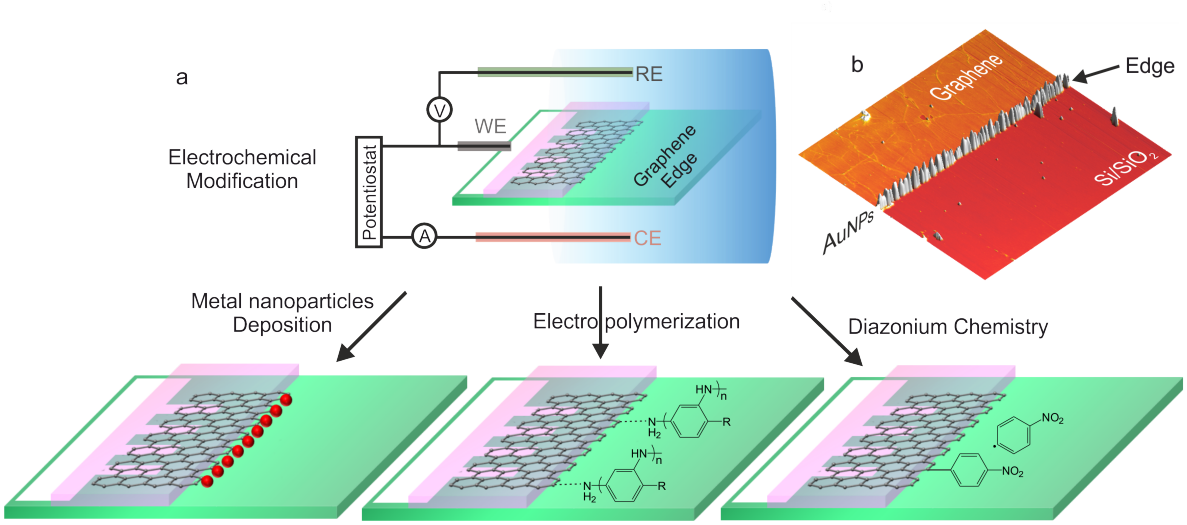

Figure 9.2: (a) Electrochemical modification of graphene edge selectively with different chemical moieties: metal nanoparticles, polymer, or diazonium salts. (b) A 3D AFM image showing gold nanoparticles modified graphene edge.

From the electrochemistry perspective (in chapter 7), graphene edge nanoelectrodes (and UMEs) offer several advantages over conventional graphene electrodes (basal plane) including insignificant electrical double layer capacitance, low background current, small active area, and negligible ohmic effects. These attributes make graphene edge nanoelectrode an important electrode material for applications such as investigation of fast electron transfer (ET) kinetics by using steady-state voltammetric response and electrochemistry in a solution containing little or even no added supporting electrolyte. For the first time, a detailed and fundamental study of ET processes (along with values of ET rate constant, k^0) at edge electrodes (in both pristine GrEdge and gold nanoparticles modified GrEdge-AuNPs) is presented (summarized in figure 9.3). This was studied using two different redox probes: outer-sphere FcMeOH, and the inner-sphere $Fe(CN)_6^{3-}$. For both the probes, the edge electrodes were found to exhibit very high mass transport rates, characteristic of nanoelectrodes (or ultramicroelectrodes). The voltammetric response strongly indicates that the realized GrEdge electrodes behave like a 1D nanowire electrode dictated by the kinetics

of heterogeneous electron transfer (HET). An analytical model was developed based on the Butler-Volmer kinetics, which provided the high ET rate constant value by the appropriate fitting of the responses. For FcMeOH, a quasi-Nernstian behavior is observed with $k^0 > 14$ cm/s. The HET at the inner-sphere redox probe $Fe(CN)_6^{3-}$ appears to be quite limited with a kinetically controlled response, and the obtained values of $k^0 > 0.06$ cm/s are among the highest reported for this probe at carbon-based electrodes until now.[158,171,276–278] Upon selective modification of the edge with gold nanoparticles (GrEdge-AuNPs), the ET characteristics has improved for $Fe(CN)_6^{3-}$, consistent with the superior ET reported for this probe at AuNPs. Therefore, HET is found to be reversible, with the voltammetric curves showing a mass-transport-limited Nernstian response for both kinds of probes at GrEdge-AuNP electrodes. This also demonstrates a way to modulate the fast ET properties and provides various kinetic regimes at the nanoscale interface of the edge by varying the dimensions (size of the AuNPs) of the nanoelectrode.

For electrochemical sensing applications, the analytical responses of both kinds of electrodes are evaluated as nanosensors for the detection of the reduced form of nicotinamide adenine dinucleotide (NADH) and flavin adenine dinucleotide (FAD) in chapter 8. The nanoscale geometry and a unique diffusional profile at the edge nanoelectrodes enable the sensing of NADH and FAD down to few micromolar concentrations with the exhibition of currents with a high signal-to-background ratio, and with low onset potential. The edge interface can be chemically modified and hence the application spectrum for chemical sensing and biological sensing can be widened. There is no effect on the sensing performance of NADH after attachment of AuNPs at the GrEdge. However, sensing of FAD improves with better redox peak characteristics as well as higher Faradaic currents after the modification of the edge with AuNPs.

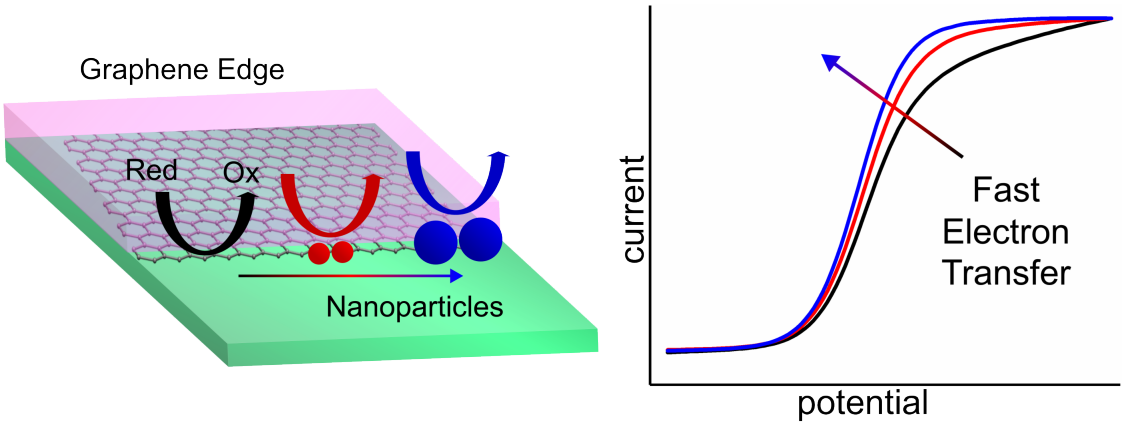

Figure 9.3: Electrochemistry at the graphene edge showing the (quasi)-steady-state voltammetric behavior with fast HET kinetics at the bare and AuNPs modified graphene edge nanoelectrodes. The fast HET can be modulated by changing the width (critical size) of the edges. Redox arrows and CV curves: Bare GrEdge (black) and after two subsequent ECMs of AuNPs at the same GrEdge (red and blue), with increase in width of the GrEdge in the same order.

The realization of such miniaturized electrodes based on the isolated graphene edge enables the availability of versatile high-aspect 1D nanoelectrodes. They have the capability to probe faradaic reactions in extremely small sample volume spaces, such as inside a single vesicle, a biological cell, or a single droplet, which are otherwise difficult or even impossible to measure with conventional electrodes. Further, the nanosize enables to study the fast electron transfer kinetics by steady-state experiments. The detailed electrochemical investigation may also help to provide further clarification on the comparative HET behavior between the edge and the basal plane. Moreover, the use of selective modification will also allow for facile detection of small amounts of electroactive species. The sensing of NADH and FAD shows that the chemistry of the nanoscale interface needs to be engineered appropriately to maximize the sensing performance of such electrodes for the analyte of interest. In this way, they can be used for the detection of other analytes such as gases and biomolecules. The effect of other metal nanoparticles such as Pt or Pd on HET kinetics of the edge, as well as on their catalytic properties needs to be investigated and evaluated further.

The development and characterization of a new class of nanoelectrodes based on isolated edges of graphene in this thesis form a promising basis within fundamental electrochemistry and electroanalytical sciences. An obvious challenge to the successful exploration of the above benefits of nanoelectrodes is their fabrication, handling, and the sensitivity of the instrumentation available with which to make reliable electrochemical measurements. One way in which the sensitivity problem can be overcome is by the fabrication of graphene edge nanoelectrodes in other forms such as linear arrays/bands of arrays or ensembles, whereby the individual electrodes in the array operate in parallel thus amplifying the signal while retaining the beneficial characteristics of the nanoelectrodes. One aspect, which may require further attention in future studies, is the effect of different configurations of edges, zigzag or armchair, on electron transfer. In the case of the edge electrodes, because of the extremely high aspect ratio, the edge is always composed of a mixture of both configurations.

10

Appendix

10.1 Electrochemical Oxidation of the Edge

The plasma etching treatment during the GrEdge fabrication can be a possible source of oxidation at the GrEdge,[97] and theoretically, modification of the graphene edge with oxygen groups is expected to modify the observed properties. This has been observed earlier in case of nanoribbons, where such oxygen groups modulated the electronic and magnetic properties.[62,279] The fabricated GrEdge consists of unstable dangling bonds, which upon the exposure to air or highly reactive species can be possibly terminated by oxygen containing groups.

GrEdge-Ox-AuNPs: GrEdge oxidation followed by AuNPs deposition The electrochemical oxidation for the carbon materials like glassy carbon, CNTs, graphite etc. is known to introduce more oxidized carbon species in the material.[280–282] A similar strategy was employed to increase the density of oxygenated carbon species at the GrEdge. The electrochemical oxidation of GrEdge was carried out using CV (figure 10.1b), scanned at anodic potentials between 0.8 V and 1.8 V (vs. Ag/AgCl) in acidic medium (0.5 M H_2SO_4). The oxidized GrEdge is referred as GrEdge-Ox. In acidic medium (as shown in figure 10.1a), the carbon structures such as carbon nanotubes, graphene, and so forth degrade by oxidation and ring opening in the graphitic structure.[280,281] The forward scan of CV shows that the oxidation current of the GrEdge gradually rises with sweeping of the anodic potential, notably at two points. First at around $\sim$ 0.95 V, a slight increase of the current is observable, attributed mainly to carbon oxidation. Then above 1.25 V, there is a large increase in current, which is due to the anodic oxidation of water (OER) and ongoing carbon oxidation. The large increase in current is presumably because the GrEdge undergoes vigorous structural changes and the formation of oxygen-containing functional groups at the edge.

As a consequence, the density of the oxygenated-carbon functional groups increases at the edge. Further, AuNPs were deposited at the oxidized GrEdge for the purpose of SERS. Figure 10.1c shows a typical chronoamperometric profile recorded at the oxidized GrEdge (GrEdge-Ox) electrode, for the attachment of the AuNPs. This was confirmed by AFM and the line profile (figure 10.1d), with an estimated size of the AuNPs at the GrEdge-Ox of ∼ 70 nm. The oxidized GrEdge modified with AuNPs is referred as GrEdge-Ox-AuNPs.

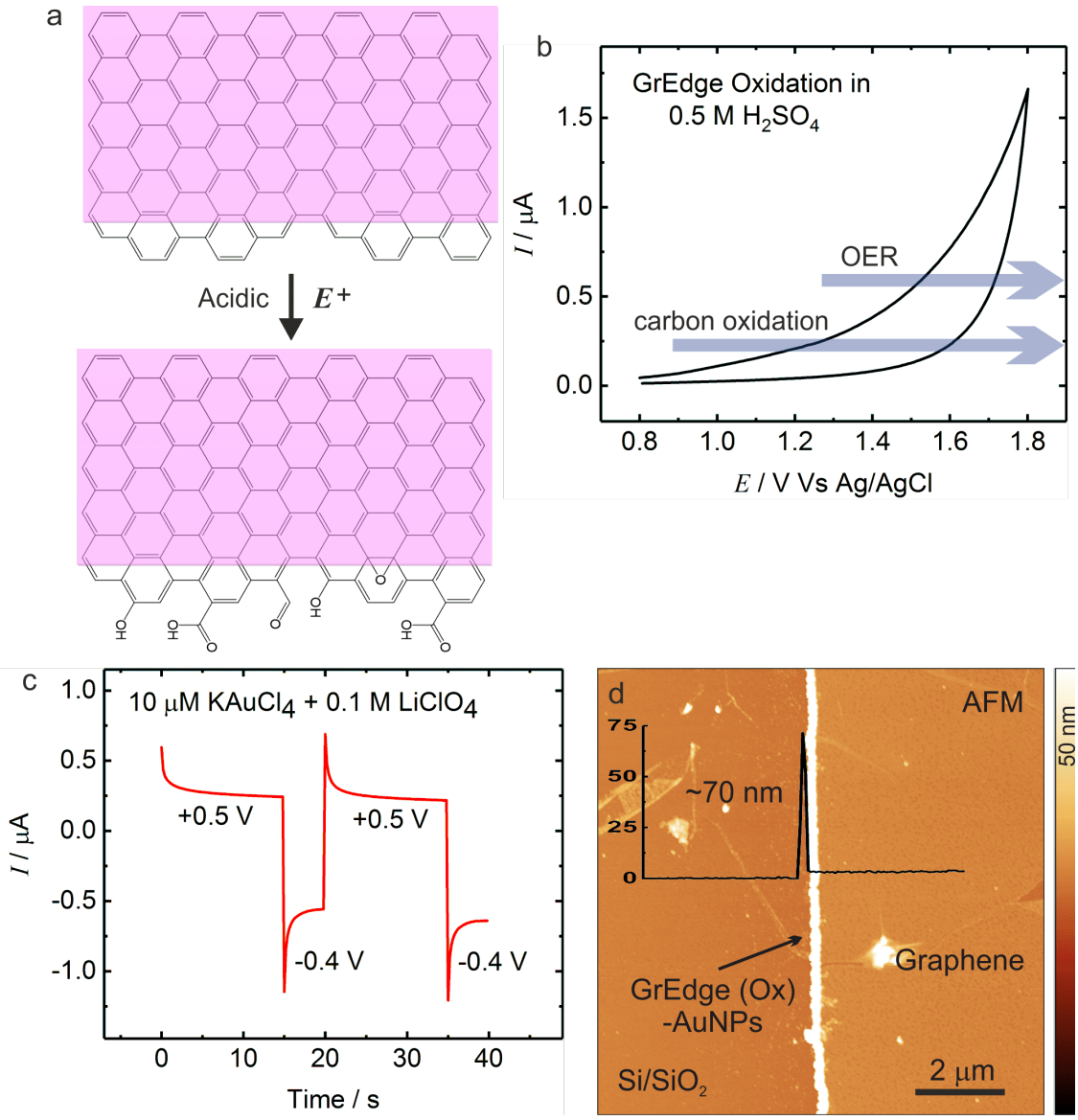

Figure 10.1: (a) Assumed mechanism for the oxidation of graphitic structures in acidic media. (b) CV of GrEdge electrodes at high anodic potentials in 0.5 M H_2SO_4 acidic solution. Scan rate: 50 mVs^{-1}. (c) Chronoamperometric profile for the electrodeposition of AuNPs at an oxidized GrEdge (GrEdge-Ox) electrode with 10 µM $KAuCl_4$ (Supporting electrolyte: 0.1 M $LiClO_4$). (d) AFM image of the oxidized GrEdge after deposition of the AuNPs, GrEdge-Ox-AuNPs.

Raman of GrEdge-Ox-AuNPs The SERS spectrum of GrEdge-Ox-AuNPs in figure 10.2a clearly shows the additional oxygen-related peaks other than the usual graphene related

peaks. The broadening of the signature graphene peaks (*D*, *G*, and *2D*) is an indication of the amorphous carbon, and is attributed to the degradation of the edge after oxidation. In addition, various oxidized carbon peaks are assigned to: epoxide, C−O−C stretching (1052 and 1445 cm^{-1}); hydroxyl, O−H bending (1415 cm^{-1}); and C=C stretching of phenyl rings (1496 and 1548 cm^{-1}).[283,284] Such oxygen-related peaks are however absent in the SERS spectra of the pristine GrEdge as shown in section 6.2.2 (see figure 6.6). This also points towards the theory that oxygen-related functional groups at the pristine GrEdge are present in rather low density, and were not detected by the Raman spectroscopy earlier even after deposition of AuNPs. Therefore, it can be concluded that the electrochemical oxidation of the patterned edge could have resulted in the formation of more oxygen related functionalities, thereby increasing the density of such groups at the edge, and SERS was able to detect them after subsequent AuNPs deposition.

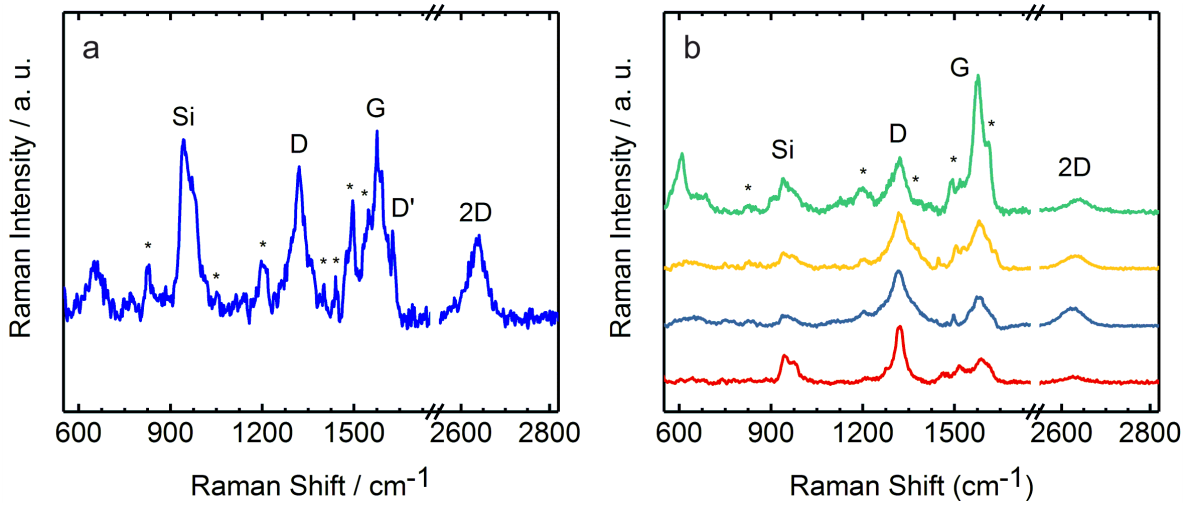

Figure 10.2: (a) Raman spectrum of GrEdge-Ox-AuNPs after the electrochemical oxidation of GrEdge and AuNPs deposition at GrEdge-Ox. (b) Raman spectra of GrEdge-Ox-AuNPs on other edge samples. (λ_{ex}: 633 nm, 4.5 mW, 1 × 1 s)

Bibliography

1. McCreery, R. L. Advanced Carbon Electrode Materials for Molecular Electrochemistry. *Chem. Rev.* **108,** 2646–2687 (2008).
2. Novoselov, K. S. *et al.* Electric Field Effect in Atomically Thin Carbon Films. *Science* **306,** 666–669 (2004).
3. Geim, A. K. & Novoselov, K. S. The rise of graphene. *Nat. Mater.* **6,** 183–91 (2007).
4. Geim, A. K. Graphene: Status and Prospects. *Science* **324,** 1530 (2009).
5. Sundaram, R. S., Gómez-Navarro, C., Balasubramanian, K., Burghard, M. & Kern, K. Electrochemical Modification of Graphene. *Adv. Mater.* **20,** 3050–3053 (2008).
6. Sharma, R., Baik, J. H., Perera, C. J. & Strano, M. S. Anomalously Large Reactivity of Single Graphene Layers and Edges toward Electron Transfer Chemistries. *Nano Lett.* **10,** 398–405 (2010).
7. Pumera, M. Graphene-based nanomaterials and their electrochemistry. *Chem. Soc. Rev.* **39,** 4146–4157 (2010).
8. Ambrosi, A. & Pumera, M. The CVD graphene transfer procedure introduces metallic impurities which alter the graphene electrochemical properties. *Nanoscale* **6,** 472–476 (2014).
9. Brownson, D. A. C., Kelly, P. J. & Banks, C. E. In situ electrochemical characterisation of graphene and various carbon-based electrode materials: an internal standard approach. *RSC Adv.* **5,** 37281–37286 (2015).
10. Shen, A. *et al.* Oxygen Reduction Reaction in a Droplet on Graphite: Direct Evidence that the Edge Is More Active than the Basal Plane. *Angew. Chem. Int. Ed.* **53,** 10804–10808 (2014).
11. Ritzert, N. L., Rodríguez-López, J., Tan, C. & Abruña, H. D. Kinetics of Interfacial Electron Transfer at Single-Layer Graphene Electrodes in Aqueous and Nonaqueous Solutions. *Langmuir* **29,** 1683–1694 (2013).
12. Yuan, W. *et al.* The edge- and basal-plane-specific electrochemistry of a single-layer graphene sheet. *Sci. Rep.* **3,** 2248 (2013).

13. Wang, X. & Dai, H. Etching and narrowing of graphene from the edges. *Nat. Chem.* **2,** 661–5 (2010).

14. Han, M. Y., Ozyilmaz, B., Zhang, Y. & Kim, P. Energy band-gap engineering of graphene nanoribbons. *Phys. Rev. Lett.* **98,** 206805 (2007).

15. Bai, J., Duan, X. & Huang, Y. Rational Fabrication of Graphene Nanoribbons Using a Nanowire Etch Mask. *Nano Lett.* **9,** 2083–2087 (2009).

16. Xie, L., Jiao, L. & Dai, H. Selective Etching of Graphene Edges by Hydrogen Plasma. *J. Am. Chem. Soc.* **132,** 14751–14753 (2010).

17. Yang, R. *et al.* An Anisotropic Etching Effect in the Graphene Basal Plane. *Adv. Mater.* **22,** 4014–4019 (2010).

18. Hwang, W. S. *et al.* Room-Temperature Graphene-Nanoribbon Tunneling Field-Effect Transistors. *npj 2D Mater. Appl.* **3,** 43 (2019).

19. Jia, X., Campos-Delgado, J., Terrones, M., Meunier, V. & Dresselhaus, M. S. Graphene edges: a review of their fabrication and characterization. *Nanoscale* **3,** 86–95 (2011).

20. Magda, G. Z. *et al.* Room-temperature magnetic order on zigzag edges of narrow graphene nanoribbons. *Nature* **514,** 608–611 (2014).

21. Son, Y.-W., Cohen, M. L. & Louie, S. G. Energy Gaps in Graphene Nanoribbons. *Phys. Rev. Lett.* **97,** 216803 (2006).

22. Niyogi, S. *et al.* Chemistry of Single-Walled Carbon Nanotubes. *Acc. Chem. Res.* **35,** 1105–1113 (2002).

23. Müllen, K. & Rabe, J. P. Nanographenes as Active Components of Single-Molecule Electronics and How a Scanning Tunneling Microscope Puts Them To Work. *Acc. Chem. Res.* **41,** 511–520 (2008).

24. Loh, K. P., Bao, Q., Ang, P. K. & Yang, J. The chemistry of graphene. *J. Mater. Chem.* **20,** 2277–2289 (2010).

25. Enoki, T., Fujii, S. & Takai, K. Zigzag and armchair edges in graphene. *Carbon* **50,** 3141–3145 (2012).

26. Bellunato, A., Arjmandi Tash, H., Cesa, Y. & Schneider, G. F. Chemistry at the Edge of Graphene. *ChemPhysChem* **17,** 785–801 (2016).

27. Fujii, S. & Enoki, T. Nanographene and Graphene Edges: Electronic Structure and Nanofabrication. *Acc. Chem. Res.* **46,** 2202–2210 (2013).

28. Li, D., Batchelor-McAuley, C., Chen, L. & Compton, R. G. Band Electrodes in Sensing Applications: Response Characteristics and Band Fabrication Methods. *ACS Sensors* **4,** 2250–2266 (2019).

29. Samuelsson, M., Armgarth, M. & Nylander, C. Microstep electrodes: band ultramicroelectrodes fabricated by photolithography and reactive ion etching. *Anal. Chem.* **63,** 931–936 (1991).

30. Dudin, P. V., Snowden, M. E., Macpherson, J. V. & Unwin, P. R. Electrochemistry at Nanoscale Electrodes: Individual Single-Walled Carbon Nanotubes (SWNTs) and SWNT-Templated Metal Nanowires. *ACS Nano* **5,** 10017–10025 (2011).

31. Kim, J. & Bard, A. J. Electrodeposition of Single Nanometer-Size Pt Nanoparticles at a Tunneling Ultramicroelectrode and Determination of Fast Heterogeneous Kinetics for Ru(NH3)63+ Reduction. *J. Am. Chem. Soc.* **138,** 975–979 (2016).

32. Oja, S. M., Wood, M. & Zhang, B. Nanoscale Electrochemistry. *Anal. Chem.* **85,** 473–486 (2013).

33. Bellunato, A. & Schneider, G. F. Electrophilic radical coupling at the edge of graphene. *Nanoscale* **10,** 12011–12017 (2018).

34. Heller, I. *et al.* Individual Single-Walled Carbon Nanotubes as Nanoelectrodes for Electrochemistry. *Nano Lett.* **5,** 137–142 (2005).

35. Dumitrescu, I., Dudin, P. V., Edgeworth, J. P., Macpherson, J. V. & Unwin, P. R. Electron Transfer Kinetics at Single-Walled Carbon Nanotube Electrodes using Scanning Electrochemical Microscopy. *J. Phys. Chem. C* **114,** 2633–2639 (2010).

36. Mackenzie, D. M. A. *et al.* Batch fabrication of nanopatterned graphene devices via nanoimprint lithography. *Appl. Phys. Lett.* **111,** 193103 (2017).

37. Akhavan, O., Ghaderi, E. & Rahighi, R. Toward Single-DNA Electrochemical Biosensing by Graphene Nanowalls. *ACS Nano* **6,** 2904–2916 (2012).

38. Brownson, D. A. C., Kampouris, D. K. & Banks, C. E. Graphene electrochemistry: fundamental concepts through to prominent applications. *Chem. Soc. Rev.* **41,** 6944–6976 (2012).

39. Li, K., Jiang, J., Dong, Z., Luo, H. & Qu, L. A linear graphene edge nanoelectrode. *Chem. Commun.* **51,** 8765–8768 (2015).

40. Banerjee, S. *et al.* Electrochemistry at the Edge of a Single Graphene Layer in a Nanopore. *ACS Nano* **7,** 834–843 (2013).

41. Xiang, Z., Dai, Q., Chen, J.-F. & Dai, L. Edge Functionalization of Graphene and Two-Dimensional Covalent Organic Polymers for Energy Conversion and Storage. *Adv. Mater.* **28,** 6253–6261 (2016).

42. Jeon, I.-Y. *et al.* Large-Scale Production of Edge-Selectively Functionalized Graphene Nanoplatelets via Ball Milling and Their Use as Metal-Free Electrocatalysts for Oxygen Reduction Reaction. *J. Am. Chem. Soc.* **135,** 1386–1393 (2013).

43. Xu, J. *et al.* Sulfur–Graphene Nanostructured Cathodes via Ball-Milling for High-Performance Lithium–Sulfur Batteries. *ACS Nano* **8,** 10920–10930 (2014).

44. Kobayashi, Y., Fukui, K.-i., Enoki, T., Kusakabe, K. & Kaburagi, Y. Observation of zigzag and armchair edges of graphite using scanning tunneling microscopy and spectroscopy. *Phys. Rev. B* **71,** 193406 (2005).

45. Ziatdinov, M. *et al.* Visualization of electronic states on atomically smooth graphitic edges with different types of hydrogen termination. *Phys. Rev. B* **87,** 115427 (2013).

46. Kato, T. *et al.* Room-Temperature Edge Functionalization and Doping of Graphene by Mild Plasma. *Small* **7,** 574–577 (2011).

47. Cai, J. *et al.* Atomically precise bottom-up fabrication of graphene nanoribbons. *Nature* **466,** 470–473 (2010).

48. Yang, X. *et al.* Two-Dimensional Graphene Nanoribbons. *J. Am. Chem. Soc.* **130,** 4216–4217 (2008).

49. Balasubramanian, K. & Burghard, M. Electrochemically functionalized carbon nanotubes for device applications. *J. Mater. Chem.* **18,** 3071–3083 (2008).

50. Balasubramanian, K., Zuccaro, L. & Kern, K. Tunable Enhancement of Raman Scattering in Graphene-Nanoparticle Hybrids. *Adv. Funct. Mater.* **24,** 6348–6358 (2014).

51. Zuccaro, L., Kern, K. & Balasubramanian, K. Identifying Chemical Functionalization on Individual Carbon Nanotubes and Graphene by Local Vibrational Fingerprinting. *ACS Nano* **9,** 3314–3323 (2015).

52. Niimi, Y. *et al.* Scanning tunneling microscopy and spectroscopy of the electronic local density of states of graphite surfaces near monoatomic step edges. *Phys. Rev. B* **73,** 085421 (2006).

53. Suenaga, K. & Koshino, M. Atom-by-atom spectroscopy at graphene edge. *Nature* **468,** 1088–90 (2010).

54. Kobayashi, Y., Fukui, K.-i., Enoki, T. & Kusakabe, K. Edge state on hydrogen-terminated graphite edges investigated by scanning tunneling microscopy. *Phys. Rev. B* **73,** 125415 (2006).

55. Liu, Z., Suenaga, K., Harris, P. J. & Iijima, S. Open and closed edges of graphene layers. *Phys. Rev. Lett.* **102,** 015501 (2009).

56. Ferrari, A. C. *et al.* Raman spectrum of graphene and graphene layers. *Phys. Rev. Lett.* **97** (2006).

57. Ferrari, A. C. Raman spectroscopy of graphene and graphite: Disorder, electron–phonon coupling, doping and nonadiabatic effects. *Solid State Comm.* **143,** 47–57 (2007).

58. Basko, D. M., Piscanec, S. & Ferrari, A. C. Electron-electron interactions and doping dependence of the two-phonon Raman intensity in graphene. *Phys. Rev. B* **80,** 165413 (2009).

59. Das, A. *et al.* Monitoring dopants by Raman scattering in an electrochemically top-gated graphene transistor. *Nat. Nanotechnol.* **3,** 210–215 (2008).

60. Ferrari, A. C. & Basko, D. M. Raman spectroscopy as a versatile tool for studying the properties of graphene. *Nat. Nanotechnol.* **8,** 235–246 (2013).

61. Casiraghi, C. *et al.* Raman Spectroscopy of Graphene Edges. *Nano Lett.* **9,** 1433–1441 (2009).

62. Cervantes-Sodi, F., Csányi, G., Piscanec, S. & Ferrari, A. C. Edge-functionalized and substitutionally doped graphene nanoribbons: Electronic and spin properties. *Phys. Rev. B* **77,** 165427 (2008).

63. Cançado, L. G. *et al.* Quantifying Defects in Graphene via Raman Spectroscopy at Different Excitation Energies. *Nano Lett.* **11,** 3190–3196 (2011).

64. Schedin, F. *et al.* Surface-Enhanced Raman Spectroscopy of Graphene. *ACS Nano* **4,** 5617–5626 (2010).

65. Heeg, S. *et al.* Polarized Plasmonic Enhancement by Au Nanostructures Probed through Raman Scattering of Suspended Graphene. *Nano Lett.* **13,** 301–308 (2013).

66. Banks, C. E., Compton, R. G., Fisher, A. C. & Henley, I. E. The transport limited currents at insonated electrodes. *Phys. Chem. Chem. Phys.* **6,** 3147–3152 (2004).

67. Brownson, D. A. C. & Banks, C. E. CVD graphene electrochemistry: the role of graphitic islands. *Phys. Chem. Chem. Phys.* **13,** 15825–15828 (2011).

68. Banks, C. E. & Compton, R. G. New electrodes for old: from carbon nanotubes to edge plane pyrolytic graphite. *Analyst* **131,** 15–21 (2006).

69. Davies, T. J., Hyde, M. E. & Compton, R. G. Nanotrench Arrays Reveal Insight into Graphite Electrochemistry. *Angew. Chem., Int. Ed.* **44,** 5121–5126 (2005).

70. Macedo, L. J. A. *et al.* Interplay of non-uniform charge distribution on the electrochemical modification of graphene. *Nanoscale* **10,** 15048–15057 (2018).

71. Heinze, J. Ultramicroelectrodes in Electrochemistry. *Angew. Chem., Int. Ed.* **32,** 1268–1288 (1993).

72. Compton, R. G., Laborda, E. & Ward, K. R. *Understanding Voltammetry* 216 (Imperial College Press, 2013).

73. Lim, C. X., Hoh, H. Y., Ang, P. K. & Loh, K. P. Direct Voltammetric Detection of DNA and pH Sensing on Epitaxial Graphene: An Insight into the Role of Oxygenated Defects. *Anal. Chem.* **82,** 7387–7393 (2010).

74. Ambrosi, A., Chua, C. K., Bonanni, A. & Pumera, M. Electrochemistry of Graphene and Related Materials. *Chem. Rev.* **114,** 7150–7188 (2014).

75. Girit, Ç. Ö. *et al.* Graphene at the Edge: Stability and Dynamics. *Science* **323,** 1705–1708 (2009).

76. Jiang, D.-e., Sumpter, B. G. & Dai, S. Unique chemical reactivity of a graphene nanoribbon's zigzag edge. *J. Chem. Phys.* **126,** 134701 (2007).

77. Yan, L. *et al.* Chemistry and physics of a single atomic layer: strategies and challenges for functionalization of graphene and graphene-based materials. *Chem. Soc. Rev.* **41,** 97–114 (2012).

78. He, K., Lee, G.-D., Robertson, A. W., Yoon, E. & Warner, J. H. Hydrogen-free graphene edges. *Nat. Commun.* **5,** 3040 (2014).

79. Wang, X., Tabakman, S. M. & Dai, H. Atomic Layer Deposition of Metal Oxides on Pristine and Functionalized Graphene. *J. Am. Chem. Soc.* **130,** 8152–8153 (2008).

80. Kaplan, A. *et al.* Current and future directions in electron transfer chemistry of graphene. *Chem. Soc. Rev.* **46,** 4530–4571 (2017).

81. Koskinen, P., Malola, S. & Häkkinen, H. Evidence for graphene edges beyond zigzag and armchair. *Phys. Rev. B* **80,** 073401 (2009).

82. Panico, R., Powell, W. H. & Richer, J.-C. *A Guide to IUPAC Nomenclature of Organic Compounds* ISBN: 0632034882 (Blackwell Science, 1993).

83. Clar, E. The Aromatic Sextet (1972).

84. Wassmann, T., Seitsonen, A. P., Saitta, A. M., Lazzeri, M. & Mauri, F. Clar's Theory, -Electron Distribution, and Geometry of Graphene Nanoribbons. *J. Am. Chem. Soc.* **132,** 3440–3451 (2010).

85. Krygowski, T. M. & Cyrański, M. K. Structural Aspects of Aromaticity. *Chemical Reviews* **101,** 1385–1420 (2001).

86. Randić, M. Aromaticity of Polycyclic Conjugated Hydrocarbons. *Chem. Rev.* **103,** 3449–3606 (2003).

87. Wu, D., Gao, X., Zhou, Z. & Chen, Z. in *Graphene Chemistry* 29–49 (John Wiley & Sons, Ltd, 2013). ISBN: 9781118691281.

88. Baldoni, M., Sgamellotti, A. & Mercuri, F. Electronic properties and stability of graphene nanoribbons: An interpretation based on Clar sextet theory. *Chem. Phys. Lett.* **464,** 202–207 (2008).

89. Wassmann, T., Seitsonen, A. P., Saitta, A. M., Lazzeri, M. & Mauri, F. Structure, Stability, Edge States, and Aromaticity of Graphene Ribbons. *Phys. Rev. Lett.* **101,** 096402 (2008).

90. Seitsonen, A. P., Saitta, A. M., Wassmann, T., Lazzeri, M. & Mauri, F. Structure and stability of graphene nanoribbons in oxygen, carbon dioxide, water, and ammonia. *Phys. Rev. B* **82,** 115425 (2010).

91. Li, X. *et al.* Large-Area Synthesis of High-Quality and Uniform Graphene Films on Copper Foils. *Science* **324,** 1312–1314 (2009).

92. Acik, M. & Chabal, Y. J. Nature of Graphene Edges: A Review. *Jpn. J. Appl. Phys.* **50,** 070101 (2011).

93. Zhi, L. & Müllen, K. A bottom-up approach from molecular nanographenes to unconventional carbon materials. *J. Mater. Chem.* **18,** 1472–1484 (2008).

94. Campos-Delgado, J. *et al.* Bulk Production of a New Form of sp2 Carbon: Crystalline Graphene Nanoribbons. *Nano Lett.* **8,** 2773–2778 (2008).

95. Elías, A. L. *et al.* Longitudinal Cutting of Pure and Doped Carbon Nanotubes to Form Graphitic Nanoribbons Using Metal Clusters as Nanoscalpels. *Nano Lett.* **10,** 366–372 (2010).

96. Kosynkin, D. V. *et al.* Longitudinal unzipping of carbon nanotubes to form graphene nanoribbons. *Nature* **458,** 872–876 (2009).

97. Bottcher, A. *et al.* Nanostructuring the graphite basal plane by focused ion beam patterning and oxygen etching. *Nanotechnology* **17,** 5889–5894 (2006).

98. Jessen, B. S. *et al.* Lithographic band structure engineering of graphene. *Nat. Nanotechnol.* **14,** 340–346 (2019).

99. Wang, M. *et al.* CVD Growth of Large Area Smooth-edged Graphene Nanomesh by Nanosphere Lithography. *Sci. Rep.* **3,** 1238 (2013).

100. Liu, G., Jin, W. & Xu, N. Graphene-based membranes. *Chem. Soc. Rev.* **44,** 5016–5030 (2015).

101. Fischbein, M. D. & Drndić, M. Electron beam nanosculpting of suspended graphene sheets. *Appl. Phys. Lett.* **93,** 113107 (2008).

102. Jones, J., Morris, C., Verbeck, G. & Perez, J. Oxidative pit formation in pristine, hydrogenated and dehydrogenated graphene. *Appl. Surf. Sci.* **264,** 853–863 (2013).

103. Walker, M. I., Weatherup, R. S., Bell, N. A. W., Hofmann, S. & Keyser, U. F. Free-standing graphene membranes on glass nanopores for ionic current measurements. *Appl. Phys. Lett.* **106,** 023119 (2015).

104. Surwade, S. P. *et al.* Water desalination using nanoporous single-layer graphene. *Nat. Nanotechnol.* **10,** 459–464 (2015).

105. Diankov, G., Neumann, M. & Goldhaber-Gordon, D. Extreme Monolayer-Selectivity of Hydrogen-Plasma Reactions with Graphene. *ACS Nano* **7,** 1324–1332 (2013).

106. Wang, W. L. *et al.* Direct Observation of a Long-Lived Single-Atom Catalyst Chiseling Atomic Structures in Graphene. *Nano Lett.* **14,** 450–455 (2014).

107. Chen, L., Hernandez, Y., Feng, X. & Müllen, K. From Nanographene and Graphene Nanoribbons to Graphene Sheets: Chemical Synthesis. *Angew. Chem. Int. Ed.* **51,** 7640–7654 (2012).

108. Chen, Z., Lin, Y.-M., Rooks, M. J. & Avouris, P. Graphene nano-ribbon electronics. *Phys. E.* **40,** 228–232 (2007).

109. Tapasztó, L., Dobrik, G., Lambin, P. & Biró, L. P. Tailoring the atomic structure of graphene nanoribbons by scanning tunnelling microscope lithography. *Nat. Nanotechnol.* **3,** 397–401 (2008).

110. Georgakilas, V. *et al.* Functionalization of Graphene: Covalent and Non-Covalent Approaches, Derivatives and Applications. *Chem. Rev.* **112,** 6156–6214 (2012).

111. Maiti, U. N. *et al.* 25th Anniversary Article: Chemically Modified/Doped Carbon Nanotubes & Graphene for Optimized Nanostructures & Nanodevices. *Adv. Mater.* **26,** 40–67 (2014).

112. Morales-Narváez, E., Baptista-Pires, L., Zamora-Gálvez, A. & Merkoçi, A. Graphene-Based Biosensors: Going Simple. *Adv. Mater.* **29,** 1604905 (2017).

113. Bottari, G. *et al.* Chemical functionalization and characterization of graphene-based materials. *Chem. Soc. Rev.* **46,** 4464–4500 (2017).

114. Santiago-Rodríguez, L., Sánchez-Pomales, G. & Cabrera, C. R. Electrochemical DNA Sensing at Single-walled Carbon Nanotubes Chemically Assembled on Gold Surfaces. *Electroanalysis* **22,** 2817–2824 (2010).

115. Kong, J., Chapline, M. G. & Dai, H. Functionalized Carbon Nanotubes for Molecular Hydrogen Sensors. *Adv. Mater.* **13,** 1384–1386 (2001).

116. Genorio, B. & Znidarsic, A. Functionalization of graphene nanoribbons. *J. Phys. D: Appl. Phys.* **47,** 094012 (2014).

117. Zhang, S., Tang, S., Lei, J., Dong, H. & Ju, H. Functionalization of graphene nanoribbons with porphyrin for electrocatalysis and amperometric biosensing. *J. Electroanal. Chem.* **656,** 285–288 (2011).

118. Chua, C. K. & Pumera, M. Covalent chemistry on graphene. *Chem. Soc. Rev.* **42,** 3222–3233 (2013).

119. Sun, Z. *et al.* Growth of graphene from solid carbon sources. *Nature* **468,** 549–552 (2010).

120. Zhao, W. *et al.* Preparation of graphene by exfoliation of graphite using wet ball milling. *J. Mater. Chem.* **20,** 5817–5819 (2010).

121. Quintana, M. *et al.* Selective organic functionalization of graphene bulk or graphene edges. *Chem. Commun.* **47,** 9330–9332 (2011).

122. He, Y. *et al.* Fusing tetrapyrroles to graphene edges by surface-assisted covalent coupling. *Nat. Chem.* **9,** 33–38 (2017).

123. Wickenburg, S. *et al.* Tuning charge and correlation effects for a single molecule on a graphene device. *Nat. Commun.* **7,** 13553 (2016).

124. Lee, G. & Cho, K. Electronic structures of zigzag graphene nanoribbons with edge hydrogenation and oxidation. *Phys. Rev. B* **79,** 165440 (2009).

125. Wang, X. *et al.* N-Doping of Graphene Through Electrothermal Reactions with Ammonia. *Science* **324,** 768–771 (2009).

126. Quinn, B. M., Dekker, C. & Lemay, S. G. Electrodeposition of Noble Metal Nanoparticles on Carbon Nanotubes. *J. Am. Chem. Soc.* **127,** 6146–6147 (2005).

127. Paulus, G. L. C., Wang, Q. H. & Strano, M. S. Covalent Electron Transfer Chemistry of Graphene with Diazonium Salts. *Acc. Chem. Res.* **46,** 160–170 (2013).

128. Maier, S. A. Plasmonics: Fundamentals and Applications. *Springer Berlin-Heidelberg* (2007).

129. Wang, J., Li, M., Shi, Z., Li, N. & Gu, Z. Electrocatalytic Oxidation of Norepinephrine at a Glassy Carbon Electrode Modified with Single Wall Carbon Nanotubes. *Electroanalysis* **14,** 225–230 (2002).

130. Hernández-Santos, D., González-García, M. B. & García, A. C. Metal-Nanoparticles Based Electroanalysis. *Electroanalysis* **14,** 1225–1235 (2002).

131. Chang, H. *et al.* Catalytic oxidation and determination of -NADH using self-assembly hybrid of gold nanoparticles and graphene. *Analyst* **136,** 2735–2740 (2011).

132. Nguyen, K. T. & Zhao, Y. Integrated graphene/nanoparticle hybrids for biological and electronic applications. *Nanoscale* **6,** 6245–6266 (12 2014).

133. Singh, M. *et al.* Noncovalently Functionalized Monolayer Graphene for Sensitivity Enhancement of Surface Plasmon Resonance Immunosensors. *J. Am. Chem. Soc.* **137,** 2800–2803 (2015).

134. Kim, K. *et al.* Selective metal deposition at graphene line defects by atomic layer deposition. *Nat. Commun.* **5,** 4781 (2014).

135. Schedin, F. *et al.* Detection of individual gas molecules adsorbed on graphene. *Nat. Mater.* **6,** 652 (2007).

136. Corio, P. *et al.* Surface-enhanced resonant Raman spectroscopy of single-wall carbon nanotubes adsorbed on silver and gold surfaces. *Phys. Rev. B* **61,** 13202–13211 (2000).

137. Zan, R., Bangert, U., Ramasse, Q. & Novoselov, K. S. Metal-Graphene Interaction Studied via Atomic Resolution Scanning Transmission Electron Microscopy. *Nano Lett.* **11,** 1087–1092 (2011).

138. Zan, R., Bangert, U., Ramasse, Q. & Novoselov, K. S. Evolution of Gold Nanostructures on Graphene. *Small* **7,** 2868–2872 (2011).

139. Freeman, R. G. *et al.* Self-Assembled Metal Colloid Monolayers: An Approach to SERS Substrates. *Science* **267,** 1629–1632 (1995).

140. Nie, S. & Emory, S. R. Probing Single Molecules and Single Nanoparticles by Surface-Enhanced Raman Scattering. *Science* **275,** 1102–1106 (1997).

141. Choi, H. C., Shim, M., Bangsaruntip, S. & Dai, H. Spontaneous Reduction of Metal Ions on the Sidewalls of Carbon Nanotubes. *J. Am. Chem. Soc.* **124,** 9058–9059 (2002).

142. Jeong, D. W. *et al.* Electron-transfer transparency of graphene: Fast reduction of metal ions on graphene-covered donor surfaces. *Phys. Status Solidi RRL* **9,** 180–186 (2015).

143. Penner, R. M. Mesoscopic Metal Particles and Wires by Electrodeposition. *J. Phys. Chem. B* **106,** 3339–3353 (2002).

144. Bauer, L. A., Birenbaum, N. S. & Meyer, G. J. Biological applications of high aspect ratio nanoparticles. *J. Mater. Chem.* **14,** 517–526 (2004).

145. Walter, E. C. *et al.* Noble and Coinage Metal Nanowires by Electrochemical Step Edge Decoration. *J. Phys. Chem. B* **106,** 11407–11411 (2002).

146. Zangwill, A. *Physics at Surfaces* (Cambridge University Press, 1988).

147. Rice, R. J. & McCreery, R. L. Quantitative relationship between electron transfer rate and surface microstructure of laser-modified graphite electrodes. *Anal. Chem.* **61,** 1637–1641 (1989).

148. Scolari, M. *et al.* Surface Enhanced Raman Scattering of Carbon Nanotubes Decorated by Individual Fluorescent Gold Particles. *J. Phys. Chem. C* **112,** 391–396 (2008).

149. Jiang, J., Zhang, P., Liu, Y. & Luo, H. A novel non-enzymatic glucose sensor based on a Cu-nanoparticle-modified graphene edge nanoelectrode. *Anal. Methods* **9,** 2205–2210 (2017).

150. Higashimura, H. & Kobayashi, S. *Encyclopedia of Polymer Science and Technology, "Oxidative Polymerization", 3rd Edition* (Newyork, Wiley, 2004).

151. Gao, M. *et al.* Aligned Coaxial Nanowires of Carbon Nanotubes Sheathed with Conducting Polymers. *Angew. Chem. Int. Ed.* **39,** 3664–3667 (2000).

152. Huang, J.-E., Li, X.-H., Xu, J.-C. & Li, H.-L. Well-dispersed single-walled carbon nanotube/polyaniline composite films. *Carbon* **41,** 2731–2736 (2003).

153. An, K. H. *et al.* High-Capacitance Supercapacitor Using a Nanocomposite Electrode of Single-Walled Carbon Nanotube and Polypyrrole. *J. Electrochem. Soc.* **149,** A1058 (2002).

154. Chen, J. *et al.* Electrochemical synthesis of polypyrrole/carbon nanotube nanoscale composites using well-aligned carbon nanotube arrays. *Appl. Phys. A* **73,** 129–131 (2001).

155. Zhao, C. *et al.* Polyaniline networks grown on graphene nanoribbons-coated carbon paper with a synergistic effect for high-performance microbial fuel cells. *J. Mater. Chem. A* **1,** 12587–12594 (2013).

156. Kurkina, T. *et al.* Self-Assembled Electrical Biodetector Based on Reduced Graphene Oxide. *ACS Nano* **6,** 5514–5520 (2012).

157. Gupta, A. K., Russin, T. J., Gutierrez, H. R. & Eklund, P. C. Probing Graphene Edges via Raman Scattering. *ACS Nano* **3,** 45–52 (2009).

158. Wehrhold, M. *et al.* pH sensitivity of interfacial electron transfer at a supported graphene monolayer. *Nanoscale* **11,** 14742–14756 (2019).

159. Tuinstra, F. & Koenig, J. L. Raman Spectrum of Graphite. *J. Chem. Phys.* **53,** 1126–1130 (1970).

160. Ferrari, A. C. & Robertson, J. Raman spectroscopy of amorphous, nanostructured, diamond-like carbon, and nanodiamond. *Phil. Trans. R. Soc. A.* **362,** 2477–2512 (2004).

161. Malard, L. M., Pimenta, M. A., Dresselhaus, G. & Dresselhaus, M. S. Raman spectroscopy in graphene. *Phys. Rep.* **473,** 51–87 (2009).

162. Reich, S. & Thomsen, C. Raman spectroscopy of graphite. *Philos. Trans. R. Soc. A* **362,** 2271–2288 (2004).

163. Iqbal, M. W., Iqbal, M. Z., Jin, X., Hwang, C. & Eom, J. Edge Oxidation Effect of Chemical-Vapor-Deposition-Grown Graphene Nanoconstriction. *ACS Appl. Mater. & Interfaces* **6,** 4207–4213 (2014).

164. Faraday, M. X. The Bakerian Lecture. —Experimental relations of gold (and other metals) to light. *Phil. Trans. R. Soc.* **147,** 145–181 (1857).

165. Moskovits, M. Surface-enhanced spectroscopy. *Rev. Mod. Phys.* **57,** 783–826 (1985).

166. Kneipp, K., Kneipp, H., Itzkan, I., Dasari, R. R. & Feld, M. S. Ultrasensitive Chemical Analysis by Raman Spectroscopy. *Chem. Rev.* **99,** 2957–2976 (1999).

167. Brownson, D. A. C., Varey, S. A., Hussain, F., Haigh, S. J. & Banks, C. E. Electrochemical properties of CVD grown pristine graphene: monolayer- vs. quasi-graphene. *Nanoscale* **6,** 1607–1621 (2014).

168. Banks, C. E., Davies, T. J., Wildgoose, G. G. & Compton, R. G. Electrocatalysis at graphite and carbon nanotube modified electrodes: edge-plane sites and tube ends are the reactive sites. *Chem. Commun.,* 829–841 (2005).

169. Cline, K. K., McDermott, M. T. & McCreery, R. L. Anomalously Slow Electron Transfer at Ordered Graphite Electrodes: Influence of Electronic Factors and Reactive Sites. *J. Phys. Chem.* **98,** 5314–5319 (1994).

170. Unwin, P. R., Güell, A. G. & Zhang, G. Nanoscale Electrochemistry of sp2 Carbon Materials: From Graphite and Graphene to Carbon Nanotubes. *Acc. Chem. Res.* **49,** 2041–2048 (2016).

171. Patel, A. N. *et al.* A New View of Electrochemistry at Highly Oriented Pyrolytic Graphite. *J. Am. Chem. Soc.* **134,** 20117–20130 (2012).

172. Ambrosi, A., Bonanni, A. & Pumera, M. Electrochemistry of folded graphene edges. *Nanoscale* **3,** 2256–2260 (2011).

173. Banks, C. E. & Compton, R. G. Exploring the electrocatalytic sites of carbon nanotubes for NADH detection: an edge plane pyrolytic graphite electrode study. *Analyst* **130,** 1232–1239 (2005).

174. Li, W., Tan, C., Lowe, M. A., Abruña, H. D. & Ralph, D. C. Electrochemistry of Individual Monolayer Graphene Sheets. *ACS Nano* **5,** 2264–2270 (2011).

175. Valota, A. T. *et al.* Electrochemical Behavior of Monolayer and Bilayer Graphene. *ACS Nano* **5,** 8809–8815 (2011).

176. Velický, M. *et al.* Electron Transfer Kinetics on Mono- and Multilayer Graphene. *ACS Nano* **8,** 10089–10100 (2014).

177. Lee, Y. H. & Tsao, G. T. *Dissolved oxygen electrodes* in *Advances in Biochemical Engineering, Volume 13* (eds Ghose, T. K., Blakebrough, N. & Fiechter, A.) (Springer Berlin Heidelberg, Berlin, Heidelberg, 1979), 35–86. ISBN: 978-3-540-35216-7.

178. Wightman, R. M. Microvoltammetric electrodes. *Anal. Chem.* **53,** 1125A–1134A (1981).

179. Bond, A., Fleischmann, M. & Robinson, J. Electrochemistry in organic solvents without supporting electrolyte using platinum microelectrodes. *J. Electroanal. Chem.* **168,** 299–312 (1984).

180. Bard, A. J. & Faulkner, L. R. *Electrochemical Methods: Fundamentals and Applications, 2nd Edition* (John Wiley and Sons, 2000).

181. Penner, R. M., Heben, M. J., Longin, T. L. & Lewis, N. S. Fabrication and Use of Nanometer-Sized Electrodes in Electrochemistry. *Science* **250,** 1118–1121 (1990).

182. Sun, P. & Mirkin, M. V. Kinetics of Electron-Transfer Reactions at Nanoelectrodes. *Anal. Chem.* **78,** 6526–6534 (2006).

183. Watkins, J. J. *et al.* Zeptomole Voltammetric Detection and Electron-Transfer Rate Measurements Using Platinum Electrodes of Nanometer Dimensions. *Anal. Chem.* **75,** 3962–3971 (2003).

184. Li, Y., Bergman, D. & Zhang, B. Preparation and Electrochemical Response of 1-3 nm Pt Disk Electrodes. *Anal. Chem.* **81,** 5496–5502 (2009).

185. Velmurugan, J., Sun, P. & Mirkin, M. V. Scanning Electrochemical Microscopy with Gold Nanotips: The Effect of Electrode Material on Electron Transfer Rates. *J. Phys. Chem. C* **113,** 459–464 (2009).

186. Aoki, K., Tokuda, K. & Matsuda, H. Theory of stationary current-potential curves at microdisk electrodes for quasi-reversible and totally irreversible electrode reactions. *J. Electroanal. Chem.* **235,** 87–96 (1987).

187. Fleischmann, M., Bandyopadhyay, S. & Pons, S. The behavior of microring electrodes. *J. Phys. Chem.* **89,** 5537–5541 (1985).

188. Oldham, K. B. & Zoski, C. G. Comparison of voltammetric steady states at hemispherical and disc microelectrodes. *J. Electroanal. Chem.* **256,** 11–19 (1988).

189. Mirkin, M. V. & Bard, A. J. Simple analysis of quasi-reversible steady-state voltammograms. *Anal. Chem.* **64,** 2293–2302 (1992).

190. Ambrosi, A. & Pumera, M. Electrochemistry at CVD Grown Multilayer Graphene Transferred onto Flexible Substrates. *The Journal of Physical Chemistry C* **117,** 2053–2058 (2013).

191. Li, X. *et al.* Transfer of Large-Area Graphene Films for High-Performance Transparent Conductive Electrodes. *Nano Lett.* **9,** 4359–4363 (2009).

192. Kim, K. S. *et al.* Large-scale pattern growth of graphene films for stretchable transparent electrodes. *Nature* **457,** 706–710 (2009).

193. Song, J. *et al.* A general method for transferring graphene onto soft surfaces. *Nat. Nanotechnol.* **8,** 356–362 (2013).

194. Hu, F. M., Ma, T., Lin, H.-Q. & Gubernatis, J. E. Magnetic impurities in graphene. *Phys. Rev. B* **84,** 075414 (2011).

195. Iost, R. M. *et al.* Enhancing the Electrochemical and Electronic Performance of CVD-Grown Graphene by Minimizing Trace Metal Impurities. *ChemElectroChem* **1,** 2070–2074 (2014).

196. Temple, P. A. & Hathaway, C. E. Multiphonon Raman Spectrum of Silicon. *Phys. Rev. B* **7,** 3685–3697 (1973).

197. Rao, C. N. R., Sood, A. K., Subrahmanyam, K. S. & Govindaraj, A. Graphene: The New Two-Dimensional Nanomaterial. *Angew. Chem., Int. Ed.* **48,** 7752–7777 (2009).

198. Wang, Q. H. *et al.* Understanding and controlling the substrate effect on graphene electron-transfer chemistry via reactivity imprint lithography. *Nat. Chem.* **4,** 724 (2012).

199. Chen, J. H. *et al.* Charged-impurity scattering in graphene. *Nat. Phys.* **4,** 377–381 (2008).

200. Zhang, Y., Brar, V. W., Girit, C., Zettl, A. & Crommie, M. F. Origin of spatial charge inhomogeneity in graphene. *Nat. Phys.* **5,** 722–726 (2009).

201. Güell, A. G., Ebejer, N., Snowden, M. E., Macpherson, J. V. & Unwin, P. R. Structural Correlations in Heterogeneous Electron Transfer at Monolayer and Multilayer Graphene Electrodes. *J. Am. Chem. Soc.* **134,** 7258–7261 (2012).

202. Bard, A. J. Effect of Electrode Configuration and Transition Time in Solid Electrode Chronopotentiometry. *Anal. Chem.* **33,** 11–15 (1961).

203. Myland, J. C. & Oldham, K. B. Experimental study of the edge effect at an inlaid electrode. *J. Electroanal. Chem.* **147,** 295–300 (1983).

204. Peter, Y. Y. & Cardona, M. *Fundamentals of semiconductors: Physics and Materials Properties* ISBN: 978-3-642-00710-1 (Springer, Berlin, Heidelberg, 2010).

205. Chae, D.-H. *et al.* Excitonic Fano Resonance in Free-Standing Graphene. *Nano Lett.* **11,** 1379–1382 (2011).

206. Nair, R. R. *et al.* Fine Structure Constant Defines Visual Transparency of Graphene. *Science* **320,** 1308 (2008).

207. Ghosh, S. K., Nath, S., Kundu, S., Esumi, K. & Pal, T. Solvent and Ligand Effects on the Localized Surface Plasmon Resonance (LSPR) of Gold Colloids. *J. Phys. Chem. B* **108,** 13963–13971 (2004).

208. Mooradian, A. Photoluminescence of Metals. *Phys. Rev. Lett.* **22,** 185–187 (1969).

209. Boyd, G. T., Yu, Z. H. & Shen, Y. R. Photoinduced luminescence from the noble metals and its enhancement on roughened surfaces. *Phys. Rev. B* **33,** 7923–7936 (1986).

210. Beversluis, M. R., Bouhelier, A. & Novotny, L. Continuum generation from single gold nanostructures through near-field mediated intraband transitions. *Phys. Rev. B* **68,** 115433 (2003).

211. Tam, F., Goodrich, G. P., Johnson, B. R. & Halas, N. J. Plasmonic Enhancement of Molecular Fluorescence. *Nano Lett.* **7,** 496–501 (2007).

212. Haynes, C. L. & Van Duyne, R. P. Plasmon-Sampled Surface-Enhanced Raman Excitation Spectroscopy. *J. Phys. Chem. B* **107,** 7426–7433 (2003).

213. Balasubramanian, K. *et al.* Electrical Transport and Confocal Raman Studies of Electrochemically Modified Individual Carbon Nanotubes. *Adv. Mater.* **15,** 1515–1518 (2003).

214. Heinze, J., Frontana-Uribe, B. A. & Ludwigs, S. Electrochemistry of Conducting Polymers-Persistent Models and New Concepts. *Chem. Rev.* **110,** 4724–4771 (2010).

215. Massoumi, B., Aali, N. & Jaymand, M. Novel nanostructured star-shaped polyaniline derivatives and their electrospun nanofibers with gelatin. *RSC Adv.* **5,** 107680–107693 (2015).

216. Zuccaro, L., Krieg, J., Desideri, A., Kern, K. & Balasubramanian, K. Tuning the isoelectric point of graphene by electrochemical functionalization. *Sci. Rep.* **5,** 11794 (2015).

217. Laurentius, L. *et al.* Diazonium-Derived Aryl Films on Gold Nanoparticles: Evidence for a Carbon–Gold Covalent Bond. *ACS Nano* **5,** 4219–4227 (2011).

218. Liu, Y.-C. & McCreery, R. L. Reactions of Organic Monolayers on Carbon Surfaces Observed with Unenhanced Raman Spectroscopy. *J. Am. Chem. Soc.* **117,** 11254–11259 (1995).

219. Dyke, C. A. & Tour, J. M. Covalent Functionalization of Single-Walled Carbon Nanotubes for Materials Applications. *J. Phys. Chem. A* **108,** 11151–11159 (2004).

220. Shul, G., Ruiz, C. A. C., Rochefort, D., Brooksby, P. A. & Bélanger, D. Electrochemical functionalization of glassy carbon electrode by reduction of diazonium cations in protic ionic liquid. *Electrochim. Acta* **106,** 378–385 (2013).

221. Li, Q., Batchelor-McAuley, C., Lawrence, N. S., Hartshorne, R. S. & Compton, R. G. The synthesis and characterisation of controlled thin sub-monolayer films of 2-anthraquinonyl groups on graphite surfaces. *New J. Chem.* **35,** 2462–2470 (2011).

222. Ni, Z. H. *et al.* On Resonant Scatterers As a Factor Limiting Carrier Mobility in Graphene. *Nano Lett.* **10,** 3868–3872 (2010).

223. Ferrari, A. C. & Robertson, J. Interpretation of Raman spectra of disordered and amorphous carbon. *Phys. Rev. B* **61,** 14095–14107 (2000).

224. Chou, S. G. *et al.* Length characterization of DNA-wrapped carbon nanotubes using Raman spectroscopy. *Appl. Phys. Lett.* **90,** 131109 (2007).

225. Hulman, M., Skákalová, V., Roth, S. & Kuzmany, H. Raman spectroscopy of single-wall carbon nanotubes and graphite irradiated by γ rays. *J. Appl. Phys.* **98,** 024311 (2005).

226. Lucchese, M. *et al.* Quantifying ion-induced defects and Raman relaxation length in graphene. *Carbon* **48,** 1592–1597 (2010).

227. Martins Ferreira, E. H. *et al.* Evolution of the Raman spectra from single-, few-, and many-layer graphene with increasing disorder. *Phys. Rev. B* **82,** 125429 (2010).

228. Clarkson, J. & Ewen Smith, W. A DFT analysis of the vibrational spectra of nitrobenzene. *J. Mol. Struct.* **655,** 413–422 (2003).

229. Minaev, B. F., Bondarchuk, S. V. & Gîrţu, M. A. DFT study of electronic properties, structure and spectra of aryl diazonium cations. *J. Mol. Struct.* **904,** 14–20 (2009).

230. Tao, L. *et al.* Edge-rich and dopant-free graphene as a highly efficient metal-free electrocatalyst for the oxygen reduction reaction. *Chem. Commun.* **52,** 2764–2767 (2016).

231. Schneider, G. F. *et al.* DNA Translocation through Graphene Nanopores. *Nano Lett.* **10,** 3163–3167 (2010).

232. Zhang, Z., Zhang, J., Chen, N. & Qu, L. Graphene quantum dots: an emerging material for energy-related applications and beyond. *Energy Environ. Sci.* **5,** 8869–8890 (2012).

233. Yadav, A. *et al.* Selective electrochemical functionalization of the graphene edge. *Chem. Sci.* **10,** 936–942 (2019).

234. Sun, P., Zhang, Z., Guo, J. & Shao, Y. Fabrication of Nanometer-Sized Electrodes and Tips for Scanning Electrochemical Microscopy. *Anal. Chem.* **73,** 5346–5351 (2001).

235. Liu, B., Rolland, J. P., DeSimone, J. M. & Bard, A. J. Fabrication of Ultramicroelectrodes Using A "Teflon-like" Coating Material. *Anal. Chem.* **77,** 3013–3017 (2005).

236. Campbell, J. K., Sun, L. & Crooks, R. M. Electrochemistry Using Single Carbon Nanotubes. *J. Am. Chem. Soc.* **121,** 3779–3780 (1999).

237. Day, T. M., Unwin, P. R. & Macpherson, J. V. Factors Controlling the Electrodeposition of Metal Nanoparticles on Pristine Single Walled Carbon Nanotubes. *Nano Lett.* **7,** 51–57 (2007).

238. Reiser, A. *et al.* The molecular mechanism of novolak–diazonaphthoquinone resists. *Eur. Polym. J.* **38,** 619–629 (2002).

239. Teh, W. H., Dürig, U., Drechsler, U., Smith, C. G. & Güntherodt, H.-J. Effect of low numerical-aperture femtosecond two-photon absorption on (SU-8) resist for ultrahigh-aspect-ratio microstereolithography. *J. Appl. Phys.* **97,** 054907 (2005).

240. Yang, R., Shi, Z. W., Zhang, L. C., Shi, D. X. & Zhang, G. Y. Observation of Raman G-Peak Split for Graphene Nanoribbons with Hydrogen-Terminated Zigzag Edges. *Nano Lett.* **11,** 4083–4088 (2011).

241. Elias, D. C. *et al.* Control of Graphene's Properties by Reversible Hydrogenation: Evidence for Graphane. *Science* **323,** 610–613 (2009).

242. Sahin, H., Leenaerts, O., Singh, S. K. & Peeters, F. M. Graphane. *Wiley Interdiscip. Rev.: Comput. Mol. Sci.* **5,** 255–272 (2015).

243. Wang, Y. *et al.* Toward High Throughput Interconvertible Graphane-to-Graphene Growth and Patterning. *ACS Nano* **4,** 6146–6152 (2010).

244. Mirkin, M. V., Richards, T. C. & Bard, A. J. Scanning electrochemical microscopy. 20. Steady-state measurements of the fast heterogeneous kinetics in the ferrocene/acetonitrile system. *J. Phys. Chem. C* **97,** 7672–7677 (1993).

245. Wang, Y., Velmurugan, J. & Mirkin, M. V. Kinetics of Charge-Transfer Reactions at Nanoscopic Electrochemical Interfaces. *Isr. J. Chem.* **50,** 291–305 (2010).

246. Sun, Z., Kohama, S.-i., Zhang, Z., Lomeda, J. R. & Tour, J. M. Soluble graphene through edge-selective functionalization. *Nano Res.* **3,** 117–125 (2010).

247. Sheridan, E., Hjelm, J. & Forster, R. J. Electrodeposition of gold nanoparticles on fluorine-doped tin oxide: Control of particle density and size distribution. *J. Electroanal. Chem.* **608,** 1–7 (2007).

248. Eustis, S. & El-Sayed, M. Aspect Ratio Dependence of the Enhanced Fluorescence Intensity of Gold Nanorods: Experimental and Simulation Study. *J. Phys. Chem. B* **109,** 16350–16356 (2005).

249. Cochet, M. *et al.* Theoretical and experimental vibrational study of polyaniline in base forms: non-planar analysis. Part I. *J. Raman Spectrosc.* **31,** 1029–1039 (2000).

250. Cochet, M., Louarn, G., Quillard, S., Buisson, J. P. & Lefrant, S. Theoretical and experimental vibrational study of emeraldine in salt form. Part II. *J. Raman Spectrosc.* **31,** 1041–1049 (2000).

251. Lambert, J. B., Shurvell, H. F., Lightner, D. A. & Cooks, R. G. *Introduction to organic spectroscopy* ISBN: 0023673001 (Macmillan Publishing Company, 1987).

252. Bernard, M. C. & Hugot-Le Goff, A. Quantitative characterization of polyaniline films using Raman spectroscopy: I: Polaron lattice and bipolaron. *Electrochim. Acta* **52,** 595–603 (2006).

253. Bernard, M.-C., Cordoba de Torresi, S. & Goff, A. H.-L. In situ Raman study of sulfonate-doped polyaniline. *Electrochim. Acta* **44,** 1989–1997 (1999).

254. Lai, S. C. S., Patel, A. N., McKelvey, K. & Unwin, P. R. Definitive Evidence for Fast Electron Transfer at Pristine Basal Plane Graphite from High-Resolution Electrochemical Imaging. *Angew. Chem., Int. Ed.* **51,** 5405–5408 (2012).

255. Yadav, A., Wehrhold, M., Neubert, T. J., Iost, R. M. & Balasubramanian, K. Fast Electron Transfer Kinetics at an Isolated Graphene Edge Nanoelectrode with and without Nanoparticles: Implications for Sensing Electroactive Species. *ACS Appl. Nano Mater.* **3,** 11725–11735 (2020).

256. Wehmeyer, K. R., Deakin, M. R. & Wightman, R. M. Electroanalytical properties of band electrodes of submicrometer width. *Anal. Chem.* **57,** 1913–1916 (1985).

257. Rand, D. & Woods, R. A study of the dissolution of platinum, palladium, rhodium and gold electrodes in 1 m sulphuric acid by cyclic voltammetry. *J. Electroanal. Chem. Interf. Electrochem.* **35,** 209–218 (1972).

258. Xia, S. & Birss, V. A multi-technique study of compact and hydrous Au oxide growth in 0.1 M sulfuric acid solutions. *J. Electroanal. Chem.* **500,** 562–573 (2001).

259. ZHANG, W., BAS, A. D., GHALI, E. & CHOI, Y. Passive behavior of gold in sulfuric acid medium. *Transactions of Nonferrous Metals Society of China* **25,** 2037–2046 (2015).

260. Yoo, J. J. *et al.* Ultrathin Planar Graphene Supercapacitors. *Nano Lett.* **11,** 1423–1427 (2011).

261. Wei, C. *et al.* Approaches for measuring the surface areas of metal oxide electrocatalysts for determining their intrinsic electrocatalytic activity. *Chem. Soc. Rev.* **48,** 2518–2534 (2019).

262. Kim, J. & Bard, A. J. Application of the Koutecký-Levich Method to the Analysis of Steady State Voltammograms with Ultramicroelectrodes. *Anal. Chem.* **88,** 1742–1747 (2016).

263. Mirkin, M. V. in *Handbook of Electrochemistry* (ed Zoski, C. G.) 639–660 (Elsevier, Amsterdam, 2007). ISBN: 978-0-444-51958-0.

264. Fischer, A. E., Show, Y. & Swain, G. M. Electrochemical Performance of Diamond Thin-Film Electrodes from Different Commercial Sources. *Anal. Chem.* **76,** 2553–2560 (2004).

265. Szabo, A., Cope, D. K., Tallman, D. E., Kovach, P. M. & Wightman, R. Chronoamperometric current at hemicylinder and band microelectrodes: Theory and experiment. . *Electroanal. Chem.* **217,** 417–423 (1987).

266. Xu, M. *et al.* Nanoskiving fabrication of size-controlled Au nanowire electrodes for electroanalysis. *Analyst* **144,** 2914–2921 (2019).

267. Zhang, Y. *et al.* Single gold nanowire electrodes and single Pt@Au nanowire electrodes: electrochemistry and applications. *Chem. Commun.* **53,** 2850–2853 (2017).

268. Chen, S. & Kucernak, A. Electrocatalysis under Conditions of High Mass Transport: Investigation of Hydrogen Oxidation on Single Submicron Pt Particles Supported on Carbon. *J. Phys. Chem. B* **108,** 13984–13994 (2004).

269. Moiroux, J. & Elving, P. J. Mechanistic aspects of the electrochemical oxidation of dihydronicotinamide adenine dinucleotide (NADH). *J. Am. Chem. Soc.* **102,** 6533–6538 (1980).

270. Pumera, M. *et al.* A Mechanism of Adsorption of -Nicotinamide Adenine Dinucleotide on Graphene Sheets: Experiment and Theory. *Chemistry – A European Journal* **15,** 10851–10856 (2009).

271. Wang, J. & Musameh, M. Carbon Nanotube/Teflon Composite Electrochemical Sensors and Biosensors. *Anal. Chem.* **75,** 2075–2079 (2003).

272. Raju, D. *et al.* Polymer modified carbon fiber-microelectrodes and waveform modifications enhance neurotransmitter metabolite detection. *Anal. Methods* **11,** 1620–1630 (2019).

273. Mohanaraj, S. *et al.* Gold Nanoparticle Modified Carbon Fiber Microelectrodes for Enhanced Neurochemical Detection. *JoVE* **147,** e59552 (2019).

274. Pumera, M. Electrochemical properties of double wall carbon nanotube electrodes. *Nanoscale Res. Lett.* **2,** 87 (2007).

275. Hefti, M. H., Vervoort, J. & van Berkel, W. J. H. Deflavination and reconstitution of flavoproteins. *Eur. J. Biochem.* **270,** 4227–4242 (2003).

276. McDermott, M. T., Kneten, K. & McCreery, R. L. Anthraquinonedisulfonate adsorption, electron-transfer kinetics, and capacitance on ordered graphite electrodes: the important role of surface defects. *J. Phys. Chem.* **96,** 3124–3130 (1992).

277. Kneten, K. R. & McCreery, R. L. Effects of redox system structure on electron-transfer kinetics at ordered graphite and glassy carbon electrodes. *Anal. Chem.* **64,** 2518–2524 (1992).

278. Tan, C. *et al.* Reactivity of Monolayer Chemical Vapor Deposited Graphene Imperfections Studied Using Scanning Electrochemical Microscopy. *ACS Nano* **6,** 3070–3079 (2012).

279. Hod, O., Barone, V., Peralta, J. E. & Scuseria, G. E. Enhanced half-metallicity in edge-oxidized zigzag graphene nanoribbons. *Nano Lett.* **7,** 2295–9 (2007).

280. Dimiev, A. M. & Tour, J. M. Mechanism of Graphene Oxide Formation. *ACS Nano* **8,** 3060–3068 (2014).

281. Yi, Y. *et al.* Electrochemical corrosion of a glassy carbon electrode. *Catal. Today* **295,** 32–40 (2017).

282. Yi, Y. *et al.* Electrochemical Degradation of Multiwall Carbon Nanotubes at High Anodic Potential for Oxygen Evolution in Acidic Media. *ChemElectroChem* **2,** 1929–1937 (2015).

283. Kumarasinghe, A. R. *et al.* Self-Assembled Multilayer Graphene Oxide Membrane and Carbon Nanotubes Synthesized Using a Rare Form of Natural Graphite. *J. Phys. Chem. C* **117,** 9507–9519 (2013).

284. Wang, L., Zhao, J., Sun, Y.-Y. & Zhang, S. B. Characteristics of Raman spectra for graphene oxide from ab initio simulations. *J. Chem. Phys.* **135,** 184503 (2011).

Publications

Publications related to the work submitted in this thesis:

1. **Anur Yadav**, Michel Wehrhold, Tilmann J. Neubert, Rodrigo M. Iost and Kannan Balasubramanian, Fast Electron Transfer Kinetics at an Isolated Graphene Edge Nanoelectrode with and without Nanoparticles: Implications for Sensing Electroactive Species. *ACS Appl. Nano Mater.* 2020, 3, 11725-11735.

2. **Anur Yadav**, Rodrigo M. Iost, Tilmann J. Neubert, Sema Baylan, Thomas Schmid, and Kannan Balasubramanian, Selective electrochemical functionalization of the graphene edge. *Chem. Sci.* 2019, 10, 936-942.

3. Lucyano J. A. Macedo, Filipe C. D. A. Lima, Rodrigo G. Amorim, Raul O. Freitas, **Anur Yadav**, Rodrigo M. Iost, Kannan Balasubramanian and Frank N. Crespilho, Interplay of non-uniform charge distribution on the electrochemical modification of graphene. *Nanoscale* 2018, 10, 15048-15057.

4. Michel Wehrhold, Tilmann J. Neubert, **Anur Yadav**, Martin Vondráček, Rodrigo M. Iost, Jan Honolka and Kannan Balasubramanian. pH sensitivity of interfacial electron transfer at a supported graphene monolayer. *Nanoscale* 2019, 11, 14742-14756.

Other Publications:

5. Nur Selin Kaya, **Anur Yadav**, Michel Wehrhold, Laura Zuccaro and Kannan Balasubramanian, Binding Kinetics of Methylene Blue on Monolayer Graphene Investigated by Multiparameter Surface Plasmon Resonance. *ACS Omega* 2018, 3, 7133-7140.

6. Pradeep K. R., Debdipto Acharya, Priyanka Jain, Kushagra Gahlot, **Anur Yadav**, Andrea Camellini, Margherita Zavelani-Rossi, Giulio Cerullo, Chandrabhas Narayana, Shobhana Narasimhan and Ranjani Viswanatha, Harvesting Delayed Fluorescence in Perovskite Nanocrystals Using Spin-Forbidden Mn d States. *ACS Energy Lett.* 2020, 5, 353-359.

7. Bharat Tandon, **Anur Yadav**, Deepak Khurana, Pranavi Reddy, Pralay K. Santra, and Angshuman Nag, Size-Induced Enhancement of Carrier Density, LSPR Quality Factor,

and Carrier Mobility in Cr-Sn Doped In_2O_3 Nanocrystals. *Chem. Mater.* 2017, 29, 9360-9368.

8. **Anur Yadav**, Bharat Tandon and Angshuman Nag, Reduction of Mn^{3+} to Mn^{2+} and near infrared plasmonics from Mn-Sn codoped In_2O_3 nanocrystals. *RSC Adv.* 2016, 6, 79153-79159.

9. Bharat Tandon, **Anur Yadav** and Angshuman Nag, Delocalized Electrons Mediated Magnetic Coupling in Mn-Sn Codoped In_2O_3 Nanocrystals: Plasmonics Shows the Way. *Chem. Mater.* 2016, 28, 3620-3624.

Thesis DOI: https://doi.org/10.18452/23114